

REMARKS

Claims 34-36 and 38-54 are pending. Claims 1-33 and 37 are canceled. Claims 34, 38, 40, 41, 43, 44, 47, 48, 50, 51 and 52 are amended to more closely recite the subject matter that the Applicant regards as his invention. Claim 54 is new.

Claim 34 has been amended by combination with a portion of claim 50, and claim 50 has been amended by deleting those portions combined with claim 34. Support for the amended claims can also be found in the specification at, e.g., ¶¶ 29-33, 46, 51-53, 58 and 66.¹

Support for the amendments to claim 38, 40 and 41 can be found in the specification respectively: at, e.g., ¶¶ 23 and 76; at, e.g., ¶ 68; and at, e.g., ¶ 69 and Fig. 5. Support for the amendments to claim 47 and also for new claim 54 can be found in the specification at, e.g., ¶¶ 31-33. Claim 48 has been amended to depend from new claim 54.

Claims 51 and 52 have been amended without change of scope to have proper antecedent basis with respect to their amended parent claims 34 and 50. Support for these amendments can also be found in the specification at, e.g., ¶¶ 49 and 56.

Finally, claim 43 has been amended to properly depend from claim 41.

It is submitted that these amended and new claims introduce no new matter; their entry is respectfully requested.

INTERVIEW SUMMARY

The undersigned thanks the Examiner for the thoughtful and in-depth interview of 08/11/2011. In this interview, the Applicant discussed the nature of the invention, how claim 34 recites the invention, and the Moriceau reference (US 6756286).

Specifically, the Applicant explained that the spongy transformation of the intermediate layer is caused by the extrinsic atoms which were deposited along with that layer in the first depositing step. Atoms implanted after deposition of the intermediate layer, e.g., by implantation, are not part of the invention.

This feature is recited in the third step of amended claim 34 by virtue of the limitation that "the as-deposited extrinsic atoms or molecules ... [cause] an irreversible formation of

¹ All references to the specification and figures are to US 2008/0038564 A1 published February 14, 2008.

microbubbles or microcavities in the intermediate layer.” The “as-deposited extrinsic atoms or molecules” refers of course to the “extrinsic atoms or molecules” deposited in the first depositing step. In other words, the “as-deposited” limitation means that the “extrinsic atoms or molecules” are necessary and sufficient for the spongy transformation. Other materials may be present in the intermediate layer other than the base material and extrinsic atoms, but such other materials do not cause the spongy transformation and are not part of the invention.

The Examiner did not disagree that amended claim 34 is limited to the “extrinsic atoms or molecules” that were deposited in the first depositing step, but did request Applicant in the response to the pending Office action to point to support in the specification for this amendment.²

The Applicant then discussed the Moriceau reference and pointed out that Moriceau never describes or suggests that “as-deposited extrinsic atoms or molecules” can cause a spongy transformation. The Office Action contends the opposite and cites several portions of Moriceau for support. These cited portions describe formation of inclusions, which are roughly analogous to the “microbubbles or microcavities” of this invention. Applicant submitted that in all cited portions inclusions that are not solid, and thus that might be “microbubbles or microcavities,” are formed by implantation. In the only cited portion where inclusions are not formed by implantation, they are oxygen precipitates which are solid.

The Examiner did not disagree with the Applicant’s points concerning Moriceau and thus that disclosure does not teach “microbubbles or microcavities” as in this invention.

CLAIM OBJECTIONS

Claims 37, 44 and 47 are objected to for various reasons.

In response, claim 37 has been canceled; claim 44 has been amended as required; and claim 47 has been amended to delete the word “or.”

Claim 47 has been further amended to clarify that preferred intermediate layers can comprise “phospho-silicate glasses” or “boro-phospho-silicate glasses.” However, preferred intermediate layers cannot comprise “boro-silicate glass” alone, that is a glass without any phosphorous at all. See the specification at, e.g., ¶¶ 31-33.

² If the Examiner later disagrees that amended claim 34 is limited as described, the Applicant earnestly requests the opportunity to correct the amended claim, prior to the issuance of a further Action, in such a manner

It is submitted that these amendments overcome the rejections, and their withdrawal is respectfully requested.

THE INVENTION

The present invention is directed to fabricating and using multilayer substrates which include at least one insulating intermediate layer that becomes spongy is thereby weakened by a suitable heat so that the substrates become releasable.

The characteristics of the intermediate layer are key to the invention, and one particularly key characteristic of the intermediate layer is that, upon suitable heat treatment, it becomes filled with numerous "microbubbles or microcavities" (referred to herein as a "spongy-transformation") and is, therefore, weakened. But even more key is that such a spongy-transformation is a built-in property of the intermediate layer that is present in the as-deposited intermediate layer. See, e.g., ¶¶ 29-33, 46, 51-53, 58 and 66. An intermediate layer can, immediately after deposition and without any further processing (i.e., as-deposited), undergo a spongy transformation; absolutely no modification of the as-deposited intermediate layer (other than by a suitable heat treatment) is contemplated or claimed by this invention. Specifically, no implantation of gaseous species is needed, no application of stresses, no treatment with various chemicals, in fact, no post-depositional processing of any sort.

Although Applicant submits that the "as-deposited" property of the intermediate layer is readily apparent throughout the specification, the interview of August 11th has led Applicant to believe it would be useful to present an extended discussion of how the specification supports this property. It is submitted that this property is supported: because there is no actual description present in the specification, either direct or by inference, that teaches one of ordinary skill that implantation into the intermediate layers of this invention is necessary for their subsequent spongy transformation; and further, because all descriptions of intermediate layers and spongy transformations that are present in the specification clearly teach one of ordinary skill that the intermediate layer alone is sufficient for a spongy transformation.

that the Examiner agrees that the corrected claim is limited as described. This opportunity would advance efficient and compact prosecution of this application.

In more detail, it is submitted that simply because there is no description of implantation into intermediate layers, one of ordinary skill would understand implantation is not part of the present invention. It is a long established principle that patent specifications need not specifically describe every detail or specifically explicitly exclude all alternatives. It follows, therefore, that absence of description of a feature is enough by itself to teach that features absence.

As an example of this principle, Applicant contrasts the present application with one of his more significant prior patents, e.g., US patent 5,374,564, that first described and claimed that light-ion implantation (preferably H, He or combinations thereof) alone can split a thin surface layer from a semiconductor substrate upon subsequent heat treatment (because of formation of a layer of micro-bubbles). Throughout this prior patent's specification, only light-ion implantation is described as a preferred embodiment, and it has, therefore, been universally understood as teaching that only light ion implantation alone is sufficient. Despite this patent's failure to explicitly exclude other means of splitting surface layers, e.g., by deposition of the intermediate layers of this application, no ordinarily skilled artisan has ever contended that any such other means, e.g., deposition of intermediate layers, is also necessary for splitting.

Similarly, the present application describes that as-deposited intermediate layers alone can undergo a spongy transformation upon subsequent heat treatment; implantation into as-deposited intermediate layers is never described. Therefore, analogously to US patent 5374564, it is submitted the ordinarily skilled artisan understands this application as teaching that as-deposited intermediate layers alone are sufficient for a spongy transformation. Specifically, it is understood that implantation into intermediate layers, even though not explicitly excluded in so many words, is nevertheless not necessary for a spongy transformation, is not part of this invention, and can be properly excluded from the claims.

Next, positive descriptions of intermediate layers and their spongy transformation is found primarily in ¶¶ 29-33, 46, 51-53, 58 and 66, and these paragraphs describe that as-deposited intermediate layers alone can undergo spongy transformations. Paragraph 29 states:

In an embodiment, said intermediate layer includes at least one base material having distributed therein atoms or molecules termed extrinsic atoms or molecules which differ from the atoms or molecules of the base material so that, under the effect of a heat treatment, the intermediate layer becomes plastically deformable and the presence of the selected extrinsic atoms or molecules in the selected base material causes the irreversible formation of micro-bubbles or micro-cavities in the intermediate layer.

The specification, here, makes entirely clear that it is the extrinsic atoms which cause the spongy transformation. Subsequent implantation is not described at all, and certainly is not described as necessary for the extrinsic atoms to cause the spongy transformation.³

Then, paragraphs 51-53 teach, most importantly, how the intermediate layer comes to be, that is how the base material and the extrinsic atoms, the latter causing the spongy transformation, come to intervene between a substrate and a superstrate. These paragraphs state:

Next, a layer of silicon containing or doped with a high percentage of phosphorus and/or boron⁴ is deposited on the oxidized face 5 of superstrate 2 to obtain the intermediate layer 4 composed of a material of the phospho-silicate glass (PSG) or boro-phospho-silicate glass (BPSG) type. As an example, the percentage of phosphorus in the material constituting the intermediate layer 4 may be in the range from 6 to 14. Such a deposit may be produced using known techniques in deposition machines of the CVD, LPCVD or PECVD type. The thickness of the intermediate layer 4 so constituted may be in the region of five microns.

³ This teaching is emphasized in ¶ 46, which states:

In general, the intermediate layer 4 is formed from at least one base material having distributed therein atoms or molecules termed extrinsic atoms or molecules which differ from the atoms or molecules of the base material, and has a composition such that, when a suitable heat treatment is applied to the structure 1, micro-bubbles or micro-cavities, in particular of a gaseous phase, are irreversibly formed such that said intermediate layer 4 transforms to become spongy and, as a correlation, it is likely to increase in thickness.

And it is further reiterated in ¶ 66, which states:

regarding the selected materials ... applying such a heat treatment ... causes the irreversible formation of a gas phase constituted by micro-bubbles or micro-cavities 7 in the intermediate layer and, as a correlation, an increase in the thickness of said layer 4.

⁴ Paragraphs 30-33 then teach that the base material comprises silica, that the extrinsic atoms comprise phosphorous, and that the extrinsic atoms may also comprise boron.

And the specification, here, makes entirely clear that the base material and the extrinsic atoms are “deposited on” the face of a substrate. This fact alone rules out implantation, because implantation cannot be onto the “face” of substrate but must be into the bulk of a substrate.⁵

Implantation is ruled out even more clearly because the deposition onto the face is performed “using known techniques in deposition machines of the CVD, LPCVD or PECVD type.” It hardly needs stating that “deposition machines” cannot implant; implantation can only be performed in machines capable of accelerating ions by voltage on the order of 100 kev.

Applicant submits that considerations and observation such as the above make entirely clear to those of ordinary skill in the art that implantation into the intermediate layer is not part of this invention, and can properly be excluded from the claims

In view of the above, independent claim 34 recites that this spongy transformation is a built-property of the intermediate layer, present immediately in the as-deposited layer, in the following manner:

34. (currently amended) A method for fabricating a structure in the form of a plate which method comprises:

depositing at least one intermediate layer on either of a substrate and/or a superstrate wherein the intermediate layer comprises at least one base material having distributed therein extrinsic atoms or molecules which differ from those of the base material;

assembling the substrate and the superstrate so that the intermediate layer is interposed between the substrate and the superstrate to form a structure; and

applying a heat treatment to the structure in a temperature range that causes the intermediate layer to become plastically deformable with the as-deposited extrinsic atoms or molecules in the base material causing an irreversible formation of microbubbles or microcavities in the intermediate layer in a configuration and amount sufficient to weaken the intermediate layer.

In a first step, the intermediate layer is deposited, and, as-deposited, it comprises compounds, mixtures or associations (or the like) of at least two constituents, a “base material” and “extrinsic atoms or molecules.” Claim 34 requires that these two constituents be present in the as-deposited layer. No post-depositional processing is needed to, e.g., introduce the

⁵ The present invention does contemplate implantation, but only for thinning a substrate or a superstrate. ¶ 63. Such implantation is only into the substrate or the superstrate. This implantation is not into the intermediate layer.

“extrinsic atoms or molecules” into the “base material” from outside (such as might occur during a subsequent step of implantation of atomic species, or during a subsequent second step of deposition, or the like), or to, e.g., actualize, or cause the formation of, “extrinsic atoms or molecules” within the base material (such as might occur consequent to the application of stresses or the like).

Then, in a subsequent step, a suitable heat treatment is applied in order to cause the “base material” and the “as-deposited extrinsic atoms or molecules” to interact so that the intermediate layer undergoes the recited irreversible, spongy-transformation characterized by the formation of “microbubbles or microcavities.” The “as-deposited extrinsic atoms or molecules” are key to this transformation. Claim 34 specifically requires that it is the “as-deposited extrinsic atoms or molecules” that actually cause the spongy transformation. Stated differently, even if a heat treatment created “microbubbles or microcavities” in some hypothetical intermediate layer, if these “microbubbles or microcavities” were not caused by the “as-deposited extrinsic atoms or molecules” then this situation is not within claim 34. For example, if they were caused by implantation of gaseous ions or atoms, then these “microbubbles or microcavities” are not within claim 34.

With this background, the meaning of the language of claim 34 becomes unquestionably clear. “The as-deposited extrinsic atoms or molecules” which the third step of claim 34 requires be the cause of the spongy transformation are indeed the very same “extrinsic atoms or molecules” which were deposited in the first step. In other words, the antecedent basis of the phrase “extrinsic atoms or molecules” used in the third step is found in the same phrase as it appears in the first step.

Further properties of the multilayer substrate structures of this invention are recited in the dependent claims. Claims 35, 36 and 38 recite that these multilayer substrate structures are releasable because of the presence and properties of the intermediate layer (after suitable heat treatment). Nothing more is required, e.g., no implantation of gaseous atoms or molecules.

Claims 39, 47, 48 and 54 recite that intermediate layers preferably comprise a glass, and more preferably a phospho-silicate glass, and even more preferably a phospho-silicate glass having a phosphorous concentration from about 6% up to about 14%. ¶¶ 15-17 and 31-33. Boron is a strictly optional component the phospho-silicate glasses of this invention. In these claims, boron need not be present at all, as it may be present at a concentration of 0%.

If boron is present, its concentration preferably does not exceed about 4%. A boro-silicate glass, i.e., a glass without phosphorous, is not included in these claims.

CLAIM REJECTIONS UNDER 35 USC § 102

Claims 34-36, 41, 46, 50 and 53 are rejected under 35 U.S.C. § 102(b) as being anticipated by International patent publication WO 99/35674 to Moriceau et al. WO 99/35674 corresponds to US patent no. 6,756,286 (Moriceau) which will be referred to herein.

These rejections are traversed at least because Moriceau does not disclose an intermediate layer which, as-deposited, possesses the above-described key characteristics, that is comprises “as-deposited extrinsic atoms or molecules” that cause a spongy transformation in response to heat treatment. Instead, for Moriceau’s materials to form “micro-cavities” and to become weakened in response to heat treatment, Moriceau’s materials require additional post-depositional processing, specifically, they require post-depositional “implantation of the said gaseous compounds.” Moriceau’s describes the disclosed process as follows:

Therefore, the purpose of the invention is a process for the transfer of at least one thin film of solid material delimited in an initial substrate, characterized in that it comprises the following steps:

a step in which a layer of inclusions is formed in the initial substrate at a depth corresponding to the required thickness of the thin film, these inclusions being designed to form traps for gaseous compounds which will subsequently be implanted;

a subsequent step for implantation of the said gaseous compounds, in a manner to convey the gaseous compounds into the layer of inclusions, the dose of implanted gaseous compounds being sufficient to cause the formation of micro-cavities likely to form a fracture plane along which the thin film can be separated from the remainder of the substrate.

Moriceau at col. 3, ll. 1-16. The first step of this process forms inclusions the sole pertinent property of which is that they form traps for “gaseous compounds which will subsequently be implanted.” Then, the second step implants the “gaseous compounds” into the layer of inclusions, and it is these implanted “gaseous compounds” that causes “the formation of micro-cavities.”

The Moriceau reference is thus twice deficient. It does not describe depositing any intermediate layer whatever its properties that intervenes between a substrate and a

superstrate. Therefore, it certainly does not describe depositing any intermediate layer that, by itself, and in its as-deposited form,” is capable of irreversibly forming “microbubbles or microcavities” during a subsequent heat treatment.

Moriceau is also deficient because it describes forming “micro-cavities” only after implantation of gaseous compounds. However, in the present invention, it is “the as-deposited extrinsic atoms or molecules” that form the recited “microbubbles or microcavities.” These “the as-deposited extrinsic atoms or molecules” are not implanted after deposition, but are deposited along with the rest of the intermediate layer.

The current Office action (the Action) does not address the first deficiency, and thus cannot establish the prima facie anticipation of the rejected claims.

The Action does address the second deficiency, and contends to the contrary that Moriceau does describe the last step of claim 34. It points to Moriceau at col. 3, ll. 52-65; col. 4, ll. 10-13; col. 4, ll. 26-29; col. 8, ll. 60-67; col. 9, ll. 30-46; col. 10, ll. 13-21; col. 12, ll. 58-64 as allegedly describing this step. But Applicant has carefully studied these portions of Moriceau, and indeed the entire Moriceau reference, and submits they, in fact, do not disclose the claimed intermediate layer, namely, an intermediate layer which, after deposition, can undergo on its own a spongy transformation in the absence of any further treatments, such as implantation of gaseous compounds.

In all but one of these cited portions, Moriceau states that “microcavities” are formed by implantation of gaseous species followed by heat treatment. In the remaining cited portion, “microcavities” are not actually present. Each of these cited portions is examined in the following. First, col. 3, ll. 52-65 describes only that Moriceau’s inclusions are formed by the “implantation of elements in a substrate layer” and that heat treatment may “modify the morphology and/or composition of the inclusions.”⁶ Not only are these inclusions formed by implantation, but, even after heat treatment, they are not “microbubbles or microcavities” because for the most part they are solid.

Next, col. 4, ll. 10-13 describes only that a heat treatment can weaken substrates at inclusion layers. Immediately prior, Moriceau explains that this weakening is not due to the inclusions themselves, but instead is actually due to implanted “gaseous compounds” which have become trapped at the inclusion layer. See, e.g., col. 4, ll. 1-3. Thus, taken together,

⁶ All references that appear subsequently in this section are to Moriceau.

these portions of Moriceau do not teach that the substrates can be weakened solely by an inclusion layer to an extent sufficient for their separation. Implantation of gaseous compounds is always required.

Next, col. 8, ll. 60-67 is cited, but col. 8, ll. 53-67 are the relevant lines. These relevant lines describe again that inclusions may be formed by implantation of gaseous compounds, here implantation of O₂. Col. 9, ll. 1-10. Again, not only are these inclusions also formed by implantation, but they are not even "microbubbles or microcavities" because for the most part they are solid. O₂ implantation into Si is well known to generate only inclusions of solid SiO₂ particles or a "thin oxide layer."

Next, col. 10, ll. 13-21 describes again that, in Moriceau's second step, inclusions may be formed by implantation of gaseous compounds.

Next, col. 12, ll. 58-64 must be understood in the context of col. 12, ll. 51-54. So understood, these lines merely describe heat treatment conditions suitable to cause splitting after implantation of gaseous compounds (not after formation of inclusions alone).

Finally, the last citation pointed to be the action is col. 9, ll. 30-46. These lines describe that inclusions in the form of oxygen precipitates may be formed by heat treatment of monocrystalline silicon wafers. This is especially so for wafers obtained by Czochralski pulling. The O₂ forming these precipitates is not implanted. However, oxygen precipitates are well known to be solid SiO₂ particles, and certainly not to be the recited "microbubbles or microcavities." See, e.g., Borghesi et al. 1995, Oxygen precipitates in silicon, *J. Applied Physics* 77(9) 4169 (in particular, the first column on page 4170). Further, oxygen precipitates formed in Si by heat treatments are scattered throughout the bulk of the Si; they not present only in a deposited intermediate layer.

Taken together, it is clear that Moriceau does not describe or suggest the claimed intermediate layer, which undergoes a spongy transformation caused by "as-deposited extrinsic atoms or molecules." Actually, Moriceau throughout, and in particular in the portions pointed to by the Action, describes only that "microbubbles or microcavities" can be formed only after a step of implantation of gaseous elements. Claims 35, 36, 41, 46, 50 and 53 (and other claims dependent from claim 34) are submitted to be patentable because they are dependent from patentable claim 34. Withdrawal of all the present rejections is respectfully requested.

CLAIMS 41 AND 50

It is submitted that claims 41 and 50 are patentable for the following additional reasons.

Claim 41 recites in relevant part that “at least some the microbubbles or microcavities have a volume such that they are open on both the substrate and superstrate side or furthermore are mutually open to constitute channels which are open to the side ends of the intermediate layer.” The Action rejects this claim, first, by contending that such “microbubbles or microcavities” are “implicit.” But it is submitted that it cannot be inherent that inclusions, which can be as small as “a few tens of nanometers,” can span a layer up to several micrometers thick, or that nanometer inclusions can overlap sufficiently to form channels which extend across an entire several inch substrate. Moriceau at col. 2, ll. 31-33. Only certain “microbubbles or microcavities” have such characteristics.

Second, the Action’s rejection points to Moriceau at col. 2, ll. 31-33; col. 3, ll. 37-39 and 63-65; col. 6, ll. 37-40; col. 8, ll. 65-67 as support. To the contrary, these portions are respectfully submitted not to disclose the substance of claim 41. First, col. 2, ll. 31-33 states the “these volumes [of the inclusions] may have a variety of shapes and their dimensions may vary from a few tens of nanometers to several hundreds of micrometers.” However, it has already been pointed out that nearly all samples with only nanometer sized inclusions will not have the recited characteristics. Further, most of Moriceau’s inclusions are solid. Thus, again, this portion does not establish that the recited characteristics are inherent in Moriceau.

The remaining portions of Moriceau pointed to by the Action describe, respectively:

The layer of inclusions may be formed by a film deposition technique.
It may then consist of generating columns or generating grains.

...

The inclusions layer may also be obtained by heat treatment of the film(s) and/or by applying stresses to the film(s) in the film structure.

...

Granular growth was provoked inside structure 6 to build up an inclusions layer 7 that will be used as a zone of traps for gaseous compounds to be implanted.

...

Their morphology and size may be modified by heat treatment and/or single and/or multiple implantation of the same or a different element.

The Applicant cannot discern any disclosure, suggestion or teaching in any of these portions that is relevant to the substance of claim 41.

Claim 41 is submitted to be patentable for these additional reasons.

Next, because the substance of previously pending claim 50 now appears in claims 34 and 50 taken together, for simplicity, Applicant considers claim 50 as it was prior to the current amendment when it recited:

50. The method as claimed in claim 34, which further comprises, prior to conducting the heat treatment, carrying out an operation for depositing the intermediate layer on either of the substrate or the superstrate, and attaching the superstrate or substrate to the intermediate layer by molecular wafer bonding.

It is submitted that the Actions purported rejections of this claim are based on a misunderstanding or mischaracterization of Moriceau in view of the claimed substrate structure. Very briefly, claim 50 recites a method during which a superstrate and a substrate, one of which carries an intermediate layer on its surface, are assembled together to form a superstrate-intermediate-layer-substrate structure; and then the intermediate layer in this structure is made to undergo a spongy transformation so as to weaken the superstrate-intermediate-layer-substrate structure.

All the portions of Moriceau pointed to by the Action, in fact, describe thin film layer transfer and bonding to a support substrate, where the bonding is aided by a bonding layer. The Action contends that such a bonding layer is an intermediate layer. But this cannot be the case because a bonding layer is for strengthening, not weakening, a structure while the intermediate layer of this invention is for weakening, not strengthening, a structure.

Specifically, the Action points to col. 4, ll. 34-41, col. 11, ll. 56-60, and col. 12, ll. 3-6 and 55-57 for support. But col. 4, ll. 34-41 describes:

The process may also comprise a step in which the thin film delimited in the substrate is put into intimate contact with a support onto which the thin film will bond after it has separated from the remainder of the substrate. The film may be put into intimate contact directly (for example by wafer bonding) or through an added on material. A heat treatment step may be used to reinforce the bond between the thin film delimited in the substrate and the added on support.

Here, the "added material" forms a bonding-type layer because it improves bonding between the "thin film" and the "support." A bonding-type layer cannot be the recited intermediate layer.

Next, col. 11, ll. 56-60 and col. 12, ll. 3-6 describe, respectively:

The transfer process designed to obtain a final film structure on a support assumes that the initial material is added onto a second support during a third step. The contact is made directly by wafer bonding, or through a bond layer.

...

Thus, in the example of a structure covered with an SiO₂ film to be transferred to a silicon support, a temperature of the order of 200 °C will be sufficient to reinforce the wafer bond.

Here also, these portions describe a “bond layer” or an “SiO₂ film” for reinforcing bonding. Such bonding-type layers cannot be the recited intermediate layer.

Finally, col. 12, ll. 55-57 describe:

The surface 35 is then made to bond to a silicon plate by wafer bonding reinforced by heat treatment at 250 °C for 30 minutes.

This portion describes no more than wafer bonding reinforced by heat treatment. A bonding-type layer is not present.

Claim 50 is submitted to be patentable for these additional reasons.

Withdrawal of the rejections of claims 51 and 50 (also 34) is respectfully requested for these additional reasons.

CLAIM REJECTIONS UNDER 35 USC § 103

Claims 39, 40, 42 and 47-49 are rejected under 35 U.S.C. § 103(a) as being unpatentable over Moriceau. These rejections are traversed at least because all of these claims depend from claim 34 and Moriceau does not make obvious claim 34.

It is submitted that claims 47, 48 and 54 are patentable for the additional reason that they all require the presence of phosphorous in the intermediate layer, and Moriceau never once mentions phosphorous. Applicants submit that it cannot be obvious to add a material that is not even mentioned in the cited reference.

CLAIM REJECTIONS UNDER 35 USC § 103

Claims 37, 39, 43, 44, 45, 51 and 52 are rejected under 35 U.S.C. § 103(a) as being unpatentable over Moriceau in view of one or US patent 5,854,123 to Sato et al. (Sato) or of US patent 6,417,075 to Habberger et al. (Habberger).

These rejections are traversed at least for the following reasons: because all of these claims depend from claim 34; because Moriceau does not make obvious claim 34; and because Sato and Habeger do not make up for Moriceau's lack of disclosure.

Indeed the Action does not so contend concerning Sato and Habeger. Sato is relied on only for disclosing various means of separating substrates bonded through a porous intermediate layer. Habeger is relied on only for disclosing that thickness reduction of a substrate/superstrate material is sometimes preferable.

Withdrawal of all the present rejections is respectfully requested.

CONCLUSION

In view of the above amendments and remarks, the applicant respectfully submits that the current Office action has been fully and completely responded to and that the application is now in condition for allowance. Should the Examiner have any suggestions or find any deficiencies in the current paper, a telephone call is respectfully requested to expedite their resolution.

Respectfully submitted,



Date: August 24, 2011

Allan A. Fanucci, Reg. No. 30,256

WINSTON & STRAWN LLP

Customer No. 28765

212-294-3311

Oxygen precipitation in silicon

A. Borghesi

Dipartimento di Fisica dell'Università, via Campi 213 a, I-41100 Modena, Italy

B. Pivac

Rudjer Boskovic Institute, P.O. Box 1016, HR-41000 Zagreb, Croatia

A. Sassella and A. Stella

Dipartimento di Fisica "A. Volta" dell'Università, via Bassi 6, I-27100 Pavia, Italy

(Received 15 June 1994; accepted for publication 14 December 1994)

A review is presented of the recent advances in the study of oxygen precipitation and of the main properties of oxide precipitates in silicon. After a general overview of the system "oxygen in silicon," the thermodynamics and the kinetics of the precipitate formation are treated in detail, with major emphasis on the phenomenology; subsequently, the most important techniques for the characterization of the precipitates are illustrated together with the most interesting and recent results. Finally, the possible influence of oxygen precipitation on technological applications is stressed, with particular attention to recent results regarding device yield. Actually, the essential novelty of this review rests on the attempt to give an extended picture of what has been recently clarified by means of highly sophisticated diagnostic methods and of the influence of precipitation on the properties of semiconductor devices. © 1995 American Institute of Physics.

TABLE OF CONTENTS

I. Introduction.....	4170	C. Precipitate morphology.....	4197
II. Oxygen in silicon.....	4170	1. Precipitate free-energy.....	4197
A. Growth processes.....	4170	2. Influence of annealing temperature and time.....	4198
1. Float-zone growth.....	4170	D. Phenomenology.....	4199
2. Czochralski growth.....	4171	1. Thermal history effect.....	4199
B. Fundamental properties of isolated oxygen atoms in silicon.....	4174	2. Effect of single-step annealing.....	4200
1. Position of isolated oxygen atoms in the silicon lattice.....	4174	3. Effect of two-step annealing.....	4205
2. Oxygen segregation.....	4174	4. Effect of rapid thermal annealing.....	4206
3. Oxygen solubility.....	4175	5. Effect of dopant and impurities.....	4206
4. Oxygen diffusivity.....	4176	IV. Techniques for oxide precipitates characterization.....	4209
C. Techniques for oxygen content determination in silicon.....	4179	A. Wet chemical etching.....	4209
1. Infrared spectroscopy.....	4179	1. Etch formulation and application.....	4209
2. Gas fusion analysis.....	4182	2. Chrysallographic defects evidenced by selective etching.....	4209
3. Secondary ion mass spectrometry.....	4182	3. Optical microscopy.....	4210
4. Other methods.....	4183	4. Detection of SiO _x precipitates.....	4212
III. Thermodynamics and kinetics of precipitate formation.....	4184	B. Transmission electron microscopy.....	4212
A. Nucleation.....	4184	C. Infrared absorption.....	4215
1. Homogeneous strain-free nucleation.....	4184	1. Indirect precipitate detection.....	4216
2. Homogeneous nucleation with strain.....	4187	2. Direct precipitate detection.....	4216
3. Heterogeneous nucleation.....	4188	D. Small angle neutron scattering.....	4222
4. Nucleation in as-grown crystals.....	4190	E. Optical scattering.....	4224
B. Precipitation.....	4190	1. Laser scanning tomography.....	4224
1. Spherical precipitates with fixed radius.....	4191	2. Scanning infrared microscopy.....	4225
2. Spherical precipitates with increasing radius.....	4194	F. X-ray topography.....	4226
3. Disc precipitates with varying thickness.....	4196	1. Transmission topography.....	4227
		2. Reflection topography.....	4228
		V. Technological interest of oxygen precipitation....	4229
		A. Influence of precipitation on the mechanical properties of silicon.....	4230

B. Influence of precipitation on the electrical properties of silicon.....	4231
C. Denuded zone.....	4233
D. Influence of precipitation on the device yield: some examples.....	4236

I. INTRODUCTION

Starting from the 1950s, a lot of work has been performed on the behavior of oxygen in silicon. The growing demand to understand and clarify details concerning various aspects of this type of impurity-matrix coupling has encouraged the use of more and more sophisticated techniques.

The recent developments can be extracted from the enormous amount of scientific articles in the field, which have been stimulated by the new and wide-range silicon-based applications, particularly in the direction of very large-scale integration (VLSI) and the related integrated circuit processing. As a matter of fact, Czochralski (Cz) -grown silicon single crystals are used to fabricate VLSI devices, due to the lower cost with respect to the float-zone growth technique. In the Cz growth process oxygen is incorporated into the silicon directly from the silica crucible, as an unavoidable impurity. The presence of oxygen in silicon, however, is not to be superficially and globally considered just as a drawback, since it has effects that are also positive (mainly related to intrinsic gettering properties), in addition to the negative ones (formation of defects in the active regions related to oxygen precipitation). In this connection, one might stress that, aiming at the large-scale applications, fabrication of dislocation-free single crystals with a low concentration of contaminants and a not too high level of oxygen is obviously an important goal to be reached.

As a direct consequence, oxygen in silicon represents a challenging prototype to study solid-state reactions also from a fundamental point of view. Oxygen is incorporated as an interstitial impurity or in complexes. It should be stressed that at temperatures characteristic of device processing ($\leq 1200^\circ\text{C}$) Cz silicon containing oxygen is a supersaturated solid solution, since oxygen is incorporated at about 1400°C . Looking at Fig. 1 it is evident that the amount of oxygen which, at high temperature, gives rise to a solid solution, at lower temperatures leads to a phase separation between silicon and silicon oxide. In other words, at temperatures lower than 1400°C the equilibrium state of the Si-O system is reached by means of oxygen precipitation, i.e., formation of SiO_2 particles (oxide precipitates) in the silicon crystal. The processing temperature (together with other parameters such as thermal history and initial oxygen concentration) plays an essential role in determining the formation and the morphology of oxide precipitates: In general, we can say that while nucleation is favored in the temperature range $600\text{--}900^\circ\text{C}$, precipitate growth is predominant from about 1000 to 1200°C . The variety of possible size, shape, orientation, etc., of the oxide precipitates in silicon imposes the use of high-performance characterization techniques for an adequate understanding of the different and multiple details.

In this article we review the recent developments concerning both precipitate formation and characterization, with the aim of presenting to the reader a picture which, if not

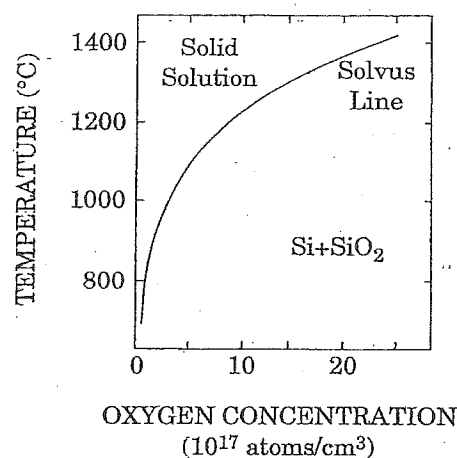


FIG. 1. Partial phase diagram of the Si-O system.

complete (unfortunately this could not be avoided due to the huge quantity of articles published in the last years), should be (hopefully) rather homogeneous and up to date.

II. OXYGEN IN SILICON

To study oxygen behavior in silicon we briefly review the current techniques for industrial production of single-crystal silicon ingots and describe the mechanisms that lead to oxygen incorporation into the growing crystal, its thermodynamically stable positions in the lattice, its solubility, and diffusion mechanism. We also review the most common techniques used to study isolated oxygen atoms in silicon.

A. Growth processes

1. Float-zone growth

In the float-zone (FZ) technique a radio-frequency (rf) coil is used to melt a narrow zone in a vertically mounted polycrystalline silicon rod. The molten zone is seeded with single-crystal silicon and then passed from one end of the rod to the other. This zoning can be repeated many times to obtain high-purity crystals. Dopants are introduced either by melting pills into the molten zone or by gas-phase doping.

Since the container or crucible is not directly in contact with the molten zone and multiple zone passes are possible, high crystal purity is readily attainable; however, since the molten zone is supported by the lateral surface tension and solid-liquid interface tension, it is difficult to grow crystals much larger than 75 mm in diameter. Furthermore, no techniques have been developed to incorporate significant oxygen amounts (oxygen concentration within the bulk is typically $10^{15}\text{--}5\times 10^{16}$ atoms/cm³), which is a prerequisite for successful ultralarge-scale-integration (ULSI) device manufacture. As a result FZ does not play an important role in ULSI silicon application (its applications are limited to about 20% of the market). Therefore, being oxygen free and not widely used for applications, silicon crystals grown by this technique are not considered any longer.

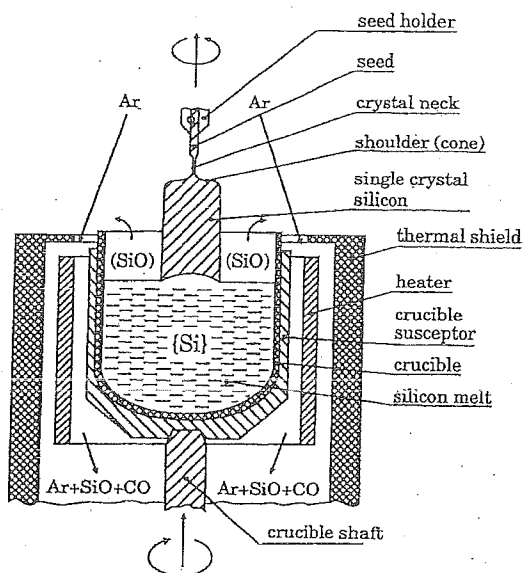


FIG. 2. Cz single-crystal pulling (from Ref. 5).

2. Czochralski growth

The experimental setup for the pulling of single crystals by the Cz method is illustrated in Fig. 2. Molten polycrystalline silicon is held in a crucible, a single-crystal seed is first dipped into the melt and then slowly withdrawn vertically to the melt surface, whereby the liquid Si crystallizes around the seed. The method is named after Czochralski, who introduced it in 1916 in the framework of the study of crystallization velocity of metals.¹ For the growth of silicon and germanium single crystals the Cz method was first applied in 1950 by Teal, Little, and Bühler.^{2,3} The silicon single crystals of the early years were not dislocation free. In 1958 Dash⁴ developed a special pulling technique to obtain dislocation-free crystals.

Polycrystalline silicon is melted in a crucible that is supported by a graphite susceptor. While rf heating is sometime used, all modern Cz crystal pullers use resistance heaters. The growth chamber is evacuated to ~ 10 – 20 Torr and maintained at this pressure with argon or helium flow during the growth process.

Molten silicon reacts to a large extent with every crucible material. This is due to its high binding forces for the light elements and to the high dissolving power of the melt for most elements. It is then essential to find a crucible material that only slightly reacts with the melt, and in addition does not affect the crystal quality required for electronic applications.

Almost all crucible materials, especially metals and their alloys, are quickly dissolved by liquid silicon. Only dense carbon, particularly vitreous carbon, dissolves slowly, so that a silicon melt can be held in such a crucible over a longer period, for example, to pull a polycrystalline rod. There are several compound materials, namely some carbides, nitrides, and oxides, which also react slowly. All these materials are dissolved by liquid silicon with an erosion rate of at least several microns per hour.⁵ For example, vitreous silica dissolves with an erosion rate of $7 \mu\text{m/h}$ at temperatures near

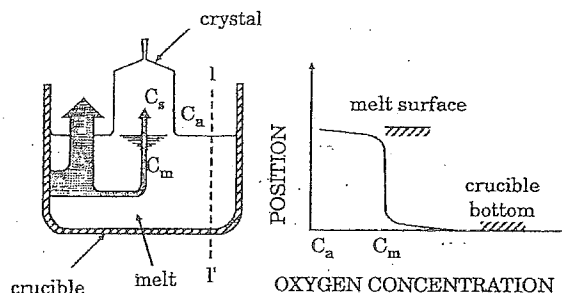


FIG. 3. Diagrams showing oxygen transportation during Cz silicon growth (left-hand side), and oxygen concentration profile in the melt along $l-l'$ (right-hand side) (from Ref. 7).

the melting point of silicon in a 1 bar argon atmosphere. Due to uninterrupted dissolution, the silicon melt is soon enriched to higher concentrations of the constituents of the crucible material. Therefore, materials containing metals or dopants are not suitable, as, for example, titanium carbide, boron nitride, or aluminum oxide. Only silicon compounds such as silicon carbide, nitride, or oxide, are considered as potential crucible materials.

Up to now only vitreous silica has been used in the production of Cz silicon crystals, since silicon monoxide produced in the reaction between silicon melt and silica crucible evaporates easily from the melt. Therefore, under the usual pulling conditions, oxygen concentration in the melt never reaches the solubility limit and no disturbance of crystal growth by oversaturation occurs. Under the usual pulling conditions less than 1% of the reacting oxygen gets into the crystal and more than 99% of oxygen evaporates out of the melt in the form of gaseous SiO.

Oxygen fluxes in the Cz silicon growth system are shown in Fig. 3. Oxygen enters the melt as the silica crucible dissolves in the liquid silicon. As already mentioned, part of the dissolved oxygen is incorporated into the growing crystal, while another part is lost by evaporation of SiO from the melt surface. In modern conventional growth systems an argon purge is usually introduced somewhere above the melt to help sweep off SiO from the crystal growth area. Due to strong convective flows, mixing in the melt is virtually complete and significant oxygen concentration differences exist only at the three boundaries involved:

- (1) the crucible/melt interface;
- (2) the solid/melt interface; and
- (3) the melt/ambient interface.

At steady state the amount of oxygen leaving the melt must equal the amount entering the melt, so that

$$\text{oxygen in melt} = \text{oxygen from crucible}$$

$$- \text{oxygen evaporated}$$

$$- \text{oxygen incorporated.}$$

The steady-state conditions have been studied by many authors.⁶⁻⁹ The results can be briefly summarized as follows.

(1) At the crucible/melt interface

$$\text{oxygen flux} = A_c D (C_c - C_m) / \delta_c, \quad (1)$$

where A_c is the area of the crucible/melt interface, D is the diffusion coefficient of oxygen in molten silicon (see Sec. II B 4), C_c and C_m are the oxygen concentrations in the crucible and in the melt, respectively, and δ_c is the interface thickness.

(2) At the melt/ambient interface

$$\text{oxygen flux} = A_s D (C_a - C_m) / \delta_s, \quad (2)$$

where A_s is the area of the free melt surface, C_a is the oxygen concentration in the ambient, and δ_s is the interface thickness.

(3) At the solid/melt interface

$$\text{oxygen flux} = A_R v k_e C_m, \quad (3)$$

where A_R is the cross-sectional area of the growing crystal, v the linear growth rate, and k_e the effective segregation coefficient of oxygen in silicon (see Sec. II B 2).

The oxygen fluxes involve, therefore, three diffusion boundary layers and three surface areas. The thickness of the boundary layers depends on the convective flows in the melt and on the purge flow conditions, while the surface areas are determined by the amount of polycrystalline silicon (charge), by the crucible size and shape, and by the crystal diameter.

The large silica crucibles used in contemporary growth systems are approximately cylindrical. During crystal growth the crucible/melt interface constantly decreases with the melt volume, while the free melt surface remains unchanged during most of the growth process. As a result, less oxygen enters the melt but evaporation remains constant as the crystal growth proceeds, thus influencing oxygen distribution along the ingot length.

More uniform distributions can be obtained if the ratio of the crucible/melt surface area to the free melt surface area is maintained constant during crystal growth. This can be realized in crucibles of special shape, e.g., a truncated cone;¹⁰ however, the charge size in such crucibles is limited with respect to conventional crucibles of the same size. A much more practical solution is the continuously recharged system in which feed is continuously supplied during the crystal growth. In this way, the ratio crucible/melt surface area to free surface area can be maintained constant. The uniformity of oxygen axial distribution obtained in such a way was first described by Fiegl.¹¹

In general, the oxygen distribution within the silicon ingot on microscopic as well as on macroscopic scale does not correspond to the distribution of the other elements. The effective segregation coefficient of oxygen is close to one and depends only a little on the growth rate (see Sec. II B 2). On the other hand, the incorporation of oxygen into the growing crystal strongly depends on the pattern of the convective flows in the melt. Figure 4 illustrates a few melt flow characteristics in Cz silicon melts for isorotation of crystal and crucible. Clearly, unsteady melt flows cause unsteady supply of oxygen and oxygen striations in the crystals which are thicker than the dopant striations. It is difficult to measure

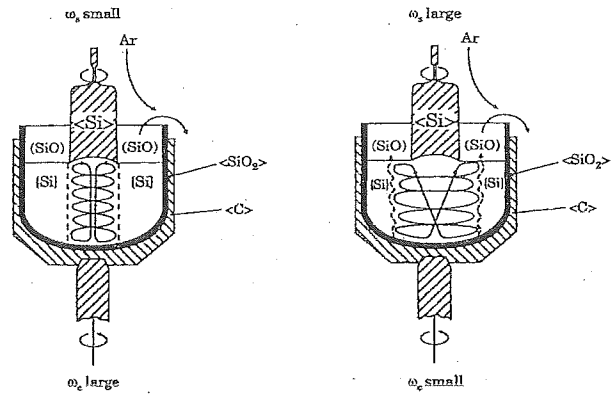


FIG. 4. Melt flow characteristics in Cz silicon melts for isorotation of crystal and crucible (from Ref. 5).

the oxygen striations straightforwardly, but there are ways to visualize them indirectly. For example, one possibility is to generate oxygen-related thermal donors by annealing at 450 °C when their formation takes place with a strict correlation with oxygen concentration. A second possibility is to induce oxygen precipitation and to make the precipitates visible by preferential etching.

The flow patterns in the melt are by far the dominant factor in determining oxygen content and distribution in the crystal. Figure 5 shows the axial oxygen distribution for eight Cz crystals grown from silica crucibles. All crystals have the same length, diameter (50 mm), orientation, and doping, while crystal and crucible rotation during pulling were different. All other pulling and growing parameters were held constant. As shown in the figure, variations of oxygen content in Cz crystals by a factor of about 10 was achieved by simply adjusting crystal and crucible rotation; however, a very good axial homogeneity was obtained. Modern pulling techniques allow one to obtain a nicely flat radial oxygen distribution, as shown in Fig. 6.

To control and/or modify oxygen incorporation in the silicon lattice a new method of Cz growth in magnetic field (MCz) has been developed.

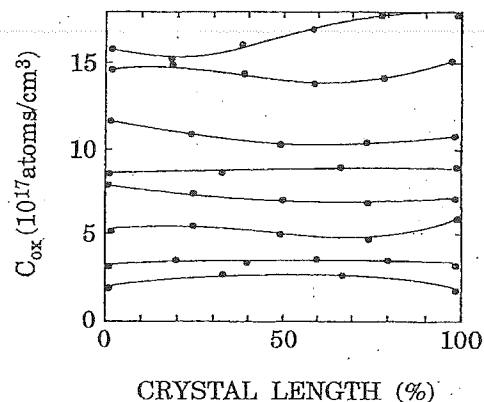


FIG. 5. Axial oxygen distribution for eight Cz crystals grown in the same conditions with different crystal and crucible rotations (from Ref. 5).

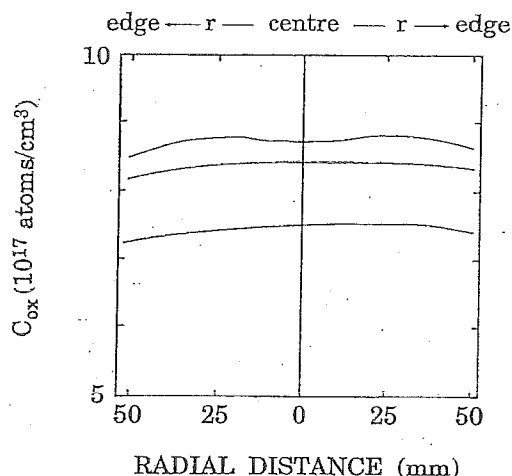


FIG. 6. Radial oxygen distribution in Cz single crystal at three different axial lengths. The higher oxygen concentration values correspond to the seed-end and the lower ones to the tail-end of the crystal (from Ref. 5).

It has been established that a magnetic field can suppress the convection of electrically conductive fluids. In 1966 Chedzey and Hurle¹² and in 1970 Utech and Flemings¹³ pointed out that a magnetic field can be used to obtain high-quality InSb crystals by means of a horizontal crystal-growth method. Soon Cz InSb crystal growth in a magnetic field transversal with respect to the growth direction was presented.¹⁴ Recently a transversal magnetic field was applied for Cz silicon crystal growth¹⁵ to improve the quality of the crystals. More specifically, the convection flows are suppressed when a magnetic field of more than 0.15 T is applied to molten silicon, which has an electrical conductivity comparable to that of mercury. Therefore, the applied magnetic field suppresses convection, reduces the growth of striations, and allows to control oxygen concentration in the silicon crystal.

Figure 7 shows the experimental results¹⁵ of the effect of magnetic field on the concentration of oxygen atoms incorporated into a crystal. A substantial amount of oxygen is eliminated from crystals grown under the effect of a magnetic field of 0.15 T. A smooth melt surface was observed with small temperature fluctuations. The suppression of con-

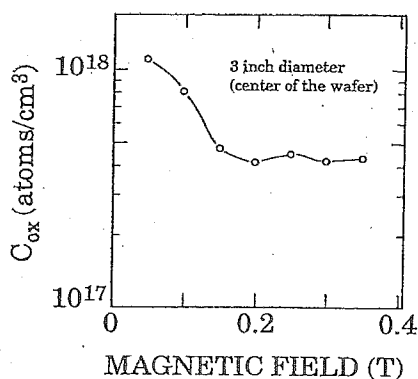


FIG. 7. Effect of magnetic-field strength on the oxygen concentration in silicon crystal (from Ref. 15).

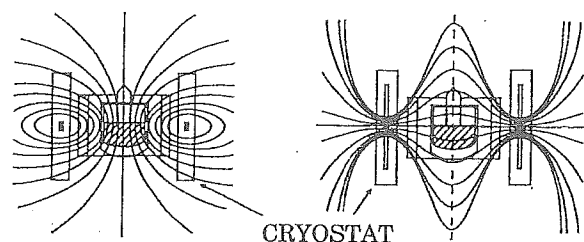


FIG. 8. Two flat coil configurations for magneto-Cz silicon single-crystal growth. Vertical or axial configuration (left-hand side) and horizontal or transversal configuration (right-hand side) (from Ref. 16).

vection in the melt causes a decrease in decomposed oxygen atoms moving from the silica crucible to the growth interface.

The magnetic field was applied in the two configurations, vertical and horizontal, shown in Fig. 8. The results obtained by comparing¹⁶ vertical and horizontal MCz can be summarized as follows.

For vertical field configuration it is easy to get crystals with an oxygen concentration over 2×10^{18} atoms/cm³ and eliminate the striations caused by temperature variation under lower magnetic field, that is, less than 0.1 T.

For horizontal field configuration it is easy to get crystals with an oxygen content lower than 1×10^{18} atoms/cm³, with high pulling speed. A magnetic field of about 0.25–0.3 T is required to reduce temperature variations.

The oxygen content in MCz crystals can be controlled by adjusting the applied magnetic field, or, at fixed value of the magnetic field, by varying the crucible rotation rate during the crystal growth, similar to what is done for the conventional Cz growth.

Figure 9 shows longitudinal oxygen profiles in crystals grown with the MCz method, and typical “low-oxygen” range (shaded area) obtainable with the standard Cz technique.¹⁷

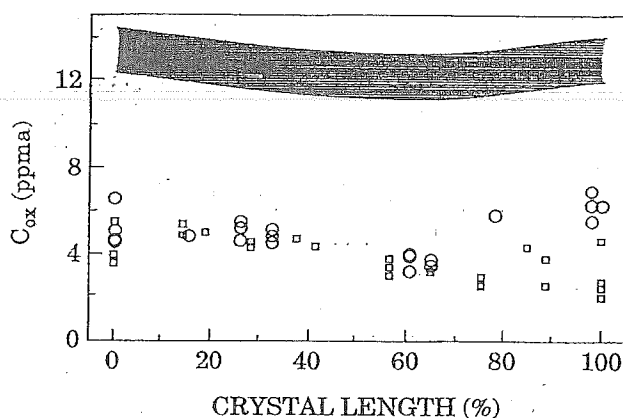


FIG. 9. Longitudinal profiles of oxygen concentration in low-oxygen crystals grown with the MCz method. Circles and squares refer to 6 and 4 in. ingot diameter, respectively. Shaded area on the top of the figure represents the typical low-oxygen range obtainable with the standard Cz technique (from Ref. 17).

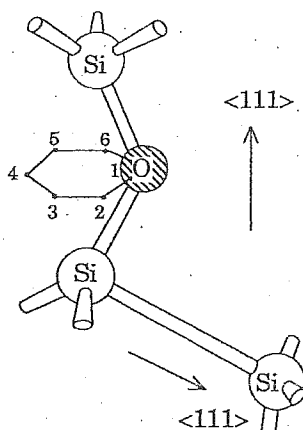


FIG. 10. Interstitial position of oxygen atom in silicon lattice, covalently bonded with two neighboring silicon atoms. The equivalent interstitial positions are indicated (1–6).

B. Fundamental properties of isolated oxygen atoms in silicon

The fundamental properties of isolated oxygen atoms placed in a silicon crystal, such as their lattice position, segregation, solubility, and diffusivity, as a prerequisite for its more complex behavior, have been studied for almost 4 decades. It is widely accepted nowadays that oxygen is thermodynamically stable at interstitial sites. Recent studies on the solubility and diffusivity yield convergent indications in a wider temperature range; however, the agreement among data concerning segregation and anomalous diffusion mechanism at lower temperatures is less satisfactory.

1. Position of isolated oxygen atoms in silicon

Infrared (IR) measurements on oxygen-doped silicon led Kaiser, Keck, and Lange^{18,19} to conclude that oxygen is placed interstitially in silicon lattice and is covalently bonded with two neighboring silicon atoms (see Fig. 10). Such interstitial oxygen is electrically inactive.

Oxygen interstitial position was further confirmed by x-ray-diffraction measurements of the silicon lattice parameter as a function of the oxygen concentration.²⁰ Corbett, McDonald, and Watkins²¹ by measuring stress-induced dichroism of the IR band at 1107 cm^{-1} , and Stavola²² for the bands at 1107 and 515 cm^{-1} , confirmed this model as well. Besides this model O'Mara²³ proposed, on the basis of the IR data by Bosomworth *et al.*,²⁴ that oxygen can be present simultaneously at interstitial and substitutional sites. The key for such a proposal was the observation that the 515 cm^{-1} band does not fit in the band scheme given by Bosomworth *et al.*²⁴ In the O'Mara model substitutional oxygen manifests double donor activity. This would explain the donor behavior of oxygen (see Sec. III D) as well as the segregation coefficient larger than one, as observed by Yatsurugi *et al.*²⁵ However, there is no general agreement on the existence of oxygen on substitutional sites, and furthermore Stavola²² has shown, from stress-induced IR dichroism data, that the 515 cm^{-1} band is not due to substitutional oxygen, but to the symmetric stretching vibration of interstitial silicon, i.e., of the Si-O-Si quasimolecules.

Recently, Chen *et al.*²⁶ proposed a new model predicting that most of the oxygen atoms in Si are at interstitial sites in bonded Si_2O configuration, with a binding energy $E_b \sim 0.8\text{--}1.0\text{ eV}$, for temperatures up to 600 K . At higher temperatures a new "quasifree interstitial oxygen" and the bonded Si_2O configuration coexist. In the quasifree interstitial oxygen state the Si—O bonds are broken, but oxygen migration is hindered by the lattice with a potential barrier $E_L \sim 1.5\text{--}1.6\text{ eV}$. With this model they explained the enhanced oxygen diffusivity (see Sec. II B 4).

It can be concluded that at room temperature the interstitial position of isolated oxygen atoms dissolved in silicon is nowadays widely accepted.

2. Oxygen segregation

The behavior of oxygen in silicon upon various thermal treatments is strictly dependent on the processes leading to its incorporation into the crystal during growth. The distribution of impurities into the solid phase of the crystal growing from the melt is related to its segregation. The equilibrium segregation coefficient k_0 of oxygen in silicon is defined as

$$k_0 = \frac{C_s}{C_m}, \quad (4)$$

where C_s and C_m are the oxygen concentrations in the solid and in the melt, respectively.

The above equation holds for equilibrium processes. Although the Cz growth process is rather slow (the maximum growth speed is a few mm/min), it is still far from equilibrium; therefore, segregation is described by the effective segregation coefficient k_e . A detailed analysis of the phenomena at the growth interface shows that they are related to the thickness δ of the diffusion boundary layer and growth speed v . By using these parameters, Burton, Prim, and Slichter^{27,28} could write k_e as a function of δ ,

$$k_e = \frac{k_0}{[k_0 + (1 - k_0)\exp(-v\delta/D)]}, \quad (5)$$

where δ is given by

$$\delta = 1.6D^{1/3}\nu^{1/6}\omega^{-1/2}. \quad (6)$$

D is the diffusion coefficient of oxygen in the melt, ν the kinematic viscosity of the melt, and ω the rotation rate of the crystal. This theory gave a satisfactory explanation of the actual impurity distribution along the growth direction for several dopants in Cz crystals.²⁹

According to Eq. (5), $k_0 = 1$ implies that the oxygen incorporation is not dependent on the growth rate variations, i.e., that the oxygen redistribution within the ingot is uniform. This is, however, in disagreement with experimental findings, which give values of k_0 different from unity.

Several attempts have been made to determine k_0 , which displays values in the range from 0.25 to 1.48, as shown in Table I. Such large discrepancies in the experimentally determined values for k_0 are due to the fact that oxygen behavior in the silicon melt is driven by dynamic processes and, therefore, is not simply related to the equilibrium segregation coefficient.

TABLE I. Comparison of k_0 values for oxygen in silicon, as determined by different techniques. FTIR, CPAA, SIMS, and SRP denote Fourier transform infrared spectroscopy, charged particle activation analysis, secondary-ion-mass spectrometry, and spreading resistance probe, respectively.

k_0	Method	Ref.
1.48	growth rate-IR	30
1.25 ± 0.17	CPAA	31
1 ± 0.25	FTIR	23
1.0 ± 0.1	growth rate	31
1	growth rate-IR, SIMS, SRP	32
~ 1	FTIR	9
$0.36-0.9$	calculated	34
0.5	vacuum fusion	35
0.3	growth rate-IR	36
0.25	growth rate	37

One of the difficulties for the determination of the segregation coefficient is the continuous supply of oxygen from the crucible walls and the evaporation of SiO from the melt surface. The balance between supply and evaporation fluctuates so that oxygen concentration in the crystal varies. Consequently, many researchers gave scattered values of the equilibrium segregation coefficient for oxygen in silicon.^{9,30-37} Harada *et al.*³² took into account these effects and furthermore suppressed oxygen evaporation by encapsulation, i.e., they increased the ingot diameter up to the inner diameter of the crucible, to completely cover the melt surface. From the uniform distribution of the oxygen through the P and Sb striations they concluded that the segregation coefficient is equal to unity. Lin and Hill³⁷ and Lin and Stavola³⁶ have grown small-diameter silicon crystals under constant growth rate conditions trying to reach equilibrium conditions by keeping the area of the melt in contact with the crucible and of the melt surface nearly constant. By comparing the axial distribution of oxygen and of the doping atoms, they found a value of 0.25 for the segregation coefficient;³⁷ from the comparison of microscopic arsenic and oxygen striations, a value of 0.3 was found.³⁶ In similar crystal pulling experiments Series and Barraclough³¹ kept the temperature of the melt constant during the crystal growth, thus avoiding changes of the oxygen concentration in the melt. This experiment resulted in a segregation coefficient equal to 1.0 ± 0.1 .

Attempts to determine the segregation coefficient from IR measurements^{9,23,30-36} are limited by the presence of oxygen complexes and other IR inactive species. Therefore the use of complementary techniques is required to determine the total amount of incorporated oxygen.

From the analysis of the phase diagram Sosman³⁸ determined a segregation coefficient smaller than one. However, the accuracy of the available phase diagrams for oxygen in silicon is far from being satisfactory, since they were determined in the early days of silicon pulling.

Recently Kim and Langlois³⁹ developed a model for oxygen segregation in Cz and MCz crystals. This model takes into account the oxygen source (ablation of the silica crucible), the transport in the melt, and the segregation at the

TABLE II. Literature data for the constant C_{OI} and the dissolution enthalpy E_s . SIMS, SRP, IR, CPAA, and XRD denote secondary-ion-mass spectrometry, spreading resistance probe, infrared spectroscopy, charged particle activation analysis, and x-ray diffraction, respectively.

C_{OI} (10^{22} atoms/cm ³)	E_s (eV)	Method	Temperature (°C)	Ref.
0.14	2.53	SIMS, outdiffusion	700-1160	42
0.13	2.50	SIMS, implanted O	700-1100	43
1100	2.3 ± 0.3	SRP	1250-1400	44
6.3	1.65 ± 0.17	IR	1100-1200	45
9	1.52	SIMS, CPAA, IR	800-1400	40
3.2	1.4	IR	850-1050	41
9.3	1.20 ± 0.13	CPAA (¹⁶ O)	1000-1375	46
0.27	1.10	XRD	1100-1200	47
	1.08 ± 0.02	CPAA (¹⁶ O)	1000-1280	48
0.10	1.03	IR	950-1350	49
0.13	0.95 ± 0.1	IR	1000-1250	50
0.055	0.89	IR	460-900	51

growth interface. The sink is represented by evaporation of SiO from the free surface of the melt, which is a fast process compared to O diffusion through the melt and incorporation in the growing crystal. The equilibrium segregation coefficient was set to 1.25, i.e., the melt under the interface is depleted of oxygen. The comparison between simulations and experimental results for the radial oxygen profiles and the ablation of the crucible shows excellent agreement.

3. Oxygen solubility

Oxygen incorporated from the melt into the growing Cz crystals is frozen in during the cooling of the ingots and gives rise to a solid solution. Therefore, in Cz wafers oxygen is present in a supersaturated state for all temperatures of standard processing. At the melting point oxygen solubility in silicon C_{ox}^* was shown to be $2.75 \pm 0.15 \times 10^{18}$ atoms/cm³, as shown by Yatsurugi *et al.*²⁵ The temperature dependence of C_{ox}^* is expected to have the form

$$C_{ox}^*(T) = C_{OI} \exp\left(-\frac{E_s}{kT}\right), \quad (7)$$

where C_{OI} is a constant and E_s is the dissolution enthalpy. Oxygen solubility at various temperatures has been studied by means of various techniques: Table II shows the data from the literature, scattered up to an order of magnitude. A best fit of the experimental results from different groups is given by Mikkelsen,⁴⁰ who found $C_{OI} = 9 \times 10^{22}$ atoms/cm³ and $E_s = 1.52$ eV. Figure 11 gives an overview of the most important experimental results and the line represents Eq. (7). The discrepancies are related to the different analytical techniques used.

Let us first consider the IR solubility measurements. The wide scattering in the published data has been recently discussed by Livingston *et al.*⁴¹ in conjunction with their study of oxygen precipitation in silicon, devoting a particular attention to the different calibration procedures. They have also shown that since the reported IR measurements were not

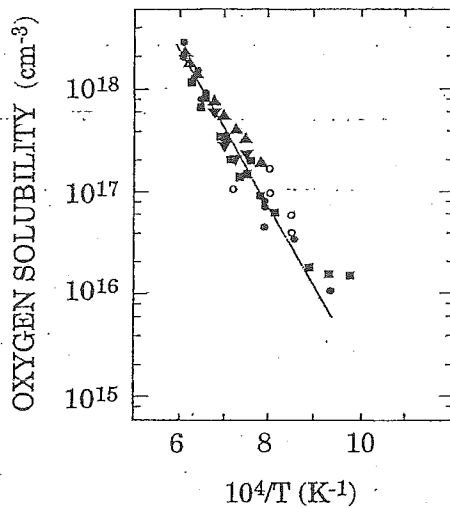


FIG. 11. Oxygen solubility in silicon as determined by SIMS (circles); IR (solid squares), and CPAA (triangles); the solid line represents the best fit (from Ref. 40).

all performed at 4.2 K, it would be extremely difficult to separate the absorption due to precipitates from that of dissolved oxygen. The data in Table II are recalibrated with the 3.03 calibration constant. A more detailed discussion about calibration factors is given in the next paragraphs. Furthermore, they noticed that most authors have limited the times of heat treatment in precipitation experiments to less than 200 h, apparently too short for the low-temperature anneals. These problems were avoided in the experiments of Craven,⁴⁹ who studied silicon wafers doped by nuclear transmutation, thus having high density of heterogeneous nucleation sites. The results of Craven are in close agreement with those of Hrostowski and Kaiser⁵⁰ obtained by IR spectroscopy and of Takano and Maki⁴⁷ obtained by x-ray diffraction.

Other analytical methods such as secondary-ion-mass spectrometry (SIMS), charged particle activation analysis (CPAA), and x-ray diffraction evaluate the oxygen solubility from the surface oxygen concentration and diffusion profiles. It is assumed that this concentration is established by the intrinsic solubility as a boundary condition for normal (Fickian) diffusion. It is, however, critical to ensure that no oxygen precipitation and/or complexing took place during the thermal treatment, since neither SIMS nor CPAA can distinguish the various forms of oxygen in silicon. Precipitation is likely to greatly affect the x-ray measurements of lattice dilatation, too.

For temperatures above 1000 °C, the oxygen solubility values determined by different techniques are comparable. Significant differences, however, affect the results at low temperatures. Livingston *et al.*⁴¹ have shown that below 850 °C the solubility is enhanced. An increase in oxygen solubility below 650 °C, compared to the exponential dependence given in Eq. (7), was evidenced by Messoloras *et al.*⁵² This was attributed to the changes in the structure or in the morphology of the SiO_x precipitates. However, Vanhellemont and Claeys⁵³ recently attributed this effect to the pres-

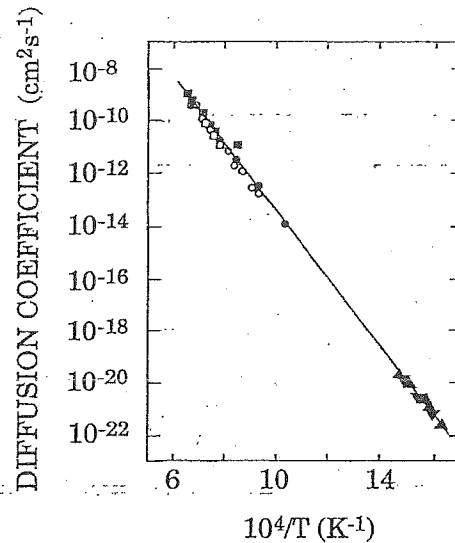


FIG. 12. Oxygen diffusivity in silicon measured by SIMS (circles), CPAA (squares), dichroism (triangles up), and kinetic data (triangles down); solid line: best fit (from Ref. 40).

ence of a high self-interstitial supersaturation and to the higher interface and strain energy of precipitates at these low temperatures, making precipitation more difficult than at higher temperatures.

Mikkelsen^{54,55} investigated the influence of oxidizing annealing ambients on the oxygen solubility, which was found much higher than that measured under vacuum annealing conditions. Similar results were obtained both with oxidation in O₂ and in H₂O, but it should be pointed out that these treatments did not lead to equilibrium. Furthermore, they found that oxygen solubility is a factor of 2 higher for steam than for dry ambients and is also a factor of 2 larger for <111> than for <100>-oriented wafers. A similar result was obtained by Lee and Nichols⁴² from SIMS analysis of the oxygen out-diffusion profile. The observed effect is explained by the increase of the oxygen steady-state solubility in the presence of the high silicon self-interstitial concentrations induced by the oxidation process.⁵⁴

The influence of other chemical impurities on the solubility of oxygen in silicon is not clear. Gass *et al.*⁴⁸ showed that the oxygen solubility limit does not depend on B and P doping. Instead, Al and Ga seem to influence the solubility, but this may depend on sample preparation. Mikkelsen⁴⁰ reported that silicon crystals heavily doped with As tend to show defect regions which attract oxygen in excess with respect to the solubility limit, but the presence of precipitated oxygen cannot be ruled out. In the case of heavy P doping, both Heck, Tressler, and Monkowski⁵⁶ and Lee and Nichols⁴² observed that the concentration of oxygen in diffusion profiles was somewhat lower than that obtained under inert ambient annealing. These results are difficult to interpret due to very complex processes occurring at the surface.

4. Oxygen diffusivity

a. Intrinsic oxygen diffusivity. Different techniques, such as, e.g., x-ray diffraction,⁴⁷ CPAA,⁴⁸ and Cs⁺ ion-beam

TABLE III. Oxygen diffusivity D_0 and activation energy E_D as deduced by CPAA, SIMS, IR, SANS (small-angle neutron scattering), and XRD measurements.

D_0 (cm ² /s)	E_D (eV)	Method	Temperature (°C)	Ref.
22.6	3.15	CPAA (¹⁸ O)	1100–1280	48
3.2	2.9	CPAA (¹⁶ O)	1150–1375	46
0.23	2.56	stress-induced dichroism	1100–1280	21,63
0.7	2.54	stress-induced dichroism	330–1240	57
0.14	2.53	SIMS, O out-diff.	700–1160	42
0.13	2.53	SIMS, CPAA, IR	330–1280	40
0.11	2.51	IR, SANS	650–1050	41
0.11	2.51	stress-induced dichroism	330–1200	64
0.07	2.44	SIMS, O in-diff.	700–1240	65
0.091	2.4	lattice parameter XRD	1100–1280	47

SIMS depth profiling,^{40,54} have been used to study oxygen diffusivity in silicon in the high-temperature range (700–1200 °C). The agreement among the results obtained by the different techniques is excellent, as shown in Fig. 12. On the other hand, in the low-temperature range (220–360 °C), IR spectroscopy was used to study oxygen diffusivity by means of stress-induced dichroism measurements.^{21,57,58} Oxygen diffusivity in the silicon crystal D_0 is related to values of τ through the relation

$$D_0 = a^2 / (8\tau), \quad (8)$$

where a is the silicon lattice parameter and τ is the relaxation time.

SIMS measurements have been performed at different experimental conditions. ¹⁸O in-diffusion in FZ silicon wafers, as well as ¹⁶O out-diffusion from supersaturated Cz crystals were considered.^{40,42,43,56,59} It has been shown that oxygen diffusivity does not depend on wafer orientation ($\langle 100 \rangle$ or $\langle 111 \rangle$), annealing ambient (dry or wet oxidizing, or inert), doping concentrations, nor pulling technique.^{40,42}

On the other hand, Gass *et al.*⁴⁸ have shown by CPAA that B or P doping has no influence on oxygen diffusion, which, however, might be somewhat affected by Al and Ga doping. It has been also suggested that complexing of As may influence the O diffusion.⁶⁰ The influence of heavy Sb doping on oxygen diffusivity has been investigated,^{60–62} and no effect has been found. Wijaranakula and co-workers⁶⁰ studied oxygen diffusivity in a wider range of Sb doping concentrations, concluding that point defects, such as silicon self-interstitials or vacancies, have little or no effect on oxygen diffusion.

The temperature dependence of the diffusion coefficient D is expected to have the form

$$D = D_0 \exp\left(-\frac{E_D}{kT}\right), \quad (9)$$

where D_0 is diffusivity and E_D is the activation energy of diffusion process. Diffusion coefficient data have been obtained in a wide range of temperatures as shown in Table III, and it is now well understood over twelve orders of magnitude (see Fig. 12). Fitting the results of both low and high temperatures Mikkelsen⁴⁰ has shown that the values for D_0 and E_D are 0.13 cm²/s and 2.53 eV, respectively. The interstitial oxygen diffusivity under thermal equilibrium conditions is dominated by the process of jumping from one interstitial site to another.^{43,57,63}

Heck and co-workers⁵⁶ found differences concerning diffusivity at 1100 °C during steam and HCl oxidation, suggesting that oxygen diffuses via a vacancy-dominant mechanism. According to this model oxygen hopping takes place via a substitutional site previously occupied by a vacancy. This model implies that oxygen hopping directly from one to another interstitial site should involve a too large lattice distortion; therefore, it is suggested that oxygen atoms hop through an intermediate substitutional position. On the other hand, Lee and Nichols^{42,43} measured oxygen diffusivity in the temperature range 700–1160 °C, under the various conditions known to lead to a large supersaturation of point defects. They found that over more than two orders of magnitude in point defect concentration oxygen diffusivity is not affected by the variations of such conditions. Their findings clearly indicate that the oxygen diffusion above 700 °C is dominated by an interstitial hop mechanism.

b. Anomalous oxygen diffusivity. The phenomenon of enhanced oxygen diffusivity has been the object of several studies and attributed to different causes. Oates *et al.*⁶⁶ found that electron irradiation induced an enhanced oxygen diffusion, while other groups found its dependence on thermal history,^{57,67–69} on the presence of metallic contamination,⁶⁹ and on interactions with carbon^{70,71} or hydrogen.^{64,72,73} Enhanced oxygen diffusion is also invoked to explain the formation of thermal donors and rodlike precipitates at low temperatures.

Enhanced oxygen diffusivity observed on electron-irradiated samples was studied by stress-induced dichroism.⁶⁶ The effect was explained with the formation of oxygen-vacancy complexes (A centers), or dioxygen vacancy complexes.⁷⁴ The capture of silicon interstitials by these complexes results in emission of oxygen interstitials. Such a process, i.e., successive capture and emission of vacancies, is assumed to occur faster than the normal oxygen hop, and it dominates the oxygen diffusion process above 300 °C. On the other hand, no evidence of interaction between silicon self-interstitials and oxygen atoms in the temperature range 25–500 °C has been given.

Stavola *et al.*⁵⁷ found that the oxygen hopping time is two orders of magnitude shorter in crystals subjected to an “oxygen stabilization” heat treatment (900 °C for 2 h), as compared to crystals in which oxygen has been well dispersed (heated at 1350 °C for 20 h). This suggests that thermal history of silicon wafers may significantly influence oxygen diffusivity.^{67,75}

The presence of metallic contaminants (Fe, Cu) can enhance oxygen diffusion⁶⁹ up to two orders of magnitude.

This effect is also explained by the presence of vacancies due to metallic contaminants.

Enhancement of oxygen diffusion was observed⁶⁴ upon treatment in a hydrogen plasma at low temperatures. At 300 °C an increase of the diffusivity by a factor of 300 is reported. Such an effect was not observed with other kinds of plasma treatments and, therefore, is not related to ion damage. More recently, Newman *et al.*⁷² extended these measurements to the temperature range 225–350 °C. They revealed oxygen profiles by measuring the IR dichroism ratio as a function of the depth by grinding the surface after each measurement. It was found that oxygen hopping is favored by collision with diffusing hydrogen atoms, thus causing the enhancement of oxygen diffusion. Very recently, Zhong and Shimura⁷³ showed, by means of SIMS measurements, that even at higher temperatures (>1000 °C) annealing in hydrogen atmosphere produces an enhanced oxygen diffusion. They interpreted the results with a model based on the direct interaction between hydrogen and interstitial oxygen.

Shimura and co-workers⁷⁰ studied the outdiffusion behavior of oxygen and carbon in carbon-doped Cz silicon wafers by SIMS. They showed that the diffusion of both oxygen and carbon is greatly enhanced at 750 °C, but is significantly slowed down at 1000 °C. Enhanced oxygen diffusion is attributed to fast diffusing molecularlike O-C complexes. Wijaranakula⁷¹ found also that at temperatures below 690 °C oxygen diffusion in silicon doped with carbon is enhanced. This phenomenon is attributed to C_i-O_i complexes, which could act either as a mobile species or as an activated state.

A possible explanation of thermal donor formation is based on an enhancement of the oxygen diffusivity at 250–500 °C of 3–4 orders of magnitude;⁷⁶ however, such enhancement is no longer a necessary requirement in a recently proposed model in which thermal donors are described as silicon self-interstitial agglomerates.^{58,68,74}

Thermal treatment of silicon supersaturated with oxygen in the temperature range 500–625 °C produces rodlike defects. Transmission electron microscopy (TEM) studies of such defects lead to the conclusion that they contain coesite, i.e., the high-pressure phase of SiO_2 .⁷⁷ This requires, however, that oxygen diffusion be enhanced by four orders of magnitude.⁷⁸ Recently, Bourret showed that the concentration of oxygen in the “coesite” particles was, in fact, very low.⁷⁹ Such features were reinterpreted as hexagonal silicon inclusions, presumably produced by the stress fields set up by the local condensation of silicon self-interstitial atoms; similar features were found in irradiated silicon. The fact that the defects have not been revealed by small-angle neutron scattering (SANS) measurements provides additional evidence that they do not contain significant amounts of oxygen and the local density of silicon atoms is not very different from that of the matrix. The new interpretation immediately eliminates the need for enhanced oxygen diffusion.

Several models have been proposed to explain enhanced oxygen diffusion in silicon, and are briefly reviewed here.

Gösele and Tan⁸⁰ proposed a model that explains enhanced oxygen diffusivity by the fast diffusion of molecular oxygen. Gaslike O_2 quasimolecules oriented along the $\langle 111 \rangle$ direction and centered at a tetrahedral site were studied by

Needels *et al.*,⁸¹ with evidence of just a small buildup of charge between the silicon and oxygen atoms, indicating that the Si-O interaction is extremely weak, thus supporting the model of a very mobile O_2 molecule. However, Oehrlein and Corbett⁸² showed that the assumption of gaslike molecular oxygen diffusion leads to unrealistic values for oxygen diffusivity around and slightly above room temperature.

An alternative model for a fast gaslike oxygen dimer (O_2) with C_{2v} symmetry is proposed by Snyder *et al.*^{83,84} From their theoretical modeling they conclude that the diffusivity of oxygen dimers is eight orders of magnitude higher than that of interstitial oxygen atoms.

Several authors proposed models that include complexes formed with point defects such as vacancies or self-interstitials to explain enhanced diffusivity. Oates *et al.*⁶⁶ attributed enhanced oxygen diffusion under electron irradiation at room temperature to the formation of V-O complexes which capture silicon self-interstitials so that the O atoms are reinjected in the lattice as interstitials, but at a much higher rate. Furthermore, Newman proposed the following reaction:⁷⁴



where V is the vacant site occupied originally by a Si atom. I defects would be mobile and it seems likely that $[O_i-O_i-V]$ complexes would be more mobile than single O_i atoms, possibly by repeated emission and recapture of I atoms.

Ourmazd, Schröter, and Bourret⁸⁵ proposed that the fast diffusing species are oxygen-silicon self-interstitial complexes. In heavily carbon-doped Cz silicon, however, Newman *et al.*⁷² showed that the reduction of $[O_i]$ concentration is not distinguishable from that in carbon-free samples, where self-interstitials are expected to have a longer lifetime. Thus, there is no evidence that the presence of self-interstitials enhances oxygen diffusivity.

Moleculelike C_i-O_i complexes or perturbed C(3) centers have been proposed by Shimura and co-workers⁷⁰ to explain enhanced oxygen diffusion in carbon-doped Cz silicon; however, from the variations in carbon and oxygen concentrations upon thermal treatment, Wijaranakula⁷¹ deduced that such C_i-O_i complexes may contain more than 35 oxygen atoms. This result is not compatible with two or three oxygen atoms as proposed by Shimura and co-workers.⁷⁰ It implies that an enhanced oxygen diffusion could involve several mechanisms, and therefore an alternative model was proposed. The local strain field surrounding an isolated oxygen is compressive along the $\langle 111 \rangle$ axis, while that of the interstitial carbon is tensile along the $\langle 110 \rangle$ axis. If the C_i-O_i complexes are activated, the local strain field surrounding the complex would lower the energy barrier so that jumping of oxygen atoms is favored. Thus, enhanced oxygen diffusion could be a result of a strain field effect.

Recent reports that oxygen diffusion is enhanced by the presence of hydrogen^{72,73} confirmed the model proposed by Estreicher,⁸⁶ according to which rapidly diffusing H atoms form complexes with O_i impurities as a transient species, and an oxygen diffusion jump may occur when a complex dissociates.

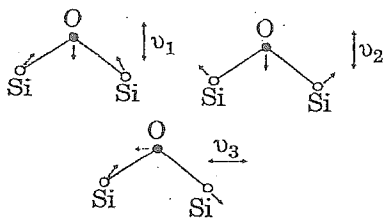


FIG. 13. Normal vibrations of the Si-O-Si defect molecule. $\nu_1=1205\text{ cm}^{-1}$, $\nu_2=515\text{ cm}^{-1}$, and $\nu_3=1107\text{ cm}^{-1}$ are the wave numbers corresponding to symmetric stretching, bending, and antisymmetric stretching vibration modes, respectively.

Not only enhanced, but also retarded oxygen diffusivity has been measured on several occasions. Heck and co-workers⁵⁶ reported that under oxidizing conditions at 1100°C oxygen diffusion is retarded, and this retardation is found to be larger for steam than for dry oxidation. The observed difference was taken as evidence that oxygen diffuses via a vacancy dominant mechanism.

A variation in oxygen diffusivity was also reported by Shimura and co-workers.⁷⁰ From SIMS measurements on carbon-free and carbon-doped Cz silicon annealed at 750°C , where precipitation is small, a good correspondence with the expected profile was obtained. On the other hand, results for annealing at 1000°C show a strong retardation of oxygen diffusion, and a much stronger retardation in heavily carbon-doped samples. This additional retardation can be related primarily to the stronger oxygen precipitation, resulting in higher densities of silicon self-interstitials in the near-surface region. Consequently, this result suggests that oxygen diffusion is retarded by the presence of silicon self-interstitials and, in turn, supports a vacancy-dominant diffusion mechanism for oxygen in silicon.

C. Techniques for oxygen content determination in silicon

IR spectroscopy, with grating or with Fourier transform infrared (FTIR) spectrometers, is widely accepted and used as a nondestructive technique for routine measurements of interstitial oxygen concentration in silicon. It should be pointed out that IR spectroscopy is the only technique that can discriminate between interstitially dissolved oxygen and oxygen in complexes or precipitates. Other techniques such as SIMS, CPAA, photon activation analysis, x-ray diffraction, and gas fusion analysis are used to detect the total oxygen concentration in the bulk. It has also been shown that low-temperature IR spectroscopy could be used to detect oxygen in Fz or crucibleless-grown silicon crystals, where the oxygen concentration can be 3–4 orders of magnitude less than in Cz crystals.⁸⁷ IR spectroscopy can be employed for quantitative analysis after comparison with the results obtained by means of other techniques, as is discussed later. We briefly describe these techniques and underline their main characteristics, relevant for the measurements of oxygen in silicon.

1. Infrared spectroscopy

a. Room-temperature measurements. There are three absorption bands in the mid-IR spectral range observable at room temperature, one at 1205 cm^{-1} , one at 1107 cm^{-1} , and the third one at 515 cm^{-1} . Hrostowski and Kaiser⁸⁸ originally assigned these bands to symmetric and antisymmetric stretching and bending vibrations of the triatomic Si-O-Si “defect molecule,” respectively (see Fig. 13). The 1107 cm^{-1} is the strongest and has been used for many years to measure the concentration of interstitial oxygen in silicon. This band is broad ($\sim 30\text{ cm}^{-1}$) at room temperature and splits into a number of features at low temperatures: The assignment to an antisymmetric vibration (ν_3 in Fig. 13) is well established.^{21,89} The assignment of the 515 cm^{-1} band is much more uncertain. Bosomworth *et al.*²⁴ have left this band unassigned and suggested that it is due either to a symmetric motion or to impurity-induced lattice absorption. The fact that this band loses intensity more quickly than the band at 1107 cm^{-1} upon oxygen precipitation heat treatments,^{23,90,91} as observed by measuring stress-induced IR dichroism, offers a variety of possible interpretations; however, Stavola²² showed that such a band is due to symmetric vibrations of interstitial oxygen.

The transmittance T , i.e., the ratio of the transmitted to the incident light intensity, depends on the wavelength λ . For accurate measurements the influence of multiple reflections on the wafer surfaces has to be taken into account. This is particularly important when both surfaces are polished. At normal incidence on a plane-parallel plate with polished surfaces the transmittance T is given by⁹²

$$T = \frac{(1-R)^2 e^{-\alpha d}}{1 - R^2 e^{-2\alpha d}}, \quad (11)$$

where R is the reflectivity which is related to the refractive index n (when extinction coefficient ~ 0) by

$$R = \left(\frac{n-1}{n+1} \right)^2. \quad (12)$$

For silicon $n \approx 3.42$ in the wavelength range from 5 to 50 μm , i.e., $R \approx 0.3$.

From Eq. (11) the absorption coefficient α can be derived,

$$\alpha = \frac{-1}{d} \ln \left(\frac{1}{R^2} \left\{ \frac{-(1-R)^2}{2T} + \left[R^2 + \left(\frac{(1-R)^2}{2T} \right)^2 \right]^{1/2} \right\} \right). \quad (13)$$

The absorption coefficient measured at 1107 cm^{-1} is the sum of three contributions due to interstitial oxygen α_O , free carriers α_{FC} , and multiphonon lattice absorption α_L . Thus,

$$\alpha = \alpha_O + \alpha_{FC} + \alpha_L. \quad (14)$$

For lattice absorption at 1107 cm^{-1} the value $\alpha_L = 0.85\text{ cm}^{-1}$ can be used.⁹³ This value was measured directly at the National Institute of Standards and Technology from the spectrum of a 4.7-mm-thick polished FZ silicon crystal. Nevertheless, the calculation of the absorption coefficient α is not much affected by this value. For example, a change of 10% in this parameter would result in a change of 0.25% in the calculated value of the absorption coefficient.

The term describing the free-carrier absorption α_{FC} depends on the resistivity of the analyzed sample. It is well known that free-carrier absorption can be neglected for concentrations below 10^{15} atoms/cm³. Above that value, however, the absorption coefficient increases drastically.⁹⁴ For highly doped silicon with resistivities in the range of m Ω cm the free-carrier absorption becomes high enough to hide other contributions. Schomann and Graff⁹⁴ studied samples with different resistivities and they found that the sum of absorption coefficients $\alpha_L + \alpha_{FC}$ at 1107 cm⁻¹ can be given as a function of the free-carrier concentration x (in 10^{15} atoms/cm³),

$$\alpha = 0.825e^{0.07x} \text{ (cm}^{-1}\text{)}, \quad (15)$$

with $1 \leq x \leq 20$.

The problem of free-carrier absorption in a highly doped material has been circumvented by Tsuya *et al.*⁹⁵ by high-flux electron irradiation, which results in trapping of the free carriers. Oates and Lin⁹⁶ have proposed a "short baseline technique" which takes into account the effects of the free carriers for the measurements of interstitial oxygen in heavily doped silicon. Recently, Borghesi *et al.*⁹⁷ have discussed an alternative method which uses a curved baseline. It was shown that their technique, which gives results equivalent to those of Oates and Lin, requires a simpler analytical procedure and is quite suitable for computerised routine measurements.

In order to obtain interstitial oxygen concentration C_{ox} (in atoms/cm³) the absorption coefficient α_0 (in cm⁻¹) has to be multiplied by the calibration constant χ (in atoms/cm²),

$$C_{ox} = \chi \alpha_0. \quad (16)$$

The exact determination of the calibration constant has been a matter of long studies and interlaboratory round-robin experiments: A wide range of values differing up to a factor of 2.5 is reported. A recent worldwide interlaboratory calibration yields the IOC-88 standard,⁹³

$$\chi = (3.14 \pm 0.09) \times 10^{17} \text{ atoms/cm}^2. \quad (17)$$

This calibration factor is in close agreement with the JEIDA value of 3.03×10^{17} atoms/cm² (Iizuki *et al.*⁹⁸). On the other hand, it deviates a lot from the value of the ASTM F 121-83 and the DIN 50 438/1 standards of 2.45×10^{17} atoms/cm² and the old ASTM F 121-79 standard of 4.81×10^{17} atoms/cm² used previously. A full compilation of all reported calibration factors is given by Baghdadi *et al.*⁹³ The optimum wafer thickness that results in the best accuracy for α_0 is given by $d = 1/\alpha_0$. Therefore, a slice with thickness of 2 mm is recommended for measurement of C_{ox} in Cz silicon. Commercially produced wafers are much thinner (typically of the order of 700 μ m for wafers of 150 mm in diameter): This causes a lower accuracy of the measurements of oxygen content. An additional difficulty with measurements of standard wafers is their backside roughness that results in the loss of intensity due to light scattering. This effect can reduce the transmittance of wafers when both surfaces are rough by approximately 40% with respect to that of double-side-polished wafers and by only few percent with respect to single-side-polished wafers.

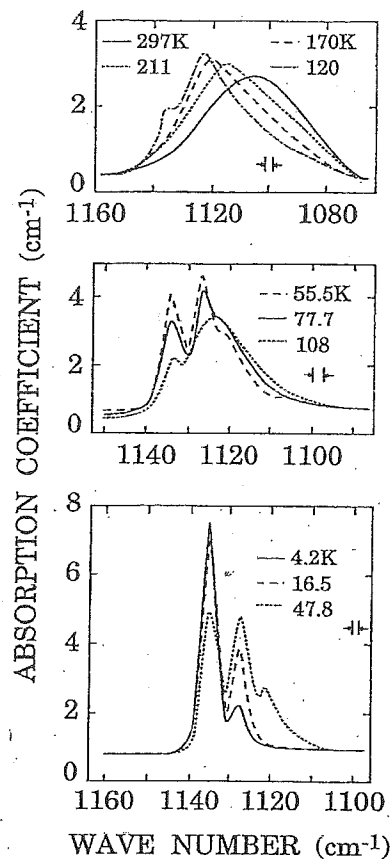


FIG. 14. Absorption coefficient of the antisymmetric vibration mode of Si-O-Si molecule at different temperatures (from Ref. 88).

Schomann and Graff⁹⁴ discussed the factors influencing the accuracy of measurements of oxygen content in silicon. They showed that the highest error comes from surface roughness which is important also in single-side-polished wafers. Both the sample temperature during measurement and the free-carrier absorption are also important, while the thickness variations, spectral resolution, and instrumental errors are less significant.

Usually, for the determination of oxygen content, FZ oxygen- and carbon-free silicon wafers are used as reference samples. Optimum measurement conditions require the same doping level, backside polishing, and precisely determined thickness both of the unknown and the reference wafer. Recently, a new method to determine precisely the O_i concentration in single-side-polished wafers was proposed.⁹⁹ The method is based on IR transmission measurements performed with p -polarized light impinging on the sample at the Brewster angle. In this case the 1107 cm⁻¹ absorption band is easily distinguishable from the contribution due to light scattering at the backside surface from the difference between absorbance spectra of single-side- and double-side-polished wafers. This is due to the lack of multiple reflections for measurements with p -polarized light at the Brewster angle on single-side-polished wafers.

b. Low-temperature measurements. Under progressive cooling from room temperature, the 1107 cm⁻¹ band gets distorted and shifts toward higher energies, as shown in Fig.

14. At 77 K there are three bands at 1121.4, 1127.5, and at 1135.8 cm^{-1} and the most intense one is centered at 1127.5 cm^{-1} with a full width at half-maximum (FWHM) of about 5 cm^{-1} . In this case, the ratio $\alpha_{1127.5}(77 \text{ K})/\alpha_{1107}(300 \text{ K})$ is 2.56 ± 0.02 , therefore the calibration factors found for room-temperature measurements are no more valid. New calibration constant values were proposed by Pajot⁹² to obtain the O_i concentration (in atoms/ cm^3) at 77 K,

$$C_{\text{ox}} = \chi_{77 \text{ K}} \alpha_{1127.5}, \quad (18)$$

where

$$\chi_{77 \text{ K}} = 1.1 \pm 0.1 \times 10^{17} \text{ atoms/cm}^2. \quad (19)$$

$\alpha_{1127.5}$ is the absorption coefficient (in cm^{-1}) of the 1127.5 cm^{-1} band measured with a resolution equal or better than 1 cm^{-1} to avoid instrumental distortion.

At liquid-helium temperature the bands at 1121.4 and 1127.5 cm^{-1} disappear.²⁴ The 1135.8 cm^{-1} line shifts to 1136.4 cm^{-1} getting sharp and prominent with two weaker satellites at 1134.5 and 1132.7 cm^{-1} , due to the silicon isotopes with mass 29 and 30 (see Ref. 22). The FWHM of the 1136.4 cm^{-1} is only 0.6 cm^{-1} and, as the integrated intensity of the band is nearly the same at room temperature and at 8 K, the maximum absorption coefficient rises strongly so that $\alpha_{1136.4}(8 \text{ K})/\alpha_{1107}(300 \text{ K}) \sim 30$. This fact allows one to detect this band even in FZ silicon at 8 K.

Low-temperature measurements can also be used to measure oxygen absorption in very thin Cz samples: The limit of the sample thickness for observing O_i is calculated to be about 0.2 μm for 8 K transmission measurements. For thicker Cz silicon samples the huge increase of the O_i absorption band at 8 K leads to a saturation of the 1136.4 cm^{-1} band preventing accurate measurements. In this case, room-temperature measurements are more favorable. The detection limit for the O_i concentration reachable with the liquid-He temperature measurements, for a 1-cm-thick silicon sample, with a reasonable integration time, is about 3×10^{13} atoms/ cm^3 .

To determine the conversion factor for measurements at temperatures near liquid He some difficulties rise, due to the sharpness of the 1136.4 cm^{-1} band. In fact, only by measuring the band profile with an instrumental resolution eight times lower than the FWHM of the band can it be reasonably inferred that the measured profile is free of instrumental distortion. In this case, the maximum absorption coefficient is independent of the instrumental resolution and proportional to the integrated intensity. When the above conditions are not fulfilled, the maximum absorption coefficient measured decreases with the ratio between the FWHM of the band and the instrumental resolution, strongly depending on the latter. Then, for comparative measurements the spectral resolution used must be specified.

Since it is very difficult to measure the profile of the 1136.4 cm^{-1} band with the appropriate instrumental resolution, Pajot⁹² proposed a conversion coefficient to determine the O_i concentration from liquid-He measurements, which takes into account $\Delta\omega_{\text{obs}}$, the observed FWHM of the 1136.4 cm^{-1} band. The proposed calibration coefficient to obtain C_{ox} in atoms/ cm^3 is

TABLE IV. Conversion factors χ for the determination of interstitial oxygen concentration C_{ox} (in atoms/ cm^3) from IR-absorption measurements at different temperatures.

Band position (cm^{-1})	χ (10^{17} atoms/ cm^2)	T (K)	Ref.
1107	3.14 ± 0.09	300	93
1127.5	1.1 ± 0.1	77	92
1136.4	$0.14 \pm 0.02 \Delta\omega_{\text{obs}}$	8	92
1136	0.169 ^a	4	100
515	1	300	100

^aWith 1 cm^{-1} resolution.

$$\chi_{8 \text{ K}} = 1.4 \pm 0.2 \times 10^{16} \Delta\omega_{\text{obs}} \text{ atoms/cm}^2. \quad (20)$$

It should be pointed out that the measurements of this band at low temperatures are very sensitive to the temperature of the sample and to the resolution of the instrument; therefore, the exact calibration strongly depends on the experimental conditions.

Recently Wagner¹⁰⁰ discussed the influence of the sample temperature on the absorption coefficient; for a resolution of 1 cm^{-1} he gave the calibration factor to determine the O_i concentration in atoms/ cm^3 , for temperatures close to 4 K, to be

$$\chi = 1.69 \times 10^{16} \text{ atoms/cm}^2. \quad (21)$$

Low-temperature measurements of interstitial oxygen concentration are of particular importance if oxygen precipitates exist within the bulk, giving rise to the broad band close to 1107 cm^{-1} at room temperature, which significantly hides the real signal. In fact, measurements at low temperature have no influence on this broad band but strongly enhance the interstitial oxygen absorption band, so that precise measurements are possible.

Another approach is based on using the 515 cm^{-1} band, which has no underlying precipitate response, as a measure of interstitial oxygen concentration. The calibration factor for this band is¹⁰⁰

$$\chi_{515} = 1 \times 10^{17} \text{ atoms/cm}^2, \quad (22)$$

which is temperature independent. This coefficient gives C_{ox} in atoms/ cm^3 with α in cm^{-1} . The 515 cm^{-1} band, however, is much weaker than the 1107 cm^{-1} band and disappears much more quickly, so that it can be used only for samples with very high concentration of interstitial oxygen.

In silicon samples stressed along the $\langle 110 \rangle$ directions, the interstitial oxygen atoms are preferentially situated along the $\langle 111 \rangle$ directions, where lattice stress is minimized. By reducing the temperature while maintaining the stress, the preferential orientation can be frozen in. The temperature dependence of the reduction rate of the resulting dichroism of the 1107 cm^{-1} absorption band^{21,22,58} yields information on the hop frequency of the interstitial atoms. Table IV summarizes the χ values for different temperatures for the 1107 and 515 cm^{-1} absorption bands.

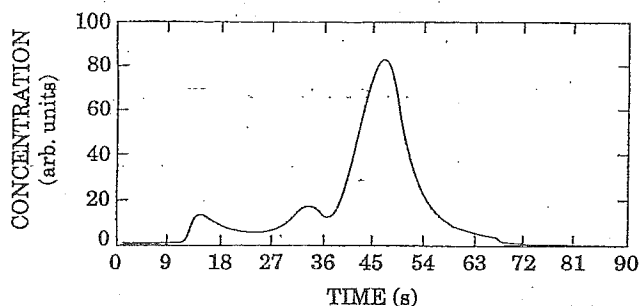


FIG. 15. Oxygen evolution from a silicon sample vs time. The first peak evidences surface contamination, the second one surface oxide, and the third one bulk oxygen (from Ref. 104).

2. Gas fusion analysis

Gas fusion analysis (GFA) is a well established method in metallurgy for the analysis of several gases (e.g., oxygen, nitrogen, and hydrogen) in solids. In the case of silicon, the samples are heated to above the melting point (up to 1500–1700 °C) in a special graphite crucible where the dissolved oxygen reacts with the carbon, producing CO. The developed CO gas is carried by flowing helium through a CuO bed heated at 400 °C where the reaction is completed, so that CO is converted into CO₂. The amount of this gas is subsequently detected by IR-absorption measurements, with a sensitivity about four times higher for the CO₂ than for the CO gas. Before reaching the samples the high-purity He carrier gas is purified by drying agents and by exposure to Cu turnings at 600 °C to remove the oxygen traces.

A different procedure is also possible where the CO gas is extracted into a vacuum system (vacuum fusion analysis) and then analyzed.

Baker, in 1970,¹⁰¹ used GFA as a comparative tool in the quantitative determination of oxygen in silicon by IR spectroscopy (see Sec. II C 1). Later on it was used to a limited extent.^{102–104} GFA has been developed primarily for measuring the oxygen content in heavily doped silicon, since it is suitable for any type or concentration of the doping material, while other methods (e.g., IR spectroscopy) are not suitable for heavily doped samples. The GFA method detects the whole oxygen content, hence, it cannot distinguish between interstitial and precipitated oxygen.

Prior to the measurement the samples are degreased, etched to remove the contaminated area close to the surface (typically in CP 4 etchant), then rinsed in de-ionized water, and etched in HF (40%) to remove any surface oxide. Finally, they are rinsed again and dried at 100 °C at a pressure lower than 5 Torr.

A typical GFA spectrum,¹⁰⁴ i.e., oxygen signal plotted vs time, is illustrated in Fig. 15. The three partially separated peaks indicate three sources of oxygen evolution from the sample. The first peak, occurring after about 15 s, is made up of various easily liberated oxygen-containing species from surface contaminants. The second and third ones are due primarily to surface oxide and bulk oxygen, respectively, although they may have other components. These two peaks can be well separated from each other by appropriate program of power inputs. The third peak is due primarily to bulk

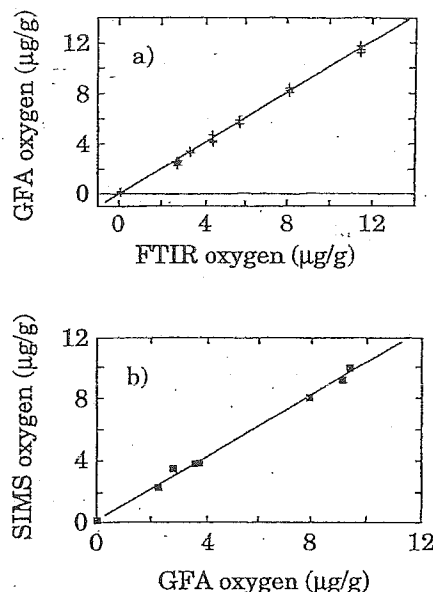


FIG. 16. Correlation of GFA relative oxygen concentration results with (a) FTIR data and (b) SIMS data (from Ref. 105). The continuous line represents the linear regression results.

oxygen but it could also be affected by the oxidation at the surface. Shaw and co-workers¹⁰⁴ demonstrated that such influence could be of the order of 10% of the typical oxygen level in Cz silicon. Such an effect is tentatively attributed to a very stable surface or near-surface oxide. Nonoxidized samples show excellent correlation between SIMS and GFA measurements.

The GFA technique needs calibration which is usually performed in two steps. For precalibration measurements standard steel samples are used. Basic elements of the second step are standard gas mixtures and silicon slices cut from selected ingot positions and measured with FTIR. The bulk oxygen content of the silicon sample is calculated in μg/g or atoms/cm³. The correlation factor to convert μg/g to atoms/cm³ is 0.877×10^{17} . The detection limit for a typical instrument can be $<1 \times 10^{16}$ atoms/cm³ with a reproducibility of $<\pm 2\%$ for 5–10 μg/g and $\pm 3\%$ –4% for 2–3 μg/g.

Figure 16 shows the correlation of GFA results with FTIR [Fig. 16(a)] and SIMS [Fig. 16(b)] data in the range from 0 to 12 μg/g. Correlation factors of 0.997 and 0.994 are found with FTIR and SIMS, respectively.¹⁰⁵

3. Secondary-ion mass spectrometry

SIMS has become a very versatile analytical technique in the semiconductor industry aimed at bulk impurity measurements. Determination of oxygen in silicon samples by SIMS is possible independently of doping type and concentration. Generally, the primary ion beam used to bombard the sample surface is constituted by a noble gas; however, the secondary ion yield can be increased through the use of oxygen or cesium primary ion beams. Electropositive gas such as cesium can enhance negative secondary ion yield of electronegative species.^{106,107} Williams *et al.*¹⁰⁶ showed the feasibility of using Cs⁺ bombardment combined with the detection of negative secondary ions in a depth profiling mode. It

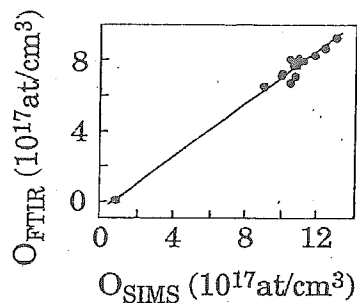


FIG. 17. Regression straight-line fit for oxygen concentration measured by FTIR and SIMS in highly doped silicon samples. The lowest point corresponds to undoped FZ silicon (from Ref. 97).

has been demonstrated that a high sensitivity can be obtained in the detection of oxygen in silicon. Typically, 10 mA/cm^2 of primary current density is used, which yields an oxygen background limit corresponding to $1 \times 10^{17} \text{ atoms/cm}^3$ as calibrated using ion-implanted samples. Usually SIMS instruments use lower current density, implying a worse background limit for oxygen detection. In fact, the detection limit for oxygen in silicon is controlled by the balance established between the adsorption rate of oxygen from the residual gas of the vacuum system and the rate of sample erosion during sputtering with primary ion beam. Thus, ultra high-vacuum (UHV) conditions are necessary in order to obtain reliable results. A further increase in sensitivity is possible using a very high sputter rate. Wittmaack¹⁰⁷ demonstrated the importance of highly focused primary ion beam and UHV conditions in determining the background levels of oxygen in silicon. Moreover, the background level can be further lowered by using a secondary ion optics designed to preferentially extract ions from the central area of the rastered crater.

Bleiler *et al.*¹⁰⁸ developed a methodology for accurate and reproducible measurements of oxygen in heavily doped silicon wafers. Prior to measurements the samples were baked for approximately 30 min at 100°C to remove adsorbed water. A proper vacuum system and a liquid-nitrogen-cooled shroud surrounds the sample holder ensuring about $2\text{--}3 \times 10^{-9}$ Torr pressure during the analysis. Another factor influencing the detection limit can be the natural abundance of different oxygen isotopes. While for ^{16}O resolution limit is $1 \times 10^{17} \text{ atoms/cm}^3$, for ^{18}O , in-diffused from H_2^{18}O or $^{18}\text{O}_2$ ambients, a detection limit approximately 500 times better can be obtained.

In addition, it is well known that the SIMS secondary ion yield varies quite drastically for different elements and for the same element in different materials (matrix effect).¹⁰⁹ To obtain quantitative SIMS data is thus not straightforward, and a careful calibration for an accurate comparison with other techniques is essential. Calibration of the oxygen yield by means of a known oxygen ion implantation profile results in an accuracy of about 30%, while the depth scale calibrated with a profile measurement of the sputter crater gives an accuracy of about 10%. The precision of the method is $\pm 2\%$ on a routine basis.¹¹⁰

The comparison between SIMS analysis and FTIR transmission measurements performed by Borghesi *et al.*⁹⁷ is

given in Fig. 17. The figure shows O_{FTIR} vs O_{SIMS} straight-line fits. The correlation between the two sets of data is satisfactory, as indicated by the high value of the linear correlation coefficient (0.97) and by the low standard deviation ($0.37 \times 10^{17} \text{ atoms/cm}^3$) of the fits.

4. Other methods

In CPAA a silicon crystal doped with ^{18}O is irradiated with a 4.6 MeV proton beam or with α particles of 18–23 MeV, to produce the nuclear reactions^{46,48,98}



or



respectively. Both reactions produce the unstable fluorine isotope ^{18}F , which decays into ^{18}O with half-lifetime of 109.7 min by emitting a β^+ particle.

Oxygen content depth profiling is possible by repeated measurements after sequential etching of the surface layer.

The presence of the surface native oxide layer interferes with the signal of the oxygen in silicon. Therefore, care has to be taken in completely removing this oxide and the oxygen adsorbed during the measurement (this is usually performed by the *in situ* sputtering with a beam of argon ions). With reaction (24) this problem could be overcome by using highly ^{18}O -enriched oxides as diffusion sources and by etching back this oxide before the measurements, so that a native oxide with the normal low ^{18}O abundance is formed. The detection limit of CPAA is $1 \times 10^{15} \text{ atoms/cm}^3$ and the accuracy about 20%.

The total oxygen content in silicon can also be measured by activation with high-energy photons, generated by bombardment of a tungsten target with 30 MeV electrons with a maximum of bremsstrahlung in the range of about 20 MeV. This technique is known as photon activation analysis (PAA). The mentioned energy range yields a giant resonance for the nuclear reaction¹⁰²



with half-lifetime of 2.03 min. During the irradiation the sample rotates, in order to be homogeneously activated. After irradiation the samples are etched with the solution nitric acid/hydrofluoric acid (1:1) in order to remove the activated surface oxide and to eliminate background problems. GFA (see Sec. II C 2) is then performed with iron as a metallic bath. The sample is completely dissolved at 2000°C under helium gas flux. The sample collection efficiency is about 100%.

The determination of the activated oxygen is based on the annihilation radiation, generated by β^+ radiation of ^{15}O , which reacts with an electron under emission of two γ rays of 511 keV, that are further measured with two detectors in coincidence to determine oxygen decay curve and content.

Figure 18 shows a comparison of oxygen concentrations determined by PAA versus absorption coefficient of IR oxygen band at 1107 cm^{-1} . The accuracy of the method is typically better than $\pm 15\%$ and the detection limit is $5 \times 10^{15} \text{ atoms/cm}^3$.

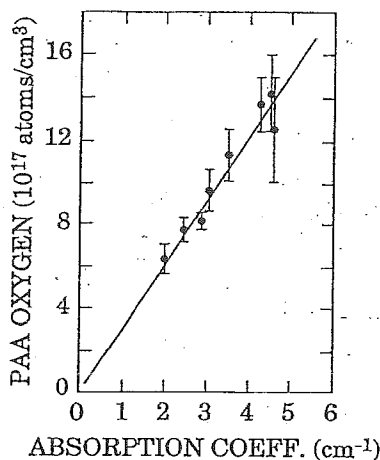


FIG. 18. Least-mean-squares fit of oxygen concentration data obtained by IR spectroscopy and PAA (from Ref. 102).

Two indirect methods of measuring oxygen in silicon also exist:

- (1) determination of the lattice dilatation due to interstitial oxygen atoms by x-ray diffraction analysis;
- (2) spreading resistance profiling of thermal donors, whose concentration is considered proportional to a power of starting interstitial oxygen concentration.

Takano and Maki⁴⁷ quantified the lattice dilatation due to the presence of interstitial oxygen atoms within the silicon lattice, considering the value of oxygen concentration as determined using IR-absorbance measurements. By stepwise removal of silicon from the surface they obtained dilatation profiles that were subsequently converted in oxygen diffusion profile. The sensitivity limit of this method is 1×10^{17} atoms/cm³, on the basis of the determination of the diffusivities and solubilities only for a temperature range from 1100 to 1200 °C. Nevertheless, these measurements are in excellent agreement with those obtained by means of other methods.

The thermal donor profiling by spreading resistance measurements relies on the formation of thermal donors arising from oxygen related complexes. The rate of formation is proportional to the starting oxygen concentration to the third or fourth power. Thus, the gradient of oxygen concentration is converted in gradient of thermal donor concentration; however, such a correlation would require the comprehension of donor formation process, which has not yet been achieved.

III. THERMODYNAMICS AND KINETICS OF PRECIPITATE FORMATION

A. Nucleation

The first stage of oxygen precipitation in silicon is nucleation, a process leading to the formation of aggregates of a few O atoms, the so-called nuclei or precipitate embryos, within the silicon lattice. Once formed, precipitation nuclei can either further grow and form oxide precipitates or dissolve, depending on the characteristics of silicon crystals and

on the thermal treatments performed. The fundamental parameter for nucleation (and, therefore, precipitation) is the degree of supersaturation of the solid solution constituted by the Si crystal (solvent) and the interstitial oxygen (solute), i.e., the ratio between the concentration of oxygen present in the Si crystal C_{ox} and its solubility limit C_{ox}^* (which is a function of temperature).

Nucleation can occur at crystal lattice sites where few interstitial oxygen atoms are close to each other (homogeneous nucleation^{111–117}), or at lattice defects (heterogeneous nucleation^{118–128}). Both processes lead to the formation of nuclei having different distributions and size.

In this subsection a general discussion about nucleation theory and related experimental results is reported, describing both homogeneous and heterogeneous processes. Moreover, some nucleation models¹²⁴ are illustrated and the mechanisms of nucleus dissolution, occurring during particular thermal treatments of silicon wafers, are described.¹²⁵

1. Homogeneous strain-free nucleation

A very important parameter in the theory of nucleation is the critical radius r_c , distinguishing the nuclei which upon thermal treatment grow further ($r > r_c$) from those which are going to dissolve ($r < r_c$). It depends on several characteristics of the silicon crystal such as, for example, self-interstitial and vacancy concentrations, impurity type and content, elastic properties, and temperature.^{114,115}

As a first step a theory for strain-free nucleation is illustrated, i.e., a theory that describes nucleation by completely neglecting the strain energy related to the structural difference between silicon and the oxide composing the nuclei. Under this assumption, the free energy ΔG required to form a spherical nucleus with radius r is given by the sum of two contributions: The particle-matrix interface energy and the chemical energy of supersaturation. The first term is positive since energy is needed to increase the nucleus surface, while the second one is negative since chemical energy of supersaturation decreases when solute atoms (oxygen) are removed from the solution and incorporated into the nucleus. The total free energy ΔG is therefore

$$\Delta G = 4\pi r^2 \gamma - \frac{4}{3}\pi r^3 \Delta G_v, \quad (26)$$

where γ is the interface energy per unit area and ΔG_v is the volume free energy, related to the variation of the chemical energy of supersaturation per unit volume after oxygen atom removing from the solution. ΔG_v can be written as

$$\Delta G_v = \frac{k_B T}{v_P} \ln \frac{C_{ox}}{C_{ox}^*}, \quad (27)$$

where k_B is the Boltzmann constant, T is the absolute temperature, and v_P is the particle volume per oxygen atom (i.e., volume per oxygen atom in the silicon oxide SiO_x composing the nuclei).

The critical radius is defined as the value $r = r_c$ for which $d(\Delta G) = 0$ (equilibrium); in the case of strain-free nucleation it can be derived from Eq. (26),

$$r_c = \frac{2\gamma v_P}{k_B T \ln(C_{ox}/C_{ox}^*)}. \quad (28)$$

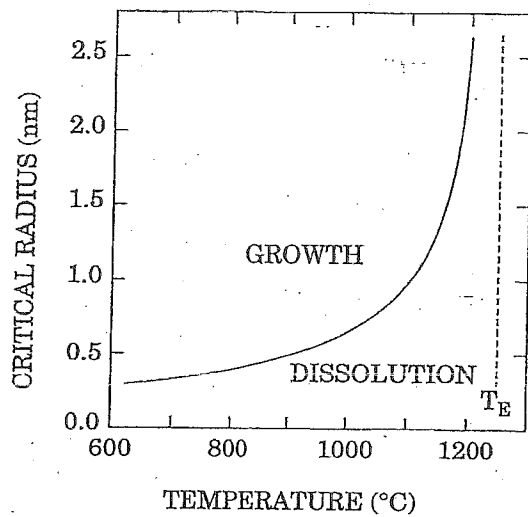


FIG. 19. Temperature dependence of the critical radius as determined from Eq. (28). T_E is the temperature at which the actual C_{ox} should equal C_{ox}^* (from Ref. 113).

When the nucleus radius r is smaller than r_c the volume free energy is lower than the surface free energy and, therefore, the nucleus dissolves. On the contrary, when $r > r_c$ the surface free energy is the smaller term in Eq. (26) and a precipitate can grow. From the expression of r_c it is clear that high temperatures and high oxygen concentrations enhance precipitate growth, reducing the nucleus critical radius. On the other hand, low temperatures correspond to low C_{ox}^* , which also causes r_c to decrease. These trends lead to a monotonically increasing function $r_c(T)$. Figure 19 reports the plot of $r_c(T)$ as deduced from Eq. (28), considering $\gamma = 410$ erg/cm², $v_p = 37.66$ Å³, and $C_{ox} = 11 \times 10^{17}$ atoms/cm³. T_E in the figure is the temperature at which the actual value C_{ox} should equal C_{ox}^* .

In the classical theory of nucleation¹¹⁸ the number N of nuclei of radius r per unit volume follows a Boltzmann distribution,

$$N(r) = c \exp\left(-\frac{\Delta G}{k_B T}\right), \quad (29)$$

where c is the number of nucleation sites per unit volume. The nucleation rate $J_0 = N/t$, where t is the time, is given by

$$J_0 = 4\pi r_c^2 c (D/d) Z n(r_c), \quad (30)$$

where D is oxygen diffusion coefficient, d is the so-called atomic jump distance of oxygen, and Z is the Zeldovich factor ($Z \approx 10^{-2}$), corresponding to the fraction of oxygen atoms which are included in the precipitate nuclei immediately after nucleation. The nucleation rate dependence on the interstitial oxygen content and on the temperature as deduced from a best fit of experimental data¹²⁹ with Eq. (30) is reported in Figs. 20(a) and 20(b) respectively.¹¹⁵

In Fig. 20(a) the experimental data fit very well with the calculated line, while in Fig. 20(b) the agreement is less satisfactory, probably because of the neglected dependence of Z on the temperature. Figure 20(c) reports the function $J(T)$ for different interstitial oxygen contents and shows that for

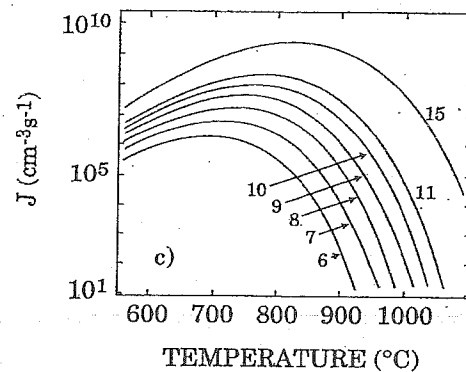
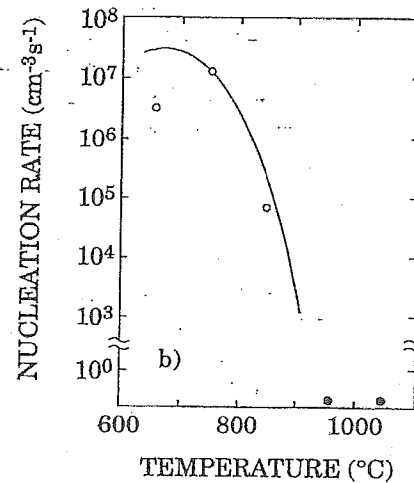
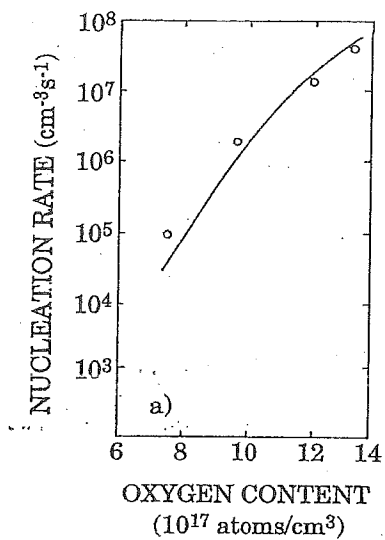


FIG. 20. Dependence of the nucleation rate on (a) the oxygen content and (b) the temperature. Open circles indicate the experimental data, solid circles show the detectability limit for two temperatures, and the lines are the best fit (from Ref. 115). (c) Dependence of the nucleation rate J on the temperature for crystals with different interstitial oxygen content (indicated in 10^{17} atoms/cm³ units).

typical Cz wafers ($C_{ox} = 7-10 \times 10^{17}$ atoms/cm³) the optimum temperature range for nucleation is from 650 to 850 °C.

All the relations derived up to this point disregard the possible time dependence of the thermodynamic state of the solid solution. A nonsteady-state theory of nucleation can be used to describe the process occurring after a sudden cooling

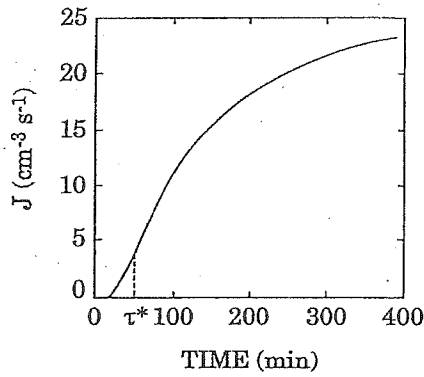


FIG. 21. Time dependence of the nucleation rate J . The value of the induction time τ^* is indicated.

of the Si crystal, where a supersaturation state suddenly develops. Such a theory can be particularly interesting for the comparison with experimental results regarding precipitation rate, being more adequate to the real process. In the nonsteady-state the nucleation rate is

$$J(t) = J_0 \exp\left(-\frac{\tau^*}{t}\right), \quad (31)$$

where J_0 is the steady-state nucleation rate of Eq. (30) and τ^* is called the nucleation time (or induction time). Figure 21, which reports the plot of $J(t)$, shows that the nucleation rate reaches its steady-state value J_0 as t approaches infinity (τ^* is also explicitly indicated). The nucleation time can be written as

$$\tau^* = \frac{n^2}{f}, \quad (32)$$

where $n = \frac{4}{3}\pi r_c^3 N$ is the number of oxygen atoms in the nucleus (N is the atomic concentration in the precipitates) and f the frequency of atom sticking to a critical nucleus. τ^* decreases with increasing the temperature, as shown in Fig. 22,¹¹⁵ which reports $\tau^*(T)$ for different C_{ox} values (indicated in units of 10^{17} atoms/cm³) obtained by using the same best-fit parameters as in Fig. 20. Higher temperature, as already pointed out and shown in Fig. 19, leads to smaller r_c

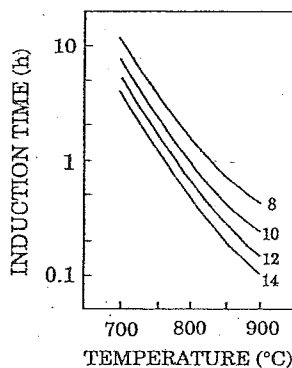


FIG. 22. Temperature dependence of induction time. Each curve is labeled by the C_{ox} value in 10^{17} atoms/cm³ units (from Ref. 115).

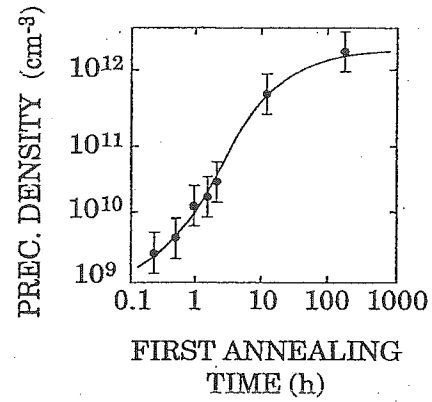


FIG. 23. Precipitate density in a sample with initial $C_{ox} = 8.8 \times 10^{17}$ atoms/cm³ annealed for 10 h at 1000 °C as a function of the duration of the nucleation annealing at 750 °C (from Ref. 129).

values and, therefore, to a τ^* decrease. Moreover, at high temperatures the oxygen atomic diffusivity is high and also f increases, leading in turn to low τ^* .

τ^* can be obtained both from Eq. (31) and experimentally from the increase of precipitate density with time. The two evaluations lead to $\tau^* \approx 1$ h and $\tau^* \approx 10^2$ h, respectively,¹¹⁵ but this discrepancy can be ascribed to the fact that probably not all the oxygen atoms reaching a nucleus remain there.

The nucleation rate has been deduced by Inoue and co-workers¹²⁹ to slow down, reaching a saturation value, as the duration of the nucleation annealing increases. Figure 23 shows the precipitate density as a function of nucleation annealing time for samples annealed at 750 °C (nucleation) and then for 10 h at 1000 °C (precipitation). The precipitate density has been measured¹²⁹ by the surface etching technique (see Sec. IV A) after the second annealing. The authors propose an explanation for the described saturation. It can take place when the diffusion layers surrounding each nucleus overlap, so that further oxygen diffusion leads to the growth of the existing nuclei more likely than to the creation of new ones. The diffusion layer has been assumed as spherical, with radius \sqrt{Dt} , where D is the diffusion coefficient of oxygen in silicon and t is the nucleation time. Saturation occurs when the average distance between two adjacent nuclei is of the order of \sqrt{Dt} . The following relation between the number density of nuclei N and \sqrt{Dt} is therefore assumed

$$N^{-1/3} = (Jt)^{-1/3} = \sqrt{Dt}. \quad (33)$$

Then the time t_s when saturation begins and the saturation number density of nuclei N_s can be determined,

$$t_s = \left(\frac{4}{3}\pi D^{3/2} J\right)^{-2/5} \quad (34)$$

and

$$N_s = J^{3/5} \left(\frac{4}{3}\pi D^{3/2}\right)^{-2/5}. \quad (35)$$

This model for the saturation in nucleation is well confirmed by the good agreement between experimental and calculated $N(t)$ values, shown in Fig. 24 for various annealing temperatures, for a silicon crystal with $C_{ox} = 11 \times 10^{17}$ atoms/cm³.

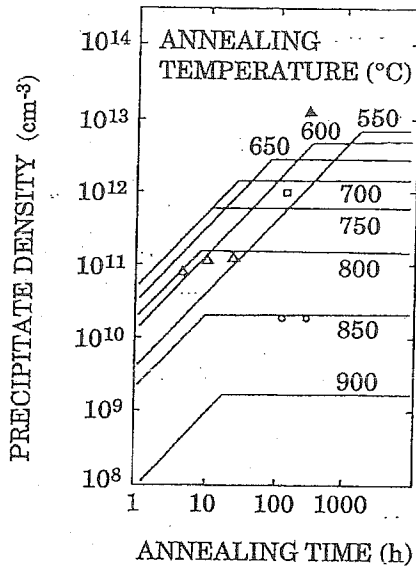


FIG. 24. Experimental data of the density of nuclei as a function of annealing time for different annealing temperatures: 650 °C (solid triangle); 750 °C (open squares); 800 °C (open triangles); and 850 °C (open circles). The lines are the $N(t)$ functions calculated for different temperatures according to Eq. (35) (from Ref. 129).

Homogeneous nucleation has been reported^{115,125} as responsible for a phenomenon called time lag in precipitate growth, which is considered the experimental evidence of the time dependence of Eq. (31). Time lag consists in a “delay” of precipitation detected in samples subjected to a short high-temperature preannealing (e.g., 5 min at 1200 °C) before the precipitation treatment (several hours at low temperature). Considering Eq. (31) (or looking at Fig. 21), time lag can simply be related to the initial transient $\Delta t \approx 3 - 4 \tau^*$, when $J(t)$ is still noticeably different from the steady-state value J_0 . Some authors¹¹² disagree, considering time lag a piece of evidence for heterogeneous nucleation (see Sec. III A 3).

Figure 25¹¹⁵ reports experimental data regarding time lag

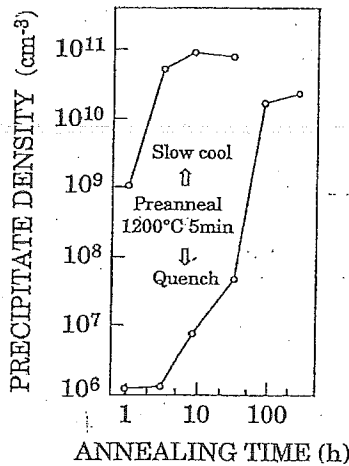


FIG. 25. Time dependence of precipitate density during anneal at 800 °C for two samples subjected to preanneal at 1200 °C for 5 min. The upper curve refers to a slowly cooled sample, the lower one to a quenched sample (from Ref. 115).

in precipitation, i.e., the precipitate density detected in silicon wafers subjected to different thermal treatments, which is directly related to the initial concentration of nuclei. The precipitate density in the sample subjected to a short preannealing and then quenched is initially very low, abruptly increasing after about 70 h. This initial delay has been related to the nucleation time.

2. Homogeneous nucleation with strain

The assumption of nucleation as a strain-free process imposes a serious limit for the theory outlined in Sec. III A 1, even if it results in qualitatively good agreement with experimental data and partially includes (implicitly) the lattice strain when considering the interface energy γ . More adequate models have been proposed^{114,116,130,131} to explicitly take into account the strain-energy contribution to the total free-energy variation ΔG . Indeed, the difference between the volume per Si atom in the precipitate V_p and in the silicon crystal V_{Si} (volume misfit) causes an increase of precipitate strain energy during growth (in particular for the case of SiO_2 in Si, $V_p > V_{Si}$). Absorption of n_V vacancies from the bulk of silicon and/or emission of n_I self-interstitial atoms release part of this strain.^{116,117} Consideration of this last contribution leads us to include intrinsic point defects in the nucleation process, although the term homogeneous nucleation is still used to distinguish this case from that which involves extrinsic defect contribution or intrinsic defects as the main constituents of the nuclei.

On the basis of these arguments about strain, it is clear that Eq. (26) has to be modified. According to Hu,¹¹⁴ it is useful to describe the volume variation of a precipitate, when its radius r increases by dr , in terms of elastic properties of silicon. When a few Si atoms are included in a precipitate nucleus, they leave a cavity in the bulk of the silicon. Such a cavity can be described as a sphere of radius r_0 to compare with the growing particle. At the same time the growing particle has a different radius $r = (1 + \delta)r_0$, where δ is the linear misfit between Si and SiO_x lattices ($\delta \sim 0.3$ for SiO_2). To reach a common radius r_p (the actual nucleus radius) the cavity must be expanded, while the nucleus must be compressed. The final radius r_p falls between r_0 and r , i.e., $r_p = r_0(1 + \epsilon)$, where $0 < \epsilon < \delta$. Considering the shear modulus of silicon μ and the bulk compressibility of SiO_x K and assuming $\epsilon, \delta \ll 1$, the strain ϵ compressing the precipitate is

$$\epsilon = \frac{\delta}{1 + 4\mu/3K}. \quad (36)$$

The final radius r_p can also be written as

$$r_p = r \frac{(1 + \epsilon)}{(1 + \delta)}. \quad (37)$$

Then, ΔG of a SiO_x spherical precipitate, considering an increase dr of the radius r , is

$$\Delta G = \left[(1 + \delta + \epsilon)^3 \frac{xrk_B T}{V_p} \left(-n_I \ln \frac{C_I}{C_I^*} - n_V \ln \frac{C_V}{C_V^*} - \ln \frac{C_{ox}}{C_{ox}^*} \right) + 2\gamma + 6\mu\delta\epsilon r \right] 4\pi r dr, \quad (38)$$

where n_I and n_V are the numbers of interstitials and vacancies emitted and absorbed, respectively, C_I and C_V are the concentration of interstitials and vacancies, respectively, and C_I^* and C_V^* are the solubility limits of these defects in silicon. The term $(6\mu\delta\epsilon)4\pi r dr = (6\mu\delta\epsilon)dV$ is the change in the total elastic energy of a spherical nucleus related to a volume variation dV .

From Eq. (38) a more complete expression for the critical radius r_c that also considers strain energy is obtained,

$$r_c = 2\gamma \left[\frac{(1 + \delta - \epsilon)^3 x k_B T}{V_P} \ln \frac{C_{ox}}{C_{ox}^*} \left(\frac{C_V}{C_V^*} \right)^{n_V} \left(\frac{C_I^*}{C_I} \right)^{n_I} \right]^{-1} \quad (39)$$

Besides the strain-related contribution, this expression also illustrates the role of interstitial Si atoms and vacancies in strain relief. It is important to note that in the case of strain-free nucleation, i.e., $\epsilon = \delta = 0$, Eq. (39) is identical to Eq. (28).

Equation (39) can be rewritten in a useful form using the following expressions for C_{ox} , C_{ox}^* , C_I , C_I^* , C_V , and C_V^* :

$$C_X = c_X \exp \left(- \frac{T_X}{T_s^X} \right) \quad (40a)$$

and

$$C_X^* = c_X \exp \left(- \frac{T_X}{T_s^X} \right), \quad (40b)$$

where c_X is a constant and $X = I, V, ox$. T_X is the characteristic temperature derived from the heat of solution $H_X = k_B T_X$ and T_s^X is the temperature at which the actual X content should be soluble ($T_s^{ox} = T_E$ in Fig. 19). By substituting Eqs. (40) in Eq. (39) we obtain

$$r_c = \frac{2\gamma v_P}{x k_B T} \frac{T_s^{ox}}{\xi T_s^{ox} - \lambda T}, \quad (41)$$

where

$$\xi = (1 + \delta - \epsilon) \left(1 + \frac{n_V T_V}{T_{ox}} - \frac{n_I T_I}{T_{ox}} \right) - \frac{6\mu\delta\epsilon v_P}{x k_B T_{ox}}$$

and

$$\lambda = (1 + \delta - \epsilon) \left[1 + \left(\frac{n_V T_V T_s^{ox}}{T_{ox} T_s^V} - \frac{n_I T_I T_s^{ox}}{T_{ox} T_s^I} \right) \right].$$

In intrinsic thermal equilibrium conditions ($T = T_s^I = T_s^V$), the critical radius becomes

$$r_c = \frac{2\gamma v_P}{x k_B T} \frac{T_s^{ox}}{\xi' T_s^{ox}}, \quad (42)$$

where

$$\xi' = (1 + \delta - \epsilon) - \frac{6\mu\delta\epsilon v_P}{x k_B T_{ox}}.$$

Equation (42) relates the critical radius r_c to the temperature at which the actual interstitial oxygen content should be soluble T_s^{ox} . This is very interesting because the initial oxygen concentration is usually a known parameter and can be controlled.

Another interesting model for homogeneous nucleation involves thermal donors, considered as aggregates of several oxygen atoms.¹³² Assuming that only one type of thermal donors dominates carrier increase during thermal donor formation and considering the results of the classical nucleation theory about the concentration of nuclei and the nucleation rate [see Eqs. (29) and (30)], the dominant thermal donors are deduced to act as nuclei for oxygen precipitation in Cz silicon above 600 °C. This result allows one to predict the nucleation rate dependence on initial oxygen concentration, annealing temperature, and carrier concentration, which are found to well reproduce the experimental findings. Nevertheless, in Ref. 132 the authors underline that there is also some experimental evidence of heterogeneous nucleation which they believe to simultaneously occur and compete with homogeneous nucleation.

Other nucleation models including intrinsic point defects as active elements have been proposed^{112,119,120} and are illustrated in the following subsection as heterogeneous nucleation models.

3. Heterogeneous nucleation

Nucleation of oxide precipitates can occur on lattice defects, mainly substitutional carbon atoms, carbon-oxygen complexes, and point defects. A clear description of the mechanisms involved in this phenomenon is not yet available, but some general trends have been evidenced^{119–123,125–127} from the analysis of a lot of experimental data.

Regarding the influence of carbon, several phenomena enhancing oxygen nucleation and precipitation are widely accepted to occur. First of all, in C-rich samples the variation of interstitial oxygen concentration, usually related to precipitation, has been shown to increase. At the same time, substitutional carbon concentration, measured through the IR absorption of Si—C bonds, decreases. Probably, oxygen aggregating on carbon atoms during precipitate nucleation makes C undetectable, due to the variation of the vibrational properties of Si—C—Si bonds.

Carbon atoms in the silicon lattice can form SiC particles, which produce a volume contraction of about 50%. Therefore, C presence can cause the formation of free volume in the silicon crystal, available for nuclei and precipitates. Moreover, this free volume leads to a C_I decrease and, therefore, also to a r_c decrease [see Eq. (39)].

Besides single C atoms, carbon-oxygen complexes have also been proposed to act as heterogeneous nuclei for oxygen precipitation in Cz silicon.^{122,133–136} The same experimental data reported in support of the assumption of nucleation related to substitutional C atoms might also lead to the hypothesis of a significant role of C-O complexes. The variation of IR-absorption bands related to C-O complexes has been connected to changes in the interstitial-oxygen peak due to precipitation. Therefore, C-O complexes are deduced to be involved in precipitation as the most probable nuclei. On the basis of these findings heterogeneous nucleation is indicated as predominant at low temperatures, while the homogeneous mechanism predominates at higher temperatures. In Fig. 26 the IR spectra of samples annealed at 900 °C for different

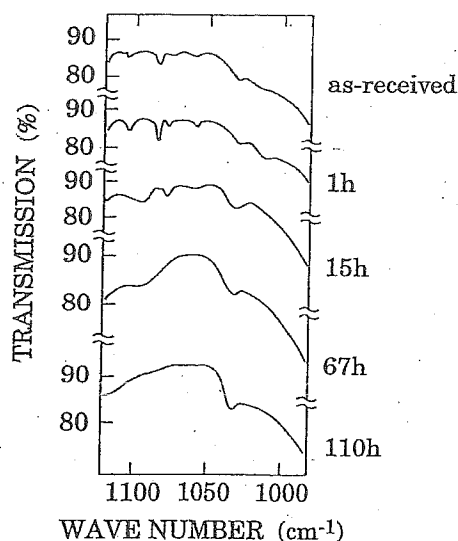


FIG. 26. IR transmission spectra of Cz silicon samples heated at 900 °C for various times in N₂, showing the C-related absorption bands (from Ref. 122).

times are reported.¹²² The absorption bands present in the spectrum of the as-received sample related to C-O complexes decrease with the interstitial-oxygen band as the annealing time is increased and precipitation takes place. After 110 h annealing, the intensity of all these bands is below the detection limits.

Intrinsic point defects, in particular vacancy clusters formed in the silicon crystal during growth and including also solute atoms, have been assumed to be possible nuclei^{112,119,137} (modified homogeneous nucleation). One of the main arguments supporting this hypothesis is the role of the clusters in releasing the volume misfit associated with precipitate growth. At high temperatures these centers can also dissolve, due to the self-interstitial generation in the Si crystal. This phenomenon has been indicated¹¹² as responsible for the above-mentioned time lag in precipitation, instead of the explanation based on the homogeneous model for nucleation. Moreover, the hypothesis that clusters of vacancies can be part of the nuclei is supported by the experimental data about precipitation reduction in samples treated in oxidizing ambient,^{111,114} where vacancy clusters are known to annihilate. On the basis of the hypothesis of heterogeneous nucleation occurring at vacancy-solute atom clusters, Ravi¹¹⁹ suggested two possible models for nucleation, which can also explain the Si crystal faceting observed on the sample surface after precipitation. The first one postulates a direct nucleation of SiO₂ at vacancy clusters. The second one is a multistep mechanism, involving stacking faults. Indeed, extrinsic stacking faults can nucleate at vacancy clusters during heat treatments, then becoming nucleation sites for SiO₂ precipitates during further annealing. The mentioned faceting of the Si crystal surface arises from the inhibition of oxidation at the precipitate sites.

Other possible centers for heterogeneous nucleation have been indicated in the so-called swirl defects,^{120,121} whose nature is not clear, but in any case related to the condensation of self-interstitials. High concentrations of these defects re-

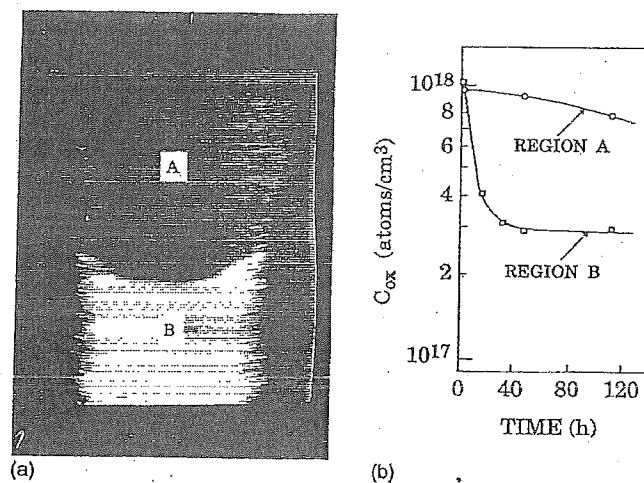
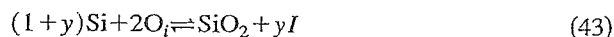


FIG. 27. X-ray topography (left-hand side) of a longitudinal section of a quenched silicon crystal pulled at 1 mm/min and annealed at 1000 °C for 16 h. Region A contains swirl defects, while region B is defect free. Interstitial oxygen concentration vs annealing time at 1000 °C (right-hand side) measured at crystal axis in regions A and B (from Ref. 120).

duce precipitation, while silicon crystal doping can enhance the process. Indeed, doping reduces swirl-defect concentration, thus preventing their detrimental effect on precipitation. Figure 27 (left-hand side) shows the x-ray topography of a longitudinal section of an undoped Si ingot annealed at 1000 °C for 16 h.¹²⁰ Region A is rich in swirl defects, while region B is defect free. In Fig. 27 (right-hand side) the interstitial-oxygen concentration at different stages of the annealing is also reported.¹²⁰ In region B the decrease of O_i concentration, connected with precipitation, is much more evident, confirming the retardation role of swirl defects.

On the other hand, self-interstitials seem to help precipitation of oxygen, acting as nuclei, when the oxygen supersaturation ratio s (C_{ox}/C_{ox}^*) is smaller than 5. If s is increased their influence decreases and becomes negligible for $s=20$. Also the mentioned retardation of precipitation in samples treated in oxidizing ambients has been related^{111,114} to the decreased self-interstitial concentration in such samples.

Retardation of precipitation, experimentally observed using IR spectroscopy in samples subjected to prolonged nucleation treatments (2–16 h), has also been related¹²⁵ to the possible dissolution of the nuclei, described by an interesting model. According to that model, dissolution takes place at the onset stage of the precipitate-growth annealing, due to the large supersaturation of silicon self-interstitials. Indeed, this increases r_c and a large fraction of nuclei dissolve, because the reaction



is driven to the left-hand side. The generation of self-interstitials, also taking place at the initial stage of the growth annealing, is essentially due to the need of an accommodation volume for the precipitates (remember that $V_p > V_{Si}$).

To complete this overview on heterogeneous nucleation it is worth mentioning the findings of Wada *et al.*,¹²³ who

deduced nucleation in as-grown silicon crystals to be heterogeneous from the characteristic nucleation temperature observed (1000–1250 °C), which is higher than those predicted for the homogeneous process. Moreover, they related precipitation to thermal fluctuations in the crystal during growth, causing the formation of the heterogeneous nucleation centers.

4. Nucleation in as-grown crystals

Oxygen precipitation in as-grown silicon crystals is a very important process, being characteristic of the starting conditions for further precipitation. Several experimental works^{113,123,128,131,138} deal with this subject and some models for nucleation in these samples have been proposed.

In the framework of a growth model for precipitates in as-grown crystals,¹¹³ essentially developed using the concept of critical radius, nucleation is assumed to be homogeneous and to proceed at the same rate as during nucleation annealing (about 10^{17} nuclei/cm³ s at 750 °C).¹³⁹ It takes place during the crystal cooling after heating cutoff, which is faster (about 100 °C/h) than crystal seed-end cooling during growth.

Another mechanism of nucleation leading to the formation of precipitates in as-grown silicon crystals has been proposed¹²³ on the basis of TEM observation and crystal cooling measurements. From the experimental results about precipitate shape, dimensions, and density in as-grown silicon samples the authors deduce that nucleation occurs via an heterogeneous mechanism, at temperatures from 1250 to 1000 °C during crystal cooling.

An interesting nucleation model including both homogeneous and heterogeneous processes has been recently developed¹²⁸ on the basis of experimental findings on particular samples. After halting the crystal growth for well-specified time intervals, therefore annealing the growth part of the crystal, the authors studied oxygen precipitation in as-grown samples. Precipitate density was found higher in the regions where the temperature during pulling halt was below 800 °C or above 1200 °C and this inhomogeneity of precipitate distribution was related to a different nucleation rate. Regarding the first regions, nuclei are assumed to be homogeneous, while the nuclei responsible for the high-temperature precipitation are assumed to be heterogeneous; probably clusters of point defects, because at such high temperature (≥ 1200 °C) C_{ox}^* was higher than C_{ox} . Moreover, when the temperature during the halt of pulling is high the density of heterogeneous nuclei depends on C content in the silicon crystal. On the basis of these experimental findings, nucleation is deduced to proceed as follows. First, some nuclei are formed at $T > 1200$ °C, remaining essentially inactive (unless the crystal is annealed at low temperature, as during cooling). Then, between 1100 and 900 °C the nuclei can incorporate C atoms and, finally, below 800 °C they become active as centers for precipitation (at this stage nucleation is heterogeneous).

Recently, Puzanov and Eidenzan¹³¹ proposed that the formation of oxygen precipitation nuclei during crystal growth proceeds through the following stages, which depend on the crystal growth regime:

- (i) recombination of intrinsic point defects near the crystal-melt interface, which determinates the type and concentration of surviving point defects in the growing crystal;
- (ii) redistribution of intrinsic point defects, their annealing at the crystal lateral surface and smoothing of concentration profile (diffusion stage);
- (iii) agglomeration of impurities and intrinsic point defects:

- (a) vacancy regime: A-defect (V-O complex) nucleation as a result of vacancy-oxygen interaction;
- (b) interstitial regime: B-defect generation as a result of coaggregation of self-interstitials and carbon atoms;

- (iv) growth and transformation of agglomerates involving consumption of intrinsic point defects:

- (a) vacancy regime: transformation of A-defect nuclei and reduction in vacancy concentration;
- (b) interstitial regime: transformation of some B-defects into A-defects; reduction in self-interstitial concentration;

(v)

- (a) vacancy regime: formation of secondary (low-temperature) nuclei;
- (b) interstitial regime: transformation of residual B-defects into centers of oxygen precipitation.

In this model each stage may depend not only upon its conditions, but also upon the results of all previous stages. Vacancy or interstitial regimes depend on the type and concentration of intrinsic point defects remaining in the crystal after recombination, depending on the ratio $\xi = V/G_0$, where G_0 is the longitudinal temperature gradient near the interface and V is the growth rate. For $\xi < \xi_t = 3.3 \times 10^{-5}$ cm² s⁻¹ K⁻¹ the remaining defects are self-interstitials and for $\xi > \xi_t$ they are vacancies. As a rule, crystals produced commercially are grown in the vacancy regime.

B. Precipitation

Oxygen precipitation in silicon is a phenomenon of aggregation of oxygen atoms, normally uniformly distributed within the Si crystal. As a consequence, small particles of SiO_x, $1 \leq x \leq 2$, form within the silicon crystal. Nowadays it is widely accepted that precipitation is driven, in a wide temperature range, by the diffusion kinetics.

In 1958 Ham proposed¹⁴⁰ a general theory to explain the kinetics of precipitation in a supersaturated solution by considering the phenomenon as diffusion limited. The validity of this model has been checked by different authors and experimentally confirmed. In particular, Patrick *et al.*,¹⁴¹ using a combination of TEM and IR measurements, showed that the growth of precipitates at about 1000 °C in a dislocation-free matrix fits very well the Ham kinetics. Wada *et al.*,^{123,142} on the basis of TEM observation, extended the validity of the model to the temperature range from 750 to 1050 °C. A detailed analysis and more extended experimental results were reported for the temperature range from 650 to 1050 °C using different techniques (see Sec. IV) such as chemical etching, optical scattering, cold neutron scattering, and infrared

absorption by Newman *et al.*¹⁴³ and by Binns *et al.*¹⁴⁴ Oxygen precipitation below 650 °C follows a kinetics that no longer agrees with Ham's theory since a negligible fraction of atoms is involved in the oxide precipitates.⁶⁸

The starting hypotheses to develop Ham precipitation model are as follows.

- (1) The silicon lattice is defect free (i.e., without any extended defects such as dislocations, besides precipitation nuclei).
- (2) The initial interstitial oxygen concentration C_0 (atoms/cm³) in the as-grown crystal is uniform.
- (3) The concentration of nuclei N (cm⁻³) remains constant during the heat treatment. This means that nucleation already occurred in as-grown material, in practice during crystal growth.
- (4) In the silicon lattice spherical precipitate nuclei having the same radius r_0 much smaller than their distances are present.
- (5) The precipitates (oxygen sinks) are made of a form of silica with oxygen concentration C_p . The oxygen concentration in the silicon matrix immediately adjacent to the precipitates C' is the equilibrium solubility limit C_{ox}^* (see Sec. II B 3) at the considered temperature (after an infinite time). The variation of C' during precipitate growth is neglected.

Assuming the particles are arranged in a simple cubic lattice and dividing the lattice into equivalent symmetrical cubic cells, each one centered at one precipitate nucleus, no oxygen flux is expected to cross the cubic cell boundaries if the distribution of nuclei is uniform.

It is worth noting that the assumption of spatially uniform distribution is not necessary, provided any crystal inhomogeneities are absent. In fact, oxygen atoms follow three-dimensional random walks and only a small probability of sticking to growing particles exists, due to the presence of oxygen concentration gradient only close to the precipitate, as is shown later.

The oxygen concentration profile $C_{ox}(r, t)$ as a function of the distance r from the center of the precipitate and time t fulfills the Fick equation,

$$\frac{\partial C_{ox}(r, t)}{\partial t} = D \nabla^2 C_{ox}(r, t), \quad (44)$$

where D is the oxygen diffusion coefficient, which is assumed to be independent of time, oxygen concentration, and position (see Sec. II B 4). This equation has to fulfill two boundary conditions:

- (i) At the precipitate/matrix interface ($r = r_0$) the oxygen concentration is equal to C' ;
- (ii) no solute flux can cross the cell boundary, due to symmetry.

We note that, taking into account the above-mentioned boundary conditions, it is sufficient to solve the Fick equation only for a single cubic cell.

To find the solution of Eq. (44) we first consider spherical precipitates with the value r_0 of precipitate radius con-

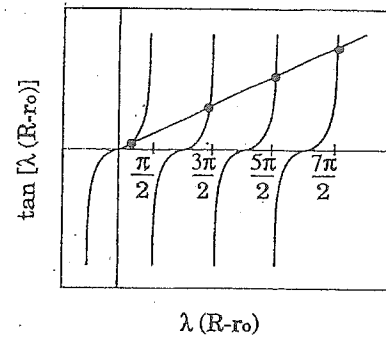


FIG. 28. Illustration indicating the solutions of $\tan[\lambda(R-r_0)] = \lambda R$.

stant and equal to its final value $r_0(\infty)$ (steady-state value, i.e., the value after infinite annealing time) and then we study the general case of increasing precipitate radius. Finally, the case of disk-shaped precipitates with increasing thickness is considered.

1. Spherical precipitates with fixed radius

In order to solve the Fick equation in this case, it is useful to expand $C_{ox}(r, t) - C'$ in terms of the eigenfunctions of the equation

$$\nabla^2 \psi_n(r) + \lambda_n^2 \psi_n(r) = 0, \quad (45)$$

obtaining

$$C_{ox}(r, t) - C' = \sum_{n=0}^{\infty} a_n(t) \psi_n(r). \quad (46)$$

To satisfy the boundary condition (i), $\psi_n(r_0)$ has to be zero $\forall n$. Then, substituting Eq. (46) into Eq. (44) and considering Eq. (45), we obtain

$$\frac{da_n(t)}{dt} = -D \lambda_n^2 a_n(t). \quad (47)$$

Therefore, $a_n(t)$ can be written as

$$a_n(t) = A_n \exp(-D \lambda_n^2 t) = A_n \exp\left(-\frac{t}{\tau_n}\right), \quad (48)$$

where A_n are normalizing constants and $\tau_n = 1/D \lambda_n^2$. From Eqs. (46) and (47) the solution of Eq. (44) expressed as $C_{ox}(r, t) - C'$ follows,

$$C_{ox}(r, t) - C' = \sum_{n=0}^{\infty} A_n \exp\left(-\frac{t}{\tau_n}\right) \psi_n(r). \quad (49)$$

Now using the Wigner-Seitz approximation we can replace the cubic cell surrounding each particle by a spherically symmetric region of equal volume with radius R satisfying the relation

$$\frac{4}{3} \pi R^3 N = 1, \quad (50)$$

where N (cm⁻³) is the average number of precipitates per unit volume, which has been assumed to be constant during annealing. Therefore, Eq. (49) in spherical polar coordinates is

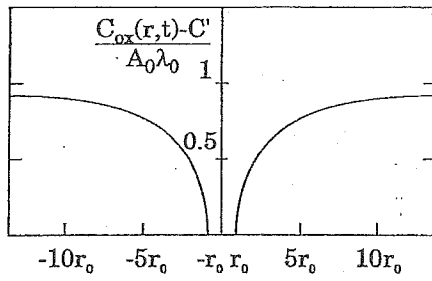


FIG. 29. Plot of interstitial oxygen concentration in the vicinity of an oxide precipitate of radius r_0 as deduced from Eq. (55).

$$C_{\text{ox}}(r,t) - C' = \sum_{n=0}^{\infty} A_n \frac{\sin[\lambda_n(r-r_0)]}{r_{1n}} \exp\left(-\frac{t}{\tau_n}\right). \quad (51)$$

The boundary condition (ii) can be written as $\{d[C_{\text{ox}}(r,t) - C']/\partial r\}_{r=R}=0$, i.e., from Eq. (51) as

$$\tan[\lambda_n(R-r_0)] = \lambda_n R. \quad (52)$$

The coefficients λ_n have the dimensions of a reciprocal length and can have infinite positive values (see Fig. 28).

The first solution of Eq. (52), considering that the precipitates usually occupy only a small fraction of the whole sphere with radius R (i.e., typically $r_0/R \approx 0.025$), is approximated as

$$\lambda_0^2 \approx \frac{3r_0}{R^3} \quad (53)$$

and then

$$\tau_0 = \frac{R^3}{3Dr_0}, \quad (54)$$

where $1/\tau_0$ is the precipitation rate.

It is possible to show that after a short initial transient, when all the solutions of Eq. (52) are significant, λ_0 gives the most important contribution to the variations of $C_{\text{ox}}(r,t)$. Therefore, after a time interval $\Delta t = \tau_0$ a pseudosteady state is reached. In that case, from Eq. (51), the concentration of oxygen remaining in the solution as a function of the distance r from the precipitate center and of the annealing time can be considered equal to

$$C_{\text{ox}}(r,t) - C' \approx A_0 \lambda_0 \left(1 - \frac{r_0}{r}\right) \exp\left(-\frac{t}{\tau_0}\right), \quad (55)$$

where $A_0 \lambda_0$ is a constant with the dimension of a concentration, equal to about $C_0 - C'$. This equation leads to interesting considerations. Fixing the annealing time t the spatial oxygen concentration profile can be obtained. In this case, as shown in Fig. 29, the oxygen concentration remaining in the solution is almost constant in the whole sphere of radius R ($R \approx 40r_0$), except for a central spherical region with radius of about $5r_0$. At a given distance from the precipitate, oxygen concentration decays exponentially to the equilibrium value C' with a time constant τ_0 given by Eq. (54).

The spatial average of oxygen concentration remaining in the solution C_m , usually measured by IR absorption, verifies this relation,

$$\frac{C_m(t) - C'}{C_0 - C'} = \exp\left(-\frac{t}{\tau_0}\right), \quad (56)$$

which allows one to determine the value of C' from the intensity of the 1107 cm^{-1} absorption band, which is proportional to $C_m(t)$. For long annealing time ($t \rightarrow \infty$), with $C_0 \gg C'$, Eq. (56) becomes

$$\lim_{t \rightarrow \infty} C_m(t) = C'. \quad (57)$$

Taking into account that the total oxygen content is conserved, we have

$$\frac{4}{3}\pi R^3 [C_0 - C_m(t)] = \frac{4}{3}\pi r_0^3 [C_P - C_m(t)]. \quad (58)$$

From this equation and considering Eq. (50), we obtain

$$C_0 - C_m(t) = \frac{4}{3}\pi r_0^3 N [C_P - C_m(t)]. \quad (59)$$

Since for $t \rightarrow \infty$ $C_m(t) = C'$, Eq. (58) gives

$$\frac{R}{r_0} = \left(\frac{C_P - C'}{C_0 - C'}\right)^{1/3}. \quad (60)$$

Then, substituting this expression into Eq. (54) we can write

$$\tau_0 = \frac{R^2}{3D} \left(\frac{C_P - C'}{C_0 - C'}\right)^{1/3}. \quad (61)$$

From Eqs. (61) and (50) the precipitate density N can be deduced,

$$N = \frac{3}{4\pi} \left(\frac{C_P - C'}{C_0 - C'}\right)^{1/2} (3D\tau_0)^{-3/2}. \quad (62)$$

A comparison between Ham's theoretical predictions and experimental data has been reported in Refs. 143 and 144. The authors studied dislocation-free Cz silicon samples, annealed for a very long time, with interstitial oxygen concentration $C_0 \approx 7 \pm 0.7 \times 10^{17} \text{ atoms/cm}^3$, as determined by IR-absorption measurements. Oxide precipitates were assumed to be constituted by SiO_2 with oxygen concentration $C_P = 4.6 \times 10^{22} \text{ atoms/cm}^3$.

The direct measurement of C' is not always possible, since it requires samples annealed for a very long time, necessary for oxygen to reach the equilibrium concentration value. Furthermore, duration of the suitable annealing depends on the temperature. For example, after 850°C annealing the value of C' was not yet reached after 800 h heating. For lower temperatures (below 750°C), even 2000 h were not enough to reach the equilibrium concentration value. This problem can be overcome by measuring at different times the amount of oxygen $C_m(t)$ remaining in the solution after the annealing time t , and extrapolating the value of $C_m(\infty)$ which is equal to C' according to Eq. (57).

Figure 30 (crosses) reports $C_m(t)$ normalized to the initial oxygen concentration C_0 after different annealing times at 850°C . The figure clearly shows that, after an initial transient (about 50–100 h) where a rapid reduction of oxygen in the solution occurs, the O concentration slowly decreases, thus approaching the equilibrium value C' . Once C' is determined, the value of τ_0 can also be easily deduced, taking into account Eq. (56), from the plot of $[C_m(t) - C']/(C_0 - C')$ as a function of time after the initial

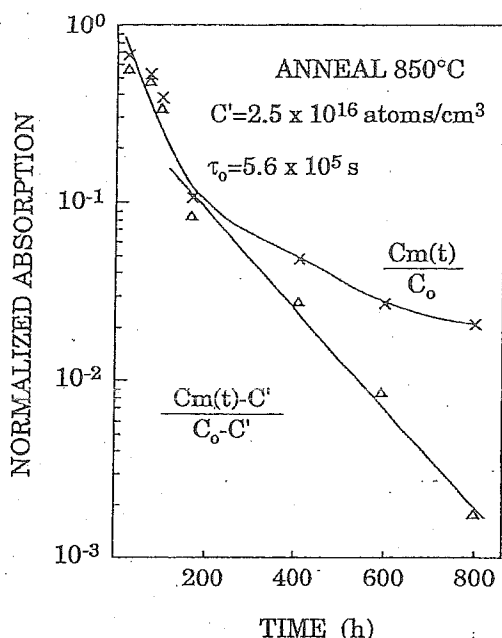


FIG. 30. IR absorption at 1107 cm^{-1} normalized to initial oxygen concentration $C_m(t)/C_0$ (crosses) and $[C_m(t) - C']/(C_0 - C')$ (triangles) for different annealing times (from Ref. 144).

transient (see triangles in Fig. 30). The values of τ_0 obtained by Newman *et al.*¹⁴³ are reported for different temperatures in Fig. 31. From the values of τ_0 the precipitate density N can then be calculated via Eq. (62) using a known value for the diffusion coefficient D . A comparison between the values of N calculated in this way (open circles) using $D = 0.07 \exp(-2.44/kT)$ (where kT is in eV, as proposed by Mikkelsen^{54,65}) and those obtained from etch-pit (crosses) and SANS measurements (open squares) are reported in Fig. 32. The very good agreement among the N values obtained with different experimental techniques (considering also their uncertainty) gives an important confirmation of the validity of the diffusion-limited kinetic model used to derive Eq. (62).

The radius of precipitates r_0 can be deduced from Eq. (59) using the obtained N values. Figure 33 shows r_0 as a function of the annealing temperature after a long heating time. Furthermore, the figure reports for comparison the ra-

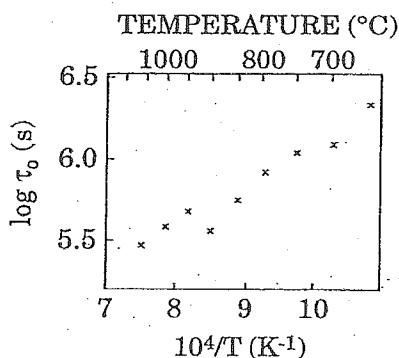


FIG. 31. Time constant τ_0 as a function of annealing temperature (from Ref. 143).

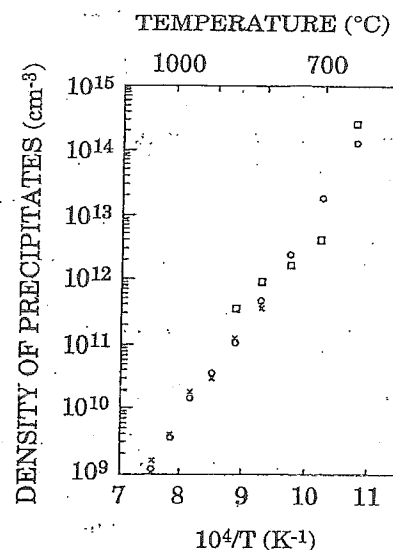


FIG. 32. Density of precipitates as a function of annealing temperature, as determined by etch-pit counts (crosses), kinetic model (circles), and SANS results (squares) (from Ref. 41).

dius of precipitates derived for the same samples by different techniques, such as neutron scattering, etch-pit measurements, and optical scattering (see Sec. IV). It is interesting to underline that the agreement among the values of r_0 obtained by different techniques is remarkably good.

In alternative to calculating of N from the kinetic data using D taken from Ref. 54, one can use the experimental N values obtained from etch-pit measurements together with the kinetic data to obtain the diffusion coefficient D . The

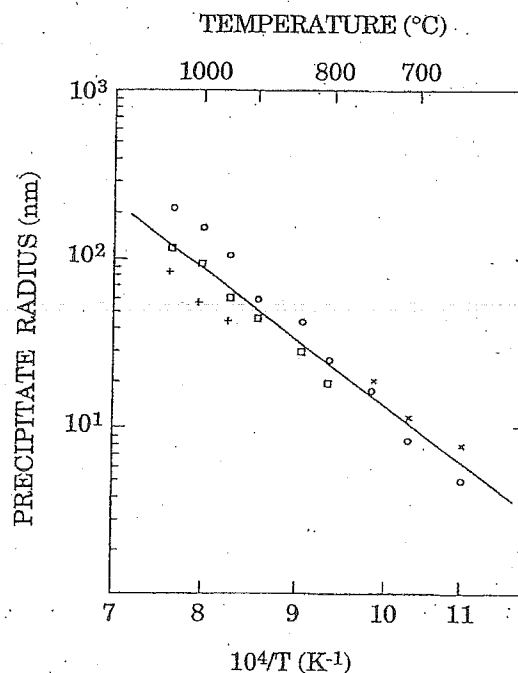


FIG. 33. Temperature dependence of precipitate radius derived from IR data and kinetic model (circles), SANS (crosses), etch-pit density (squares), and optical scattering (+). The solid line represents the best fit (from Ref. 145).

value for D obtained in such a way, for temperatures down to 650 °C, is

$$D = 0.02 \exp(-2.42/kT), \quad (63)$$

where kT is measured in eV. A comparison between the values of D obtained from the kinetic data and those reported in the literature is shown in Fig. 12. A more complete analysis of available experimental data over 12 orders of magnitude has been presented in Ref. 145 (see Sec. II B 4).

2. Spherical precipitates with increasing radius

The above-reported analysis which gives important results on the precipitation mechanism is strongly limited by the hypothesis that the precipitate radius r_0 is constant during annealing and is equal to the steady-state value. This limitation was overcome by an extension of Ham's theory taking into account the growth of the radius of precipitates as a function of annealing time.¹⁴⁰ The analysis can be limited to spherical particles since for the ellipsoidal ones only minor differences in the results are expected. This allows Ham's theory to be applied also to samples subjected to long-time heat treatment, where, as it is well known, precipitates are ellipsoidal. The assumptions for this more general model are:

- (i) The precipitates form and grow as identical spheres with $r_0 \ll R$, arranged in a simple cubic lattice, and
- (ii) the concentration of precipitates N and the diffusion coefficient of oxygen D remain constant with the annealing time.

Following the same procedure as in Sec. III B 1, the solution of Eq. (44) for growing precipitate radius is given by the relation¹⁴⁰

$$Kt = \frac{1}{6} \ln \left(\frac{[u^2(t) + u(t) + 1][u^2(0) - 2u(0) + 1]}{[u^2(t) - 2u(t) + 1][u^2(0) + u(0) + 1]} \right) - \frac{1}{\sqrt{3}} \tan^{-1} \left(\frac{2u(t) + 1}{\sqrt{3}} \right) + \frac{1}{\sqrt{3}} \tan^{-1} \left(\frac{2u(0) + 1}{\sqrt{3}} \right), \quad (64)$$

where

$$K = \frac{D}{R^2} \left(\frac{(C_0 - C')(1 + Z)}{C_P - C'} \right)^{1/3}, \quad (65)$$

$$Z = \frac{r_0^3(0)(C_P - C')}{R^3(C_0 - C')}, \quad (66)$$

$$u(t) = \left(1 - \frac{\rho(t)}{\rho(0)(1 + Z)} \right)^{1/3}, \quad (67)$$

and

$$\rho(t) = C_m(t) - C'. \quad (68)$$

The parameter Z , known as the Zeldovich factor, is the fraction of oxygen atoms in the precipitate at $t=0$ (i.e., immediately after nucleation). The value of Z in this case is 0.01 and may be assumed zero without any significant errors.

Equation (64) gives therefore the kinetics of oxygen precipitation as predicted by the diffusion-limited model. The

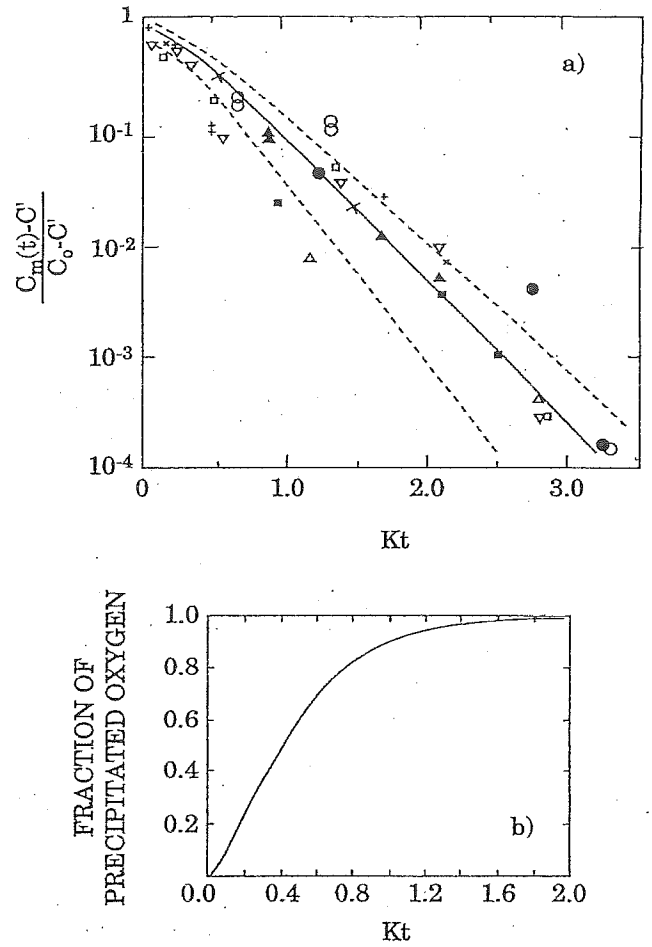


FIG. 34. (a) Interstitial oxygen concentration as a function of the reduced parameter Kt for different temperatures: 650 °C (open circles); 700 °C (closed triangles); 750 °C (+); 800 °C (open triangles up); 850 °C (open triangles down); 900 °C (closed squares); 950 °C (open squares); 1000 °C (solid circles), and 1050 °C (crosses) (from Ref. 41); (b) precipitated oxygen concentration as a function of Kt .

solid line in Fig. 34(a) illustrates the quantity $(C_m - C')/(C_0 - C')$ as a function of Kt , as obtained from this equation, while the quantity $1 - (C_m - C')/(C_0 - C')$, giving the concentration of oxygen precipitated, is shown in Fig. 34(b). The behavior of $(C_m - C')/(C_0 - C')$ vs Kt clearly shows two different regions. In the first one, where $(C_m - C')/(C_0 - C') > 0.5$ (i.e., for very short annealing times), Eq. (64) can be approximated by the simple relation

$$\frac{C_m - C'}{C_0 - C'} = \exp(-\beta t^{3/2}), \quad (69)$$

where

$$\beta = \left(\frac{2D}{R^3} \right)^{3/2} \left(\frac{C_0 - C'}{C_P - C'} \right)^{1/2}. \quad (70)$$

In the second one, where $(C_m - C')/(C_0 - C') \leq 0.5$ (i.e., for long annealing times), Eq. (64) can be approximated by a straight line,

$$\frac{C_m - C'}{C_0 - C'} = \exp\left(-\frac{t}{\tau}\right), \quad (71)$$

TABLE V. Values of the constant K and the oxygen concentration C' as determined by a fitting procedure, on the basis of IR-absorption data on samples annealed at different temperatures (from Ref. 41).

Temperature (°C)	K (10^{-3} h^{-1})	C' (10^{17} cm^{-3})
650	1.65	0.078
700	2.10	0.110
750	2.30	0.120
800	2.80	0.128
850	3.50	0.142
900	5.00	0.290
950	6.20	0.510
1000	6.50	0.710
1050	6.80	1.640

where

$$\tau = \frac{R^2}{3D} \left(\frac{C_P - C'}{C_0 - C'} \right)^{1/3} \quad (72)$$

Considering that $Z \approx 0$, from Eqs. (65) and (72) we obtain

$$\tau = \frac{1}{3K} \quad (73)$$

It is worth noting that Eq. (71), which gives the long-time behavior of $C_m(t)$, generalizes Eq. (56), obtained in the approximation of constant precipitate radius. Indeed, applying the condition of Eq. (60) to the definition of τ [Eq. (72)], the relation $\tau = R^3/3Dr_0$ is obtained, which is exactly the quantity τ_0 defined in Eq. (54). From the analysis performed on the basis of Ham theory the evolution of the precipitate radius r as a function of time can also be deduced,

$$\frac{dr(t)}{dt} = \frac{C_m(t) - C'}{C_P - C'} \frac{D}{r(t)} \quad (74)$$

Considering Eq. (71), Eq. (74) becomes

$$\frac{dr(t)}{dt} = \frac{C_0(t) - C'}{C_P - C'} \frac{D}{r(t)} \exp\left(\frac{-t}{\tau}\right), \quad (75)$$

and integrating this expression $r(t)$ can be found,

$$r^2(t) = 2\tau D \left(\frac{C_0 - C'}{C_P - C'} \right) \left[1 - \exp\left(\frac{-t}{\tau}\right) \right] \quad (76)$$

For $t \ll \tau$,

$$r^2(t) \approx 2D \left(\frac{C_0 - C'}{C_P - C'} \right) t. \quad (77)$$

Therefore, in the early stages of precipitation the particle volume increases as $t^{3/2}$.

Comparing the experimental results with the predictions of Ham's theory, Livingston *et al.*⁴¹ determined by a fitting procedure the values of K and C' at different temperatures from Eq. (64), the value of initial interstitial oxygen concentration C_0 , and the average concentration of oxygen remaining in the solution $C_m(t)$ after different annealing treatments when measured by IR absorption. The results are reported in Table V. From K and C' the quantity $[C_m(t) - C']/(C_0 - C')$ can also be determined as a function of Kt from IR experimental data. These data [experimental points in Fig.

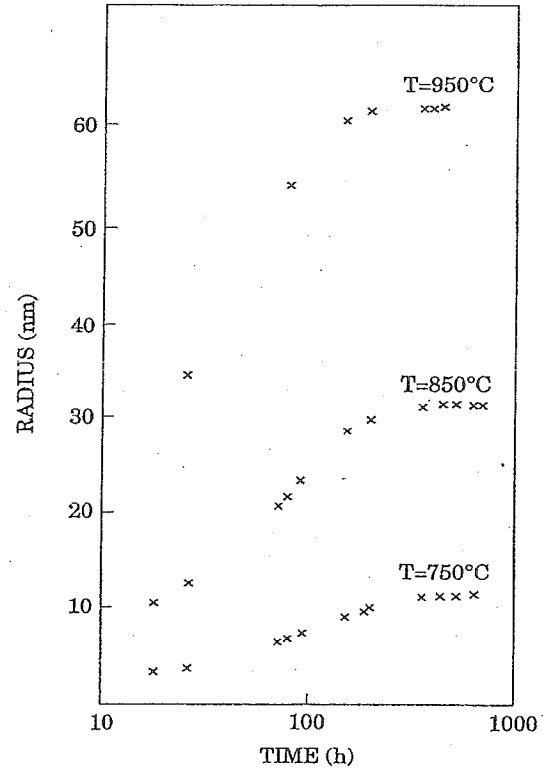


FIG. 35. Time dependence of precipitate radius for different annealing temperatures derived from Eq. (74) (from Ref. 41).

34(a)] for different temperatures are in very good agreement with those predicted by the Ham's theoretical model [solid line in Fig. 34(a)], thus confirming the validity of the model. The spread of some data can be related to the errors affecting C_0 and $C_m(t)$ measurements. The broken lines in Fig. 34(a) take into account the uncertainty of about 10% in these concentration values.

The knowledge of the values of K and C' allows one to calculate the radius of precipitates for different annealing times and temperatures from Eq. (74). As an example, in Fig. 35 the results taken from Ref. 41 for 750, 850, and 950 °C annealing temperatures are shown. It is possible to see that the value of $r(t)$ increases in the early stages of the precipitation process, becoming almost constant for annealing times as long as 200–300 h depending on the temperature.

The experimental assessment of the diffusion-limited model for oxygen precipitation in silicon is very convincing. Nevertheless, an analysis of the data reported in Fig. 34(a) reveals that some values of $[C_m(t) - C']/(C_0 - C')$ for Kt in the range from 0.5 to 1 and for heating temperatures from 750 to 900 °C are lower than the values predicted by Ham's theory. This enhanced precipitation has been explained by a systematic decrease of the precipitate concentration N with increasing annealing temperature, whereas Ham's theory assumes N to be constant. This reduction, confirmed by SANS measurements,¹⁴⁶ may be due to the fact that as precipitation proceeds some of the smaller particles dissolve while the larger particles continue to grow. Another possible explanation comes from the fact that the precipitates can assume shapes different from the sphere, as confirmed by TEM and

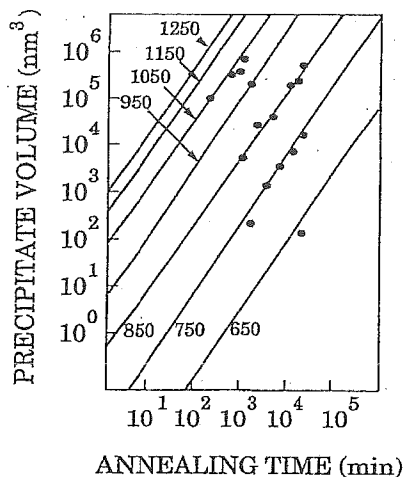


FIG. 36. Time dependence of precipitate volume for different annealing temperatures as determined from Ham theory (solid lines) and from experimental data (solid circles). Annealing temperatures are indicated in °C (from Ref. 123).

SANS results⁴¹ and widely accepted, which are not considered in the model.

Wada *et al.*, who studied silicon samples annealed for different times at the temperatures of 750, 850, and 1050 °C by TEM,^{123,142} found that oxide precipitates grow in two dimensions with constant thickness of about 40 Å. The precipitate density ranges from 10^{11} cm^{-3} at 750 °C to 10^8 cm^{-3} at 1050 °C. On the basis of these data and assuming that the results of the diffusion-limited theory of precipitation are valid also for the actual square-shaped platelet precipitates, they compared experimental values of the precipitate volume to the predicted function $V(T, t)$ derived from Eq. (77). Figure 36 shows the results of Ham's theory (solid lines) and experimental values (solid circles). In spite of the good agreement, the extension of the model to platelet precipitates has not been justified. Furthermore, the two main assumptions made in Refs. 123 and 142, i.e., that the thickness of precipitates remains constant during growth and that the rate of volume change of a platelet precipitate is equal to that of a sphere, have been considered to be incorrect.^{126,147} A model for the growth of platelets has been developed and is illustrated in the following subsection.

3. Disk precipitates with varying thickness

The study of the growth of platelet-shaped oxygen precipitates in silicon is of particular interest, since that shape is favored when the Si wafers are heated in the temperature range of device processing. Here the analysis carried out by Hu^{114,147} by applying the diffusion-limited growth model is reported.

The author starts from the hypothesis that the thickness h of the precipitates is not constant during the growth and that the rim of the disk is a perfect sink for the excess oxygen atoms. In this case the total diffusion flux through the disk surface giving the rate of volume change is

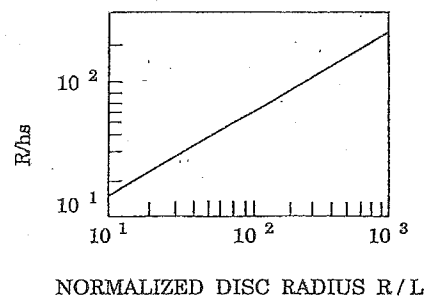


FIG. 37. Dependence of the aspect ratio R/hs on normalized disk radius (from Ref. 147).

$$V_m \{ 8RD [C_{\text{ox}}(\infty) - C_{\text{ox}}(0)] \} = \frac{d}{dt} (\pi r^2 h), \quad (78)$$

where R is the radius of the disk, V_m is the precipitate volume per oxygen atom in it, $C_{\text{ox}}(\infty)$ and $C_{\text{ox}}(0) = C'$ are oxygen concentrations far from and on the Si/precipitate interface, respectively. Considering that at a given volume the disk is the shape which minimizes the strain energy ΔG_σ (see Fig. 40 in Sec. III C) while the interface energy ΔG_γ is maximized (see Fig. 39 in Sec. III C), the equilibrium exists only for one particular value of the ratio R/h , which may vary with R . This value can be found by minimizing the total free energy of precipitates, obtaining the following implicit relation between R and R/h ,

$$R/L = \frac{(R/hs)^2}{\ln(R/hs) + \ln(8/e^2)}, \quad (79)$$

where L is a constant that in our case is equal to 0.89 Å and s is the lattice displacement per unit thickness of the disk (about 0.24 for SiO_2 in silicon). Equation (79) is plotted in Fig. 37 which reports the aspect ratio R/hs vs R/L , i.e., the variation of the precipitate thickness at different disk radii. Relation (79) can be written explicitly if the logarithmic factor is regarded as a weak power function of R/h . Introducing the average quantity $\langle R/hs \rangle$ Eq. (79) can be written as

$$h = s^{-1} (L/p)^{1-m} R^m, \quad (80)$$

where

$$m = \frac{1}{2} \frac{2 \ln \langle R/hs \rangle + \ln 64 - 6}{2 \ln \langle R/hs \rangle + \ln 64 - 5}, \quad (81)$$

and

$$p = \langle R/hs \rangle^{(1-2m)/(1-m)} [\ln \langle R/hs \rangle + \ln 8 - 2]. \quad (82)$$

For precipitates with radius very large with respect to the thickness m is about 1/2.

From Eq. (80) an interesting result of the analysis can be obtained. Substituting that expression for h in the total free energy of the platelet precipitates, under the assumption of precipitates with very large R/h (therefore $m \approx 0.5$) and integrating, one obtains

$$R \propto t^{1/(1+m)} = t^{2/3}, \quad (83)$$

which is exactly the time dependence found in the previous subsection.

C. Precipitate morphology

An interesting feature of precipitate morphology is its dependence on the annealing temperature. Three temperature ranges have been related^{77,114,148-150} to the three typical precipitate shapes, i.e., the needle, the disk, and the polyhedron.

At low temperatures (about 400–650 °C) precipitates grow as needles^{114,116,127,150} made of a high-pressure SiO₂ polymorph, which is coesite. In this temperature range the strain-energy contribution to the precipitate total free energy dominates, since the stress-relieving processes (which become important at higher temperatures) play a minor role.

At intermediate temperatures (about 650–950 °C) disk-shaped precipitates are typical^{20,41,45} (although they can be formed also by short high-temperature annealing). Self-interstitial emission and dislocation-loop formation can partially release the surface strain, therefore making the strain energy less important for shape determination. Moreover, strain energy is further diminished by the decrease of precipitate thickness, with the concomitant increase of surface energy.

At high temperatures (above 950 °C) strain is completely released and the precipitates take the shape with minimum surface energy.^{114,123,150,151} Due to the anisotropy of interface energy, such a preferential shape is the octahedron with eight equivalent {111} faces (surface energy of silicon is minimum in the {111} planes) instead of the sphere.

A lot of experimental results, mainly obtained from TEM investigations, confirm these trends (see Sec. IV B). In the following a qualitative description of the factors determining precipitate morphology is presented and some interesting conclusions derived.

1. Precipitate free energy

The general features of precipitate morphology can be justified on the basis of thermodynamics, considering the different contributions to the total free energy ΔG_{tot} associated with the oxygen precipitation process and their dependence on precipitate shape, annealing time, and temperature. Assuming the precipitates to be far apart, i.e., neglecting their possible interactions, and studying precipitate formation in regions of the silicon crystal far away from other defects, ΔG_{tot} can be considered as the volume free energy available for SiO_x formation in the regions far from the growing precipitates and as¹⁵⁰

$$\Delta G_{\text{tot}} = \Delta G_K + \Delta G_S + \Delta G_E, \quad (84)$$

where ΔG_K is the free-energy contribution associated with the phase change at the silicon/precipitate interface, ΔG_S is the free-energy contribution related to the oxygen transport, and ΔG_E is the excess free energy. This last term is associated with the creation of interface energy ΔG_γ , strain energy ΔG_σ , and interstitial-related energy ΔG_I and can be expressed as their sum,

$$\Delta G_E = \Delta G_\gamma + \Delta G_\sigma + \Delta G_I. \quad (85)$$

In the following the various contributions to ΔG_{tot} are discussed in detail.

Little is known about the energy required for the growth of the Si-SiO₂ interface. The phase-change free energy ΔG_K

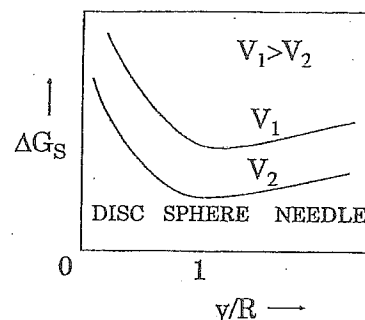


FIG. 38. Dependence of energy contribution of O_i transport on y/R for two precipitate growth velocities and for short annealing times (from Ref. 150).

can be considered proportional to the rate of silicon oxidation and only slightly dependent on crystal orientation. ΔG_K gives in general a small contribution to ΔG_{tot} , because the precipitate growth velocity is small.

The energy required for oxygen transport to the precipitate surface is a function of the precipitate shape because also the dependence of C_{ox} on the distance from the precipitate varies with the precipitate shape. ΔG_S can be expressed as a function of precipitate shape aspect ratio y/R , where the general precipitate shape is a spheroid having axes $2R = 2R \neq 2y$, and therefore $y/R=0$ results in a disk, $y/R=1$ in a sphere and $y/R=\infty$ in a needle. Figure 38 shows the ΔG_S dependence on y/R in the case of two precipitate growth velocities and for short annealing times. Spherical precipitates clearly dominate, leading to the minimum in ΔG_S . For long times the ΔG_S contribution is minimum for the needle shape, which is therefore favored.

The first contribution to ΔG_E , interfacial energy ΔG_γ , depends on the surface area as well as on the degree of coherence of the Si/SiO₂ interface. Considering a coherent interface, with free energy per unit area γ constant and isotropic, at a fixed particle volume ΔG_γ is minimum for the sphere, and this maximizes the volume/surface ratio. Nevertheless, since perfect coherence only rarely is achieved, the interfacial free energy is usually higher with respect to the ideal case. For semicoherent precipitate interfaces γ is modified as

$$\gamma' = \gamma + g, \quad (86)$$

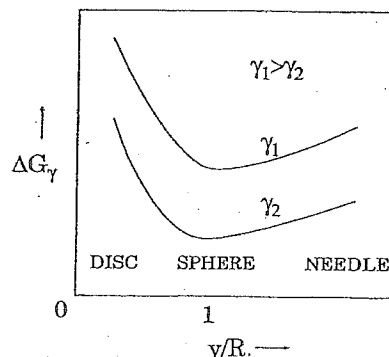


FIG. 39. Interfacial energy dependence on y/R for a coherent (γ_2) and for an incoherent (γ_1) interface (from Ref. 150).

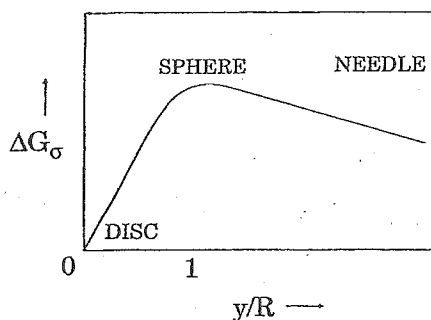


FIG. 40. Strain energy dependence on y/R (from Ref. 150).

where g depends on the crystal elastic constants and on the interface degree of coherence, while the ΔG_γ dependence on y/R , illustrated in Fig. 39 for both cases, is qualitatively preserved.

Interface coherence also influences the strain energy contribution ΔG_σ , together with the degree of elastic isotropy of silicon and silicon oxide. Given these factors, the precipitate shape is the only parameter affecting ΔG_σ . In Fig. 40 the dependence of ΔG_σ on the aspect ratio y/R is illustrated and clearly demonstrates that this contribution to the total free energy favors disk-shaped precipitates.

The last contribution to ΔG_E is the free energy of interstitial point defect formation ΔG_I . In the case of constant growth velocity, self-interstitial concentration C_I is maximum close to the precipitate (i.e., at $r=r_p$) and reaches a constant value for very large distances from the precipitate ($r \rightarrow \infty$). The value $C_I(r_p)$ is maximum for diskoidal particles, lower for needles, and minimum for spheres, although the differences are very small. Therefore, the ΔG_I follows the same trend, as shown in Fig. 41 for two values of the parameter $D_I\tau_I$, where D_I is the diffusion coefficient for self-interstitials and τ_I their diffusion time. In any case, ΔG_I is small compared to the other contributions to ΔG_{tot} .

2. Influence of annealing temperature and time

The analysis of the time dependence of the free-energy contributions described in the previous subsection gives information about the most probable precipitate shape during annealing, while their temperature dependence allows one to

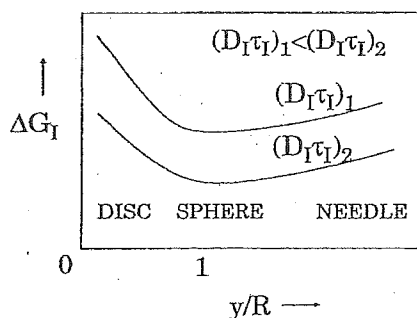


FIG. 41. Dependence of the energy required for self-interstitial creation on y/R for two values of $D_I\tau_I$ (D_I is the diffusion coefficient for self-interstitials; τ_I is the interstitial diffusion time) (from Ref. 150).

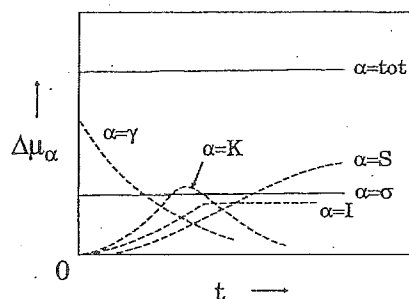


FIG. 42. Time dependence of the different contributions $\Delta\mu_\alpha$, $\alpha=K, S, \sigma, I, \gamma$ and their sum $\Delta\mu_{tot}$ (from Ref. 150).

predict the precipitate shape after a particular annealing. On this basis a significant comparison with experimental results can be made, although only qualitative arguments are proposed.

In Fig. 42 the time dependence of the free energy per interstitial O atom $\Delta\mu_\alpha = d(\Delta G_\alpha)/dC_{Ox}$, $\alpha=K, S, \gamma, \sigma, I$, tot, is reported. $\Delta\mu_K$ is proportional to the growth velocity, which reaches a maximum and then slows down for $t \rightarrow \infty$, when O transport is limited. Moreover, this long-time limit of oxygen transport makes the contribution $\Delta\mu_S$ increase with time, as shown in the figure. $\Delta\mu_\gamma$ is inversely proportional to the spheroid axis length R which increases with time, so that it decreases with increasing time. Finally, $\Delta\mu_I$ tends to saturate for long times as self-interstitials are created. From Fig. 42 the shape of oxygen precipitates in the early stages of precipitation turns out to be the sphere, which minimizes the dominant contribution $\Delta\mu_\gamma$. This conclusion, confirmed by TEM observations, supports the hypothesis of the Ham precipitation theory about the shape of precipitation nuclei.

To study precipitate shapes after long-time treatments, i.e., in the equilibrium state, the temperature dependence of the free energy per interstitial O atom also has to be analyzed. The general trend of all $\Delta\mu_\alpha$ terms is to increase with decreasing T , while only $\Delta\mu_I$ shows an opposite behavior. At low temperatures the growth velocity decreases, consequently the rate of self-interstitial emission decreases as does $\Delta\mu_I$. Figure 43 shows all the terms $\Delta\mu_\alpha$ as function of $1/T$. Looking at this figure, at low T ΔG_S and ΔG_σ turn out to be the most important contributions to the total precipitate free-energy. From Figs. 38 and 40 ΔG_S appears to give needles,

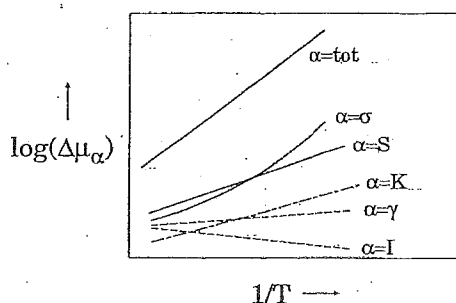


FIG. 43. Temperature dependence of the different contributions $\Delta\mu_\alpha$, $\alpha=K, S, \sigma, I, \gamma$ and their sum $\Delta\mu_{tot}$ (from Ref. 150).

and ΔG_σ disks. Nevertheless, the disk shape is related to a low stress and coesite, which has been found to compose the precipitates grown at low temperatures and which is a high-pressure oxide polymorph, cannot be stable. Considering Fig. 38, the sphere should be even more probable than the needle, but it should not be favored by ΔG_s for long annealing times (see Fig. 42). Therefore, the needle shape is the most likely one for the coesite precipitates, grown at low temperatures.

At intermediate temperatures ΔG_s promotes the formation of needlelike precipitates. On the other hand, ΔG_σ is minimum for the disks, while ΔG_γ is high (see Fig. 39). Nonetheless, this last contribution can be lowered by a good coherence of the interface, achievable along $\{100\}$ planes by both cristobalite and amorphous SiO_2 . Therefore, amorphous SiO_2 disks lying along $\{100\}$ planes are the most probable precipitates after intermediate-temperature annealing.

Finally, at high temperatures the precipitates are usually octahedra with $\{111\}$ and $\{100\}$ faces. Due to the high oxygen diffusivity and solubility limit at high T , ΔG_s is very small. Moreover, stress is almost completely released, i.e., ΔG_σ is also small, and interface coherence is no more critical. Therefore, ΔG_γ is the only contribution to take into consideration. This contribution is minimum for the spherical shape when the surface energy γ is isotropic, while a faceting of the sphere occurs when γ is anisotropic (as in the case of silicon). The planes with minimum surface energy in Si are the $\{111\}$ and $\{100\}$, therefore, the octahedron resulting from faceting presents faces along those planes. These arguments are completely in agreement with the experimental findings.

D. Phenomenology

Oxygen precipitation in dislocation-free single-crystal silicon can be influenced by many factors. Both crystal characteristics and annealing treatments performed on the wafers during device processing are important in determining oxygen precipitation. The main factors to be considered are: interstitial oxygen concentration, interstitial oxygen distribution, preannealing conditions, annealing temperature, annealing time, annealing sequence, annealing ambient, impurity and dopant concentration, impurity and dopant distribution, point defect concentration, extended structural crystal defects (dislocations, twins, etc.), and wafer surface conditions.

The earliest studies of defect generation during low-temperature (450–1000 °C) annealing of Cz-grown wafers were based on electrical measurements^{19,152,153} and IR spectroscopy.^{19,154,155} At the beginning the major interest was devoted to oxygen-related donor states formed upon annealing. Structural characterization of the lattice defects formed during single-step thermal treatments started to be important at the end of the 1970s. During the 1980s, a much more comprehensive study of the oxygen precipitation process occurring upon complex annealing sequences [such as, for example, that simulating complementary metal-oxide-semiconductor (CMOS) process] was performed by several authors.^{156,157}

Commercial Cz silicon wafers always undergo a donor killing treatment by the manufacturer, and even more cooling of ingots during the crystal pulling corresponds to a low-

temperature treatment for several hours. All these procedures differ from one manufacturer to another. Therefore, the thermal history of “as-received” wafers can significantly differ and this explains the large spread in the results of different studies.

In spite of the mentioned scattering in the characterization results, related to the high number of parameters influencing oxygen precipitation, some general trends have been found and are worth illustrating as a “phenomenology” of oxygen precipitation in silicon. We first consider the effects of thermal treatments and then the effects of different impurities and dopants present in the silicon crystals.

1. Thermal history effect

Device producers are extremely concerned about the amount of precipitated oxygen and the rate of precipitation for a given range of initial oxygen concentration.¹⁵⁸ It is often found that in wafers cut from the same crystal with equal initial oxygen concentration and subjected to the same heat treatment oxygen precipitation can take place in different ways. Several authors have shown^{159,160} that oxygen precipitation is significantly affected by the thermal history of the sample. The thermal history is generally understood as the *in situ* annealing to which Cz crystals are subjected after solidification in the crystal puller, varying along the crystal axis. The temperature variation along a silicon crystal during pulling is due to the fact that the seed-end portion of a crystal spends more time at a given temperature than the tang-end portion. This variation in thermal history along the grown crystal affects the amount of oxygen which precipitates,^{160,161} the formation of microdefects,¹⁶² the minority-carrier lifetime,¹⁶³ and, therefore, the device yield¹⁶⁴ (see Sec. V). Thermal history of the crystal also depends on the diameter and the length of the ingot, the shape of the ingot bottom, the pulling rate, the puller type, the hot-zone configuration, and the time that the ingot remains inside the puller in the course of growth process. An illustration of the temperature distribution along the ingot and in the puller during crystal growth is given in Fig. 44 as obtained by computer simulation of thermal history by Virzi and Porri.¹⁶⁵ The thermal history effect is always present: It is often enhanced by the high oxygen content in the seed-end portion of the ingot, and is influenced by the high tang-end impurity concentrations. As an example, an ingot with a higher carbon content may show a lower thermal history dependence with respect to one with lower carbon content, due to the fact that carbon is a possible factor of oxygen precipitation enhancement.¹³⁵ Whether the thermal history influences oxygen precipitation in the wafers after a subsequent thermal treatment depends also on the initial interstitial oxygen content C_0 , and on the amount of oxygen that precipitates ΔC_{ox} during the thermal treatment. In other words, it depends on the function $\Delta C_{ox} - C_0$ vs C_0 for the particular heat cycle.¹⁶⁶

In order to reduce the influence of thermal history and improve the axial homogeneity of oxygen precipitation, several different approaches were found and are recommended. As shown by Fraundorf *et al.*¹⁶⁰ the thermal history effect can be erased to a large extent by a high-temperature anneal-

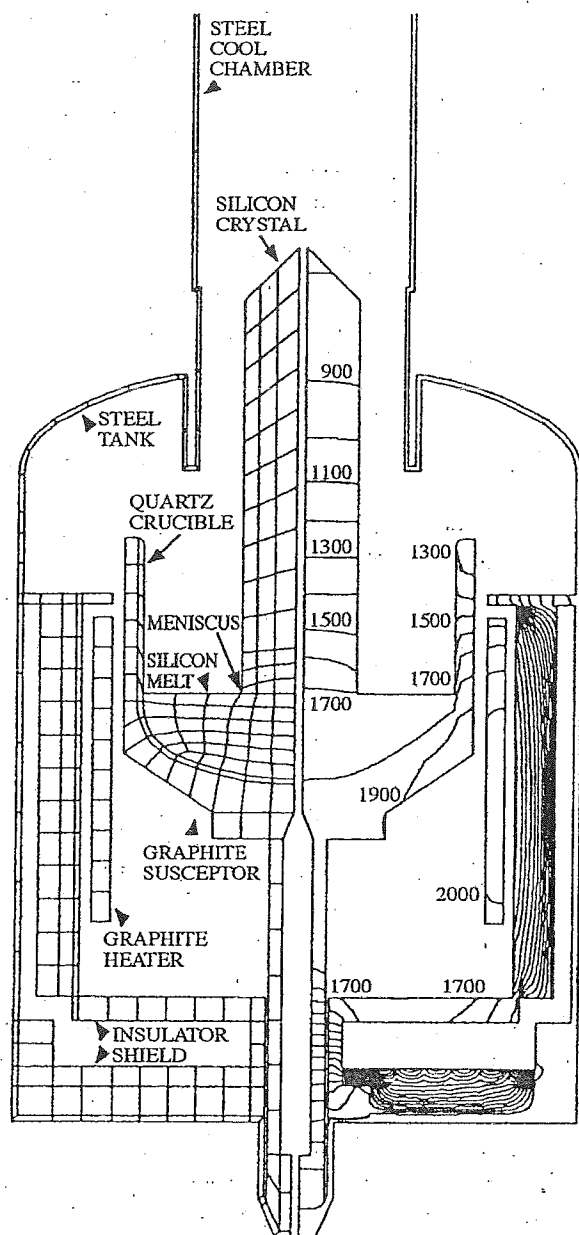


FIG. 44. Temperature distribution along the ingot and in the puller during crystal growth, obtained by computer simulation (from Ref. 165).

ing treatment (1320 °C for 3 h). To this purpose, high-temperature annealing was applied for as-grown precipitate dissolution and interstitial oxygen homogeneity, as described earlier by Shimura¹⁶⁷ and by Jastrzebski *et al.*¹⁶⁸ On the other hand, Fusegawa and Yamagishi¹⁶⁹ found that a low-temperature (450 °C for 2 h in O₂) preheating improves the axial uniformity of oxygen precipitation resulting after a two-step anneal treatment (800 °C for 4 h in N₂ + 1000 °C for 16 h in O₂).

Inoue and co-workers¹²⁹ found that there is an incubation time for the nucleation of oxygen precipitates and that the density of nuclei reaches a saturation value after some period of annealing. This incubation period depends on the thermal history of the crystals,¹²⁹ as well as on the nucleation temperature¹²⁹ and the interstitial oxygen content.¹⁷⁰

Several authors^{125,129,170} have shown the importance of low-temperature interval during the thermal history of the wafers. Recently, Fraundorf, Fraundorf, and Craven¹⁷¹ proposed the existence of a metastable oxide precursor phase with maximum nucleation temperature of about 600 °C. Such precursors have a high surface-to-volume ratio and act as seeds for the most common platelet-type oxide precipitates, which have a maximum nucleation rate at 750 °C. The precursors form during the crystal cooling process and may also grow from the thermal donors.^{171,172}

However, although a single-step preannealing at low temperature may be useful in certain thermal treatments, Fusegawa *et al.*¹⁷³ have recently shown that before specific thermal treatments during CMOS fabrication a two-step preannealing treatment is needed. In particular, they have shown that annealing at 450 °C for 2 h followed by a second step at 650 °C for 2 h is very effective in obtaining a uniform distribution of oxygen precipitates along the crystal growth axis.

Thermal history effects can also be reduced using another approach, i.e., by performing a high-temperature rapid thermal annealing (1200 °C for 2 min in Ar atmosphere) prior to a two-step annealing, as proposed by Chiou.¹⁷⁴

2. Effect of single-step annealing

When studying nucleation and precipitation of oxygen in silicon single crystals it is essential to start from a standard specimen.¹⁷⁵

The ideal conditions would be the following: treatment for as-grown precipitate dissolution and C_{ox} homogeneity at very high temperature (1320 °C); measurement of interstitial oxygen and substitutional carbon content; isochronal or isothermal annealing treatment.

Since ideal conditions are not met systematically, it is difficult to compare the experimental results obtained by different authors. Nevertheless, from the large amount of experimental data on oxygen behavior in silicon upon thermal annealing, some overall considerations could be made.

Generally, a thermal treatment is considered single step when the "as-received" wafer is annealed for the first time and only once. The high-temperature treatment usually performed to dissolve the as-grown precipitates is not taken into account. Oxygen agglomerates formed upon single-step thermal treatments can be divided in two major categories on the basis of their electrical activity:

- (i) thermal donors;
- (ii) electrically inactive precipitates.

Such a division is further supported by the fact that thermal donors are typically not directly visible by microscopic techniques and could be only revealed by electrical measurements, while the other precipitates have larger dimensions and are directly visible by means of TEM or high-resolution TEM (HREM).

Here we give only a brief overview of the electrically active structures. For general overviews on thermal donors the reader is referred to Refs. 82 and 176–179.

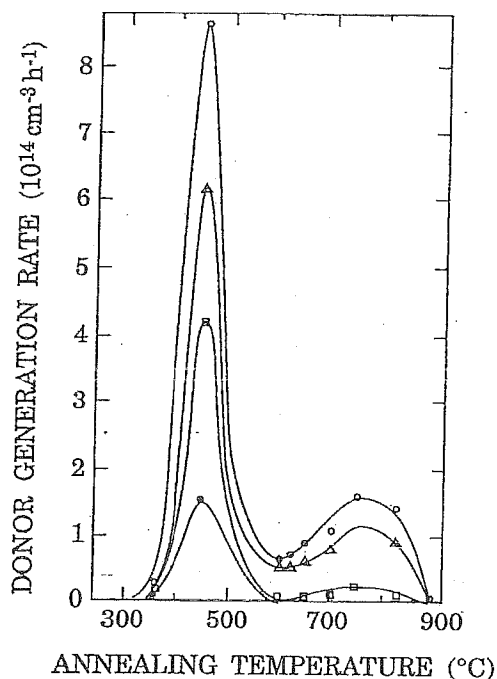


FIG. 45. Donor generation rate as a function of annealing temperature for different initial interstitial oxygen concentrations: 40 ppm (open circles), 37 ppm (triangles), 32 ppm (squares), and 24 ppm (closed circles) (from Ref. 197).

a. Thermal donors. (a) Old thermal donors: Since the early work of Fuller *et al.*^{152,180} it is now well established that heat treatment of Cz-grown oxygen-rich silicon in the 350–500 °C temperature range generates microdefects which act as shallow double donor centers, called thermal donors (OTD), since they were discovered previously with respect to other types of donors. According to the original idea of Kaiser, Frisch, and Reiss¹⁸¹ it has been widely accepted that OTD are small oxygen aggregates formed at the early stage of oxygen precipitation. Despite an overwhelming number of articles dealing with these donors, their atomic structure and the origin of their electrical activity are still not understood. OTD formation has been studied by a large number of experimental techniques: Resistivity measurements,^{182,183} IR absorption,^{154,184–186} photoluminescence,¹⁸⁷ Hall effect,^{155,188} electron paramagnetic resonance,^{189,190} electron nuclear double-beam resonance,^{191,192} and deep-level transient spectroscopy (DLTS).^{67,193} Since these defects are undesirable in commercial silicon wafers, they are usually eliminated by heat treatments above 500 °C for a few hours.

Several studies^{154,188,193} showed that the OTD are double donors with ionization energies of about 70 and 150 meV. Eleven neutral OTD⁰ and nine singly charged OTD⁺ species have been observed in IR spectra.¹⁹⁴ The individual OTD⁰ and OTD⁺ species have slightly different ionization energies ranging from 69.2 to 49.9 meV and from 156.3 to 116.0 meV. Very recently Götz, Pensl, and Zulehner¹⁹⁵ have reported the existence of five new effective-mass-like OTD species. They are supposed to develop from the known OTD species via additional atoms. The chemical nature of these

atoms is not yet identified, but it is believed that oxygen plays an important role in the formation of such nuclei.

A generation rate of the OTD proportional to the fourth power of the interstitial oxygen concentration was found.¹⁸¹ Recent results of Londos *et al.*¹⁹⁶ show a strong deviation from the fourth power dependence for several heating temperatures, although they are in agreement with that law for annealing close to 450 °C. The increase of the number of OTD is proportional to the annealing time, the proportionality factors depending on the treatment temperature. The generation rate is maximum at 450 °C and sharply decreases for both low and high temperatures, as shown in Fig. 45.¹⁹⁷ The formation kinetics of the individual OTD does not follow the monomolecular law which is observed for the total OTD concentration.¹⁹⁸ The generation rate of each donor state is different and can be studied by IR absorption. The linear relation between the oxygen loss from the solution and the OTD formation rate shows a derivative varying from below two to nine in the temperature range 300–500 °C.¹⁹⁶ This indicates that oxygen dimerization controls the OTD formation kinetics, but that the dimers become increasingly unstable above 400 °C.

Activation energy for OTD formation is recently reported by Claybourn and Newman¹⁹⁹ to be 1.7 eV for at least six of the nine different OTD⁺. Their low activation energy is the main problem for understanding the nature of the OTD.

It was found that different impurities have a significant impact on OTD generation. Some examples follow.

High carbon concentration suppresses the OTD generation.^{154,200,201} The concentration of generated OTD can be lowered by up to two orders of magnitude.

Anneal in H plasma increases both the OTD concentration and the oxygen loss from the solution in the temperature range 350–450 °C.⁷² Such a treatment increases the OTD density much more than do furnace annealings.

The influence of doping atoms on the OTD generation is still somewhat controversial. In some articles it is claimed that the donor concentration is increased in *p*-type material and unaffected by *n*-type doping;^{154,200} in some others¹³² similar results are reported for *p*-type material, with a reduced donor concentration observed in *n*-type material.

In spite of a very large number of articles published on the formation of thermal donors, there is not yet a general agreement on their exact nature. While the original models relate the thermal donors to pure oxygen complexes,^{181,202–204} more recently models involving also vacancies^{205,206} and silicon self-interstitials^{52,69,207} have been proposed.

The current view is that oxygen is involved in the OTD cores and that the different donor states evolve sequentially by addition of oxygen or self-interstitial atoms. Nevertheless, the exact structure and composition of the OTD are still unclear.

(b) New thermal donors: Upon annealing at high temperatures a different type of oxygen-related donor states is observed.^{153,155,182,200,208,209} They are known as new donors (ND) and occur in the temperature range 600–900 °C, with a maximum generation rate at about 800 °C (see Fig. 45).

Their formation strongly depends on the interstitial oxygen concentration and hence they are not observed in FZ material. Ionization energy derived from Hall-effect measurements²⁰⁹ varies between 30 and 120 meV.

The generation rate of ND is proportional to the 4.5th power of C_{ox} , i.e., very close to the behavior of OTD.¹⁵⁵ It can be increased by a preanneal at about 470–550 °C,^{155,182} while for ND annihilation heating above 1000 °C is required. The ND generation is found to be higher in *p*-type than in *n*-type wafers.¹⁸²

High carbon concentration present in the material accelerates ND formation^{155,182} (while it retards OTD formation). Furthermore, Lerouille²¹⁰ found that ND formation is inhibited in crystals where the carbon concentration is below the IR detectability threshold even with high C_{ox} . This implies that carbon plays an essential role in the formation of the new donor complexes. Recently, Hahn *et al.*²¹¹ have shown that carbon and oxygen coimplantation strongly enhances the ND formation. ND are most probably related to some kind of oxygen precipitates as they occur in a temperature range in which oxygen precipitation also takes place.²¹²

Several models have been proposed to explain the ND formation. Grinshtein *et al.*²¹³ proposed that large oxygen precipitates upon annealing dissociate in smaller complexes which then become electrically active, while Kanamori and Kanamori¹⁸² extended the Helmreich–Sirtl model²⁰⁵ for OTD to the ND. Gaworzewski and Schmalz¹⁵⁵ related ND to C–O complexes formed at the initial stage of heat treatment. Pensl *et al.*²¹² proposed a “SiO_x interface model” relating ND characteristics to the interface states at the precipitate/silicon interface and to bound states in the SiO_x precipitates. Qian *et al.*²¹⁴ explained their formation by the dangling bonds on the small dislocation loops formed by the oxygen precipitation.

Moreover, Wijaranakula and Matlock²¹⁵ found that the donors observed upon annealing in the temperature range 500–800 °C have a different nature in carbon-lean and carbon-rich material. They found that in carbon-rich material donor formation corresponds to the reduction of substitutional carbon, while interstitial oxygen concentration does not vary; therefore, they identify ND as carbon donors.

(c) Other oxygen-related donors: Besides OTD and ND, some other oxygen-related donor states have been reported.

In the low-temperature range where OTD are formed, the formation of a new type of shallow thermal donors with significantly lower concentration has been found, where nitrogen seems to play a catalytic role.^{216,217} These donors are single donors and at least seven different states have been identified with ionization energies between 34.7 and 37.4 meV.

Recently Kamiura *et al.*^{218,219} reported the formation of a new type of thermal donors upon prolonged annealing at 450–470 °C in phosphorus-doped Cz silicon. They found them to be double donors with continuously varying ionization levels and broad IR-absorption bands. These donors have a lower generation rate and a higher thermal stability than OTD. Kamiura, Hashimoto, and Yoneta²²⁰ showed that besides OTD and ND also a third and a fourth class of oxygen donor states formed at 520 °C could be distinguished.

TABLE VI. Lattice defect distribution after single- and two-step annealing treatments. An indication of the dependence of defect density on the preannealing temperature is given by the numbers from 1 (minimum) to 4 (maximum) (from Ref. 151).

T (°C)	650	700	750	800	850	900	950	1000
Low-temperature N ₂ anneal:								
Rodlike	4	4	3					
Platelike	4	4	4	3	3	2	2	2
Platelike with punching					1	2	2	2
60° dipoles	4	4	4	3				
90° dipoles	3	3	3	3				
With subsequent oxidation (1150 °C):								
Frank stacking faults	3	4	4	4	4	3	1	
Elongated loops	3	4	4	4				
Prismatic loops	3	3	3	3	3	3	3	3
Octahedral prec.	1	3	4	4	4			
Platelike prec.						3	3	3
Prismatic punch.						3	3	3
Irregular loops						3	3	3

b. Large electrically inactive precipitates. Essentially four types of electrically inactive defects caused by oxygen precipitation are known to form after a single-step annealing: rodlike defects, platelike precipitates, dislocation dipoles (60° or 90° type), and prismatic dislocation loops (see Table VI).¹⁵¹ Somewhat less-defined structures such as “loopites” and “blobs” were also reported.⁷⁸ These defects are considered electrically inactive in the sense that they do not provide free carriers to the conduction or valence band; however, they could have a certain impact on electrical properties of silicon, producing deep traps and therefore influencing the carrier lifetime.

(a) Rodlike defects: It is generally accepted that the rodlike (or ribbonlike) defects are formed upon annealing in the temperature range 465–750 °C,^{78,151,221–224} although some disagreement still exists.^{162,225}

Rodlike defects have also been observed by TEM in samples subjected to ion implantation of many different species under self- or nonself-annealing conditions^{226–228} and electron irradiation of Si in the electron microscope.²²⁹

The rodlike defects are generally aligned with dislocation dipoles^{151,221,230} and sometimes are found on dislocation cores.^{151,231} They are stable for annealing below 700 °C, as found by Tempelhoff and co-workers,²²³ while above this temperature they transform into elongated $\langle 110 \rangle$ narrow dislocation loops. Such behavior led the authors to conclude that rodlike defects are a preliminary state of the formation of dislocation dipoles. This idea is also worked out in the nucleation and growth model proposed by Tan.²³²

The ribbonlike defect density increases with anneal time and temperature and reaches a maximum at 650 °C, about $0.3 \times 10^8 \text{ cm}^{-2}$. Similar values of defect density are reported by various authors.^{77,78,151,230}

Structural characterization of these defects is performed by HREM (see Sec. IV B).^{77,151,175,177,231,233} It is found that each defect consists of a different crystalline phase in the silicon lattice elongated along the $\langle 110 \rangle$ direction. The cross section of the largest defect is up to $6 \times 1 \text{ nm}^2$, while the length goes up to several micrometers. The $\langle 100 \rangle$ silicon/

precipitate interface is incoherent, and furthermore, it is not strictly, but slightly, zig-zag shaped with small portions following {411} or {311} planes^{77,233} (see Fig. 58). On the other hand, the (110) interface is at least partially coherent. Precipitates introduce a dilatation in the [100] directions. (100) planes are displaced by $0.18 a$ [100] to $0.27 a$ [100] depending on the precipitate dimension, where a is the lattice constant.

Bourret and co-workers⁷⁷ showed that dislocations of the dipoles formed during the low-temperature annealing are decorated by a rodlike precipitate. On the other hand, Bender¹⁵¹ found such a decoration only on a small number of dislocations.

Tempelhoff *et al.*^{221,223} and Yamamoto and co-workers²³⁰ on the basis of TEM and IR analysis attributed rodlike defects to some forms of SiO_x precipitates. In addition, Bourret^{177,231} and Bender¹⁵¹ have identified rodlike defects present after low-temperature annealing of Cz silicon as SiO_2 precipitates in the coesite phase.

Other arguments supporting the interpretation involving coesite are clearly outlined by Bender and Vanhellemont.¹³⁰ They are as follows.

Bergholz and co-workers⁷⁸ showed that the balance between the oxygen reduction measured in the wafer and the oxygen incorporation into rodlike defects made of coesite is very well fulfilled at 485 °C.

The compressive stress on the precipitates is higher than the minimum pressure at which the coesite is a stable SiO_2 phase. From the temperature-pressure phase diagram of coesite, Bourret and co-workers⁷⁷ derived a pressure of 3 GPa for the transformation quartz to coesite. They have also shown the existence of a critical radius of 1.2 nm, below which coesite precipitates are stable.

After a subsequent high-temperature annealing step, during which the rodlike defects annihilate, rows of octahedral precipitates along <011> directions are observed.¹³⁰ It has been assumed that these are nucleated on the remainders of the rodlike defects. Similar findings were also reported earlier by Gaworzewski *et al.*²³⁴

On the other hand, several arguments against this interpretation have been raised by Bourret,²²⁷ Bender and Vanhellemont,¹³⁰ Reiche, Reichel, and Nitzsche,²³⁵ and Carpenter *et al.*²³⁶

On those basis, Bourret²²⁷ dropped the interpretation of the rodlike defects as coesite precipitates and proposed a new model involving hexagonal silicon.

The presence of hexagonal silicon in ion-implanted samples under self-annealing conditions was already reported on the basis of electron-diffraction data.^{237,238} Hexagonal silicon is also reported to form after mechanical deformation at moderate temperatures.^{237,239,240}

A good matching of the experimental images of the rodlike defects in oxygen-rich silicon with simulated images of the coesite structure along [100] direction exists;^{77,151} however, as shown by Bender and Vanhellemont,²³³ the simulated images of the coesite structure always look more complicated than the experimental images.

One of the major objections against the coesite nature of the defects is the required enhanced interstitial oxygen diffu-

sion at the low temperature of defect formation. Contrary to the oxygen diffusion data, the reported values for the self-interstitial diffusion scatter over a wide range, depending on the method adopted. The silicon self-interstitial diffusion coefficient reported by Bronner and Plummer²⁴¹ and by Mayer, Mehrer, and Maier²⁴² is about three to four orders of magnitude larger than the oxygen diffusion coefficient in the considered temperature range. It means that the silicon interstitial diffusion is fast enough to form the rodlike defects after the long time annealings even at the lowest formation temperatures.

It was pointed out earlier that the amount of oxygen involved in the formation of coesite defects at the lowest temperatures and of coesite and platelike precipitates at higher temperatures agrees well with the decrease of the interstitial oxygen concentration, as measured by IR spectroscopy. Therefore, the assumption of hexagonal silicon implies that much more interstitial oxygen must have precipitated in platelike form than usually assumed. This is not in contradiction with the experimental findings since small precipitates (<5 nm) cannot be detected by HREM, and therefore an accurate estimate of the precipitate density and size distribution from electron microscopy observations is not possible. Since the critical radius for homogeneous precipitation at these temperatures is very small, oxygen content in platelike precipitates or in their nucleation centers are very likely to be underestimated.

Oxygen agglomeration in platelike precipitates should be a source of silicon self-interstitials due to volume difference between the SiO_x in the precipitates and in the silicon matrix. The total number of interstitials incorporated in the rodlike defects has to correspond to the number of interstitials generated by oxygen precipitation. Bender and Vanhellemont²³³ calculated such numbers for annealing at 650 °C for 264 h. They found that the total number per cm^3 of generated self-interstitials is $C_I^g = 2.0 \times 10^{17}$ atoms/ cm^3 , while the number per cm^3 of interstitials incorporated in the hexagonal silicon rods is $C_I^{\text{hs}} = 1.5 \times 10^{16}$ atoms/ cm^3 ; however, a large density of interstitials is incorporated also in interstitial-type dislocation dipoles, whose concentration was calculated to be $C_I^{\text{dp}} = 1.5 \times 10^{17}$ atoms/ cm^3 . This shows that the required conservation of point defects, taking into account the large uncertainty of the estimates, is fulfilled. However, it should be pointed out that the observed hexagonal silicon rods play only a minor role as a sink for self-interstitials; in fact, the self-interstitial balance is mainly obtained by the formation of dislocation dipoles, which can be seen as an evolution of the rodlike defects. A similar result for oxygen balance is found assuming that the rodlike precipitates are coesite. As shown by Bourret and co-workers⁷⁷ only $\approx 10\%$ of oxygen is found in coesite precipitates.

In summary, it may be concluded that many arguments support the hexagonal silicon hypothesis, as suggested by Bender and Vanhellemont.¹³⁰

In other words, a definitive distinction between the coesite and the hexagonal silicon model for the rodlike defects cannot be obtained, either by comparison of simulated HREM images with experimental observations,²⁴³ or by comparison of the lattice spacings in the defects

with the expected values for [100]-oriented coesite or [2110]-oriented hexagonal silicon, or by performing the point defect balance.

(b) Platelike SiO_x precipitates: The second type of defects observed after a single-step heat treatment are platelike, present after sample annealing in the temperature range 650–1050 °C. Tempelhoff and co-workers²²¹ found that these defects have {100} habit planes and $\langle 110 \rangle$ edges. The IR spectrum taken on such samples is characterized by an intense double peak with maxima at 1125 and 1222 cm^{-1} . The authors related these structures to the presence of α -cristobalite and Matsushita¹⁶² also reported the presence of α -cristobalite in samples annealed at 800–1100 °C. On the other hand, Bender,¹⁵¹ on the basis of detailed studies of the precipitate morphology as a function of the anneal time and temperature, has not revealed the presence of crystalline oxide precipitates in this temperature range.

Oxygen precipitates are usually characterized in terms of number density, size, and shape by chemical etching;⁴¹ however, this technique fails for the samples heated at low temperatures since the etch-pit density becomes too large and individual pits cannot be resolved in the micrographs. TEM gives only snapshot views of the samples and the analyzed regions can be unrepresentative of the whole sample, although it has the advantage of showing the structure and morphology of the particles. After anneals below 800 °C, the platelike precipitates are observed as small black dots. Electron-diffraction contrast is caused by the strain field associated with these defects, although in this case only limited information concerning their morphology is obtained.

A more detailed structural characterization of platelike defects can be obtained from HREM imaging.^{41,151,244,245} However, even with this technique and even after long annealing time at 650 °C, the precipitates are generally only visible by their strain field which shows up as black dots in the perfect silicon matrix. Dark “blobs” with diameters ranging from 2 to 10 nm are also reported by Bergholz and co-workers⁷⁸ in samples subjected to prolonged anneals at 485 °C. Due to the instability under the electron beam the authors interpreted these defects as aggregates of interstitial atoms; however, the similarity of these defects with those reported after annealing at higher temperatures by other authors suggests that blobs are the initial stages of the oxide precipitates. The interpretation of the blobs as precursors of oxide precipitates is also supported by the loss of interstitial oxygen during the annealing.

The composition of the precipitates is measured by electron energy-loss spectroscopy (EELS) by Carpenter *et al.*²⁴⁶ as $\text{SiO}_{1.2}$ and by Skiff, Tsai, and Carpenter²⁴⁷ as $\text{SiO}_{0.95}$. It has to be remarked that electron-beam-induced damage probably plays a significant role in the quantitative results and in the peak shape of EELS spectra since the measurements are performed with very high electron current densities,¹³⁰ therefore, the reported stoichiometry is likely to be a lower limit.

Though Tempelhoff and co-workers²²¹ suggested that the platelets are composed of α -cristobalite, recent IR studies by Borghesi *et al.*^{248,249} have shown that, from the analysis of the 1230 cm^{-1} band, information on stoichiometry of the SiO_x in the platelets can be obtained (see Sec. IV C). They

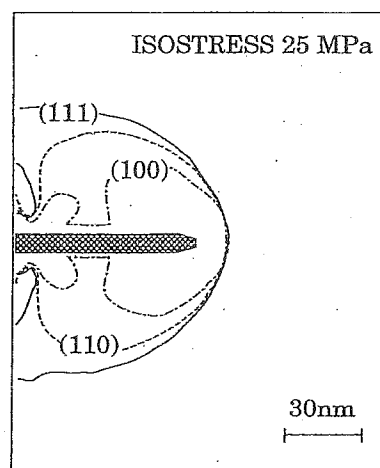


FIG. 46. Elastic isostress curves around a precipitate platelet for different platelet habit planes (from Ref. 156).

have shown that for samples heated at 1100 °C for 1 h the platelets consist of amorphous Si-rich oxide, mainly SiO_x with $x=1.8$. The band line shape indicated the presence of oxides with $x<1.8$, too.

SANS studies^{41,244} have shown a decrease of the precipitate density and an increase of the precipitate size with anneal time at 750 and 800 °C, and very good agreement among SANS, TEM, and IR analysis was found. Advances in SANS analysis led recently to the development of anisotropic measurements^{250,251} (which do not require the comparison with either IR or HREM data), that confirmed earlier findings. By means of SANS, platelets were revealed as cushion-shaped objects²⁴⁵ lying predominantly on the {100} planes, with edges along the $\langle 110 \rangle$ directions. From the comparison of the experimental and calculated scattering density in SANS, Takeda *et al.*²⁵² conclude that the composition of the platelike oxide precipitates must be oxygen-deficient SiO_{2-y} without further specifying the composition, i.e., their results are in agreement with the most recent IR studies.^{248,249}

The tendency of oxide precipitates to develop a platelet morphology on the {100} planes is related to the possibility of total strain energy minimization. For silicon, which has anisotropic elastic properties, the {100} planes are the preferred precipitate habit planes since the Young's modulus of silicon in $\langle 100 \rangle$ directions has the minimum value. Theoretical predictions are in very good agreement with the reported data on low-doped Si samples.^{253–255}

On the other hand, in an extrinsic silicon degenerately doped by means of substitutional impurities such as boron the hydrostatic compression is partially compensated by the local tensile strain introduced by the impurities. Relaxation of the lattice strain lowers the strain free energy and therefore the total free energy of the precipitate. This facilitates the precipitate growth. Wijaranakula²⁵⁶ studied the morphology of the oxide precipitates in Cz-grown silicon degenerately doped with boron. In addition to square-shaped precipitate platelets having {100} habit planes, commonly observed in lightly doped silicon, he also found oxide precipitates ex-

hibiting a disk-shaped morphology with both $\{110\}$ and $\{111\}$ habit planes. From the calculation of the elastic stress field around the precipitate platelet, as shown in Fig. 46,²⁵⁶ it is evident that the precipitate grown in a lightly doped silicon is limited to the $\{100\}$ planes. In silicon degenerately doped with boron the localized elastic modulus of silicon may be reduced and therefore the precipitate orientation is not restricted only to the $\{100\}$ planes.

(c) Extended defects formed after low-temperature annealing: A phenomenon occurring in parallel with oxygen precipitation is the formation of extended defects which play an important role in the gettering of metallic impurities and are of great importance for device production. Here we briefly illustrate their formation upon low-temperature annealing.

The major extended defects occurring after low-temperature annealing of Cz silicon are dislocation dipoles of 60° and 90° type. They consist of two parallel dislocations along the $\langle 011 \rangle$ directions, which have opposite Burgers vectors. The habit plane of the dipoles is close to a $\{311\}$ plane with a separation between the dislocations of the order of 25–35 nm. The defects are of the interstitial type, i.e., they contain extra silicon atoms.^{151,257}

At low temperatures, no dissociation or decoration of the dislocation cores with precipitates is observed, while for treatments above 750°C heavy decoration of the dislocation lines and dissociation in two partial dislocations occur. Rod-like defects are sometimes found along the dislocation lines.

The density of the 60° dipoles²³⁰ has a similar temperature and time dependence as that of the density of rodlike defects, while the density of 90° dipoles is more than one order of magnitude lower. Several authors^{222,235} reported about rodlike defect transformation into dislocation dipoles, and thus further support the self-interstitial nature of the rodlike defects.

The largest extended defects are platelike, present upon annealing above 850°C and generated by prismatic punching.^{151,258} The mechanism by which these defects form is an efficient way to release the strain on the growing precipitates.

3. Effect of two-step annealing

For most of the technological processes multistep annealing treatments are required, but only two of them are relevant for oxygen precipitation. Moreover, the two-step (for example low-high temperature) anneal is considered effective in increasing defect density: The first step leads to the generation of the nucleation centers and the second one to the defect growth. The major defects formed by such treatments²⁵⁹ are octahedral or platelike precipitates, stacking faults, and different kinds of dislocation loops (see Table VI).

a. Precipitates. For Cz silicon wafers annealed in two steps both octahedral and platelike precipitates are observed. While platelike precipitates were observed even after a low-temperature second step¹⁷⁵ (down to 650°C), the octahedral ones are formed only when the second step is performed at high temperature (above 1000°C).^{151,162,175,225,257,260} A detailed study of the precipitate morphology demonstrates its dependence on the conditions of the first low-temperature

step.¹⁵¹ If the conditions are such that the platelike precipitates remain small and thin, the lattice strain they produce is relatively small and no generation of prismatic loops takes place. Upon the subsequent high-temperature step the morphology of some precipitates changes from platelike to octahedral, so that the interface energy is minimized. On the other hand, if platelike precipitate formation is accompanied by lattice strain release through a punching mechanism, the platelike shape is stabilized during the high-temperature step and such a kind of precipitate keeps growing.

The precipitate shape is the result of the balance between different free energy contributions (as amply discussed in Sec. III C). As shown by Tiller and co-workers^{150,261} thermodynamic considerations favor spherical (polyhedral) precipitate formation at higher temperatures (950 – 1200°C). The expressions for the strain energy as a function of the precipitate shape for coherent and incoherent precipitation have been recently discussed by Vanhellemont and Claeys²⁶² and Taylor, Tan, and Gösele.²⁶³

Some authors^{260,264} reported the presence of prismatic punching around octahedral precipitates; however, as observed by HREM, the silicon lattice around all octahedral precipitates is free from measurable strain.^{151,225,259,261} The punching most probably occurs before the change of morphology from platelet to octahedron.

The octahedra have diameters ranging from 15 to 25 nm and facets along $\{111\}$ and $\{100\}$ silicon planes. Based upon the size and density of precipitates plus the drop in interstitial oxygen concentration, Ponce, Yamashita, and Hahn²⁶⁵ concluded that these precipitates are SiO_2 particles. For larger precipitates the $\{100\}$ boundary planes are absent and the precipitates are regular octahedra. HREM imaging shows that the precipitates consist of amorphous material.^{150,225}

EELS has been applied to identify the composition of the octahedral precipitates. Yang and co-workers²⁶⁴ report a SiO_x composition, without specifying the value of x .

b. Stacking faults. Stacking faults are the most prominent defects after a high-temperature treatment. They are extrinsic, i.e., formed by an extra plane of self-interstitials.

According to the work of Maher, Staudinger, and Patel²⁶⁶ and the schematic model of Mahajan, Rozgonyi, and Brasen²⁶⁷ Frank stacking faults are believed to take hexagonal shape. However, a review of TEM and x-ray topography studies of the stacking fault shape as a function of the annealing conditions¹³⁰ shows that hexagonal-like Frank defects (i.e., hexagons with rounded corners) form for anneal temperatures $\leq 1000^\circ\text{C}$. At higher temperatures the bulk defects always take a circular shape, even for sizes up to several hundred micrometers.^{151,268,269} As for precipitates, the stacking fault shape is determined by the minimum of the free energy required for their formation. The stacking fault energy is minimal for $\{111\}$ planes.

Oxidation-induced stacking faults (OSF) are defects formed in the near-surface region under oxidizing anneal conditions and take an approximately half-elliptical shape. Their growth rate parallel to the surface is much larger than the perpendicular one. Hasebe *et al.*²⁷⁰ proposed that oxide precipitates or their nuclei form around 1150°C in the cooling sequence of the crystal and that these grown-in defects

serve as nuclei for OSF during oxidation. Furthermore, it has been shown²⁷¹ that oxygen concentration affects the OSF density, but is not the main parameter in determining their distribution. Therefore, it is concluded that the temperature of the melt is the dominant factor. The experiments of Cho *et al.*²⁷² show that the formation of OSF nuclei during crystal growth is influenced by dopant type and concentration, pulling rate, and thermal history of the crystals. They propose that the ring distribution of the OSF is related to the presence of two different oxygen species in the melt. SiO_4 clusters directly incorporated in the ingot are proposed to be the nuclei for the OSF.

OSF nucleation mechanism is not yet completely understood. Essentially two models are proposed.^{267,273} Dissociation of a perfect dislocation punched out by an oxide precipitate or direct (homogeneous) precipitation of excess self-interstitials in a $\{111\}$ plane triggered by the stress of the precipitates.

c. Prismatic punching and dislocations. Upon two-step heat treatments, the first above 850 °C and the second between 900 and 1150 °C, platelike precipitates are observed together with complexes generated by prismatic punching and having the shape of loops (see Table VI). A detailed TEM investigation has shown^{151,258} that the loops lie on $\{110\}$ planes and consist of $\langle 1\bar{1}2 \rangle$ dislocation segments.

Tan and Tice²⁵⁸ found that the loops are generated by a successive cross glide of a shear loop which is initially generated in a $\{111\}$ plane. On the other hand, due to the high formation energy involved, Vanhellemont, Amerlinckx, and Claeys²⁷⁴ concluded that the direct nucleation of a small shear loop is unlikely and probably starts with an agglomeration of silicon interstitials. This initial nucleus further grows by climb related to the point defect supersaturation. After reaching a critical size, the growth by glide and cross glide can take over until the equilibrium shape is reached.

The loop size in complexes due to prismatic punching is uniform and corresponds to the projected size of the platelike precipitate in the $\langle 110 \rangle$ punch directions. This indicates that the precipitates do not significantly grow in the (001) plane after the strain release by punching has started. Then they further grow in a direction orthogonal to their habit plane, thus increasing the strain again. The punching stabilizes the size and platelike shape of the precipitates even at high annealing temperatures.

In the samples for which the first low-temperature treatment produces dislocation dipoles, elongated dislocation loops form during the high-temperature second step. The density of these loops is one order of magnitude lower than the density of the dipoles. The loops are elongated in the $\langle 110 \rangle$ directions and are up to 20 μm long.

Hexagonal dislocation loops are also found after the high-temperature step, and for all preanneal conditions, with $\{011\}$ habit plane. The larger ones are probably generated by a transformation of 90° dipoles, while the smaller ones might be formed on oxide precipitates.²⁵⁹

4. Effect of rapid thermal annealing

Modern ULSI processing often requires rapid thermal annealing (RTA) as one of the steps. It consists of a brief

(10–10⁴ s) heat pulse, typically performed at high temperatures, characterized by extremely short (few s) ramps up and down. It is interesting to find out whether and what kind of impact RTA has on oxygen precipitation in silicon.

Hawkins and Lavine²⁷⁵ have shown that only the time spent at high temperature is important and can influence precipitation, while the rapid rise or fall in temperature does not. They have further shown that for very short pulses (e.g., 2 s), precipitation is reduced by several times. As the duration of the pulse is increased to about 100 s, precipitation recovers to its initial value. For very long pulses (longer than 10⁴ s), precipitation decreases to nearly zero. There are no further changes in the precipitation characteristics for pulse times up to 5×10⁴ s. These results were interpreted assuming that the thermal pulses modify the initial distribution of heterogeneous nucleation sites. For short pulses, the decrease of sites accounts for the suppressed precipitation. For longer pulse times (about 100 s), the recovery of precipitation is due to a reduction of silicon self-interstitials by outdiffusion, which otherwise limit the rate of precipitation. For very long pulses (10⁴ s), all nuclei are dissolved, so that negligible precipitation occurs.

5. Effect of dopant and impurity effect

The study of the influence of heavy doping on oxygen incorporation during crystal growth and on oxygen precipitation started only recently. Some authors suggested that the dopant does not influence the precipitation process directly, and that differences in the precipitation behavior between n^+ , p^+ , and lightly doped silicon crystals are only due to different levels of oxygen incorporation during crystal growth.²⁷⁶ On the other hand, other groups found different thermally induced precipitate densities in n^+ , p^+ , and lightly doped wafers with the same initial oxygen concentration.^{277,278} Moreover, Bains *et al.*²⁷⁹ have recently shown that precipitation is independent of dopant type and concentration in the lightly doped wafers (dopant concentration $\leq 5 \times 10^{16}$ atoms/cm³); however, in p^+ boron-doped wafers precipitation was found to be generally enhanced, and in n^+ antimony-doped samples it was retarded, compared with lightly doped control wafers with the same oxygen concentration. A model proposed by Wada and Inoue,^{132,280} which involves free-electron effects, appears to be the most plausible explanation of these results. We illustrate now the main results for the most interesting dopants and impurities.

a. Boron. Walitzki *et al.*²⁷⁶ reported that oxygen precipitation in highly B-doped crystals is only correlated to the oxygen content and is independent of doping level. On the other hand, the experiments of Barraclough²⁸¹ on heavily B-doped crystals show that although the total oxygen concentration is similar to the one in low-doped material a significant oxygen clustering takes place already during crystal cooling. He interpretes the results in terms of carrier concentration effect on the formation of thermal donors, assumed to be nuclei for precipitation.

TEM studies of the influence of a heavy B doping on the precipitate morphology showed that:

- (i) No observable precipitates form at 650 °C, even after 128 h;
- (ii) amorphous platelike precipitates form at 800 °C;
- (iii) polyhedral precipitates with dislocation loops form at 1050 °C.^{282,283}

The precipitate density is larger in heavily than in lightly B-doped crystals, while the growth rate of platelike precipitates is smaller.²⁸⁴ Hahn *et al.*²⁸³ explain the (i), (ii), and (iii) findings with the formation of B₂O₃ clusters which enhance the oxide precipitate nucleation. The reduced growth rate of platelike precipitates can be understood by a reduced oxygen flux due to the presence of BO₃ clusters, which also diminishes the oxygen supersaturation.

The morphology of the oxide precipitates formed after a two-step anneal in wafers degenerately doped with B was studied by Wijaranakula²⁵⁶ with TEM. In addition to square-shaped precipitate platelets having {100} habit planes and commonly observed in lightly doped silicon, he found also disk-shaped precipitates both with {110} and {111} habit planes. The presence of complex dislocation loops on the polyhedral precipitates, which are not accompanied by dislocations in lightly doped material, is related to the easier dislocation nucleation and the higher dislocation mobility in heavily doped silicon, which make dislocation nucleation possible even on the stress-lean polyhedral precipitates.²⁸³ On the other hand, it has been reported²⁸⁵ that the mechanical strength increases for boron concentration above 10¹⁸ atoms/cm³. This has been explained by a pinning effect of B₂O₃ or BO₃ precipitates on dislocations.

b. Phosphorus. The influence of phosphorus on the precipitation kinetics has been studied less intensively than the influence of B and Sb. Matsumoto *et al.*²⁸⁴ reported that the oxygen precipitation kinetics is independent of P-doping level for anneals at 800 and 850 °C. Hahn *et al.*²⁸³ studied the effects of heavy P doping in a wider temperature range (450–1050 °C). They found that the precipitate morphology in heavily P-doped samples is similar to that found in highly B-doped samples, while the precipitate density is lower and the size of precipitates is larger. Diffuse x-ray scattering shows that in such samples interstitial-type defects predominate, while the formation of PO₅ clusters is not favored.

c. Antimony. A high Sb-doping level reduces the amount of precipitated oxygen.^{32,95,120,276,277,286,287} Some authors^{120,277,287} attribute this effect to the evaporation of Sb₂O₃ from the melt during the growth process. A similar tendency was reported by Walitzki *et al.*,²⁷⁶ who found that oxygen concentration in Cz-grown silicon crystals highly doped with Sb is reduced by 40% compared to low-doped crystals grown under the same conditions. Nevertheless, these authors believe that evaporation of Sb₂O₃ is thermodynamically unlikely.

Shimura *et al.*²⁷⁷ supposed that the concentration of negatively charged vacancies is reduced by the Coulomb attraction between Sb⁺ and the charged vacancies. They propose that the negatively charged vacancies serve as nucleation centers for oxygen precipitation, so that a high Sb concentration suppresses the precipitation.

Secco d'Aragona and Fejes²⁸⁸ have reported that in

highly Sb-doped wafers oxygen precipitation is reduced and eventually suppressed during high-temperature annealing (1050 °C), while it is independent of doping for low-temperature (650 °C) annealing. This finding suggests a heterogeneous precipitation mechanism for high-temperature annealing.

Barracough²⁸¹ used IR spectroscopy and photon activation analysis to study the behavior of oxygen in electron-irradiated silicon samples heavily doped with Sb or B. He found that the amount of interstitial oxygen is lower and that the precipitation is strongly retarded in the *n*⁺ material. Gupta *et al.*²⁸⁷ obtained similar results by SANS analysis.

d. Carbon. Carbon plays a major role in oxygen precipitation in silicon at low temperatures and, hence, in device yield,^{289,290} when its concentration *C_C* is above 3×10¹⁶ atoms/cm³. It is generally observed that after single-step heat treatments a substitutional carbon to interstitial oxygen ratio as high as 0.3 completely inhibits the development of large precipitates¹⁷⁵ and those eventually formed are too small to be visible even by electron microscopy. Fraundorf and co-workers¹³⁴ found a high density (10¹³ cm⁻³) of small microprecipitates which are under large elastic stress and probably have octahedral shape: No secondary defects were formed, so that interstitial emission seems to be inhibited. However, it is more likely that Si_i clusters remain undetectable because of the high density of nucleating centers (carbon related). Simultaneously, a large number of C-SiO_x complexes are formed, for example after a 750 °C treatment for 64 h.²⁹¹

For two-step annealing treatments and over a large range of *C_C/C_{ox}* ratio (from 0.3 to 0.01) a "retardation" effect is reported.^{292–295} This phenomenon consists of an initial decrease of *C_{ox}*, followed by an increase (the retardation stage) and a final decrease of interstitial oxygen content (the recovery stage) during the annealing, when the first step is performed in the range 750–850 °C,^{125,292} or below 650 °C,²⁹⁵ for 2–8 h. Tan and Kung¹²⁵ have shown that a high carbon concentration is not essential to observe this phenomenon, but can enhance the effect. The retardation is explained by the dissolution of oxide precipitates at the onset of the high-temperature (1050 °C) anneal (second step). Schrems *et al.*²⁹⁶ applied their statistical modelling of growth and dissolution of oxide precipitates to the retardation/recovery phenomenon, obtaining a very good correspondence between the experimental data of Tan and Kung¹²⁵ and the calculated curves.

A study of oxygen precipitation in carbon-rich Cz silicon by synchrotron radiation topography has shown that the samples are strain free.²⁹⁷ This indicates that coprecipitation of oxygen and carbon occurred so that the volume expansion and reduction due to either species compensate each other. This coprecipitation lowers the critical radius for precipitation and this explains the much higher density of stable precipitates.⁵³ Evidence for such coprecipitation was found also by Bender *et al.*²⁹⁸ with HREM, Shimura *et al.*²⁹⁹ with SIMS, and by Gupta *et al.*³⁰⁰ by SANS. Recently, Taylor, Gösele, and Tan³⁰¹ proposed a strain relief mechanism involving carbon and self-interstitial fluxes to explain the behavior of C and O coprecipitation in silicon.

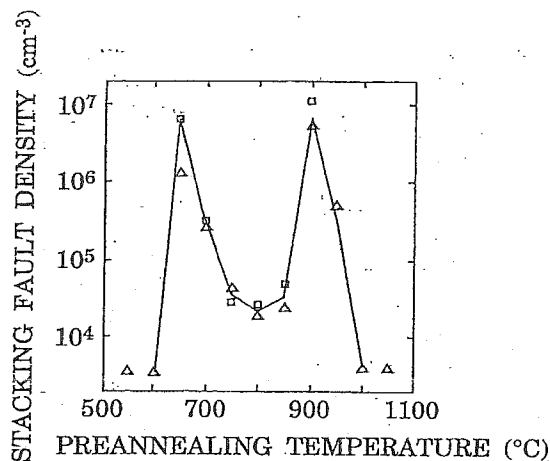


FIG. 47. Stacking fault density in C-rich Cz silicon after a two-step annealing as a function of the temperature of the first step. The second step is performed at 1050 °C for 20 h in N₂ (squares) or in wet O₂ (triangles) ambient (from Ref. 130).

A high carbon content strongly influences the oxygen precipitate morphology. It is found that at low anneal temperatures precipitates take an octahedral shape in carbon-rich more likely than in carbon-lean material.¹³⁴ A high carbon content in the precipitates reduces the strain energy so that the octahedral shape (with minimum interface energy) is favored^{134,136} (see Sec. III C).

Sun *et al.*¹³⁶ found a direct correlation between the reduction of the substitutional carbon and that of interstitial oxygen for annealings at 750 °C by means of FTIR measurements. One carbon atom is transferred to a new configuration for each two oxygen atoms leaving the interstitial position. The total number of substitutional carbon atoms involved in this process is found to be independent of the initial carbon content. They suggested a direct incorporation of carbon in the oxide precipitates, therefore resulting in strain-free octahedral particles. The interaction of substitutional carbon with silicon interstitials and the strain-free precipitates is responsible for the suppression of lattice defect generation.

The number of oxygen atoms leaving interstitial positions for each displaced substitutional carbon atom is 3 at 450 °C, 4 at 750 °C, and 5 at 850 °C, as shown by Newman *et al.*¹⁴⁶ A ratio four to one was also determined by SANS measurements.³⁰⁰ The observed differences could be attributed to the different sample thermal history.

Carbon presence in Cz silicon inhibits the rodlike defect formation,^{77,214,235} but enhances the formation of small amorphous precipitates. Simultaneously, the new donor formation is enhanced, as discussed in Sec. III D 2.

Bender *et al.*²⁹⁸ studied the variation of stacking fault density in carbon-rich Cz silicon after two-step low-high anneal, as a function of the temperature of the first step. A typical example¹³⁰ is shown in Fig. 47 where a strong reduction of the stacking fault density is reported between 700 and 850 °C for samples with $C_{ox}=8.5 \times 10^{17}$ atoms/cm³ and $C_C=4 \times 10^{17}$ atoms/cm³. The first annealing was performed in N₂ for 15 h and the second one at 1050 °C for 20 h in N₂ (squares) or in wet O₂ (triangles). In the 700–850 °C tem-

perature range the Si-C-O clusters are formed.^{134,291} It is therefore very likely that the suppression of self-interstitial supersaturation prevents the secondary defect formation.

e. Nitrogen. The widespread use of a nitrogen ambient during silicon processing and the discovery of the strong effects of nitrogen on mechanical properties of silicon^{30,302} led to an increased interest in nitrogen behavior in silicon. Several authors^{303,304} studied the influence of nitrogen on oxygen precipitation and it was concluded that it increases the number of nucleation sites. Recently, Sun *et al.*³⁰⁵ reported the evidence of defect interactions among oxygen, carbon, and nitrogen during a three-step intrinsic gettering process. They found that nitrogen enhances nucleation in the temperature range from 750 to 1100 °C. Their results were interpreted assuming that nitrogen participates in the creation of nucleation sites for heterogeneous oxygen precipitation and also assuming that nitrogen aggregates at the strain regions surrounding the precipitates, thus retarding silicon self-interstitial migration.

f. Hydrogen. Recently the behavior of hydrogen in silicon has been the object of significant interest.³⁰⁶ It is found that it passivates shallow acceptors (B,Al,Ga) and shallow donors (P,As,Sb)³⁰⁷ and enhances oxygen diffusion.^{72,73} It has been also shown that hydrogen presence enhances thermal donor formation in silicon,³⁰⁸ suggesting that it may influence oxygen agglomeration. Indeed, Hara *et al.*³⁰⁹ have shown recently that hydrogen in silicon crystal causes an enhancement of oxygen precipitation. They attributed it to an increase of the nucleation sites, related to small hydrogen aggregates.

If hydrogen affects oxygen precipitation, Hara *et al.*³⁰⁹ suggested that hydrogen must exist in the form of aggregates, as the defects enhancing oxygen precipitation have high thermal stability.³⁰⁴ Furthermore, it is well known that hydrogen in crystalline silicon tends to precipitate along the {111}, {113}, and {100} lattice planes.^{310,311}

After Hara *et al.*³⁰⁹ two mechanisms can be responsible for the enhancement of oxygen precipitation by hydrogen. One is an increase of the nucleation sites for oxygen precipitation and the other is an enhanced oxygen diffusion.

g. Intrinsic point defects. The polysilicon film deposited on the wafer back surface was found to be a good extrinsic gettering sink for its ability to generate dislocations and stacking faults at the back surface³¹² (see Sec. V). It was also found that the back-surface-deposited polysilicon also enhances oxygen precipitation, therefore increasing the gettering efficiency. The precipitation enhancement effect was thought to be a nucleation effect due to polysilicon deposition thermal cycle.³¹³ Shirai, Yamaguchi, and Shimura³¹⁴ have shown that a polysilicon layer at the wafer back surface causes localized oxygen precipitation near the back surface. The enhancement effect was attributed to the absorption of silicon self-interstitials by the polysilicon. This causes an increase in vacancy concentration in the nearby silicon layer where vacancies are considered to be effective nucleation sites.

Harada, Abe, and Chikawa³¹⁵ studied oxygen precipitation in Cz crystals with excess concentration of vacancies frozen in by detaching the ingot from the melt and by sub-

sequent rapid cooling. They proposed a new model for the enhanced oxygen precipitation in the presence of excess vacancy concentration. Their model has two consequences: One is that the incubation time for oxygen precipitation is short and the other one is that oxygen precipitation occurs even under small supersaturation of oxygen. They also found that the excess self-interstitial atoms incorporated into the crystals during the growth suppresses oxygen precipitation and generates bulk stacking faults.

Hara *et al.*³⁰⁴ studied the effect of cooling rate on oxygen precipitation in Cz silicon crystals. They found that quenching from high temperature introduces defects that enhance oxygen precipitation. These defects are related to intrinsic point defects, and they disappear upon annealing above 900 °C. Ikari *et al.*³¹⁶ obtained similar results by studying nucleation of oxide precipitates in quenched Cz silicon by means of IR spectroscopy and positron annihilation techniques. They found that oxygen clusters are introduced by quenching and that these clusters are the nuclei for the enhanced precipitation in the quenched Si crystal.

Hallberg and Lindström³¹⁷ studied the enhancement of oxygen precipitation in electron-irradiated silicon. They have shown that the effects of the presence of vacancy-oxygen (V-O) and vacancy-dioxygen (V-O₂) groups on oxygen precipitation in silicon are significant. The highest density of precipitates was found in samples with the highest initial concentration of V-O₂ defects. This suggests that the V-O₂ centers are nuclei for oxygen precipitation.

IV. TECHNIQUES FOR OXIDE PRECIPITATE CHARACTERIZATION

A. Wet chemical etching

Wet chemical etching is nowadays a very important process in semiconductor industry both for studying defects and for device processing. Although there is not a formal "theory of etching," a few general principles have been developed. Here they are reviewed and a few examples of some representative etchants and their applications described. A general standard method for detection of oxidation-induced defects by wet chemical etching in silicon wafers was developed by ASTM.³¹⁸

1. Etch formulation and application

Whenever demands for a new etchant emerge, the main role in responding to them is played by previous experience on similar materials or systems rather than by straightforward application of chemical theory.³¹⁹

Semiconductor etchants can be divided in two categories, i.e., into selective (often called preferential) and polishing. The ideal polishing etches have material removal rate which is independent of crystal orientation, strain, or chemical heterogeneities, and are inversely proportional to the local radius of curvature. Therefore, a specimen with rough or damaged surface, as cut for example, etched for a sufficient time in a polishing etch, develops a flat mirrorlike surface with rounded edges. This occurs irrespective of defects within the volume of the material. On the other hand, the ideal selective etch acts upon a highly defective but mirrorlike flat surface only at strain or chemical heterogeneities,

TABLE VII. Recipes for the solutions usually employed for silicon polishing (from Ref. 320).

Solution	Purpose	Composition (volume)
CP-4A	Polishing, lapping, saw damage removal	3 HF
		5 HNO ₃
	Polishing	3 CH ₃ COOH
		1 HF
	Slow polishing	4 HNO ₃
		2 CH ₃ COOH
Iodine	Polishing	1 HF
		6 HNO ₃
		1 CH ₃ COOH
		5 HF
		10 HNO ₃
		11 CH ₃ COOH
		0.3 g I ₂ /250 ml sol.

such as dislocations or impurity striations. However, in practical use etchants do not achieve the ideal properties, but may come close.

In principle, the chemical action of both polishing and selective etching is the same. One component of the etch solution oxidizes the surface, while another one complexes the oxidized species to make them soluble in the etching solution. A third component, usually water or acetic acid, is added as a buffer. Insoluble reaction products may be removed mechanically, this being the principle of the chemo-mechanical polishing process. During the etching process care must be taken to avoid gas formation, since the bubbles can locally block the etching action. This in turn could produce false features during selective etching.

In order to obtain a continuous etching, it is necessary that fresh reactant reaches the surface while the reaction products must be permanently removed, at least as fast as they are involved in the reaction. If the reaction rates at the surface are much higher than the diffusion rate in the liquid, the process will be diffusion limited, as almost all polishing processes are.

Some useful recipes for silicon polishing³²⁰ are given in Table VII.

2. Crystallographic defects evidenced by selective etching

Even during selective etching, for reasonable etching times, the polished damage-free surface of a perfect crystal remains flat; provided no gas develops and the reaction products do not stick to the surface. Damaged areas, however, are etched faster and grooves or pits are formed, remaining after the initially strained material has been etched away. Once formed, upon further etching the pits become flat bottomed and continue to expand only laterally. A similar situation happens in the case of defects such as stacking faults, inclusions, and small dislocation loops.

Different features are observed in the case of line defects such as threading or slip dislocations, and "sheet" inhomogeneities such as growth striations. In that case the strain is not removed. For example, the dislocation etch pits continue to grow without changing shape and maintain their morphol-

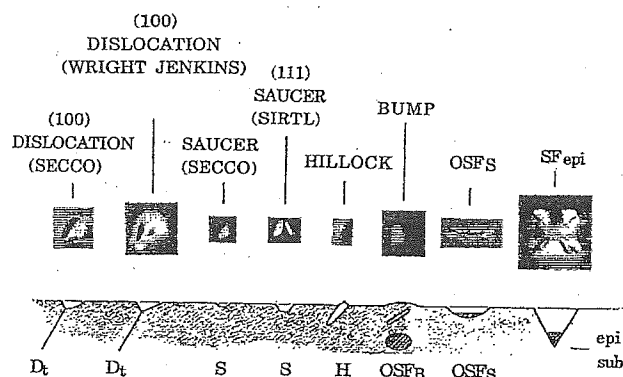


FIG. 48. Etch features found in silicon using some of the etchants listed in Table VIII: dislocation (D_t), saucer (S), hillock (H), bulk and surface oxidation stacking fault (OSF_B and OSF_S), epitaxial layer stacking fault (SF_{epi}) (from Ref. 319).

ogy. If the dislocation is not normal to the surface, the pits have a distorted morphology. Therefore, both line and localized defects may have the same morphology initially, but upon continued etching the localized defects develop pits with a flat bottom, while dislocation pits continue to deepen with a sharp bottom (see D_t and S in Fig. 48 and Fig. 49).

During selective etching etch hillocks may form, which can be easily confused with pits when observed by the optical microscope. Hillocks are usually caused by precipitates from the etch which adheres to the surface, or small unresolved oxide particles which mask the surface. Nevertheless, they can also be associated with defects, such as certain bulk precipitates or stacking faults in silicon (see H in Fig. 48).

The principles discussed above can be illustrated by the results obtained on silicon for which several highly refined selective etches have been developed, such as the so-called Sirtl,³²² Secco,³²³ Wright,³²⁴ Schimmel,³²⁵ and Yang³²⁶ etches.

Chemical recipes for silicon selective etchants are given in Table VIII.

3. Optical microscopy

The above-mentioned defects evidenced by preferential chemical etching are usually analyzed by an optical micro-

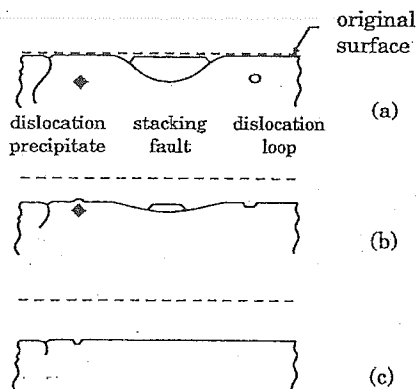


FIG. 49. (a)–(c) Scheme of three etching steps, showing the development of characteristic etch features (from Ref. 321).

TABLE VIII. Recipes for the most common selective etchants for silicon.

Etch	Composition (Volume)	Comments
Sirtl	1 HF (49%) 1 CrO_3 (5 M)	~3.5 $\mu\text{m}/\text{min}$ rate good on {111} poor on {100} faceted pits
Secco	2 HF (49%) 1 $K_2Cr_2O_7$ (0.15 M)	~1.5 $\mu\text{m}/\text{min}$ rate best in ultrasounds good on all planes non-cryst. pits
Wright	2 HF (49%) 2 CH_3COOH 1 HNO_3 (70%) 1 CrO_3 (4 M) 2 $Cu(NO_3)_2 \cdot 3H_2O$ (0.14 M)	~1.7 $\mu\text{m}/\text{min}$ rate no ultrasounds good on all planes faceted pits good shelf life
Schimmel	2 HF (49%) 1 CrO_3 (1 M)	lightly doped Si (0.6–15 $\Omega\text{ cm}$) good on {100} no ultrasounds
Schimmel (modified)	2 HF (49%) 1 CrO_3 (1 M) 1.5 H_2O	heavily doped Si good on {100} no ultrasounds
Yang	1 HF (49%) 1 CrO_3 (1.5 M)	good on all planes no ultrasounds 1–2 $\mu\text{m}/\text{min}$ rate

scope or, with much higher magnification and resolution, by a scanning electron microscope (SEM). Optical microscopy limit magnification is $\times 2000$, while SEM allows magnifications up to the order of $\times 10^5$. On the other hand, optical microscopy is a more versatile technique and is the most used for precipitate density measurements.

The resolution of optical microscope is limited by the diffraction effects, so that two points are just resolvable when they are separated by d ,

$$d = \frac{0.61\lambda}{n \sin u}, \quad (87)$$

where λ is the wavelength of light, n the index of refraction of air (or immersion oil), and u is the vertical angle of divergence that the objective lens can accept. The product $n \sin u$ is called the numerical aperture (NA). Since the NA limits the resolution of the microscope, a greater magnification obtained by means of high-power oculars with lenses of low NA does not produce more details. For example, the resolution of the best microscopes is about 0.2 μm .

Although conventional optical microscopes are still widely used in reflection mode for opaque objects such as silicon wafers, a significant improvement has been made when Nomarski and Weill in 1952 proposed the interference-contrast method.³²⁷ It has become the most important method for optical examination of semiconductor surfaces upon wet chemical etching.

The instrument based on the Nomarski interference method is essentially a two-beam microscope as illustrated in Fig. 50, showing the light beam path in the instrument. Entering from the left-hand side, the light passes through a polarizer set at 45° , being reflected downward by a half-

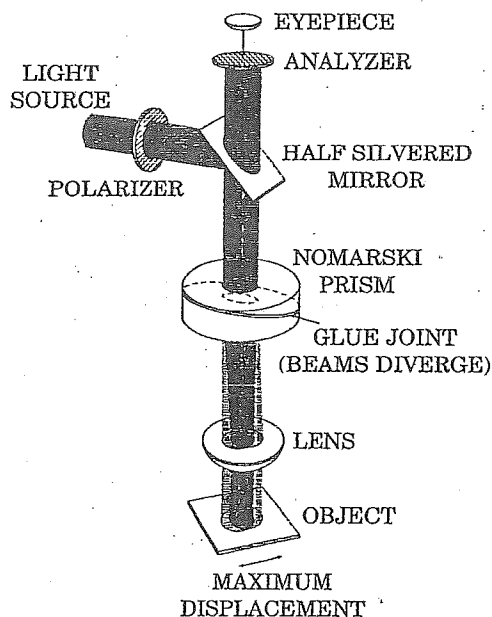


FIG. 50. Schematic diagram of the Nomarski differential interference-contrast microscope (from Ref. 319).

silvered mirror, and passes through the modified Wollaston or Nomarski prism where the light beam is split in two parts. The two beams then pass through the objective lens, are reflected from the object, and, after crossing lens, prism, mirror, and a polarizer set at 135° (analyzer), reach the eye. The Nomarski prism is made of two separate birefringent quartz prisms glued together, having perpendicular optical axes. The 45° -polarized light from the polarizer forms two components in the first birefringent prism, traveling with different speeds due to the different indices of refraction along and perpendicular to the optical axis. Then, upon striking the glue joint, they form the two divergent beams. Since the optical axis of the second prism undergoes a 90° rotation with respect to first one, the speeds are interchanged.

The thickness of the two parts of the Nomarski prism can be chosen so that the two beams come out of the prism in phase. The angle of divergence is matched up with the focal length of the objective lens so that the two beams are focused parallel onto the object. For an object having a flat surface, upon reflection the beams reach the glue joint forming a single beam that is extinguished by the analyzer set at 135° . This configuration is called the null or dark mode in the Nomarski differential interference contrast method. However, if the prism is moved to one side or the other a phase shift between beams occurs. As a result an elliptically polarized beam forms when the rays join and such a beam is not stopped by the analyzer. As a consequence, more light is transmitted.

When the prism is moved far enough, the phase shift becomes so large that the shortest visible wavelengths (dark blue) begins to interfere destructively and the resulting light becomes yellow. Additional colors appear as the prism is moved further away from the null position. It should be noted that this happens regardless of the absolute height of the flat surface observed.

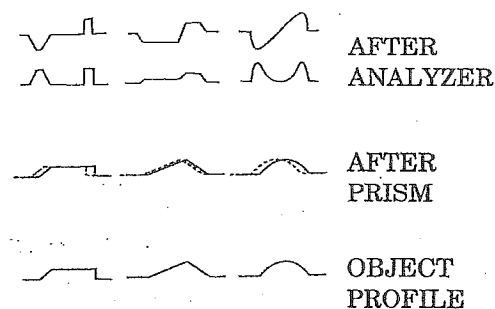


FIG. 51. Schematic illustration of object profiles, wave fronts of the displaced beams after reflection, and intensity distribution of the recombined beams after passing the analyzer for two different prism settings (from Ref. 319).

As an example, we can consider an object with a vertical relief and the beams displaced about $0.2 \mu\text{m}$ one from the other. Such a beam displacement is below the resolving power of the microscope and thus is not observed. Figure 51 illustrates an image formation for different object profiles.³¹⁹ The profiles on the bottom line represent the cross-sectional shape of three different objects. In the middle line, displacements of the wave fronts of the two beams are indicated immediately after reflection and crossing the prism. The top lines give the resulting intensity distribution after the beams have passed through the analyzer. One set of profiles (the lower one) on the top line corresponds to a null setting of the instrument which yields a black background. The other set (the upper one), which is a more common operating mode, corresponds to the prism setting slightly off null position, hence giving a grey background. The width of the displacement is magnified in the diagram and in practice it will appear just as a line. It should be pointed out that the surfaces having the same slope have the same contrast (or color), and also horizontal surfaces having different height have the same contrast. The interference contrast obtained by the microscope is proportional to the beam displacement, therefore it is maximum along the direction of displacement, and no contrast is visible in a perpendicular direction. These principles are illustrated schematically in Fig. 52. Note that only the step running parallel to the beam displacement (x direc-

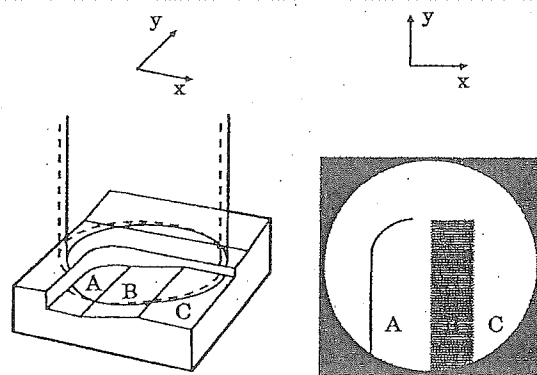


FIG. 52. Schematic illustration of an object with the two incident beams (left-hand side) and resulting images (right-hand side) (from Ref. 319).

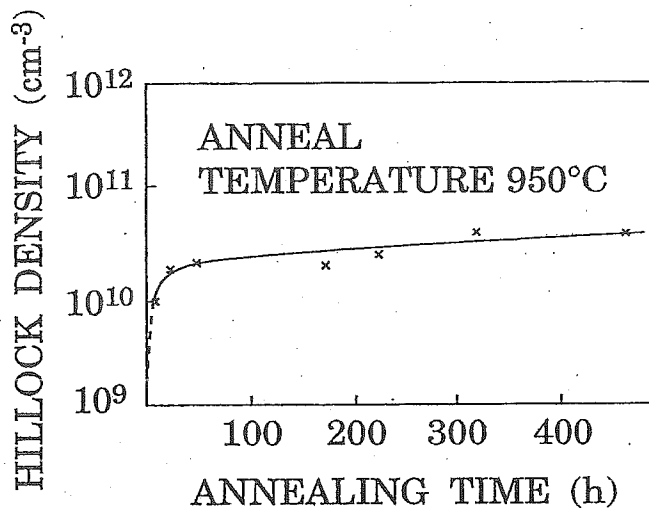


FIG. 53. Density of large etch hillocks as a function of annealing time at 950 °C (from Ref. 143).

tion) forms virtually no observable image. Step heights as low as 30 Å and the corresponding slopes (30 Å in about 0.2 μm beam separation) can be detected. Therefore, etch pits with side slopes of only a few degrees produce a sharp contrast and may appear deeper than they actually are. Absolute evaluation is possible with comparison of known features on the surface.

4. Detection of SiO_x precipitates

Wet chemical etching with optical microscopy is widely employed to measure the density per unit area of precipitates on silicon wafer surfaces, thus allowing the average density of bulk defects to be estimated. For example, Newman *et al.*¹⁴³ by analyzing silicon wafers after Wright etching and after different heating times found two types of etch features: Small pits which appeared to be present in as-grown crystals, which can be resolved after heating, and larger etch hillocks which were only observed after heat treatment. The density of the latter defects increases with the heating time up to 50 h and then remains constant (see Fig. 53). The density of small pits N (in cm⁻³), decreasing with the annealing time, when measured after long sample annealing fits the empirical relation

$$N = 0.15 \exp(2.65/kT), \quad (88)$$

with kT expressed in eV, as shown in Fig. 32 in Sec. III B, where the results are compared with the defect density deduced from the kinetic model.

Clear evidence of the nonhomogeneous axial distribution of oxide precipitates through the seed end of a Cz silicon single crystal is reported in Fig. 54.³²⁸ The figure shows the convex and concave layers of precipitates revealed after 1000 °C annealing. The distribution of precipitates in the same crystal as in Fig. 54 at different axial positions is reported in Figs. 55(a)–55(d).³²⁸ This figure shows the precipitate distribution at the center of the crystal (a), and at 1/2, 3/5, and 4/5 radius [(b), (c), and (d), respectively]. At the center the precipitates are more homogeneously distributed.

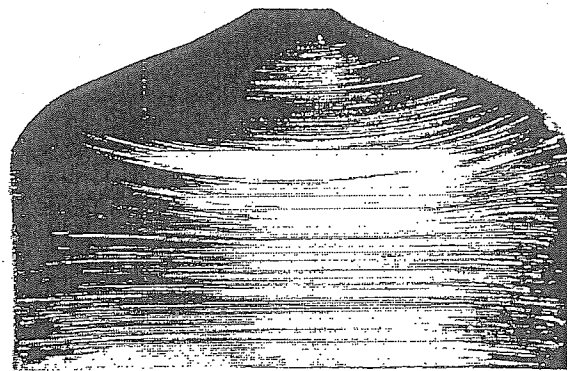


FIG. 54. Axial section of the seed end of a Cz crystal showing precipitate layers as evidenced by etching (from Ref. 328).

The layers with low precipitate density (dark stripes) are very thin, and their thickness increases with the distance from the center of the crystal [Figs. 55(b) and 55(c)]. At 4/5 radius distance [Fig. 55(d)] most of the precipitates disappeared and the residual precipitate layers are very thin.

Bains *et al.*²⁷⁹ studied oxygen precipitation in p^+ and n^+ dislocation-free Cz silicon wafers. After a three-step treatment, 16 h at 1100 °C, 64 h at 650 °C, and 20 h at 1050 °C, the Sb-doped samples were etched for 30 min with Wright etch and the B-doped ones for 4 min with the modified Schimmel etch. They found that in p^+ B-doped samples precipitation is enhanced and in n^+ Sb-doped samples it is retarded with respect to lightly doped reference samples with the same oxygen concentration, where the precipitation behavior is independent of dopant type and concentration. Figure 56 shows²⁷⁹ two images of the etched cross section of a p^+ ($[B] = 9 \times 10^{17}$ atoms/cm³) sample with 7.6 – 8.96×10^{17} atoms/cm³ interstitial oxygen concentration after the three-step annealing. The figure evidences the formation of oxygen-related platelet defects. Moreover, precipitate-free regions surrounding these defects are visible, probably caused by the gettering effect of the platelets on the oxide precipitates present in the sample.

B. Transmission electron microscopy

Transmission electron microscopy is a well-known technique, particularly powerful to study defects and small aggregates where high space resolution is needed.³²⁹ Broad range applications of electron microscopy in the high-resolution mode (HREM) have been actually devoted to study defect structures of various types (linear, planar, dislocation cores, grain boundaries, etc.). To achieve the extreme resolution limits the key parameter on which to act is the accelerating voltage of the instrument. For instance, distances and features having dimensions decreasing from 2.1 to 1.6 Å can be resolved³²⁹ when the voltage is raised from 200 to 400 keV. Therefore, the point defects can also be directly observed by TEM.

The main sources of the noise, which represents the limiting factor for detecting small clusters, are essentially two: Thickness variation of the matrix (due, for instance, to oxide formation, as in silicon) and surface roughness. The two of

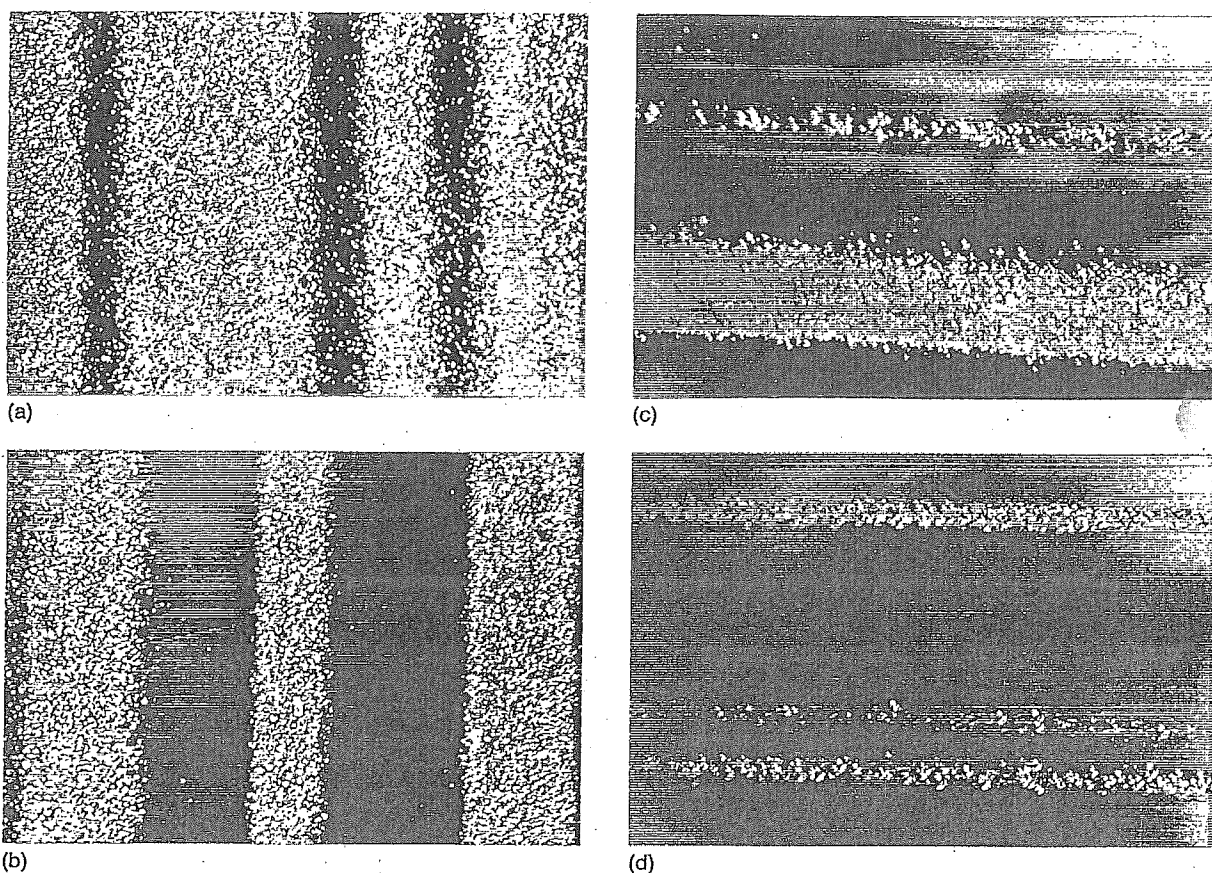


FIG. 55. Precipitate distribution (a) in the center, (b) at 1/2, (c) at 3/5, and (d) at 4/5 radius of the same crystal as in Fig. 54 (from Ref. 328).

them give a coupled contribution to statistical noise corresponding to ± 4 atomic steps if one wants to investigate small aggregates with a signal-to-noise ratio $S/N \sim 1$.³²⁹ As a consequence, 4^1 , 4^2 , and 4^3 impurity atoms should be included along the direction of the electron beam for observing linear, planar, or three-dimensional agglomerates, respectively. In order to detect aggregates of defects at such a low S/N ratio, a minimum density of 10^{15} defects/cm³ is required. Also scanning transmission electron microscopy, which allows electron microdiffraction using a subnanometer probe, is affected by the same limitations.

Information from TEM on particle size and shape is direct, since a large region in reciprocal space is sampled, whereas, e.g., SANS explores only a small volume of k

space. In other words, with TEM very small volumes are examined and the response is strictly an image of such a specific part of the sample, which might diverge even substantially from that of the bulk.

TEM is one of the most used techniques for the study of oxygen precipitation in silicon,^{141,265,266} often combined with other analytical methods such IR absorption,²³⁴ SANS,²⁴⁴ and x-ray topography. TEM, with respect to other techniques, allows one to determine the shape of individual pre-

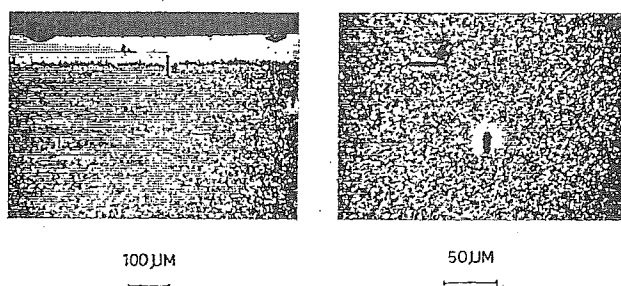


FIG. 56. Preferential etch cross sections of a p^+ wafer showing gettering of oxide precipitates by platelet defects formed after a tristep heat treatment (from Ref. 279).

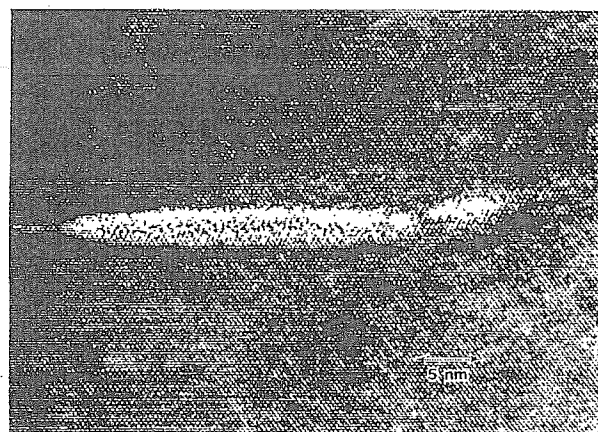


FIG. 57. HREM image of a platelet precipitate grown after annealing at 850 °C for 60 h. The image shows the amorphous structure and the orientation along $\{100\}$ silicon planes (from Ref. 150).

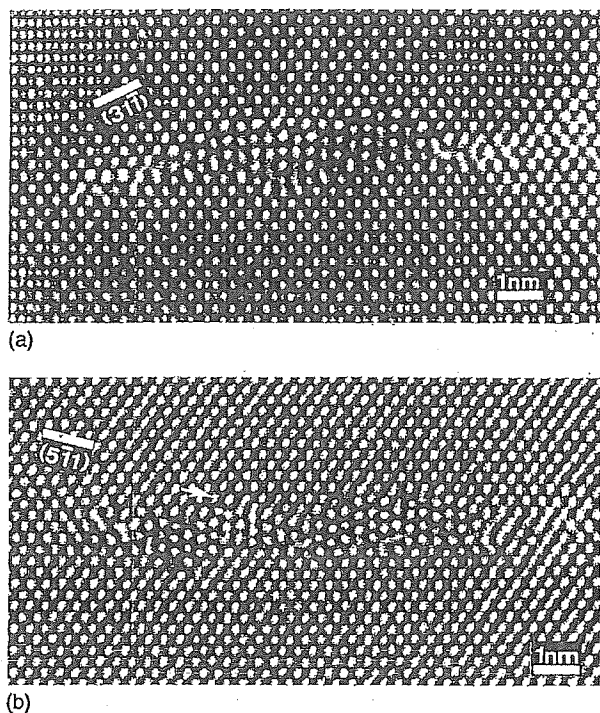


FIG. 58. High-resolution images of rodlike defects seen along their elongated axis: zig-zag shape of the defect consisting of one part along $(31\bar{1})$ plane and one along (100) plane (upper image); the arrow indicates the interface plane $(5\bar{1}1)$ (lower image) (from Ref. 233).

precipitates as well as their structure (amorphous or crystalline) and their interfaces with the host crystal. For example, TEM images are reported by Tiller and co-workers¹⁵⁰ to confirm the results of a model concerning the equilibrium shape for thermally induced microdefects in Cz silicon, based on thermodynamic and kinetic considerations (see Sec. III C). Figure 57 shows a HREM image of an amorphous platelet precipitate grown after intermediate-temperature annealing (850°C for 60 h) of a Cz silicon sample. The platelet lies parallel to $\{100\}$ silicon planes. The correlation between circular stacking faults in silicon and subsurface precipitates has also been demonstrated by a TEM study.³³⁰ As for the precipitate structure and orientation in the silicon crystal, in several articles these characteristics have been studied as a function of the particular annealing conditions. Recently, a review of the results about the structure of oxygen-related lattice defects in silicon has been presented by Bender and Vanhellemont,³³¹ with the comparison of different techniques.

A detailed TEM study of oxygen-related lattice defects in Cz silicon samples after one- and two-step annealing at different temperatures is reported by Bender.¹⁵¹ After a one-step treatment at low temperature (in the region from 550 to 1000°C) rod-shaped coesite precipitates, platelike amorphous SiO_x precipitates, dislocation dipoles, and prismatic loops were found. After a subsequent high-temperature (1150°C) step different types of defects such as Frank-type stacking faults, elongated dislocation and prismatic loops, octahedral amorphous SiO_x precipitates, and plateletlike SiO_x precipitates with prismatic dislocation loops were observed.

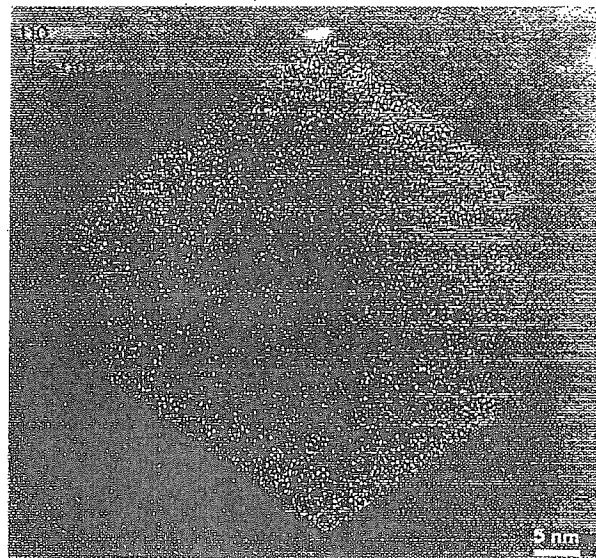


FIG. 59. High-resolution image of a truncated octahedral precipitate, showing its amorphous structure (from Ref. 151).

As an example of HREM images Fig. 58(a) and 58(b) shows rodlike defects seen along their elongated axis, detected in samples annealed at 650°C for 100 and 264 h, respectively.²³³ In the upper image the zig-zag shape of the defect is found, consisting of two parts along the $(31\bar{1})$ plane and one part along the (100) plane. The lower image shows a defect with lattice planes straight and parallel; partly $(5\bar{1}1)$ interface planes are visible (see the arrow). Figure 59 reports a HREM image of a truncated octahedral precipitate observed¹⁵¹ after a two-step annealing (850°C 15 h + 1150°C 1.5 h). The amorphous structure of this kind of precipitate is clearly evidenced.

Bergholz *et al.*²⁴⁴ studied systematically the defects induced in Cz silicon wafers with initial $C_{\text{ox}} = 10^{18} \text{ atoms/cm}^3$ by a 48, 96, and 431 h annealing at 750°C , performing also a direct comparison with SANS data (see Sec. IV D). Their results are summarized in Table IX where defect type, size, volume, and density as obtained from TEM images in Cz silicon samples annealed at 750°C for different times are reported. In the samples annealed for 48 h the defects were amorphous oxide platelets lying on $\{100\}$ planes and extrinsic stacking-fault dislocation loops on $\{111\}$ planes. The plate diameters vary from 6 to 16 nm with 1.5 nm mean thickness. The precipitate density was $1.4 \times 10^{13} \text{ cm}^{-3}$. About 60% of oxide plates present a narrow “teethlike” extension at one end. These extensions, about 35 nm long, are an extremely thin oxide layer contiguous with the main plate. Sometimes precipitates made of only the teeth (without the plate) are present, attributed by the authors to early stages of the oxygen precipitation. The samples annealed for 48 h also show SiO_2 spherical particles with an amorphous structure. They have a diameter of about 3.5 nm and their density is about 10^{12} cm^{-3} .

The main defects present in the samples annealed for 96 h are amorphous oxide plates lying on $\{100\}$ planes and extrinsic stacking-fault dislocation loops on $\{111\}$ planes. The plates have a density of $1.5 \times 10^{13} \text{ cm}^{-3}$ with a diameter of

TABLE IX. Defect type, size, volume, and density as obtained from TEM images in Cz silicon samples annealed at 750 °C for different times (from Ref. 244).

Anneal time (h)	Type	Size (nm or nm ²)	Volume (cm ³)	Density (cm ⁻³)
48	Plate	12×1.5	2.2×10 ⁻¹⁹ ^a	5.6×10 ¹²
48	Plate with teeth	12×1.5 plus 35×0.4	7.1×10 ⁻¹⁹ ^b	8.4×10 ¹²
48	Sphere	~3.5	~2×10 ⁻²⁰ ^c	~10 ¹²
48	Dislocation loop	~73		
96	Plate	20×1.7	6.8×10 ⁻¹⁹	1.2×10 ¹³
96	Plate with fins	20×1.7 plus 8×15	1×10 ⁻¹⁸ ^d	3×10 ¹²
96	Sphere	~4	~3×10 ⁻²⁰ ^c	~10 ¹²
96	Dislocation loop	~48		
431	Plate	26×2.5	1.7×10 ⁻¹⁸	3×10 ¹²
431	Plate with fins	26×2.5 plus 5×7	2.6×10 ⁻¹⁸	4.5×10 ¹²
431	Sphere	~4.5	~5×10 ⁻²⁰	~10 ¹⁴
431	Dislocation loop	~45		6×10 ¹²

^aAssumes a 12×12×1.5 nm³ square plate.

^bAssumes a 12×12×1.5 nm³ square plate plus a 35×35×0.4 nm³ square plate.

^cAssumes a sphere of diameter 3.5 nm.

^dAssumes a 20×20×1.7 nm square plate and calculated volume for plate multiplied by 1.5 to give volume for plate with fin.

20 nm and a thickness of 1.7 nm. The 80% of the precipitates have the plate shape, but the other 20% have in addition a "finlike" extension on one side or on both sides. Amorphous spherical particles with a mean diameter of 4 nm and density of about 10¹² cm⁻³ are also present.

Also in the samples annealed for 431 h the main defects are amorphous oxide plates on {100} planes and extrinsic stacking-fault dislocation loops on {111} planes. The plate diameters were about 26 nm, thickness 2.5 nm, and density about 7.5×10¹² cm⁻³. In this case the TEM micrographs showed that about 40% of the precipitates were plates and the other 60% have the "plate with fins" shape. These finlike extensions are typically 8 nm wide at the base where they join the main plate. They extend for about 15 nm in the

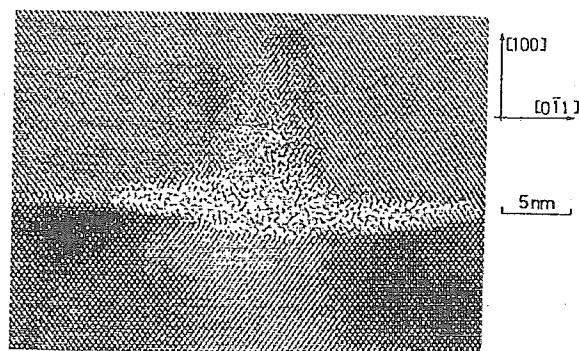


FIG. 60. HREM image of a platelike precipitate with finlike extension observed in a silicon sample annealed at 750 °C for 431 h (from Ref. 244).

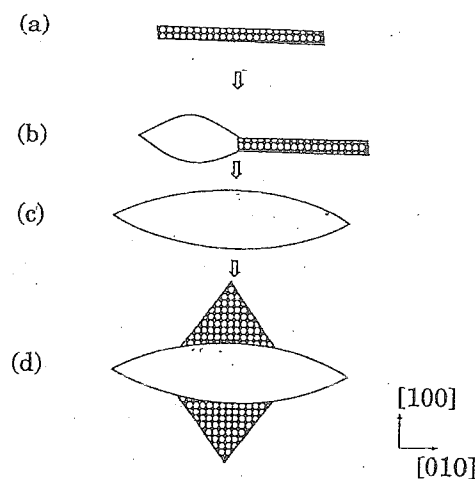


FIG. 61. Scheme of the development of a precipitate along (100) plane: (a) double-row structure; (b) double-row structure with platelet; (c) platelet; (d) platelet with fins (from Ref. 244).

directions perpendicular to the plate. This last type of precipitate is very similar to the octahedral precipitates found by several authors^{123,142,265,331,332} and predicted by thermodynamic considerations.¹⁵⁰ Figure 60 shows a HREM image²⁴⁴ of a typical platelike precipitate with a finlike extension. The main habit plane is the (100) silicon lattice plane. The TEM results just illustrated suggested to Bergholz *et al.*,²⁴⁴ for Cz silicon samples annealed at 750 °C, the precipitation sequence reported in Fig. 61. Precipitation starts with the formation of a thin oxide plate on a {100} plane, formed only by few atomic layers. At one end the thickness increases, then spreads along the tooth and leads to the formation of a bigger plate. This process is partially due to the oxygen diffusion from the thin region to the thick one, proceeding until the thin portion of the precipitate dissolves. The thick plate then develops the fins, which make the precipitates assuming the octahedral shape. To accommodate the volume of the oxide plates in the silicon, interstitial silicon atoms are produced, some of which combine forming the extrinsic stacking-fault dislocation loops observed in those samples.

HREM measurements allowed investigations of precipitate shape and composition also at early stages of oxygen precipitation⁷⁷ in Cz silicon after 5 days annealing at 650 and 870 °C. Two kinds of precipitates are observed: Rodlike-shaped precipitates made of a crystalline silica phase (coesite), and dot-shaped precipitates made of an amorphous oxide phase. Both types are detected in the samples treated at 650 °C. After heat treatment at 870 °C the small dot precipitates grow in size assuming a square shape and lying on {100} planes. The thickness of all these precipitates is so small (about 1.5 nm) that they could not be detected by conventional methods.

C. Infrared absorption

Oxygen precipitation in silicon can be studied using IR spectroscopy in two ways. One of them can be defined as an indirect method for detection and quantitative evaluation of precipitated oxygen. It is based on the measurement of inter-

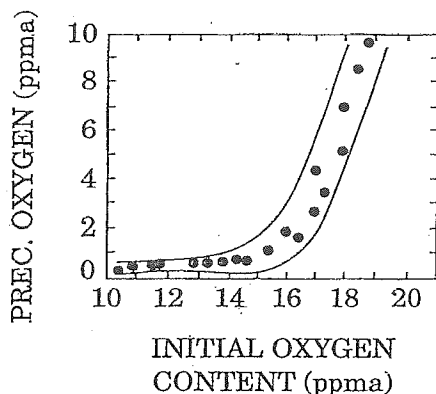


FIG. 62. Results of the statistical reduction of test A data (from Ref. 333).

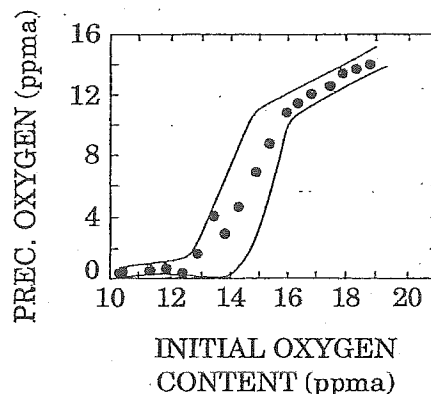


FIG. 63. Results of the statistical reduction of test B data (from Ref. 333).

stitial oxygen concentration by the intensity of the 1107 cm^{-1} band before and after the precipitation annealing. Assuming that the decrease of C_{ox} is only due to precipitation, such a decrease can be considered a measure of the concentration of precipitated oxygen. The second method, more recent and sophisticated, is a direct one and is based on the detection and analysis of precipitate-related absorption bands in the mid-IR spectral range. Although data analysis is not straightforward, this second method can provide more information about precipitates (shape, composition, orientation, local density) and can be used also for as-grown silicon, where the first method is completely ineffective due to its higher sensitivity limit. In this subsection both methods of analysis are described and the most significant experimental data available in the literature reported.

1. Indirect precipitate detection

The procedure for the evaluation of interstitial oxygen concentration C_{ox} by the IR-absorption band at 1107 cm^{-1} in the room-temperature spectrum of silicon is described in Sec. II C 1 and the conversion factors reported. Therefore, only the use of this procedure for the study of oxide precipitates is illustrated here.

The reproducibility of the results of this indirect method has been recently tested³³³ to state whether it is suitable for the development of an ASTM standard test method. B- and P-doped Cz silicon samples (100) oriented and with 10–15 $\Omega\text{ cm}$ resistivity (p type) and 1.5–7 $\Omega\text{ cm}$ resistivity (n type) are studied. The samples from different silicon material vendors have been studied in different laboratories by measuring the difference ΔO_i of interstitial oxygen concentration before and after one of two kinds of thermal treatments, called test A and B. Test A consisted of a 16 h annealing at 1050°C and test B was the same as test A, but with a 4 h preheating at 750°C . All other annealing parameters (ramp up and down, push and pull rate, ambient) were the same.

The values of ΔO_i obtained for p - and n -type wafers after A and B heat treatments are determined for samples with different initial oxygen concentrations. A statistical reduction of the data was performed by evaluating, for each 0.5 parts per million atoms (ppma) interval in initial C_{ox} , the average values of C_{ox} and ΔO_i . The results obtained in a

single laboratory by a FTIR instrument are reported in Figs. 62 and 63 for samples subjected to A and B tests, respectively. The solid lines around the data points in the figures represent the 2σ band in ΔO_i as calculated from the data of four laboratories. After test A no precipitation detectable as ΔO_i occurs in samples with initial C_{ox} lower than about $8 \times 10^{17}\text{ atoms/cm}^3$ (15–16 ppma), then precipitated oxygen increases up to $4 \times 10^{17}\text{ atoms/cm}^3$ in samples with $9 \times 10^{17}\text{ atoms/cm}^3$ initial C_{ox} . A different behavior was found for the samples subjected to test B. Precipitation begins to be detectable for initial C_{ox} as low as $6.5 \times 10^{17}\text{ atoms/cm}^3$ and rapidly increases (for samples with $7.5 \times 10^{17}\text{ atoms/cm}^3$ initial O_i concentration precipitated oxygen reaches $5\text{--}6 \times 10^{17}\text{ atoms/cm}^3$); then the precipitation rate decreases ($\Delta O_i \sim 7 \times 10^{17}\text{ atoms/cm}^3$ for $9 \times 10^{17}\text{ atoms/cm}^3$ initial O_i).

Some possible sources of error in the measurements of C_{ox} are present:

- (i) the backside roughness of the wafers;
- (ii) the different type of IR spectrometer (dispersive or Fourier transform);
- (iii) different software package to calculate C_{ox} ;
- (iv) after heat treatment the oxide precipitate band can overlap the interstitial oxygen peak leading to an incorrect value of C_{ox} . Nevertheless, some conclusions can be drawn:

- (1) No differences are evidenced in oxygen precipitation from n - and p -type silicon at the doping level tested;
- (2) the thermal treatments carried out in different laboratories give completely equivalent results;
- (3) the preheating enhances oxygen precipitation (see Sec. III D).

On this basis an ASTM standard method for oxygen precipitation characterization in silicon wafers by the measurement of interstitial oxygen reduction was developed in 1989.³³⁴ This standard illustrates a method of selection and preparation of test samples, evaluation of error sources, and calculation and interpretation of the results.

2. Direct precipitate detection

The first evidence of an effect of SiO_x precipitates on the Si optical properties was reported by Kaiser¹⁹ who detected

IR light scattering in heat-treated Cz silicon. The pioneer work by Patrick³³⁵ showed that an IR-absorption band at about 1230 cm^{-1} rises in Cz Si samples where oxygen precipitation occurred during heat treatment for long times. Hu and Patrick³³⁶ studied the effect of oxygen concentration on dislocation movements, correlating dislocation size and IR-absorption spectra. A series of indents was made to create dislocations in Si samples with C_{ox} ranging from 5×10^{17} to 15×10^{17} atoms/cm³ and annealed for different times (from 20 min to 240 h) at different temperatures (from 700 to 1300 °C). The IR-absorption spectra clearly show, for long sample annealing at 1000 °C, a significant reduction of the intensity of the 1107 cm^{-1} absorption band indicating a reduction of interstitial oxygen concentration. In the same spectra a new absorption band appears at 1230 cm^{-1} due to the clustering of oxygen atoms. From then on, the behavior of the IR-absorption band at about 1230 cm^{-1} related to precipitated oxygen was extensively analyzed. For example, Rozgonyi and Pearce³³⁷ evidenced that when oxidizing the wafers in HCl-added oxygen ambient the 1225 cm^{-1} band disappears, due to the reduction of oxygen precipitation. From IR-absorption spectra where a 1225 cm^{-1} band is present Hu¹¹¹ showed that oxidizing ambients strongly retard precipitation. The investigation of the 1225 cm^{-1} absorption band after sample annealing at different temperatures allowed Shimura *et al.*^{90,260} to conclude that the precipitates are made of cristobalite and they form through heterogeneous nucleation.

Tempelhoff *et al.*^{222,223} studied oxygen precipitation in dislocation-free Cz silicon subjected to annealing at temperatures ranging from 400 to 1000 °C and compared the results obtained from IR and TEM measurements on the same samples. They found that oxide precipitates present a different shape depending on the annealing temperature.

In the low-temperature range (from 400 to about 750 °C), where the spectra show a broad absorption peak growing in intensity and shifting its maximum from 1030 to 1100 cm^{-1} with increasing the temperature, the precipitates consist of amorphous SiO_x ($x < 2$), which transforms into SiO_2 if the annealing temperature is raised. In this temperature range TEM images show the appearance of rodlike defects and their transformation in dislocation loops.

In the intermediate temperature range (about 750–950 °C) the appearance of two intense peaks at 1125 and 1222 cm^{-1} in the high-energy region of the spectra and, at 489 cm^{-1} in the low-energy region lead the authors to the conclusion that α -cristobalite precipitates were formed. In this temperature range TEM measurements reveal the presence of dislocation loops and platelet-shaped precipitates.

After high-temperature annealing (about 950–1100 °C) a decrease in the intensity of the two high-energy peaks as well as of the low-energy peak occurs, while two peaks at 1100 and 472 cm^{-1} show up. This was interpreted by the authors as due to the conversion of α -cristobalite into amorphous SiO_2 . TEM images of the same samples show the dissolution of platelet-shaped precipitates and the formation of micro-precipitates.

Results of IR-absorption measurements and of high-resolution TEM investigation on oxide precipitates in Cz sili-

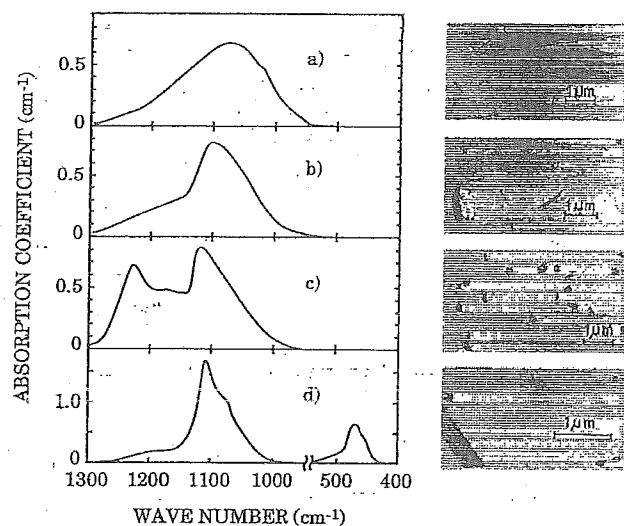


FIG. 64. Infrared-absorption spectra and high-resolution transmission electron microscopy images of different silicon samples annealed in the temperature range 600–1275 °C. The sample characteristics and annealing conditions are: (a) $C_{\text{ox}} = 1.4 \times 10^{18}$ atoms/cm³, $C_{\text{C}} = 2.2 \times 10^{16}$ atoms/cm³, annealed for 240 h at 600 °C; (b) $C_{\text{ox}} = 1.5 \times 10^{18}$ atoms/cm³, $C_{\text{C}} = 10.5 \times 10^{16}$ atoms/cm³, annealed for 64 h at 900 °C; (c) $C_{\text{ox}} = 1.4 \times 10^{18}$ atoms/cm³, $C_{\text{C}} = 6 \times 10^{16}$ atoms/cm³, annealed for 64 h at 900 °C; (d) $C_{\text{ox}} = 1.6 \times 10^{18}$ atoms/cm³, $C_{\text{C}} \leq 10^{16}$ atoms/cm³, annealed for 2 h at 1275 °C (from Ref. 234).

con specimens after heat treatments in the temperature range from 600 to 1275 °C were also reported by Gaworzewski *et al.*^{234,338} By analyzing samples with initial interstitial oxygen concentration from 0.9 to 1.5×10^{18} atoms/cm³ and with carbon concentration from 10^{16} to 10^{17} atoms/cm³, they found that at least four different kinds of precipitates exist, depending on the temperature of heat treatment, on oxygen and carbon concentrations and on the thermal history of the samples. The correlation²³⁴ between IR-absorption spectra and the corresponding TEM micrographs of the four different precipitates is shown in Fig. 64. In Fig. 64(a) the broad band centered at about 1085 cm^{-1} , obtained after annealing samples with $C_{\text{ox}} = 1.4 \times 10^{18}$ atoms/cm³ and $C_{\text{C}} = 2.2 \times 10^{16}$ atoms/cm³ for 240 h at 600 °C, is clearly correlated to the presence of rodlike defects. In Fig. 64(b) the broad band centered near 1100 cm^{-1} , less symmetrical than that reported above, is obtained after annealing samples with $C_{\text{ox}} = 1.5 \times 10^{18}$ atoms/cm³ and $C_{\text{C}} = 10.5 \times 10^{16}$ atoms/cm³ for 64 h at 900 °C. In this case TEM micrographs show the presence of a high density of globular-shaped precipitates with small size. In Fig. 64(c) the IR spectrum characterized by a double band with peaks at about 1120 and 1225 cm^{-1} obtained after annealing for 64 h at 900 °C Si samples with $C_{\text{ox}} = 1.4 \times 10^{18}$ atoms/cm³ and $C_{\text{C}} = 6 \times 10^{16}$ atoms/cm³ is reported. The authors do not confirm the presence in this case of α -cristobalite precipitates, as proposed by Tempelhoff *et al.*^{222,223} because some of the spectra do not show the characteristic absorption band of cristobalite at 485 cm^{-1} . Instead, they suggest that the double-peak structures observed in the absorption spectra of these samples may be due to the contemporary presence of the precipitates shown in Fig. 64(b) responsible for the absorption at 1120 cm^{-1} , and a new form of precipitate responsible for the absorption at

1225 cm^{-1} . This last band, as also suggested by Hu,³³⁹ can be attributed to platelet-shaped precipitates. TEM micrographs reveal the formation of irregularly shaped precipitates with a weakly decreased density with respect to those found in the samples of Fig. 64(b). The IR spectrum reported in Fig. 64(d) shows two absorption bands at 1105 and 470 cm^{-1} and refers to samples with $C_{\text{ox}} = 1.6 \times 10^{18}$ atoms/ cm^3 and an undetectable C_{C} , annealed for 2 h at 1275 °C. The spectrum shows the same features as the typical spectrum of amorphous bulk SiO_2 and was found only in Si wafers initially oxygen rich and carbon free (under the IR detection limit). The TEM pattern evidences faceted octahedral precipitates and do not show any defects of small size, except those induced by octahedral precipitates.

The first model to justify the absorption band at about 1230 cm^{-1} of SiO_2 precipitates in silicon was proposed by Hu.³³⁹ He approximated the precipitates by ellipsoids with axes (a_1, a_2, a_3) , obtaining in this way with continuity the different shapes from the needle ($a_1 = \infty$) to the sphere ($a_1 = a_2$) to the disk (or platelet, $a_1 = 0$). For small precipitates (less than 0.36- μm -long axes) the electric field E_p inside the particles can be considered uniform and is given by

$$E_p = gE_m, \quad (89)$$

where E_m is the electric field in the silicon matrix and g is a tensor. If the complex dielectric functions ϵ_m and ϵ_p of the matrix and precipitate compounds are isotropic, for a particular choice of the axes of the ellipsoid with respect to the coordinate system g becomes diagonal, with elements

$$g_i = \frac{\epsilon_m}{L_i \epsilon_p + (1 - L_i) \epsilon_m}, \quad (90)$$

where $i = 1-3$ and L_i are geometrical parameters related to the depolarization factors along the i axis of the ellipsoid. When the precipitates are randomly oriented in the silicon lattice the net effect is obtained by averaging over all the orientations, therefore g is a scalar,

$$g = \frac{1}{3}(g_1 + g_2 + g_3). \quad (91)$$

According to the effective medium theory,^{340,341} the average electric field of the composite medium E_{avg} is given by

$$E_{\text{avg}} = (1 - f)E_m + fE_p, \quad (92)$$

where f is the volume fraction occupied by the precipitates in the sample, and

$$P_{\text{avg}} = (1 - f)P_m + fP_p, \quad (93)$$

where P_{avg} , P_m , and P_p are the average polarization vectors of the composite medium, the matrix and the precipitates, respectively. From Eqs. (89), (92), and (93) the average complex dielectric function ϵ_{avg} of the composite medium is obtained as

$$\epsilon_{\text{avg}} = 1 + \frac{(1 - f)(\epsilon_m - 1) + f(\epsilon_p - 1)g}{(1 - f) + fg}. \quad (94)$$

Then, the absorption coefficient α can easily be calculated as

$$\alpha = \frac{\text{Im } \epsilon_{\text{avg}}}{\text{Re } n_{\text{avg}}} 2\pi\bar{\nu}, \quad (95)$$

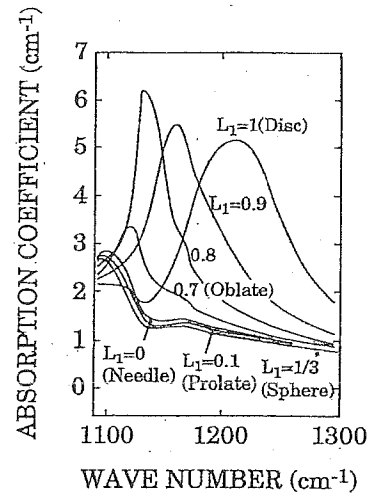


FIG. 65. Calculated infrared-absorption spectra of silicon substrates with 50 ppm volume of small SiO_2 particles of various shapes (from Ref. 339).

where n_{avg} is the average complex index of refraction calculated from ϵ_{avg} ($n = \sqrt{\epsilon}$) and $\bar{\nu}$ is the wave number.

Figure 65 shows the absorption coefficients calculated from Eq. (95) of 50 ppm of SiO_2 precipitates embedded in the silicon sample, under the hypothesis of different precipitate shapes.³³⁹ The curves are labeled using the values of the depolarization factor L_1 , i.e., with $L_1 = 1$ (disk), $L_1 = 0.9, 0.8, 0.7, 1/3$ (sphere), 0.1 and 0 (needle). The results of Fig. 65 were obtained considering the refractive index of silicon equal to 3.35 and the extinction coefficient to $2.5 \times 10^{-5} \bar{\nu}^{-3.13}$ ($\bar{\nu}$ in cm^{-1}) and ϵ_p taken from the literature SiO_2 optical functions.³⁴²

It is interesting to note that the depolarization factors $L_1 = 1$ and $L_2 = L_3 = 0$ correspond to thin plates of all shapes and, in particular, to the disk shape. This last morphology is typical of oxide precipitates in silicon after sample annealing at intermediate temperatures (see Sec. III C). Moreover, the frequency of the experimentally observed absorption band at about 1230 cm^{-1} appears reasonably close to 1215 cm^{-1} , which is the one calculated for disks. Hu³³⁹ assigned the 1230 cm^{-1} band to the longitudinal-optical (LO) mode of SiO_2 composing the precipitates, suggesting that LO mode, usually IR inactive in bulk materials, can be detected in particular system such as the disk-shaped precipitates in silicon. Figure 65 shows that the 1215 cm^{-1} band is absent in the calculated spectra of spherical SiO_2 particles embedded in silicon. In this case a less-pronounced peak at about 1095 cm^{-1} and a very weak peak at 1170 cm^{-1} show up, attributed by Hu to transverse optical (TO) mode and TO+LO mode, respectively. Finally, it is worth noting that no information comes from the reported analysis concerning the structure, crystalline or amorphous, of the precipitates.

Shimura and co-workers²⁹¹ investigated the relation between carbon atoms in substitutional positions and oxygen precipitation in Cz silicon crystals on the basis of a detailed analysis of the 1225 and 1124 cm^{-1} absorption bands related to SiO_x precipitates.

A very interesting comparison between IR spectra and

microdefects in bulk Cz silicon wafers subjected to single-step isothermal, two-step (low-high and high-high), and three-step (high-low-high) annealing was performed by Kung.³⁴³ In the absorption spectra of the single-step-annealed samples a broad peak at 1230 cm^{-1} is observed, becoming very strong in the spectra of three-step-annealed samples where also a new band at 1125 cm^{-1} is present. After the low-high two-step annealing no absorption bands in the range from 1100 to 1300 cm^{-1} were observed. After the high-high two-step annealing the spectra are very similar to those of single-step-annealed samples, but present a significantly lower peak amplitude. According to Hu³³⁹ the appearance of a sharp peak at 1230 cm^{-1} in the spectra of samples subjected to a three-step annealing reveals the presence of tiny platelet-shaped precipitates. The band at 1125 cm^{-1} in the same spectra is attributed to thicker platelets. After the single-step annealing platelet precipitates are also present, but their density in the samples is lower with respect to the density in three-step-annealed samples. Moreover, many precipitates are tangled with dislocations and do not have exactly the platelet shape. Therefore, the 1230 cm^{-1} absorption peak detected in the spectra of the single-step-annealed samples is not as sharp and intense as in the spectra of three-step-annealed samples. In the two-step annealed samples no platelet particles are observed and this clarifies why the absorption band at 1230 cm^{-1} is absent in the corresponding spectra.

IR absorption was also successfully applied, in addition to other techniques, to investigate the effect of electron irradiation on oxygen precipitation in silicon samples annealed at 900°C for up to 444 h, after the irradiation by a 2 MeV beam with doses ranging from 10^{15} to 10^{18} cm^{-2} .³¹⁷ Two kinds of defects were formed by irradiation in the silicon samples, i.e., vacancy-oxygen centers and vacancy-dioxygen centers. In all the samples an enhanced oxygen precipitation rate was detected; in the samples with the first kind of centers it was only a transient process related to a dose-dependent decreasing of the nucleation time (see Sec. III A). On the contrary, in the samples with vacancy-dioxygen centers the enhancement of precipitation is a more stable phenomenon, attributed to the fact that such defects act as nuclei for precipitation, although quite inefficient. The different nucleation times observed for the different IR-absorption bands confirm their origin from differently shaped precipitates.

An oxygen precipitation enhancement was also observed³⁴⁴ in FZ silicon samples ($C_{\text{ox}}=1.8\times 10^{17}\text{ atoms/cm}^3$) irradiated with thermal neutron doses of 2.9×10^{17} and $1.13\times 10^{18}\text{ neutrons/cm}^2$. After 30 min annealing the IR spectra of all the samples treated at temperatures higher than 600°C evidenced the typical absorption band due to SiO_x precipitates. The neutron-irradiated silicon samples present a lot of vacancy-type defects which probably act as precipitation nuclei also when the interstitial oxygen concentration is very low, as in FZ samples.

Recently, Borghesi *et al.*³⁴⁵ showed evidence of oxygen precipitation in Cz silicon samples annealed at 1100°C for only 80 min, while the usual precipitation annealing takes several hours. This was made possible by the development of

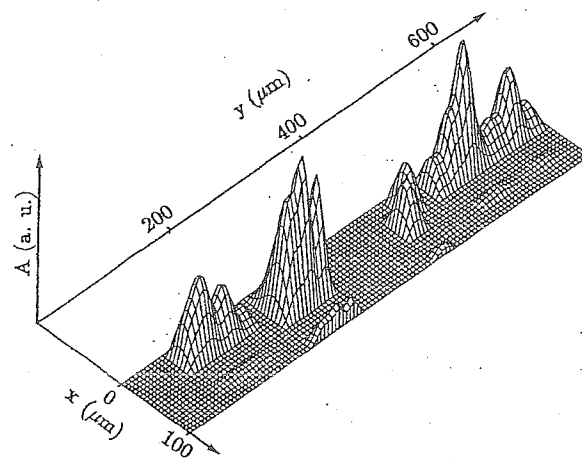


FIG. 66. Map of absorbance values at 1230 cm^{-1} as a function of the position where the spectra were taken on the sample surface (xy plane) (from Ref. 348).

a new high-spatial-resolution technique,³⁴⁶ which allows one to perform IR-absorption measurements on sample regions as small as $20\text{ }\mu\text{m}$ in diameter. Spatial resolution is higher than that used in previous microscopic IR studies,³⁴⁷ and a deeper analysis of the results can be performed, thus obtaining more information about the characteristics of SiO_x precipitates in silicon. Such a high-spatial-resolution technique applied to oxide precipitates detection gives the following two advantages. First, by performing several series of measurements on a high number of adjacent spots it is possible to draw a map of IR absorption at 1230 cm^{-1} , i.e., a map of discoidal precipitates present in the samples.³⁴⁸ In this way, the inhomogeneous precipitate distribution within the samples was detected, as shown in Fig. 66, where the absorbance values at 1230 cm^{-1} are reported as a function of the spot coordinates on the sample surface where the corresponding spectra were collected. Second, a very small average concentration of discoidal SiO_x precipitates can be re-

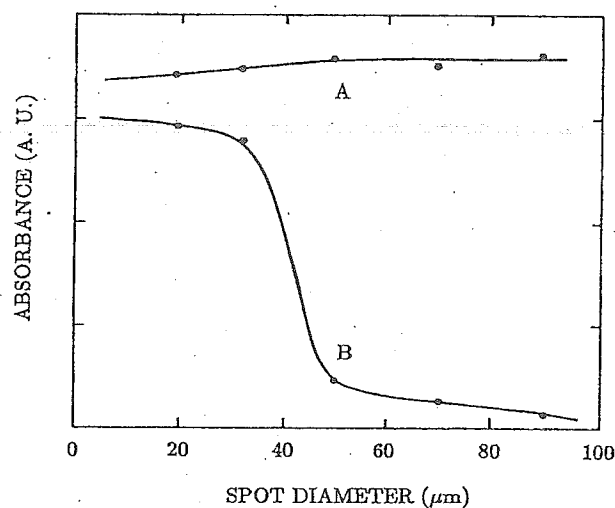


FIG. 67. Intensity of 1107 and 1230 cm^{-1} absorption bands (curve A and B, respectively) in one particular site as a function of the spot diameter used for the measurements (from Ref. 345).

vealed when using spot diameters small with respect to the standard dimensions (~ 1 cm). This was demonstrated by collecting several IR spectra at the same position on the sample using different spot sizes. For a spot diameter from 20 to 50 μm the absorption band at 1230 cm^{-1} was detected (curve B), whereas the same band is no longer observable when the spot grows larger, as shown in Fig. 67. At the same time, the 1107 cm^{-1} band intensity (curve A) remained constant, indicating a homogeneous distribution of the interstitial oxygen atoms. This has been interpreted as due to the fact that with large spots the sample volume investigated during the measurements is so large that the concentration of precipitates over all this volume decreases below the IR detection limit. Such a behavior can be related to the inhomogeneous distribution of precipitates in as-grown samples or after short annealing treatments.

Using the same technique, evidence of oxygen precipitation occurring in epitaxial silicon layers was achieved.³⁴⁹ In principle, this should not be possible, because epitaxially deposited silicon layers are oxygen free. As a matter of fact, oxygen has been shown³⁵⁰ to diffuse during epitaxial deposition to about 15–20 μm from the Cz substrate into the epitaxial layer through the detection of the 1107 cm^{-1} absorption band (related to the presence of interstitial oxygen). A summary of high-spatial-resolution IR results concerning both oxygen diffusion into the epitaxial layer and formation of SiO_x precipitates was presented by Pivac *et al.*,³⁵¹ who studied differently doped substrates and epitaxial layers.

A local preferential orientation of the disk-shaped precipitates in the silicon lattice has been deduced^{351,352} from IR measurements performed at different sample orientations with respect to the incident beam, which show a strong dependence of the 1230 cm^{-1} absorption band on orientation. According to the effective medium theory, in fact, only when the electric field of incident radiation is perpendicular to the diskoidal precipitates does absorption at 1230 cm^{-1} occur. Therefore, the detected anisotropy in IR absorption leads us to conclude that the SiO_x particles giving rise to the absorption within the analyzed volume are preferentially oriented.

The orientation effect of the disk-shaped precipitates in silicon on IR absorption has been investigated by some of the authors³⁵³ by comparing effective medium theory results and IR spectra collected with polarized light. Considering the precipitates as disks lying on the (x, y) plane, which is also the plane of incidence during IR-absorption measurements, in the coordinate system of the ellipsoid principal axes the elements of the tensor g [see Eq. (90)] become

$$g_{xx} = g_{yy} = 1, \quad (96)$$

and

$$g_{zz} = \frac{\epsilon_m}{\epsilon_p}. \quad (97)$$

Therefore, Eq. (89) for the cases of light polarized along the different axes leads to different electric field components inside the particles, i.e.,

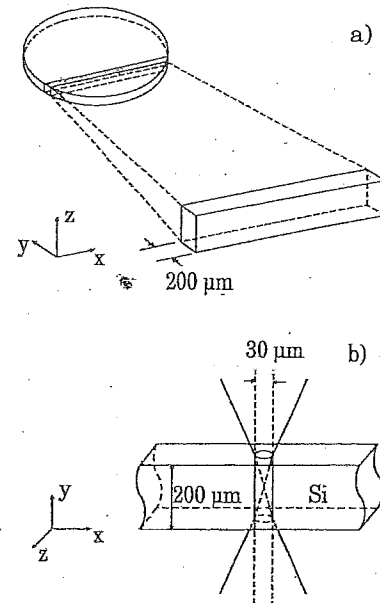


FIG. 68. (a) Picture showing the stripe cutting from the silicon wafer; (b) experimental configuration used for the absorption measurements (from Ref. 353).

$$E_p^x = \begin{pmatrix} 1 & 0 & 0 \\ 0 & 1 & 0 \\ 0 & 0 & \epsilon_m/\epsilon_p \end{pmatrix} \begin{pmatrix} E_m^x \\ 0 \\ 0 \end{pmatrix} = \begin{pmatrix} E_m^x \\ 0 \\ 0 \end{pmatrix}, \quad (98a)$$

$$E_p^y = \begin{pmatrix} 1 & 0 & 0 \\ 0 & 1 & 0 \\ 0 & 0 & \epsilon_m/\epsilon_p \end{pmatrix} \begin{pmatrix} 0 \\ E_m^y \\ 0 \end{pmatrix} = \begin{pmatrix} 0 \\ E_m^y \\ 0 \end{pmatrix}, \quad (98b)$$

and

$$E_p^z = \begin{pmatrix} 1 & 0 & 0 \\ 0 & 1 & 0 \\ 0 & 0 & \epsilon_m/\epsilon_p \end{pmatrix} \begin{pmatrix} 0 \\ 0 \\ E_m^z \end{pmatrix} = \begin{pmatrix} 0 \\ 0 \\ E_m^z(\epsilon_m/\epsilon_p) \end{pmatrix}. \quad (98c)$$

Then, following the same procedure as that illustrated above [see Eqs. (89), (92), and (93)], different expressions for ϵ_{avg} in the case of light polarized along the x (or y) axis or along the z axis can be obtained,

$$\epsilon_{\text{avg}}^x = (1-f)\epsilon_m + f\epsilon_p \quad (99a)$$

and

$$\epsilon_{\text{avg}}^z = \frac{\epsilon_m \epsilon_p}{(1-f)\epsilon_p + f\epsilon_m}. \quad (99b)$$

If the disks (precipitates) are randomly oriented the effective dielectric function of the samples should be an average of expressions (99a) and (99b), and no polarization-dependent IR spectra are expected. On the contrary, in the case of a preferential orientation of the precipitates, spectra collected with different light polarizations must be different, as confirmed with measurements performed on differently oriented samples. Figure 68 shows the sample cutting procedure (a) and the experimental configuration (b) corresponding to the

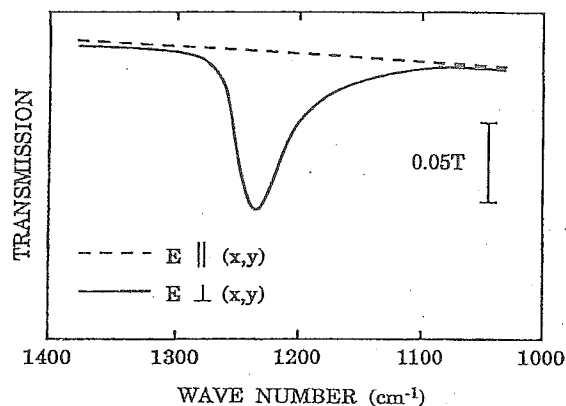


FIG. 69. Transmission spectra calculated on the basis of Eqs. (11), (95), and (99) for a 200- μm -thick sample with 5 ppm volume of oxide precipitates (from Ref. 353).

assumptions made to derive Eqs. (99a) and (99b) and used to collect the transmission spectra, while Fig. 69 shows the results of the calculations in terms of transmission of a 200- μm -thick sample with volume fraction of the precipitates $f=5$ ppm. Figure 70 reports high-spatial-resolution spectra collected with incident light unpolarized [Fig. 70(a)] or polarized [Fig. 70(b)] along the x axis (0°), along the z axis (90°), and along intermediate directions (30° and 60°). From the comparison of the results of Figs. 69 and 70 it is easy to conclude that the precipitates are strongly oriented. In particular, (x,y) plane, corresponding to the (100) crystallographic plane of silicon, is their habit plane. This conclusion is not completely equivalent to the conclusions of the kinetic

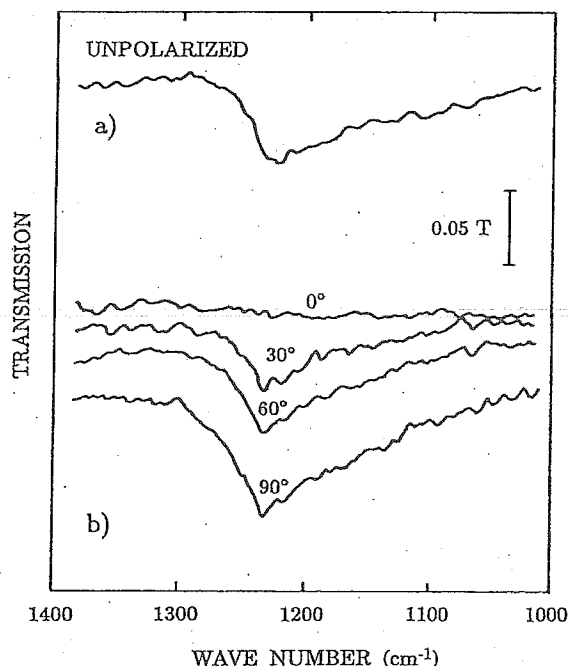


FIG. 70. (a) Relative transmission spectrum taken with unpolarized light; (b) spectra taken on the same position with light polarized along the x axis (0°), the z axis (90°), and two intermediate directions (30° and 60°) (from Ref. 353).

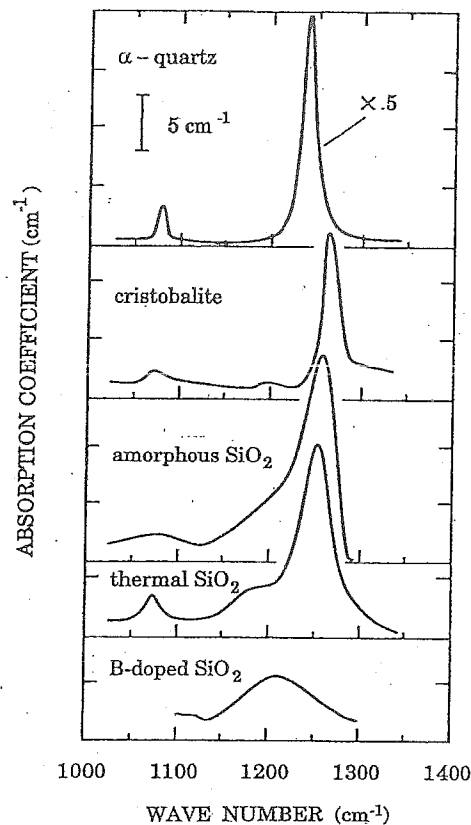


FIG. 71. Absorption coefficient calculated for silicon with 5 ppm volume of oxide precipitates made of different SiO₂ polymorphs (from Ref. 248).

model for the formation of disk-shaped SiO_x precipitates about their orientation (see Sec. III C). Also the kinetic of precipitation predicts the {100} as the habit planes, but it does not distinguish among all the equivalent {100} planes, i.e., the (100), (010), and (001). On the contrary, the IR results by Borghesi *et al.*^{248,249,353} indicate that the precipitates mainly lie on (100) planes, i.e., they are parallel to the wafer surface [all Cz silicon samples were cut from (100)-oriented wafers]. Probably, being (100) planes perpendicular to the ingot growth direction, some anisotropy was introduced in the silicon crystal during Cz growth and this should have influenced precipitate orientation in the as-grown crystal. Such an anisotropy was not removed by the short annealing treatment performed.

An additional advantage due to the high-quality spectra of high-spatial-resolution technique is the possibility of studying the exact peak position and line shape.²⁴⁸ From these analyses information about stoichiometry and structure of the oxide composing the precipitates can be obtained with a consequent quantitative evaluation of precipitate volume fraction more reliable than those previously obtained by standard IR spectroscopy. The absorption coefficient of silicon samples with 5 ppm volume fraction of diskoidal precipitates made of different SiO₂ polymorphs, both crystalline and amorphous, were calculated as a first step, to compare with experimental curves. As shown in Fig. 71, the peak positions found considering the precipitates as made of α -quartz, cristobalite, amorphous, and thermal SiO₂ and

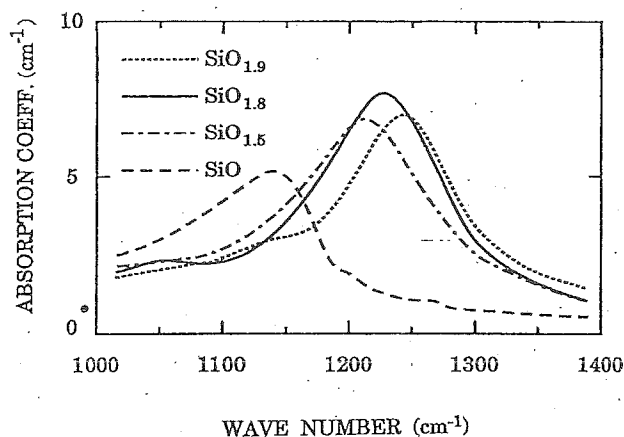


FIG. 72. Absorption coefficient calculated for silicon with 5 ppm volume of oxide precipitates made of different substoichiometric SiO_x (from Ref. 248).

B-doped SiO_2 were all different from the experimental 1230 cm^{-1} , therefore, none of these compounds is presumably the material composing the precipitates. Then, the hypothesis that this type of precipitate is composed of SiO_x with $x < 2$ was checked^{248,249} for the cases $x = 1, 1.5, 1.6, 1.8$, and 1.9 . The spectrum calculated using the optical functions of amorphous $\text{SiO}_{1.8}$ leads to a very good agreement with experimental findings, therefore showing that $x = 1.8$ is the stoichiometric index corresponding to the oxide actually composing the disk-shaped precipitates. In Fig. 72 the spectra calculated for these amorphous substoichiometric oxides are reported for comparison with the experimental ones of Fig. 70(b).

From a comparative study of the line shapes of the experimental and calculated absorption bands, the first one strongly asymmetrical and the second one symmetrical, the authors concluded that probably forms of SiO_x with $x < 1.8$ are also present as oxides composing the particles. In fact, from a decrease of x a decrease of the wave number of the peak position is predicted by the effective medium theory [Eqs. (99a) and (99b)], so that the broad shoulder at low wave number can be interpreted as a contribution from sub-oxides with $x < 1.8$.

Finally, the quantitative evaluation of the actual fraction f occupied by the precipitates has been made from the intensity comparison between experimental and calculated spectra, resulting in $f = 5 \text{ ppm}$ for the precipitates made of $\text{SiO}_{1.8}$. This very low concentration shows once again that the high-spatial-resolution technique is fundamental for detecting the precipitate absorption band in samples annealed for short times. Quantitative evaluation of precipitates made of the other oxides, responsible for the asymmetry of the absorption band, leads³⁵⁴ to even lower f values, such as 2 and 3 ppm for oxides corresponding to $x = 1$ and 1.5 . Nevertheless, some doubts about the validity of the quantitative analysis of IR absorption at 1230 cm^{-1} are raised based on the dependence of the spectra on many parameters. First of all, spectra collected with unpolarized light do not allow any reliable evaluation; moreover, even with polarized light one has to be

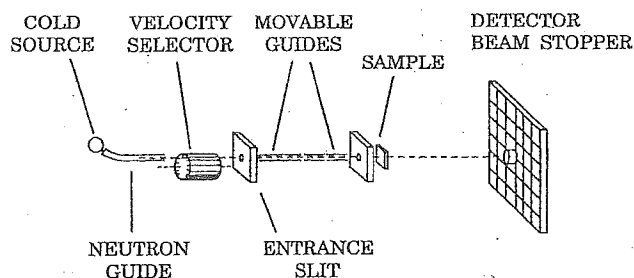


FIG. 73. Scheme of the SANS apparatus at Institut Laue Langevin in Grenoble (from Ref. 244).

sure about the exact polarizer position and the SiO_x stoichiometry.

A detailed discussion of results concerning the possible habit planes for platelet-shaped precipitates as deduced from IR measurements is reported by some of the authors¹³⁸ also for as-received Cz silicon samples (i.e., samples subjected only to the thermal-donor killing treatment prior to the measurements). The hypothesis of oxygen precipitation taking place in such samples, without any annealing, was already proposed,^{113,123,128,355} but this is the first experimental evidence of the presence of disk-shaped precipitates.

An alternative approach to effective medium theory has been recently proposed³⁵⁶ to explain IR results on oxygen precipitation in silicon, based on the Berreman effect.³⁵⁷ All the features of experimental spectra can be justified also following this interpretation. On this basis, for the case of SiO_x disks embedded in silicon the two approaches have been shown to be identical.

Recently, a low-temperature FTIR mapping of oxide precipitates in silicon has been performed.³⁵⁸ While at room temperature the absorption band related to interstitial oxygen is at 1107 cm^{-1} , at low temperature it shifts to 1136 cm^{-1} , making the precipitate absorption band at 1100 cm^{-1} also detectable. Although the kind of precipitates giving rise to the 1100 cm^{-1} absorption band is still unclear, the authors believe that from the height of both 1100 and 1230 cm^{-1} absorption bands a reliable quantitative evaluation of oxide precipitate density in the samples can be performed.

D. Small-angle neutron scattering

SANS is a powerful technique for the study of clusters or precipitates in a material when the mismatch between the neutron-scattering coherence-length of the grains and of the matrix is large enough that scattering at very small angles can be detected. The knowledge of size, density, shape, and crystal orientation is essential in order to give a complete and satisfactory description of phenomena such as oxygen precipitation in silicon. From the analysis of the scattered neutrons it is possible to obtain such a global information in a single experiment, with the additional advantage (with respect to other techniques) that large samples ($> 1 \text{ cm}^2$) can be used, so that the data obtained are representative of the bulk.

In Fig. 73 the spectrometer D11 at the Institut Laue Langevin in Grenoble is schematically reported.²⁴⁴ From the collimated beam of monochromatic neutrons, incident on the

sample, the unscattered neutrons, blocked by a beam stop, are separated from those scattered through small angles, falling on a two-dimensional detector comprising an array of 3808 1×1 cm² active elements. The neutron beams travel in evacuated tubes to minimize the scattering.

The scattered neutrons give rise to successive annular regions about 1 cm wide: The radius of each annular cell corresponds to a scattering vector Q with⁴¹

$$|Q| = \frac{4\pi \sin \theta}{\lambda}, \tag{100}$$

where θ is half of the scattering angle and λ is the wavelength of the incident neutrons. As a general rule, λ is greater than the Bragg cutoff (which in the case of silicon is 6.26 Å, i.e., twice the largest interplanar spacing).

It should be noted that incoherent scattering as well as the contributions from randomly distributed impurity atoms would give rise to negligible or very small isotropic scattering. On such a background, measurable signals can show up due to constructive interference originated by local-density fluctuations if the properties of the material deviate from those which give rise to the just-mentioned background. This takes place for instance with the presence of clusters, microcrystallites, and small aggregates of impurities, having specific characteristics. As for the space resolution, SANS allows one to resolve spatial features in the range 1–100 nm. In other words, this technique is particularly suitable when one has to study properties of space inhomogeneities having a size of that order, and the information should be extracted from the bulk or from a relatively large size volume. Furthermore, the capability of the technique to study low concentrations of defects has been demonstrated.³⁵⁹ Volume fractions down to ~10 ppm have been characterized.

The observed scattering is the Fourier transform of the geometrical shape of the precipitates and is given by²⁵¹

$$\frac{d\sigma}{d\Omega} = \frac{n}{N} \left(\Delta\rho \int_V \exp(i\mathbf{Q}\cdot\mathbf{r}) d^3\mathbf{r} \right)^2, \tag{101}$$

where σ is the scattering cross section, Ω is the solid angle, \mathbf{r} is the real-space vector, n is the number of precipitates per unit volume, N is the number of atoms per unit volume of the host lattice, $\Delta\rho$ is the contrast difference between the precipitate and the matrix, and V is the volume of one precipitate. $d\sigma/d\Omega$ is usually called the absolute differential scattering cross section. After carrying out the experiments it is also possible, with the help of a computer approach to the scattering process, to derive conclusions on shape and orientation of defect aggregates from the symmetry of the scattering pattern. Details on the SANS technique as applied to the study of precipitates in silicon are given in Refs. 41, 244, and 360.

A detailed study of oxygen precipitation in silicon annealed at 750 °C for different times has been performed by Bergholz *et al.*²⁴⁴ using SANS. The results are shown in Fig. 74 which reports the cross section $d\sigma/d\Omega$ as a function of $|Q|$. Open circles and triangles down refer to an untreated sample and shows a low and flat cross section, denoting the absence of precipitates. As the annealing time grows, the Q

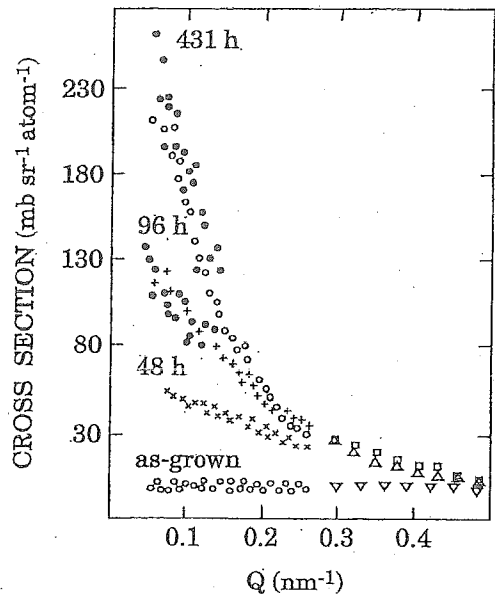


FIG. 74. Scattering cross section as a function of scattering vector for samples as-grown and annealed at 750 °C for different times. The different symbols used for each annealing time refer to different sample-detector distances during the measurements (from Ref. 244).

dependence of the cross section becomes stronger. In the same article it is also possible to find a detailed comparison among SANS, TEM, and IR-absorption results.

The orientation of the precipitates can be inferred from the anisotropy of the detected scattering pattern.²⁵⁰ In principle, the size of the precipitates could be determined from the Fourier transform of the scattering pattern (we recall that the SANS pattern is the Fourier transform of the real defect), but this approach presents some difficulties related to the limited region of the reciprocal space involved.

SANS has been used²⁵¹ to study in detail platelet-shaped precipitates formed in Cz silicon samples treated at 750 °C for different times. From the fourfold symmetry of the scattering images and from the sample orientation with respect to the incident neutron beam it was deduced that the precipi-

TABLE X. Summary of SANS and IR data for the different annealing conditions. The parameter w , the radius of the precipitates r , and the number density of precipitates N are reported (from Ref. 41).

T (°C)	t (h)	w	SANS data		IR data	
			r (Å)	N (cm ⁻³)	r (Å)	N^a (cm ⁻³)
650	2000	^b	32	2.5×10^{14}	30	1.3×10^{14}
700	808	4.5	93	4.3×10^{12}	59	1.8×10^{13}
750	16	^b	29	...	31	2.4×10^{12}
750	72	^b	54	1×10^{13}	64	2.4×10^{12}
750	208	2.0	88	3×10^{12}	95	2.4×10^{12}
750	600	4.3	143	1.2×10^{12}	113	2.4×10^{12}
750	744	6.1	133	1.5×10^{12}	114	2.4×10^{12}
800	808	6.8	146	1.1×10^{12}	196	4.6×10^{11}
800	1000	5.6	153	9.9×10^{11}	196	4.6×10^{11}
850	808	10.7	210	3.8×10^{11}	316	1.1×10^{11}

^aAssumed to be constant.

^bSpherical precipitates.

tates have cubic symmetry and that their short edge is perpendicular to (100) planes. Moreover, the narrow streaks of the pattern indicate that the other dimension of the precipitates is much larger than that along [100] direction, confirming that after the mentioned annealing the precipitates are platelets lying on {100} planes.

Recently, SANS has been demonstrated as a suitable technique also for the study of precipitates in heavily doped crystals,^{287,361} where other analytical methods such as IR-absorption spectroscopy cannot be applied.

An interesting comparison between SANS and IR-absorption results can be performed on the basis of Table X for Cz samples annealed at well specified annealing conditions.⁴¹ The precipitate radius and the number of precipitates per unit volume as determined by the two techniques are listed and show a fairly good agreement. The radius increases and the concentration decreases as the annealing temperature and time increase. This can be related to the fact that increasing the temperature more nuclei redissolve and the others grow to larger dimensions. The parameter w is defined as the ratio between the large and the small edges of the precipitate; for example, for a cube $w=1$, while for a very thin platelet w would become large. The parameter w allows one to evaluate the shape of the precipitates for the different annealing conditions: They are initially spherical, becoming progressively more platelike as the annealing time at 750 °C increases. For long annealing time at temperatures from 700 to 850 °C the precipitates are platelets, while at 650 °C they are spherical even after 2000 h annealing.

E. Optical scattering

Optical scattering is an important aspect of the interaction of electromagnetic waves with a material. Scattering due to the presence of imperfections is detectable with standard techniques and is being used as a method of investigation.³⁶² In particular, when oxide precipitates (with a diameter smaller than the wavelength) are embedded in the silicon crystal lattice, they act as scattering centers and optical scattering can be detected. In this case, using an incident electromagnetic wave in the wavelength range where both silicon and silicon oxide are transparent, i.e., from about 1 to 9 μm , Rayleigh scattering is responsible for the decrease of the intensity of transmitted radiation. Such a decrease is usually described by introducing the absorption coefficient α due to the scattering. In particular, Kaiser¹⁹ obtained the concentration N (cm^{-3}) of the scattering centers (precipitates) having a diameter of about 0.1 μm in Si wafers heat treated at 1000 °C using a radiation wavelength of 1.15 μm from the following relation

$$N = \frac{24\pi^3}{\alpha} \left(\frac{N_0 M}{2\rho A} \right)^2 \left(\frac{n_{\text{ox}}^2 - n_{\text{Si}}^2}{n_{\text{ox}}^2 + 2n_{\text{Si}}^2} \right)^2 \frac{n_{\text{Si}}^4}{\lambda^4}, \quad (102)$$

where N_0 is the number of oxygen atoms per cm^3 present in the precipitates, M is the molar weight of the particle material ($M=60$ for SiO_2), ρ is the density of particle material ($\rho=2.3 \text{ g cm}^{-3}$ for SiO_2), A is Avogadro's number, and n_{ox} and n_{Si} are the refractive indexes of SiO_2 and silicon, respectively.

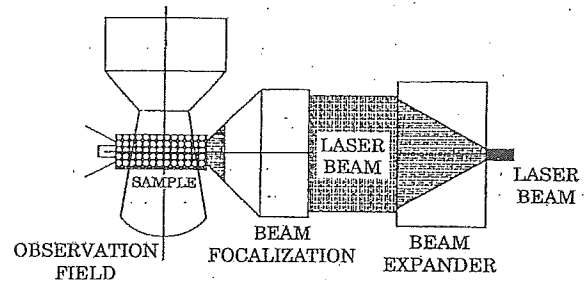


FIG. 75. Experimental setup for LST measurements (from Ref. 372).

Following the same procedure Newman *et al.*¹⁴³ obtained the behavior of N versus temperature, very similar to that obtained from etch-pit measurements. Nevertheless, the N values obtained from Eq. (102) are about three times greater than those found from etching measurements.

1. Laser scanning tomography

The analytical method just illustrated is based on bulk scattering, i.e., information is obtained by measuring the total light scattered by a given sample volume. In the 1960s a new method based on the measurement of the individual particle scattering was proposed to detect imperfections in crystals.³⁶³ This new technique enables one to study particles, inhomogeneity clusters, and dislocations using a scanning ultramicroscope.

It has been subsequently largely improved by Moriya and Ogawa^{364–366} and Ogawa and Nango,³⁶⁷ particularly in the experimental setup. They use as source a 15 mW He-Ne laser ($\lambda=1.15 \mu\text{m}$) focused on a 40- μm -diam spot on the sample and an IR microscope with a TV camera to collect the scattered light at 90° with respect to the incident light. Successive images are digitized by a frame memory and recorded in a dedicated computer. A step-by-step acquisition allows to draw a map of scattering centers. This particular approach, called laser scanning tomography (LST), offers the opportunity to investigate structural defects in semiconductors transparent to IR radiation. In particular, impurity precipitates in silicon caused by fluctuations of growth parameters, dislocations decorated by impurities or undecorated, and lattice defects were detected and made clearly visible.

It is worth noting that the scattered light is proportional to the density N of scattering centers and to their cross section Ω . In the case of an electron trapped in an electronic center with H-like structure, Ω can be written as³⁶⁵

$$\Omega = \frac{1}{2} \frac{r_e^2 \omega^4}{(\omega_0^2 - \omega^2)^2 + \Gamma^2 \omega^2} (1 + \cos^2 2\theta), \quad (103)$$

where r_e , ω_0 and Γ are the classical radius, the resonance frequency, and the damping constant of the electron, respectively; ω is the laser frequency and 2θ is the angle between incident and scattered light.

Although in the IR range the scattered intensity is reduced compared to visible light, the high detectivity and amplification obtained using a computer and a camera allow one to get high-quality images. A comparison between an IR tomograph and a Lang topograph (see Sec. IV F) for a sample

TABLE XI. Precipitate density N obtained by LST on a Si sample after different annealing times t . The measured numbers of particles are considered distributed in a $0.213 \times 10^6 \mu\text{m}^3$ volume (from Ref. 374).

Sample	t (h)	No. of particles	N ($10^9/\text{cm}^3$)
a	2	1589	7
b	5	4306	20
c	10	4977	23
d	25	5861	27

treated for 160 h at 900°C is reported in Ref. 365. The images are very similar but the deduced precipitate densities are different because IR tomography detects only the precipitates present in a slab about $40 \mu\text{m}$ thick (i.e., of the order of the laser spot dimension), while the sample thickness investigated by Lang topography is equal to the thickness of the whole sample (in this example 2 mm).

The application of LST to oxide precipitates in silicon was further developed by Gall *et al.*³⁶⁸⁻³⁷² Their experimental setup is reported in Fig. 75. A Nd:YAG laser ($\lambda=1.06 \mu\text{m}$) is focused on the lateral face of a silicon wafer and the laser beam enters the material as a nearly parallel beam, due to the high refractive index of Si. The scattered light is collected at 90° with respect to the laser beam direction by a TV camera with a PbS-PbO vidicon tube. The silicon wafer is then moved step by step and the corresponding images are stored in a computer to obtain a two-dimensional scattering pattern. In this way an image of the scattering particles lying in a "tomographic plane" parallel to the wafer surface can be obtained. The thickness of the tomographic plane depends on the size of the laser spot. The diameter of the beam, typically $30\text{--}50 \mu\text{m}$, can be reduced down to $5\text{--}10 \mu\text{m}$ for high-resolution images. The method is powerful enough to detect very small defects, with dimensions lower than 100\AA and density up to 10^{12}cm^{-3} .³⁷³

From the analysis of a series of LST images the concentration N of precipitates was studied as a function of annealing time, as reported in Table XI. LST is very useful to detect small nucleation sites and can reveal precipitate densities below the etch-pit detection limit.³⁷⁵

2. Scanning infrared microscopy

A different approach to use light scattering for the study of impurities and defects is the laser scanning microscope, first developed by Wilson and Sheppard³⁷⁶ using a visible laser light focused on the sample surface. The reflected light coming from the mechanically rastered-scanned specimen was collected by a photodiode detector to produce an image of the sample surface.

In the last years a scanning infrared microscope (SIRM) was developed³⁷⁷⁻³⁷⁹ on the basis of the same general principles. SIRM uses an IR laser beam (Nd:YAG at $1.32 \mu\text{m}$) which can be focused not only on the sample surface but also within the sample bulk. The light reflected or transmitted at different angles due to scattering gives dark-field (DF) or bright-field (BF) images, respectively, as shown in Fig. 76. SIRM supplies three-dimensional images of precipitates, voids, localized point defects, and microstrains, in other

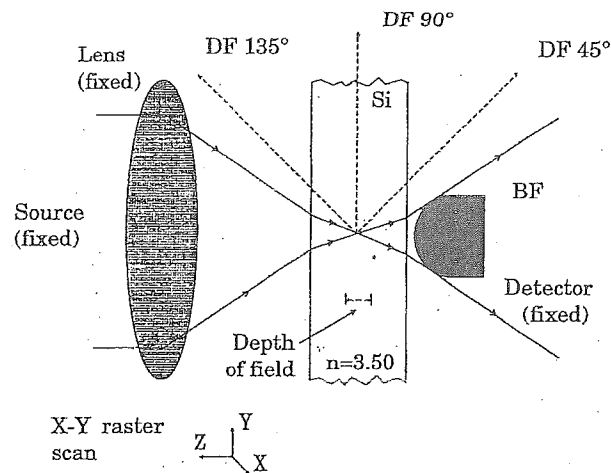


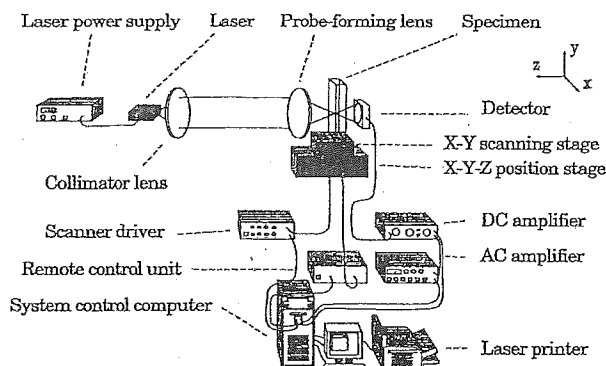
FIG. 76. Scheme of the optic geometries used during SIRM measurements (from Ref. 380).

words of any kind of scatterers. Dislocations and particles decorating the dislocations can also be revealed.

The size of the spot, typically ranging from 1 to $3 \mu\text{m}$, depends on the numerical aperture of the focusing system and on the refractive index of the material under study. For BF images the transmitted light is collected by a Ge photodiode. When a particle moves to the laser focus the incident light is scattered and the photodiode signal is reduced. A dark two-dimensional image of the particles can be drawn by moving the specimen with a high-precision translator along the x and y directions (with fixed z) synchronously with the position of the pixels of a screen. Three-dimensional images can then be obtained performing the same measurements at different depths z and by scanning the xz or yz planes. A similar procedure carried out after placing the photodiode at different angles (such as 45° , 90° , 135° indicated in Fig. 76) provides a three-dimensional image of the light scattered from the particles, which in this case appear bright in a DF image. The instrument is fully automated and computer elaboration is performed to improve image quality. The schematic diagram of SIRM operating in BF mode is shown in Fig. 77. The typical volume analyzed is $1.5 \times 1.5 \times 15 \mu\text{m}^3$ in a standard configuration. The use of a pin hole in front of the detector (confocal mode) allows to improve spatial resolution up to an analyzed volume of about $1 \times 1 \times 7 \mu\text{m}^3$.^{380,381}

Images collected with polarized light allow one to determine the Burgers vector of dislocations present in the sample. SIRM can be used for particle densities of about $10^6\text{--}10^9 \text{cm}^{-3}$ and a single particle down to 30nm in size can be detected. A summary of the SIRM operating modes and mechanisms producing the contrast and information obtainable are reported in Fig. 78.

Images in BF and DF taken from a (011) cross section of a Cz Si wafer heat treated to grow oxide particles in the bulk of the wafer and to obtain a denuded zone have been analyzed in Ref. 380 and are shown in Fig. 79. Single particles are detected in the BF image as dark spots and in the DF image as bright spots. Moreover, the presence of a denuded zone in the surface region where the density of particles is very low is observed. Quantitative data of precipitate density



are obtained by counting the number of spots present in the volume analyzed. The values obtained at different depths from the analysis of narrow stripes parallel to the wafer surface is reported in the lower profile of Fig. 80. This profile clearly shows the presence of the denuded zone, which is about 40 μm thick, followed by a region of about the same thickness in which particle density progressively increases from below the detection limit (about 10^6 cm^{-3}) to the bulk value ($1.5 \times 10^7 \text{ cm}^{-3}$). The upper profile in Fig. 80 is obtained from the analysis of a wafer subjected to the same thermal treatment, except that the time of the first annealing step at 1100 $^{\circ}\text{C}$ was reduced from 16 to 8 h. The lower annealing time of these samples produced only a region with a partially reduced density of particles (extended to about 60 μm from the surface) and the denuded zone is not completely evident.

F. X-ray topography

FIG. 78. Summary of SIRM operating modes and information obtainable (from Ref. 380).

FIG. 79. BF and DF SIRM images of a (011) cross section of a silicon wafer heat treated to grow oxide precipitates in the bulk, creating a denuded zone (from Ref. 380).

FIG. 80. Profiles of precipitate density along the thickness for a sample annealed at 1100 °C for 16 h, at 800 °C for 8 h, and at 1100 °C for 16 h (lower profile) and one subjected to the same thermal cycle, with a shorter (8 h) first step (upper profile) (from Ref. 380).

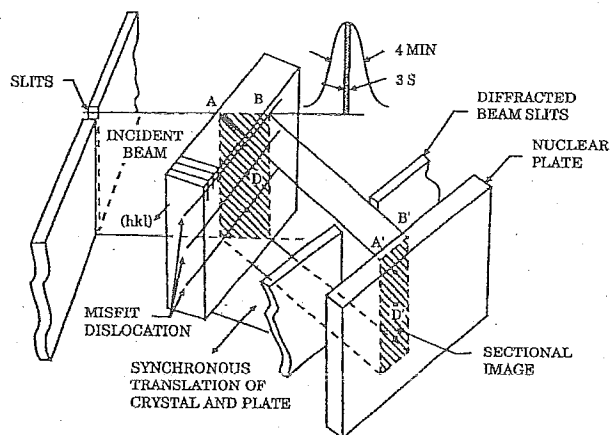


FIG. 81. Schematic representation of the defect imaging process by Lang x-ray topography (from Ref. 319).

where λ is the x-ray wavelength, d is the distance between the diffracting crystal planes and θ_B is the angle between scattered beam and diffracting planes (Bragg angle).

Basically, x-ray topography experiments can be carried out in two modes of operation, i.e., transmission and reflection.

1. Transmission topography

Transmission x-ray topography is usually performed with the instrumental setup designed by Lang in 1958.³⁸⁶⁻³⁸⁸ The Lang camera is schematically represented in Fig. 81.³¹⁹ It provides the possibility to synchronously scan the crystal and the nuclear (photographic) plate using a tall narrow beam of x-rays. Diffracted x rays passing through the crystal give the transmission x-ray topograph. The very sharp incident beam typically consists of a characteristic line whose horizontal divergence is limited to about 4 min of arc by a slit at the end of the collimation tube. The vertical divergence of the incident beam is controlled by using a point source of x-rays and adjusting the divergence between source and sample. The crystal under study is usually oriented so that a set of lattice planes (hkl) fulfills the Bragg equation. In this way, as shown in Fig. 81, a sectional image of the crystal lattice is collected at the plate. The diffracted beam coming out from the back of the sample passes through a slit which prevents the transmitted beam and fluorescent radiation from influencing the photographic emulsion. As shown in Fig. 81, the emulsion is exposed to the beam A'B' yielding an image of a cross section of the crystal at the position AB.

It is important to note that Bragg condition does not apply simultaneously to the perfect regions of the sample and to the regions where the lattice spacing or orientation locally varies due to crystal defects. Consequently, the diffracted x-ray intensity recorded on the photographic plate changes in correspondence of the points where irregularities of the crystal lattice are present. For example, any defect or strain center located at position D within the bulk creates intensity variations that are observed as a contrast at position D' on the photographic plate. This yields a section topographic image that can be used to locate the position of the imperfection

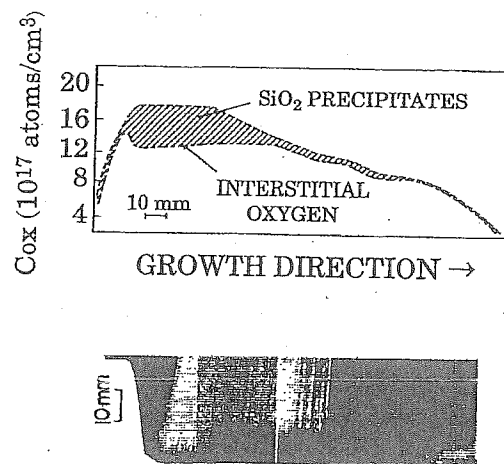


FIG. 82. Comparison between infrared determination of interstitial and precipitated oxygen (upper figure) and a sectional x-ray topograph (lower figure) of a silicon crystal (from Ref. 392).

within the bulk of the crystal. By activating a scanning mechanism, an image of the entire sample can be obtained. An automatic control is generally used to maintain the Bragg condition during the scanning process. X-ray topography was also developed for *in situ* measurements³⁸⁹ to follow step-by-step dynamical processes.

Due to its peculiarity, x-ray topography is widely used in the studies of oxygen precipitation after heat treatments of silicon crystals.^{269,390,391} The opportunity of x-ray topography to obtain images of large sample sections is very useful in the study of oxide precipitate distribution both in wafers and in ingot sections. For example, Fig. 82 shows a comparison between oxygen precipitation in a 180-mm-long silicon single crystal produced by high-oxygen and low-growth-rate pulling, as detected by IR-absorption bands at 1107 and 1230 cm^{-1} (related to interstitial and precipitated oxygen, respectively), and a sectional x-ray topograph of the same crystal, as reported by Abe.³⁹² The interstitial and precipitated oxy-

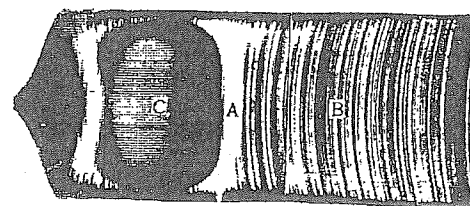
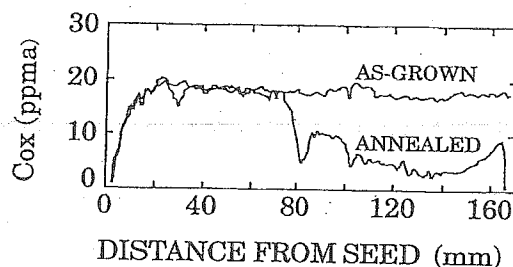


FIG. 83. Interstitial oxygen profile along a longitudinal section of a crystal detached from the melt and annealed a 1000 °C for 16 h in Ar (upper figure); x-ray topograph of the same sample (lower figure) (from Ref. 392).



FIG. 84. X-ray topograph of a silicon wafer subjected to a thermal treatment for denuded zone formation (from Ref. 321).

gen concentrations in the as-grown crystal are inhomogeneously distributed along the growth direction.

Nowadays, in standard as-grown single crystals it is very difficult to evidence any defects generated during growth; however, some defects such as oxide precipitates, present in as-grown materials as nuclei or very small particles, become detectable during the heat treatments following the growth. A very interesting example³⁹² is shown in Fig. 83 referring to a longitudinal section of a silicon ingot detached from the melt and heat treated for 16 h at 1000 °C. The lower image in Fig. 83 shows the x-ray topograph and the upper one reports the interstitial oxygen concentration C_{ox} measured by IR spectroscopy at different distances from the seed. For comparison also the C_{ox} in the as-grown crystal is reported. While the O_i distribution in the as-grown material is uniform, after the heat treatment a reduction of interstitial oxygen concentration from point A indicates that in the end side of the crystal oxygen precipitation took place. This is due to the rapid cooling of this part of the crystal from growth temperature to room temperature (caused by the detachment) generating by thermal stress a lot of nucleation sites for oxygen precipitation. The reduction of interstitial oxygen evidenced by IR-absorption measurements corresponds to the white contrast regions in the x-ray topograph.

An x-ray topographic image of a section of a 450- μm -thick silicon wafer after denuded zone formation³²¹ is shown in Fig. 84, where the device (surface) region is evidenced to be precipitate free, while the central region presents a high precipitate density (black dots).

X-ray topography has been useful to Freeland *et al.*³⁹³ to clearly evidence the effect of preheating on oxygen precipitation. They studied dislocation-free Cz crystals containing 8×10^{17} atoms/cm³ of interstitial oxygen and annealed for 8 h at 1200 °C. One of the samples was also subjected to a pre-

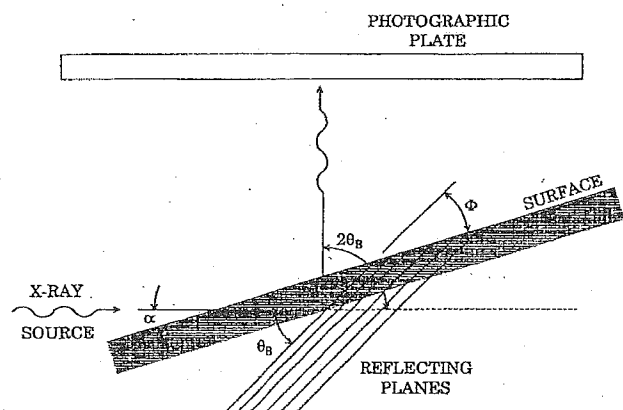


FIG. 85. Scheme of the camera for reflection-mode x-ray topography (from Ref. 319).

heating for 2 h at 700 °C. In the as-grown crystal with no pretreatment no defects are visible after 8 h annealing at 1200 °C, while the crystal which received such a preliminary treatment shows a large number of defects.

2. Reflection topography

Besides the transmission geometry, x-ray topographs can also be obtained by diffracting the x-rays back through the entrance sample surface. This mode is called reflection, Berg-Barrett,^{394,395} or Bragg geometry. Figure 85 schematically illustrates the inherent simplicity of the camera for reflection-mode topography. Operationally, the angle of incidence α should be small for maximum illumination of the sample and minimum interference with the photographic plate, the angle between the incident and diffracted directions $2\theta_B$ should be near 90°. Also, the diffracted x-rays should be absorbed perpendicularly to the emulsion. This minimizes photoelectron track lengths and image distortion in the thick emulsions.

It is important to point out that in the reflection geometry only the first layers of a sample are investigated, typically 2–10 μm and occasionally down to a depth of 50 μm . Therefore, the reflection mode is particularly suitable for the study of epitaxial layers and of material processing problems where surface strain is important.

Reflection topography of semiconductor samples has not been so popular as the transmission mode, where the images are characterized by a better contrast. Nevertheless, there are many situations where the selective imaging of the surface defect structures by reflection topography is advantageous, e.g., when the dislocation density is such that counting dislocation sites is simpler than analyzing overlapping lines.

In the analysis of crystal surfaces by reflection topography a choice of the diffracting plane is an important issue. The penetration depth of x-rays, the magnitude of the distortions in the vicinity of the defects, and the angular range of reflection for regions of perfect crystal, called the Darwin-Prins half-width,³⁹⁶ determine the ability to image dislocations and/or surface strain gradients. Other factors such as geometrical image distortions and diffracted beam intensity must be also evaluated. All these variables are coupled through the (hkl) plane which produces the image. A very useful analysis and compilation of data for all possible (hkl) planes for six semiconductor materials (Si, Ge, GaP, GaAs, InAs, and InSb) has been given by Halliwell, Childs, and O'Hara³⁹⁷ for wafers with $\{100\}$, $\{110\}$, or $\{111\}$ surface orientations. The use of reflection-mode topography for depth analysis is also discussed by Rozgonyi and Miller.³⁸⁵

Double- and triple-crystal reflection topography have also been developed^{384,398} utilizing two (or three) successive Bragg reflections. The first crystal (or the first two) act as a monochromator, while the second one (or the third) is the sample to be studied. These configurations are very sensitive to strain (measurable $\Delta d/d \sim 10^{-8}$) and this reduces the spatial resolution of the technique, since the strain field extends far from the generating crystal defects.

Recently, x-ray topography has also been used to study the distribution and size of oxide precipitates after heat treatment of MCz silicon samples.^{399,400} The low density of pre-

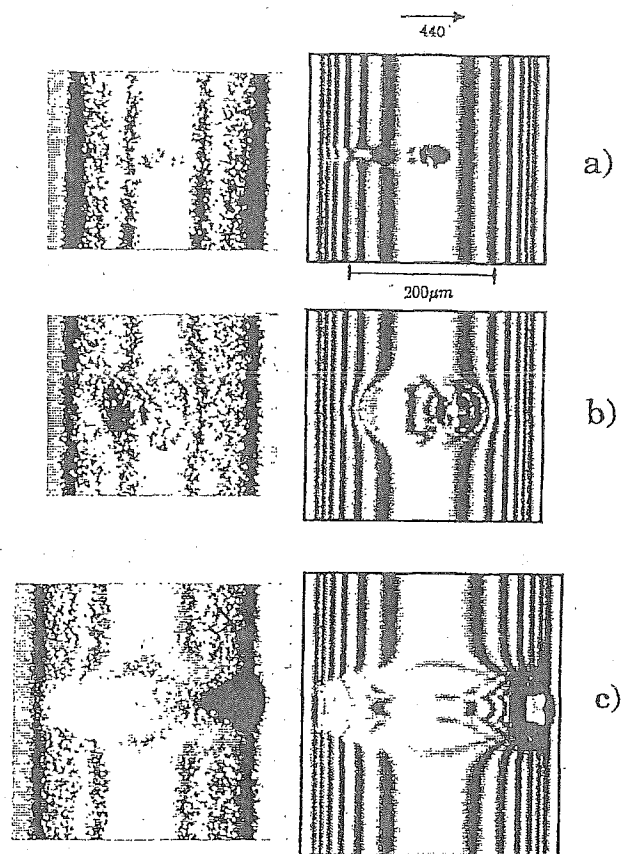


FIG. 86. Experimental (left-hand side) and simulated (right-hand side) images of oxide precipitates in a MCz sample annealed at (a) 450, (b) 650, and (c) 800 °C for 18 h (from Ref. 399).

precipitates present in these samples allows one to study the individual particles. In Ref. 399 images obtained by x-ray topography have been compared with numerical simulations. This procedure allows one to estimate the magnitude and the sense of the strain field generated by precipitation. Three MCz 430- μm -thick samples have been studied after annealing for 18 h at 450, 650, and 800 °C. In Fig. 86 the experimental (left-hand side) and simulated (right-hand side) images of precipitates for the different annealing temperatures are shown. The parameter accounting for the strain effects, determined by matching the illustrated images, increases monotonically with annealing temperature.³⁹⁹

V. TECHNOLOGICAL INTEREST OF OXYGEN PRECIPITATION

The fabrication of high-performance analog and digital integrated circuits (IC) requires rather complex processing sequences involving several high-low temperature treatments in both inert and oxidizing ambients. Each thermal treatment may result in the formation of a lot of defects in the silicon substrate and in the surface region which can have detrimental effects on the IC performances and yield.⁴⁰¹ For example, in the 1 Gbit electrically erasable read-only memory the minimum linewidth is predicted to be about 0.15 μm with a defectivity lower than 1 defect/km. To significantly reduce their defectivity, the devices are generally produced on high-

quality epitaxial films and not directly on the silicon wafer surface, which is sometimes damaged. The perfection of these films depends on several factors such as the cleanliness of the substrates, the deposition parameters, and, especially, the imperfections of the substrate surface.

Since one of the main sources of bulk and surface defects is oxygen precipitation, a direct correlation between device yield reduction and oxygen precipitation has been evidenced. Nevertheless, when oxide precipitates form far from the epi-substrate interface they can have a beneficial effect, acting as gettering centers for metal impurities.

Usually, to reduce the impurity content in the device regions two different gettering techniques are applied. The first one, called external or extrinsic gettering, can be provided by several processes such as HCl oxidation, back-surface implant, phosphorus back-surface diffusion, sand blasting, abrading, laser irradiation, polysilicon deposition, or film stress. The second one is called intrinsic or internal or *in situ* gettering (IG) and is provided by bulk SiO_x precipitates. In particular, for each SiO_x particle formed during precipitation, some Si self-interstitials are produced, due to volume expansion. The so-emitted self-interstitials can form dislocation loops, since a dislocation loop represents an energetically more favorable state than randomly arranged self-interstitials. Moreover, the large volume increase associated to the precipitation is not completely released by the Si self-interstitial emission and each precipitate particle is normally surrounded by a strain field. The dislocation loops, which usually contain an extrinsic stacking fault,⁴⁰² and the strain field surrounding the precipitates provide the IG.

In the surface region the situation is quite different. Indeed, during annealing oxygen diffuses out from the bulk leaving an oxygen-depleted zone close to the surface, called the denuded zone [(DZ), see Sec. V C].^{49,65,401,402} This process can be explained considering that oxygen is a rather fast diffusing element (its diffusion coefficient is more than two orders of magnitude larger than that of other doping impurities in silicon). Out-diffusion reduces the interstitial oxygen concentration and then the chemical driving force for oxygen precipitation.^{166,403,404} As the degree of supersaturation falls the precipitation rate is drastically reduced, reaching zero near the surface region. As a consequence, in this region the defects caused by oxygen precipitation are strongly reduced.⁴⁰⁵

DZ formation and IG are the main procedures used in the IC industry to increase device yield. In fact, the presence of bulk stacking faults or precipitates close to the wafer surface leads to the formation of stacking faults and dislocations, respectively, in the epitaxial layer, i.e., in the region where the devices are created. Therefore, it is very important to find the relation between the defect density in the epitaxial layer and the DZ depth, although this is not straightforward. A careful examination of the region close to the interface between epitaxial layer and substrate shows occasional precipitates also in the DZ area, sometimes extending to all the epitaxial film. This means that the DZ is not homogeneous and its width (or depth) is not constant, therefore the above-mentioned relation can be found only on a statistical basis. In this respect, Rossi *et al.*⁴⁰⁴ suggested an interesting study of

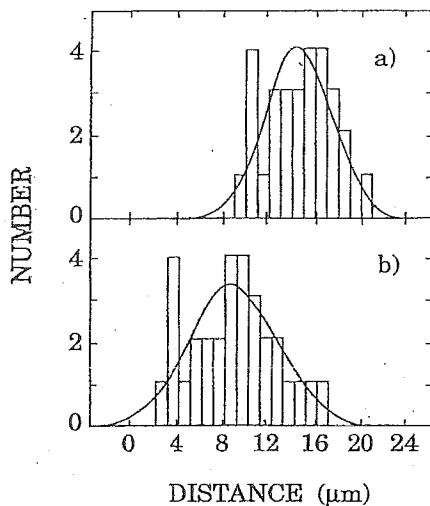


FIG. 87. Histograms of the number of precipitates as a function of distance from epilayer/substrate interface for two different samples (a and b) and normal curve best fit (solid lines) (from Ref. 404).

the relation between surface defects and DZ depth, based on an operational definition of the DZ depth. They proposed the following procedure:

- (i) Determination of defect density on epilayer surface by wet chemical etching;
- (ii) cleavage, angle polishing, and etching of the wafer cross section;
- (iii) measurement of the distance of the precipitates from the epilayer/substrate interface along the entire wafer diameter, obtaining a distribution;
- (iv) construction of the histogram of the number of precipitates versus distance and fitting by a normal curve;
- (v) calculation of the probability of finding defects at the epilayer/substrate interface, given by the area under the normal curve extending in the epilayer region; and
- (vi) plotting of the defect density in the epitaxial layer measured in step (i) versus the probability of finding a defect at the epilayer/substrate interface, deduced in step (v). Two examples of histograms obtained by Rossi *et al.*⁴⁰⁴ are reported in Fig. 87. In the upper figure (a) the histogram and the normal curve fit (solid line) refer to a silicon wafer where the average distance of the first precipitates from the surface is about 14 μm . The standard deviation of the distribution is about 2.8 μm and the probability of finding a defect at the interface is 10^{-4} , corresponding to a measured defect density at the epilayer surface of 4 defects/ cm^2 . Figure 87(b) reports the same results for a different wafer, where the average distance of the first precipitates is only 8 μm (standard deviation 2.8 μm), the probability of finding a defect at the epilayer/substrate interface is 10^{-2} , and the measured defect density on the epilayer surface is 237 defects/ cm^2 . The empirical relation between the probability of finding defects at the epilayer/substrate interface and the defect density on the epilayer surface was deduced by Rossi *et al.*⁴⁰⁴ for different samples and is reported in Fig. 88. The

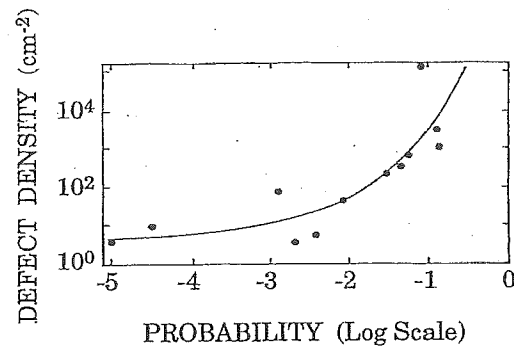


FIG. 88. Experimental data (dots) of epitaxial defect density as a function of the probability of finding a defect at the epilayer/substrate interface. The solid line represents the best fit (from Ref. 404).

figure clearly evidences that materials having a 10% probability of finding defects at the interface show a defect density at the epilayer surface of 10^3 – 10^5 defects/ cm^2 (right-hand side of Fig. 88) and therefore are not suitable for any device fabrication. From the analysis of the curve it is possible to deduce that in order to minimize the defect density on the epilayer surface, the probability of finding a defect at the interface with the substrate must be as small as 10^{-4} . For these probability values no substrate contribution to the epilayer surface defects is found and the defects eventually present have a different origin. Rossi *et al.*⁴⁰⁴ suggest that the probability value 10^{-2} dotted line in Fig. 88 separates the region where the substrate contribution is significant (right-hand side) from that where different factors affect the defect density on the epilayer surface (left-hand side).

A. Influence of precipitation on the mechanical properties of silicon

During wafer heating or cooling a large temperature gradient between the center and the edge of the wafers is created which generates dislocations, when the mechanical stress exceeds the silicon elastic limit (critical shear stress). These dislocations propagate from the edge to the center of the wafer and their generation and mobility strongly depend on the temperature and on the availability of dislocation sources like oxide precipitates.^{321,406} While in nonprecipitated wafers dislocations are mainly generated at the wafer edge, in precipitated wafers they are generated in the center region. Patel and Chaudhury⁴⁰⁷ reported the first study of the critical stress as a function of oxygen precipitation, dislocation density, temperature, and strain rate. More recently an accurate study of warpage, defined as the deviation exhibited by the center line of a wafer from the planar condition, when such a deviation includes both concave and convex regions, was performed by Leroy and Plougonven.⁴⁰⁸ They determined the temperature dependence of the critical shear stress as a function of precipitated oxygen concentration. The data of the critical stress at the center of the wafer are reported in Fig. 89. The figure clearly shows that as the precipitated oxygen increases the temperature marking the critical shear stress decreases. In other words, the higher the oxygen precipita-

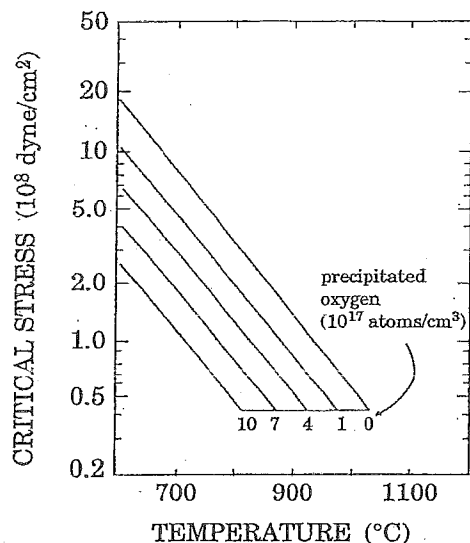


FIG. 89. Critical stress at the center of the wafer as a function of annealing temperature for different precipitated oxygen concentrations (from Ref. 408).

tion the lower the mechanical strength. An important result is that warpage increases with wafer diameter, so that the use of thicker wafers is necessary.

Dislocation generation, especially when it occurs at the center of the wafers, produces warping, therefore influencing the wafer mechanical properties. A study of the influence of oxygen precipitation and dislocations on mechanical properties of heat-treated Cz grown silicon was performed by Yasutake, Umeno, and Kawabe⁴⁰⁹ on samples with $9-10 \times 10^{17}$ atoms/cm³ interstitial oxygen content and with $8-12 \times 10^{16}$ atoms/cm³ (crystal I) or undetectable (crystal II) carbon content. They evidenced that after annealing at 800 °C for 240 h the stress in crystal I does not decrease, probably due to the fact that the very small oxygen clusters (<50 Å) present in this sample do not act as dislocation sources, but as obstacles to their movement. On the other hand, the stress in crystal II is remarkably lower, probably due to the presence of glide

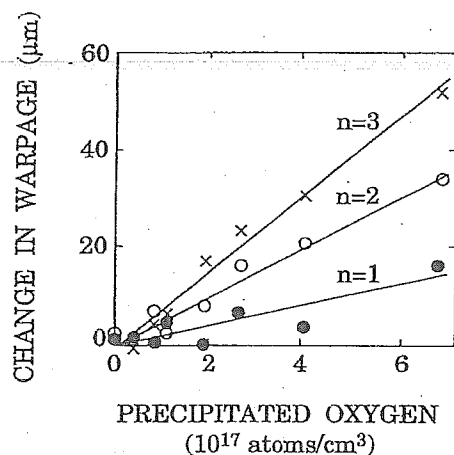


FIG. 90. Change in warpage as a function of precipitated oxygen concentration after n thermal cycles at 1000 °C (from Ref. 410).

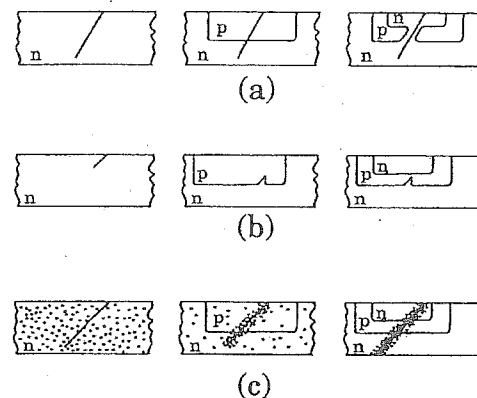


FIG. 91. Scheme of various models proposed to explain emitter-collector shorts: (a) Enhanced diffusion of emitter dopant along the crystal defect; (b) locally retarded base-dopant diffusion; (c) precipitation of fast diffusing impurities (from Ref. 415).

dislocations nucleated on platelike precipitates, present with large densities ($\sim 10^9$ cm⁻³) and dimensions. The direct influence of precipitated oxygen on wafer warpage for different sample heat treatments is illustrated in Fig. 90.⁴¹⁰ The figure refers to the warpage change as a function of precipitated oxygen after n thermal cycles at 1000 °C on samples preannealed at 800 °C. The change in warpage is defined as the difference in the bow along two orthogonally crossed <010> and <001> directions with respect to an untreated wafer. The warpage change increases as precipitated oxygen increases. This confirms that oxide precipitates act as sites for dislocation generation, which results in plastic wafer deformation. The wafer warpage is therefore inversely proportional to interstitial oxygen concentration.⁴¹¹

B. Influence of precipitation on the electrical properties of silicon

Electrical properties of IC devices are strongly influenced by the presence of defects like those induced by oxygen precipitation in crystalline silicon. For example, leakage currents, which increase in presence of oxide precipitates, are responsible for device degradation. In particular, they increase the current in reverse-biased $p-n$ junctions, reduce refresh time in dynamic random access memories (RAM), and are responsible for the large collector-emitter current in bipolar transistors when the base terminal is open. The leakage current is related to different types of dislocations and to stacking faults, both intrinsic and extrinsic,⁴¹²⁻⁴¹⁴ originating from oxide precipitates. These defects strongly affect the device yield being present in the active regions of the wafers (where the devices are located), both at the wafer surface and in the epitaxial layer. For example, in shallow junction transistors, emitter-collector shorts (pipes) increase the leakage current and constitute the dominant failure mechanism. Several factors have been proposed as responsible for the formation of pipes and are schematically illustrated in Fig. 91.⁴¹⁵

- (i) The enhanced diffusion of emitter dopant along the crystal defects [Fig. 91(a)];

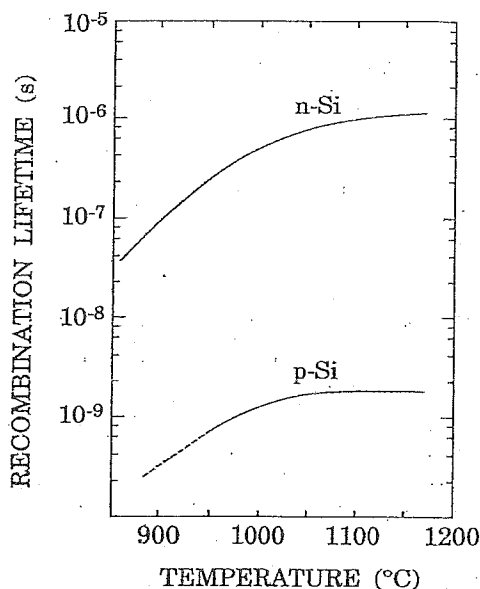


FIG. 92. Recombination lifetime as a function of the second-annealing temperature for *n*- and *p*-type silicon (from Ref. 423).

- (ii) the locally retarded base-dopant diffusion [Fig. 91(b)]; and
- (iii) the precipitation of fast diffusing impurities on crystal defects [Fig. 91(c)].

At the present time, the model involving factor (i) proposed by Miller⁴¹² is accepted to a larger extent, although many questions remain still unsolved about the physical mechanisms involved.

It was found that the formation of SiO_x precipitates within the bulk of Cz wafers affects both the recombination and the generation lifetimes.⁴¹⁶ This has been found by using various techniques, such as the pulsed MOS capacitor method,^{417–419} the diode recovery method,⁴²⁰ the photoconductive method,⁴²¹ the surface photovoltage method,⁴¹⁸ and the measurement of the diode leakage current.⁴²² Nevertheless, it is not yet clearly established what causes the lifetime degradation, and questions on the following points are still open: The dominant source for lifetime degradation (precipitates, secondary defects such as dislocation loops or stacking faults, point defects); the relation of the carrier lifetime to the density and the size of precipitates and to the Si/precipitate interface; the differences and similarities between the known Si/ SiO_2 interface and the Si/precipitate interface.

Variation of the recombination lifetime in Cz silicon with the temperature of the second annealing in a two-step anneal sequence as determined experimentally⁴²³ for both *p*- and *n*-type bulk silicon is given in Fig. 92. Data concerning samples subjected to different heat treatments fit well on the curves. From DLTS measurements Hwang and Schroder⁴²³ concluded that Si/precipitate interface states are the dominant recombination centers; responsible for the lifetime degradation. They developed a model to explain the difference between *p*- and *n*-type materials, based on the existence of fixed positive charges in the oxide near the Si/precipitate interface.

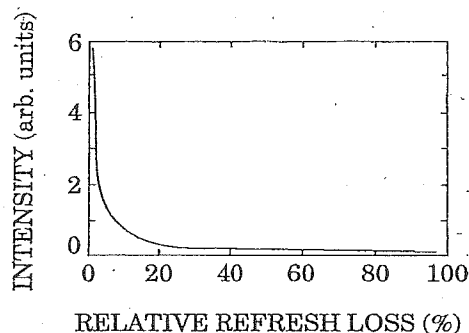


FIG. 93. Relative diffracted x-ray intensity as a function of relative refresh loss in a MOS dynamic RAM cell (from Ref. 164).

Kim, Kim, and Min⁴²⁴ also studied the effects of electron traps on generation lifetime in heat-treated *n*-type Cz wafers by DLTS. They found that the volume defects induced by oxygen precipitation are related to the formation of deep traps. Furthermore, they found a relation between the increase of generation lifetime in MOS devices caused by Dz formation and the decrease of defects due to the aggregation of the deep traps created by oxygen, vacancies, and dislocation loops in the region where oxygen precipitates.

It has been reported⁴²⁵ that in MCz crystals with 10 ppm of interstitial oxygen smaller amounts of oxide precipitates, dislocation loops, and stacking faults are produced after heat treatments as compared to conventional Cz crystals. Furthermore, it has been also shown⁴²⁶ that MCz crystals have a higher minority-carrier generation lifetime than FZ and Cz crystals. Most of the earlier studies^{426,427} showing that oxygen influences recombination lifetime were performed on processed material, the process conditions, process-induced impurities, and defects being possible causes of erroneous conclusions about the role of oxygen. To eliminate these problems, Pang and Rohatgi⁴²⁸ measured the lifetime before and after processing on wafers cut from different sections of the same MCz-grown ingot, therefore having different oxygen concentrations. They found that oxygen-related defects formed during crystal growth, such as microprecipitates, lower the lifetime at a moderate injection level. On the contrary, these defects do not affect the lifetime associated with defect-related extrinsic recombination mechanisms in high-quality MCz with oxygen concentration <10 ppm.

Carrier lifetime in oxidized samples was found to decrease with oxygen concentration at lower as well as at moderate injection levels, while this is not true for as-grown material. The lifetime degradation at lower injection level is attributed to the interaction between process-induced impurities and oxygen.

Bipolar devices containing dislocations and stacking faults in the *p*-*n* junction region exhibit an enhanced reverse current,⁴²⁹ which may reach values up to five orders of magnitude higher with respect to a *p*-*n* junction without defects. An increase of the forward voltage drop⁴³⁰ and a reduced breakdown voltage⁴³¹ were also reported. The minority-carrier lifetime, defined as the mean time spent by excess charge carriers before they recombine to reestablish the ther-

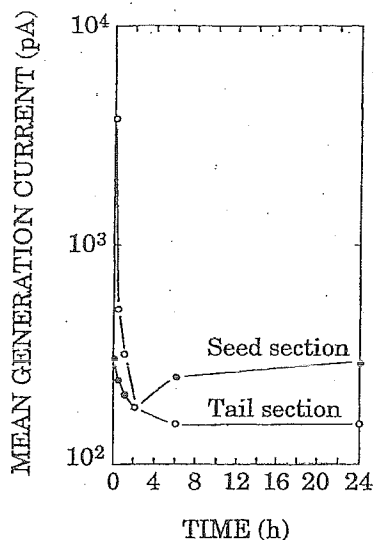


FIG. 94. Mean generation current as a function of 1000 °C annealing time for MOS devices created on wafers cut from the seed-end and the tail-end parts of a Cz silicon crystal (from Ref. 434).

mal equilibrium carrier concentration, is reduced when oxygen precipitation increases⁴³² and electrical characteristics of n^+-p junctions on wafers with high oxygen content (and then high precipitated oxygen content) strongly depends on preheating treatment conditions.⁴³³

The beneficial effects of precipitated oxygen on MOS devices was extensively studied from different points of view. Huff *et al.*,¹⁶⁴ by analyzing the performances of n -channel MOS dynamic RAM, were able to correlate the refresh time to the MOS minority-carrier generation lifetime and to the amount of oxygen precipitated in the bulk of the wafer, as determined by x-ray topography. From the data reported in Fig. 93, where the relative diffracted x-ray intensity versus the relative refresh loss is illustrated, the authors clearly demonstrate that an increased oxygen precipitation in the bulk can be related to a reduced wafer refresh loss, also for wafers supplied by different vendors. The absence of data in the upper right-hand side of the figure is significant and shows that high refresh losses are associated with minimum oxygen precipitation in the bulk. Patrick, Hu, and Westdorp⁴³⁴ reported the beneficial effect of oxide precipitates in reducing the generation currents in MOS capacitors, where they act as gettering sites. The value of the generation current, measured by the method of capacitance relaxation of a pulse-depleted MOS capacitor, strongly depends on the heat treatment of the wafers, i.e., on the oxide precipitate concentration. The value of the mean generation current in wafers obtained from the seed-end and tail-end parts of a silicon crystal as a function of 1000 °C annealing time is reported in Fig. 94, demonstrating that the generation current in MOS capacitors is strongly reduced by the increase of the wafer annealing time, i.e., by the increase of oxygen precipitation. On the contrary, when the precipitation-induced defects lie within the active region, large generation currents result.

Beyer *et al.*⁴³⁵ studied the effect of a preannealing treat-

TABLE XII. Average precipitated oxygen and average MOS leakage current for different vendor wafers after MOS process simulation (from Ref. 435).

Vendor	Anneal process (°C)	Average precipitated oxygen (ppm)	MOS leakage current (pA)
I	1150+900	1.4 ± 0.8	73 ± 48
I	1150	1.6 ± 0.9	43 ± 53
I	900	4.5 ± 2.0	176 ± 126
I	none	4.6 ± 2.5	212 ± 122
II	1150	8.3 ± 2.2	29 ± 45
II	1150	23.4 ± 1.5	35 ± 59
III	1150+900	4.5 ± 1.8	38 ± 50
III	1150	25.2 ± 1.9	38 ± 57

ment on wafers supplied by different vendors subjected to the MOS thermal process sequence on oxygen precipitation and on MOS leakage current. Small variations of the MOS leakage current were detected in the different wafers after an initial 30 min 1150 °C heat treatment in O_2 and HCl. Without preannealing the MOS leakage current is significantly higher as shown in Table XII. During the simulation of MOS process the oxide precipitate concentration is significantly different in wafers supplied by different vendors and, within a given set of wafers coming from the same vendor, also from wafer to wafer. The reduction of MOS leakage current is correlated by Beyer *et al.*⁴³⁵ to the presence of different defect distributions in annealed with respect to unannealed samples, mainly due to the oxygen outdiffusion from the surface and consequently to the formation of a DZ.

C. Denuded zone

As illustrated before, the oxygen presence in silicon can play a positive or a negative role on the devices grown directly on the wafers or on epitaxial layers. Defects induced by oxygen precipitation in the device area during device processing, in particular those decorated by heavy metals, strongly reduce the yield. However, defects present in the bulk of the silicon wafers have a beneficial effect on device performances by acting as gettering sites for contaminating atoms, which otherwise would reach the active regions leading to the reduction of device yield. To be able to successfully use IG in production lines it is necessary to balance the amount of oxygen in different states during the circuit fabrication process. In particular, the amount of precipitated oxygen and the morphology of precipitates and their distribution, related to the depth of the DZ, have a strong influence on the gettering efficiency and therefore on the device yield. The conditions for effective intrinsic gettering by oxide precipitates were studied by Tice, Tan, and Gardner.^{436,437} They found that after wafer annealing at 1150 °C the SiO_x precipitates and the related dislocations are mainly concentrated in the middle of the wafer section, leaving a defect-free region many micrometers thick near the section edges (wafer surface). The effect of this defect distribution is the reduction of the leakage current in p - n junctions.

A new IG technique based on the use of a two-step annealing was proposed by Nagasawa, Matsushita, and

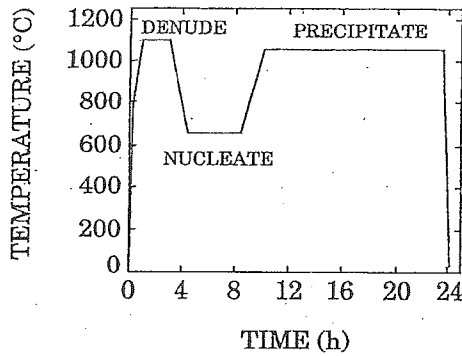


FIG. 95. Typical tristep thermal cycle.

Kishino.⁴³⁸ The first step, at high temperature ($\sim 1000^\circ\text{C}$), is carried out in order to out diffuse interstitial oxygen present near the wafer surface. The second step, at low temperature ($\sim 650^\circ\text{C}$), introduces a high density of microdefects in the inner part of the wafer. This produces a wafer having both a defect-free DZ near the surface and a region rich in gettering sites in the bulk. More recently, the tristep thermal cycle shown in Fig. 95 has been recommended for IG applications⁴³⁹ and is usually applied. The steps are as follows.

The first is a high-temperature step where the oxygen concentration near the surface is lowered due to out-diffusion and where precipitation does not occur. During this step the grown-in nuclei are dissolved. The width of the DZ can be well controlled by the duration and the temperature of this step.⁴⁴⁰

The second is a low-temperature (or preannealing) step, where the nuclei for precipitation form. The duration of this step determines the oxygen precipitation rate observed in the wafers. No measurable precipitation nor diffusion take place during this step.

The third is a precipitation step, frequently corresponding to the fabrication process.

The first step performed at high temperature is the most important one for DZ formation. The simplest model to calculate the out-diffusion of oxygen from the wafer is based on the solution of the one-dimensional diffusion equation,⁴⁴¹

$$\frac{\partial C_{\text{ox}}(x,t)}{\partial t} = D \frac{\partial^2 C_{\text{ox}}(x,t)}{\partial x^2}, \quad (105)$$

where $C_{\text{ox}}(x,t)$ is the interstitial oxygen concentration and D the diffusion coefficient. Considering the following boundary conditions, C_0 being the initial interstitial oxygen concentration and C_s the solid solubility concentration of oxygen at the wafer surface, Eq. (105) gives the solution⁴⁴¹

$$C_{\text{ox}}(x,t) = C_s + (C_0 - C_s) \operatorname{erf}\left(\frac{x}{2\sqrt{Dt}}\right), \quad (106)$$

expressing $C_{\text{ox}}(x,t)$ as a function of the position x with respect to the wafer surface and of time t . Using for C_s and D the values suggested by Andrews,⁴⁴¹ i.e.,

$$C_{\text{ox}}(x,t) = 1.63 \times 10^{21} \exp(-11\,973/T) \text{ (cm}^{-3}\text{)}. \quad (107)$$

and

$$D = 0.17 \exp(-29449/T) \text{ (cm}^2\text{ s}^{-1}\text{)}, \quad (108)$$

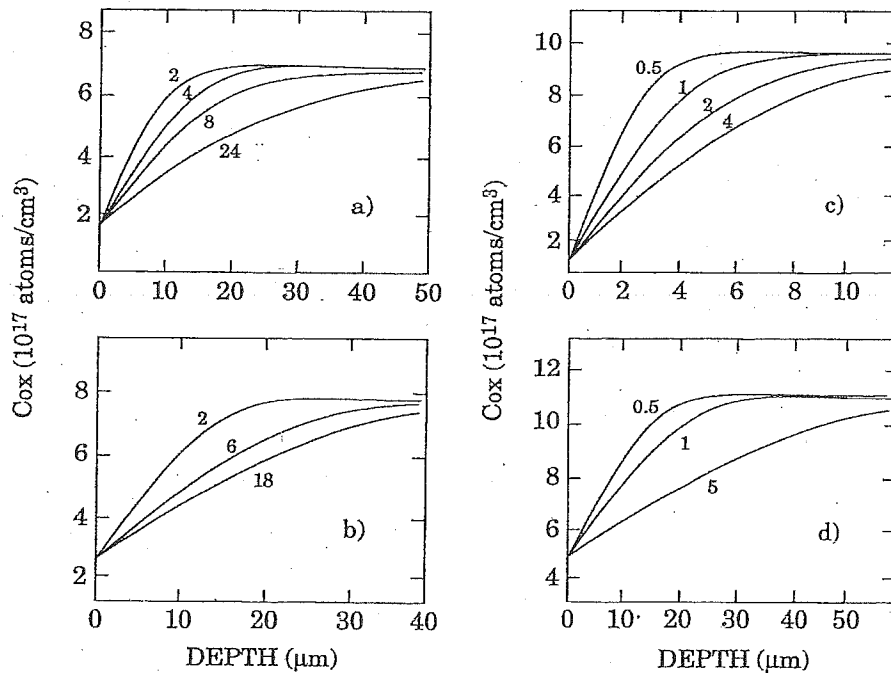


FIG. 96. Interstitial oxygen profiles as a function of depth for different first-step annealing times (marked on the curves in hour units): (a) $C_0 = 7 \times 10^{17}$ atoms/cm³, $T = 1050^\circ\text{C}$; (b) $C_0 = 8 \times 10^{17}$ atoms/cm³, $T = 1100^\circ\text{C}$; (c) $C_0 = 10 \times 10^{17}$ atoms/cm³, $T = 1000^\circ\text{C}$; (d) $C_0 = 11 \times 10^{17}$ atoms/cm³, $T = 1200^\circ\text{C}$ (from Ref. 442).

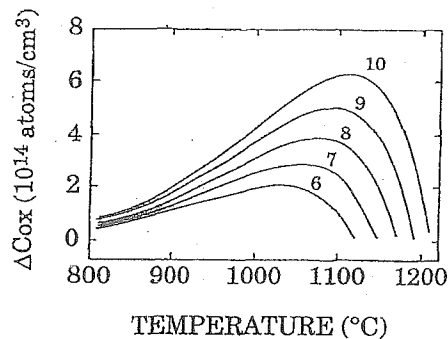


FIG. 97. Total interstitial oxygen removed per cm^2 area from a silicon wafer ΔC_{ox} as a function of temperature of the 5 h first-step annealing for various initial oxygen contents (marked on the curves in 10^{17} atoms/ cm^3 units) (from Ref. 442).

it is possible to obtain a family of different interstitial oxygen concentration profiles for various times of the high-temperature first annealing step. Figures 96(a)–96(d) report the families of interstitial oxygen profiles as a function of the depth x for initial oxygen content of 7, 8, 10, and 11×10^{17} atoms/ cm^3 , respectively, and for different temperatures.⁴⁴² To optimize the first step of the annealing cycle it is necessary to find, for a given initial oxygen concentration, the temperature and annealing time corresponding to the maximum quantity of interstitial oxygen removed from the silicon wafer by out-diffusion. The total quantity Q of oxygen removed from 1 cm^2 of surface area of the wafer can be calculated by integrating the difference between the initial oxygen content C_0 and the oxygen concentration $C_{\text{ox}}(x, t)$ given in Eq. (106),

$$Q = \int_0^\infty [C_0 - C_{\text{ox}}(x, t)] dx$$

$$= (C_0 - C_s) \int_0^\infty \text{erfc}\left(\frac{x}{2\sqrt{Dt}}\right) dx, \quad (109)$$

obtaining

$$Q = 2 \left(\frac{Dt}{\pi} \right)^{1/2} (C_0 - C_s) \quad (\text{cm}^{-2}). \quad (110)$$

A plot of Q as a function of the annealing temperature for 5 h denuding time, calculated from Eq. (110) by Villa and Paciaroni,⁴⁴² is shown in Fig. 97 for various initial interstitial oxygen concentrations. The competition effect between oxygen diffusivity and solubility at different temperatures causes a maximum in Q . From the figure the best temperature for oxygen removal can be easily found for the different values of initial oxygen content.

Temperature and duration of the first-step annealing determine the DZ width (DZW). From experimental data fitting the following general analytical expression for DZW dependence on the duration of the first annealing has been found:^{440,441,443}

$$\text{DZW} = A + B\sqrt{t}, \quad (111)$$

TABLE XIII. Summary of experimental data of denuded zone width (DZW) as a function of first annealing temperature T and time t , nucleation annealing conditions N , precipitation annealing conditions P , and initial interstitial oxygen content C_{ox} .

T (°C)	t (h)	N	P	C_{ox} ($\times 10^{17}$ atoms/ cm^3)	DZW (μm)	Ref.
1100	1	700 °C	1050 °C	11	11	441
	2	24 h	2 h		16	
	4				23	
	8				25	
1100	2	750 °C	1000 °C	8	10	443
	6	6–24 h	8–48 h		17	
	10				24	
	10				24	
1000	0.5	650 °C	1050 °C	10	3	49
	1	4 h	16 h		5	
	2				7	
	4				8	
1100	0.5	650 °C	1050 °C	10	7	49
	1	4 h	16 h		10	
	2				12	
	4				15	
950	2	750 °C	1000 °C	7	8	405
	4	10–20 h	24 h		10	
	8				14	
	24				18	
1000	2	750 °C	1000 °C	7	11	405
	4	10–20 h	24 h		14	
	8				18	
	24				29	
1050	2	750 °C	1000 °C	7	15	405
	4	10–20 h	24 h		22	
	8				31	
	24				44	
1200	0.5	700 °C	1000 °C	11	12	440
	1	16 h	6 h		17	
	5				31	
	5				31	
1180	1	730 °C	1000 °C	9	16	444
	3	8 h	10 h		27	
	5				35	
	5				35	
1180	3	650 °C	1000 °C	9	22	444
		8 h	10 h			
1180	3	800 °C	1000 °C	9	~28	444
		8 h	10 h			
1180	5	730 °C	1000 °C	8	36	444
		8 h	10 h			
1000	5	730 °C	1000 °C	8	25	444
		2–16 h	~5 h			

where A and B are constants. A summary of experimental data of DZW as a function of different thermal treatments is reported in Table XIII.⁴⁴⁴

The second step is the most important one for the IG and has to be performed at low temperature (650–950 °C) before device fabrication. The high efficiency of this low-temperature annealing in generating the precipitation nuclei is clearly evident from the dependence of the nucleation rate J on the degree of supersaturation σ .⁴⁴⁵ Considering the mole fraction of interstitial oxygen in the silicon crystal $X_{\text{ox}} = N_{\text{ox}}/(N_{\text{ox}} + N_{\text{Si}})$, where N_{ox} is the number of oxygen moles dissolved in a silicon wafer of N_{Si} moles, and the mole fraction corresponding to saturation X_{ox}^* , σ is defined as

$$\sigma = \frac{X_{\text{ox}}}{X_{\text{ox}}^*} - 1. \quad (112)$$

$$J = K\sigma^\gamma, \quad (113)$$

where K is a constant depending on the thermodynamic conditions of the silicon crystal and γ is a constant related to the number of oxygen atoms included in the nuclei. σ being inversely proportional to the temperature, J becomes higher if the temperature is decreased. At the low temperatures that are adequate for nucleation, no significant oxygen diffusion occurs, since the oxygen diffusion coefficient D is very small. On the contrary, at high temperatures the nucleation rate is negligible ($\sigma=0$), while oxygen diffusion is favored so that the growth of the nuclei previously formed can take place.

A more detailed description of nucleation can be given considering that the nucleation annealing is usually performed for such times that Eq. (30) holds, i.e., the saturation regime has not yet been reached (see Sec. III A and Figs. 19–22 therein). On the basis of this equation and looking at Fig. 19(c), the existence of an optimum temperature range for nucleation can be evidenced. If the interstitial oxygen concentration is varied from 6 to 20×10^{17} atoms/cm³ the optimum nucleation temperature ranges from 650 to 950 °C. In particular, for the C_{ox} of the wafers used for technological applications, typically from 6 to 8.5×10^{17} atoms/cm³, the annealing temperature corresponding to the maximum nucleation rate is between 650 and 800 °C. At lower and higher temperatures the number of generated nuclei is almost negligible.

The third annealing step at high temperature (precipitation annealing) is responsible for the precipitate growth. The nuclei formed during the previous step increase their size with the concomitant growth of oxide precipitates, thus reducing the interstitial oxygen concentration in the surrounding regions of the crystal. The radius of the precipitates strongly depends on the annealing temperature (D is a function of temperature), on the interstitial oxygen content, on the annealing time, and on the precipitation rate $1/\tau$, as discussed above [see Sec. III B and Eq. (76)]. Since the interstitial oxygen concentration C_{ox} is not constant along the wafer depth due to the first out-diffusion step, the distribution of precipitates is also expected to vary as a function of depth. In particular the region near the surface is expected to be precipitate free, while the bulk region is precipitate rich. The separation between surface and bulk regions is not sharp, but a wide transition layer forms.

The profile of the precipitated oxygen distribution in the silicon wafer as a function of depth can be evaluated on the basis of the interstitial oxygen depth profile $C_{ox}(x)$ obtained during the outdiffusion annealing (first step) and taking into account the results illustrated in Sec. III B. Considering Eq. (62) and assuming $Z=0$, Eq. (65) can be rewritten as

$$K = DN^{2/3} \left[\left(\frac{4}{3} \pi \right)^2 \frac{C_0 - C'}{C_p - C'} \right]^{1/3} \quad (114)$$

Given the conditions of the precipitation annealing, all parameters entering Eq. (114) are determined, and N can be evaluated from the relation $N = Jt_{nuc}$. The nucleation rate J is a function of temperature and interstitial oxygen concen-

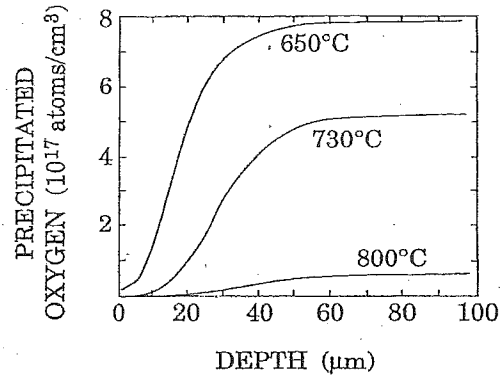


FIG. 98. Precipitated oxygen profiles as a function of depth for different temperatures of the 8 h nucleation annealing. Precipitation annealing is performed at 1000 °C for 10 h (from Ref. 444).

tration, as discussed in Sec. III A, and its value for the nucleation temperature and the C_{ox} of interest can be found from Fig. 19(c). Therefore, from the $C_{ox}(x)$ profile a $K(x)$ profile is obtained. Then, through Eq. (64), the quantity $K(x)t_{prec}$, where t_{prec} is the duration of the precipitation annealing, can be related to the precipitated oxygen concentration $\Delta C_{ox} = 1 - [(C_m - C')/(C_0 - C')]$ [see Fig. 31(b)]. The depth distribution of precipitated oxygen $\Delta C_{ox}(x)$ is therefore determined. As an example, Fig. 98 shows such profiles for silicon crystals subjected to a 10 h precipitation annealing performed at 1000 °C after an 8 h nucleation annealing at 650, 730, or 800 °C. From this figure the importance of the nucleation annealing for the final profile of precipitated oxygen is evident.

D. Influence of precipitation on device yield: Some examples

A detailed study of the yield of bipolar, CMOS, and charge-coupled-device (CCD) devices as a function of oxygen precipitation was performed by Jastrzebski *et al.*¹⁵⁸ Their work clearly shows that IG obtained during typical bipolar, CMOS, and CCD processes can be successfully used to improve the device yield. The best gettering efficiency is achieved for a certain amount of precipitated oxygen. Figure 99 shows the efficiency of internal gettering during the bipo-

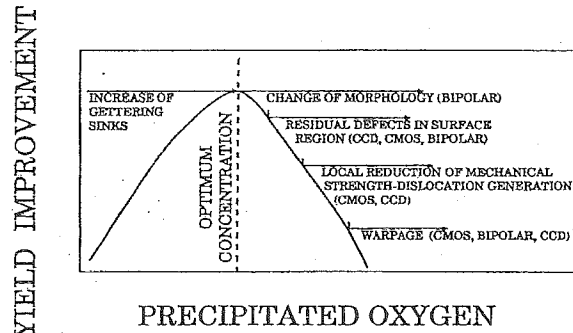


FIG. 99. Efficiency of IG as a function of the amount of precipitated oxygen. The contributions of various mechanisms are indicated (from Ref. 158).

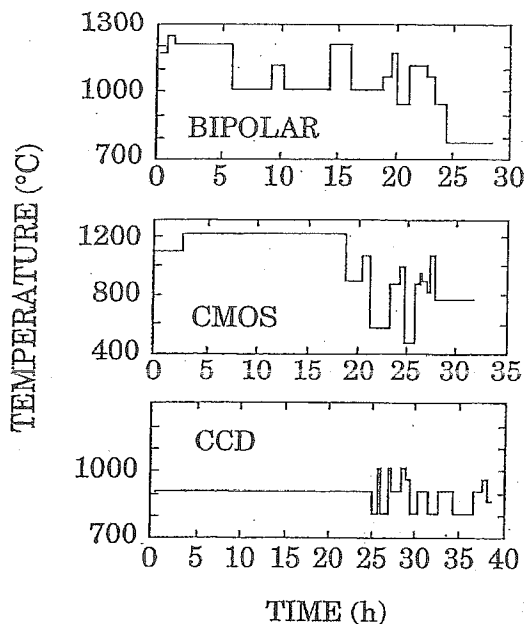


FIG. 100. Thermal cycles used to simulate bipolar, CMOS, and CCD process (from Ref. 158).

lar, CMOS, and CCD processes (simulated by the thermal cycles illustrated in Fig. 100), expressed through the normalized yield as a function of the amount of precipitated oxygen. Initially, the gettering efficiency increases with the amount of precipitated oxygen. This is related to the increase of the number of gettering sites; the decrease of gettering efficiency found for higher amounts of precipitated oxygen is due instead to different phenomena, shown in Fig. 99. In the wafers subjected to the simulated bipolar process the maximum gettering efficiency is reached for 10 ppm of precipitated oxygen, while a decrease of the gettering efficiency is found for higher concentrations, mostly due to the precipitate morphology. In fact, in the case of low oxygen precipitation a low density of large stacking faults (which have been found to be the most efficient gettering centers for bipolar process) was observed. When the precipitated oxygen is more than 10 ppm high densities of small precipitates and stacking faults are usually observed (thus reducing the gettering efficiency).

The CMOS devices are less sensitive to contaminations than bipolar circuits. The optimum concentration of precipitated oxygen for internal gettering is 16 ppm, induced by the high-temperature treatment during CMOS process. Any attempt to increase the concentration of oxide precipitates by wafer preannealing prior to CMOS process results in a yield reduction. The reduction is mainly caused by the increase of residual defects close to the surface, which worsen the device performances. The best yield results are obtained with 28–32 ppm of initial interstitial oxygen concentration. The authors found that wafers with the same initial oxygen content supplied by different vendors show large differences in the amount of precipitated oxygen and attributed this effect to differences in the number of nucleation centers for oxide precipitates.

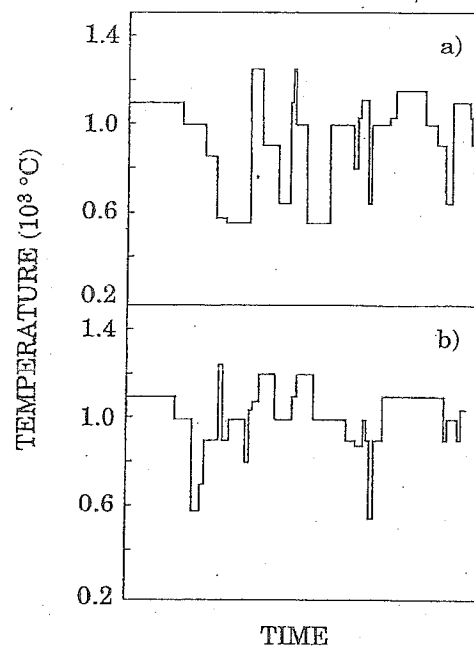


FIG. 101. Thermal cycles used to fabricate the (a) bipolar and (b) DMOS devices studied in Ref. 444.

The performances of CCD are more affected by crystallographic defects than those of bipolar circuits and CMOS. Defects producing a recombination current of a few tenths of pA are observable as white or black spots in the display. The concentration of precipitated oxygen which gives the maximum yield after a CCD process is about 14 ppm. An additional three-step preheating is necessary (1100 °C for 3 h, 650 °C for 10 h, and 1100 °C for 4 h). The wafers that give the best results contain 28–31 ppm of initial interstitial oxygen. The increase of the amount of precipitated oxygen does not improve the yield, due to the presence of residual defects in the surface region, to the local reduction of mechanical strength, to the generation of dislocations, to the wafer warpage, and to slip formation.

Interesting results regarding the correlation between oxygen precipitation in silicon wafer substrates and device yield [for smart power bipolar and double diffused MOS (DMOS) devices] are illustrated by Villa and Paciaroni.⁴⁴² The devices were fabricated on 15- μm -thick epitaxial layers grown on substrates with interstitial oxygen concentration ranging from 6 to 8.5×10^{17} atoms/cm³. The wafers were grouped in five sets, each one covering approximately a 0.5×10^{17} atoms/cm³ C_{ox} range. The thermal cycles used to produce the bipolar and DMOS devices are reported in Figs. 101(a) and 101(b), respectively. The parameters used to evaluate the device yield were I_{CE_0} (i.e., the current circulating between collector and emitter with open basis) for bipolar transistors and I_{DSS} (i.e., the current circulating between drain and short-circuited gate and source) for DMOS devices. I_{CE_0} is required to be less than 10 μA when a 20 V voltage is applied between emitter and collector, while I_{DSS} is required to be less than 10 μA when a 60 V voltage is applied between the drain and the short-circuited gate and

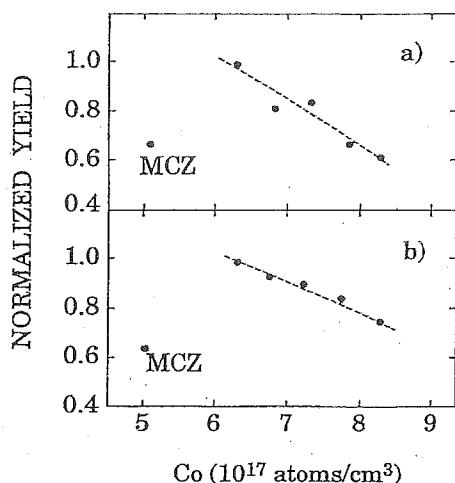


FIG. 102. Normalized yield of (a) bipolar and (b) DMOS devices as a function of initial oxygen content in the substrates. The data labeled MCZ refer to devices created on MCZ substrates (from Ref. 444).

source. The normalized yield for bipolar and DMOS devices fabricated on each group of wafers without any DZ treatment is reported in Figs. 102(a) and 102(b) respectively, as a function of initial C_{ox} . The decrease of the device yield by increasing the interstitial oxygen content of the wafers is clearly evidenced for both types of device. This effect is probably due to the increase of defects such as stacking faults which are generated in the bulk of oxygen-rich wafers and reach the epitaxial layer. There they originate pipes causing device failure.

Using wafers obtained from MCZ ingots as substrates (i.e., wafers with a very low oxygen content, $3\text{--}5 \times 10^{17}$ atoms/cm³), the device yield is strongly reduced (see Fig. 102).⁴⁴⁴ This means that a particular C_{ox} value corresponding to the maximum device yield exists (in this case it is about 6.5×10^{17} atoms/cm³). The reduction of yield for devices fabricated on MCZ wafers is probably due to the large warpage observed in such wafers, related to their low C_{ox} [see Sec. V A]. In fact, warpage is extremely critical in processes requiring a lot of masking and alignment procedures.

ACKNOWLEDGMENTS

This work is dedicated to Professor A. Gigli Berzolari on the occasion of his 74th birthday. We would like to thank R. Falster, J. Vanhellemont, and F. F. Villa for helpful discussions and suggestions, and F. Capasso for encouragement. Many colleagues gave important contributions in different ways to our work and we would especially like to mention T. Abe, S. K. Bains, K. G. Barraclough, A. Bourret, A. J. R. de Kock, P. Gall, P. Gaworzewski, B. O. Kolbesen, Z. J. Laczik, R. C. Newman, S. Pahlke, M. Pedrotti, M. L. Polignano, F. A. Ponce, M. Porri, P. Rossetto, G. A. Rozgonyi, R. J. Stewart, B. K. Tanner, W. A. Tiller, P. Wagner, W. Wijaranakula, and W. Zulehner for their kind collaboration. The technical assistance of M. Moscardini was particularly

appreciated. This work was partially supported by the Progetto finalizzato "Materiali e Dispositivi per Elettronica a Stato Solido" of Consiglio Nazionale delle Ricerche.

- ¹ J. Czochralski, *Z. Phys. Chem.* **92**, 219 (1917).
- ² G. K. Teal and J. B. Little, *Phys. Rev.* **78**, 647 (1950).
- ³ G. K. Teal and E. Bühler, *Phys. Rev.* **87**, 190 (1952).
- ⁴ W. C. Dash, *J. Appl. Phys.* **30**, 459 (1959).
- ⁵ W. Zulehner, in *Semiconductor Silicon 1989*, edited by G. Harbeke and M. J. Schulz (Springer, Heidelberg, 1989), p. 2.
- ⁶ A. Murgai, in *Semiconductor Silicon 1981*, edited by H. R. Huff and R. J. Kriegler (The Electrochemical Society, Pennington, NJ, 1981), p. 113.
- ⁷ K. Hoshikawa, H. Hirata, H. Nakanishi, and K. Ikuta, in *Semiconductor Silicon 1981*, edited by H. R. Huff and R. J. Kriegler (The Electrochemical Society, Pennington, NJ, 1981), p. 101.
- ⁸ T. Carlberr, T. B. King, and A. F. Witt, *J. Electrochem. Soc.* **129**, 189 (1982).
- ⁹ J. W. Moody, in *Semiconductor Silicon 1986*, edited by H. R. Huff, T. Abe, and B. Kolbesen (The Electrochemical Society, Pennington, NJ, 1986), p. 100.
- ¹⁰ A. M. J. G. van Run, U.S. Patent No. 4,474,641 (1984).
- ¹¹ G. Fiegl, *Solid State Technol.* August, 121 (1983).
- ¹² H. A. Chedzey and D. T. J. Hurle, *Nature* **210**, 933 (1966).
- ¹³ H. P. Utech and M. C. Flemings, *J. Appl. Phys.* **37**, 2021 (1970).
- ¹⁴ A. F. Witt, C. J. Herman, and H. C. Gatos, *J. Mater. Sci.* **5**, 822 (1970).
- ¹⁵ T. Suzuki, N. Isawa, Y. Okubo, and K. Hoshi, in *Semiconductor Silicon 1981*, edited by H. R. Huff and R. J. Kriegler (The Electrochemical Society, Pennington, NJ, 1981), p. 90.
- ¹⁶ M. Ohwa, T. Higuchi, E. Toji, M. Watanabe, K. Homma, and S. Takasu, in *Semiconductor Silicon 1986*, edited by H. R. Huff, T. Abe, and B. Kolbesen (The Electrochemical Society, Pennington, NJ, 1986), p. 117.
- ¹⁷ M. Porri and P. Rossetto, in *Symposium on Materials and Devices for Power Electronics*, edited by F. Ferraris (GEDA, Torino, 1991), p. 90.
- ¹⁸ W. Kaiser, P. H. Keck, and C. F. Lange, *Phys. Rev.* **101**, 1264 (1956).
- ¹⁹ W. Kaiser, *Phys. Rev.* **105**, 1751 (1957).
- ²⁰ W. L. Bond and W. Kaiser, *J. Phys. Chem. Solids* **16**, 44 (1960).
- ²¹ J. W. Corbett, R. S. McDonald, and G. D. Watkins, *J. Phys. Chem. Solids* **25**, 873 (1964).
- ²² M. Stavola, *Appl. Phys. Lett.* **44**, 514 (1984).
- ²³ W. C. O'Mara, in *Defects in Silicon*, edited by W. M. Bullis and L. C. Kimerling (The Electrochemical Society, Pennington, NJ, 1983), p. 120.
- ²⁴ D. R. Bosomworth, W. Hayes, A. R. L. Spray, and G. D. Watkins, *Proc. R. Soc. London Ser. A* **317**, 133 (1970).
- ²⁵ Y. Yatsurugi, N. Akiyama, Y. Endo, and T. Nozaki, *J. Electrochem. Soc.* **120**, 975 (1973).
- ²⁶ C. S. Chen, F. Q. Zeng, Y. X. Huang, H. J. Ye, C. M. Hu, and D. K. Schroder, *Appl. Phys. A* **55**, 317 (1992).
- ²⁷ J. A. Burton, P. C. Prim, and W. P. Slichter, *J. Chem. Phys.* **21**, 1987 (1953).
- ²⁸ J. A. Burton, P. C. Prim, and W. P. Slichter, *J. Chem. Phys.* **21**, 1991 (1953).
- ²⁹ H. Kodera, *Jpn. J. Appl. Phys.* **2**, 212 (1963).
- ³⁰ T. Abe, K. Kikuchi, S. Shirai, and S. Muraoka, in *Semiconductor Silicon 1981*, edited by H. R. Huff and R. J. Kriegler (The Electrochemical Society, Pennington, NJ, 1981), p. 54.
- ³¹ R. W. Series and K. G. Barraclough, in *Extended Abstracts Electrochemical Society Fall Meeting* (The Electrochemical Society, Pennington, NJ, 1987), p. 1009.
- ³² H. Harada, T. Itoh, N. Ozawa, and T. Abe, in *VLSI Science and Technology 1985*, edited by W. M. Bullis and S. Broydo (The Electrochemical Society, Pennington, NJ, 1985), p. 526.
- ³³ L. Jastrzebski, *IEEE Trans. Electron Devices* **ED-29**, 475 (1982).
- ³⁴ R. J. Jaccodine and C. W. Pearce, in *Defects in Silicon*, edited by W. M. Bullis and L. C. Kimerling (The Electrochemical Society, Pennington, NJ, 1983), p. 115.
- ³⁵ F. A. Trumbore, *Bell. Syst. Tech. J.* **39**, 205 (1960).
- ³⁶ W. Lin and M. Stavola, *J. Electrochem. Soc.* **132**, 1412 (1985).
- ³⁷ W. Lin and D. W. Hill, *J. Appl. Phys.* **54**, 1082 (1983).
- ³⁸ R. B. Sosman, *Trans. J. Br. Ceram. Soc.* **54**, 655 (1955).
- ³⁹ K. M. Kim and W. E. Langlois, in *Semiconductor Silicon 1990*, edited by H. R. Huff, K. G. Barraclough, and J. Chikawa (The Electrochemical Society, Pennington, NJ, 1990), p. 81.
- ⁴⁰ J. C. Mikkelsen, Jr., in *Oxygen, Carbon, Hydrogen, and Nitrogen in Sili-*

- con, edited by J. C. Mikkelsen, Jr., S. J. Pearton, J. W. Corbett, and S. J. Pennycook (Materials Research Society, Princeton, NJ, 1986), p. 19.
- ⁴¹F. M. Livingston, S. Messoloras, R. C. Newman, B. C. Pike, R. J. Stewart, N. J. Binns, W. P. Brown, and J. G. Wilkes, *J. Phys. C* **17**, 6253 (1984).
- ⁴²S. T. Lee and D. Nichols, *Appl. Phys. Lett.* **47**, 1001 (1985).
- ⁴³S. T. Lee and D. Nichols, in *Oxygen, Carbon, Hydrogen, and Nitrogen in Silicon*, edited by J. C. Mikkelsen, Jr., S. J. Pearton, J. W. Corbett, and S. J. Pennycook (Materials Research Society, Princeton, NJ, 1986), p. 31.
- ⁴⁴R. A. Logan and A. J. Peters, *J. Appl. Phys.* **30**, 1627 (1959).
- ⁴⁵A. R. Bean and R. C. Newman, *J. Phys. Chem. Solids* **32**, 1211 (1971).
- ⁴⁶Y. Itoh and T. Nozaki, *Jpn. J. Appl. Phys.* **24**, 279 (1985).
- ⁴⁷Y. Takano and M. Maki, in *Semiconductor Silicon 1973*, edited by H. R. Huff and R. R. Burgers (The Electrochemical Society, Princeton, NJ, 1973), p. 469.
- ⁴⁸J. Gass, H. H. Müller, H. Stüssi, and S. Schweitzer, *J. Appl. Phys.* **51**, 2030 (1980).
- ⁴⁹R. A. Craven, in *Semiconductor Silicon 1981*, edited by H. R. Huff and R. J. Kriegler (The Electrochemical Society, Pennington, NJ, 1981), p. 254.
- ⁵⁰H. J. Hrostowski and R. H. Kaiser, *J. Phys. Chem. Solids* **9**, 214 (1959).
- ⁵¹W. Wijaranakula, *Appl. Phys. Lett.* **59**, 1185 (1991).
- ⁵²S. Messoloras, R. C. Newman, R. J. Stewart, and J. H. Tucker, *Semicond. Sci. Technol.* **2**, 14 (1987).
- ⁵³J. Vanhellemont and C. Claeys, *Mater. Sci. Forum* **38-41**, 171 (1989).
- ⁵⁴J. C. Mikkelsen, Jr., *Appl. Phys. Lett.* **41**, 871 (1982).
- ⁵⁵J. C. Mikkelsen, Jr., in *Defects in Silicon*, edited by W. M. Bullis and L. C. Kimerling (The Electrochemical Society, Pennington, NJ, 1983), p. 95.
- ⁵⁶D. Heck, R. E. Tressler, and J. Monkowski, *J. Appl. Phys.* **54**, 5739 (1983).
- ⁵⁷M. Stavola, J. R. Patel, L. C. Kimerling, and P. E. Freeland, *Appl. Phys. Lett.* **42**, 73 (1983).
- ⁵⁸R. C. Newman, A. S. Oates, and F. M. Livingston, *J. Phys. C* **16**, L667 (1983).
- ⁵⁹J. C. Mikkelsen, Jr., in *Impurity Diffusion and Gettering in Silicon*, edited by R. B. Fair, C. W. Pearce, and J. Washburn (Materials Research Society, Pittsburgh, PA, 1985), p. 205.
- ⁶⁰W. Wijaranakula, J. H. Matlock, and H. Mollenkopf, *Appl. Phys. Lett.* **53**, 1068 (1988).
- ⁶¹A. S. Oates and W. Lin, *Appl. Phys. Lett.* **53**, 2659 (1988).
- ⁶²M. Pagani, *J. Appl. Phys.* **68**, 3726 (1990).
- ⁶³G. D. Watkins, J. W. Corbett, and R. S. McDonald, *J. Appl. Phys.* **53**, 7097 (1982).
- ⁶⁴R. C. Newman, A. R. Brown, R. Murray, A. Tipping, and J. H. Tucker, in *Semiconductor Silicon 1990*, edited by H. R. Huff, K. G. Barraclough, and J. Chikawa (The Electrochemical Society, Pennington, NJ, 1990), p. 734.
- ⁶⁵J. C. Mikkelsen, *Appl. Phys. Lett.* **40**, 336 (1982).
- ⁶⁶A. S. Oates, M. J. Binns, R. C. Newman, J. H. Tucker, J. G. Wilkes, and A. Wilkinson, *J. Phys. C* **17**, 5695 (1984).
- ⁶⁷J. L. Benton, L. C. Kimerling, and M. Stavola, *Physica B* **116**, 271 (1983).
- ⁶⁸R. C. Newman, *J. Phys. C* **18**, L967 (1985).
- ⁶⁹R. C. Newman, A. K. Tipping, and J. H. Tucker, *J. Phys. C* **18**, L861 (1985).
- ⁷⁰F. Shimura, T. Higuchi, and R. S. Hockett, *Appl. Phys. Lett.* **53**, 69 (1988).
- ⁷¹W. Wijaranakula, *J. Appl. Phys.* **68**, 6538 (1990).
- ⁷²R. C. Newman, J. H. Tucker, A. R. Brown, and S. A. McQuaid, *J. Appl. Phys.* **70**, 3061 (1991).
- ⁷³L. Zhong and F. Shimura, *J. Appl. Phys.* **73**, 707 (1993).
- ⁷⁴R. C. Newman, in *Defects in Electronic Materials*, edited by M. Stavola, S. J. Pearton, and G. Davies (Materials Research Society, Pittsburgh, PA, 1988), p. 25.
- ⁷⁵M. Stavola and L. C. Snyder, in *Defects in Silicon*, edited by W. M. Bullis and L. C. Kimerling (The Electrochemical Society, Pennington, NJ, 1983), p. 61.
- ⁷⁶S. T. Lee and P. Fellingner, *Appl. Phys. Lett.* **49**, 1793 (1986).
- ⁷⁷A. Bourret, J. Thibault-Desseaux, and D. N. Seidman, *J. Appl. Phys.* **55**, 825 (1984).
- ⁷⁸W. Bergholz, J. C. Hutchison, and P. Pirouz, *J. Appl. Phys.* **58**, 3419 (1985).
- ⁷⁹A. Bourret, in *Microscopy of Semiconducting Materials 1986*, Inst. Phys. Conf. Ser., Vol. 87 (ICP, Bristol, 1987), p. 39.
- ⁸⁰U. Gösele and T. Y. Tan, *Appl. Phys. A* **317**, 79 (1982).
- ⁸¹M. Needels, J. D. Joannopoulos, Y. Bar-Yam, and S. T. Pantelides, *Phys. Rev. B* **43**, 4208 (1991).
- ⁸²G. S. Oehrlein and J. W. Corbett, in *Defects in Semiconductors II*, edited by S. Mahajan and J. W. Corbett (North-Holland, New York, 1983), p. 107.
- ⁸³L. C. Snyder and J. W. Corbett, in *Oxygen, Carbon, Hydrogen, and Nitrogen in Silicon*, edited by J. C. Mikkelsen, Jr., S. J. Pearton, J. W. Corbett, and S. J. Pennycook (Materials Research Society, Princeton, NJ, 1986), p. 207.
- ⁸⁴L. C. Snyder, J. W. Corbett, P. Deak, and R. Wu, in *Defects in Electronic Materials*, edited by M. Stavola, S. J. Pearton, and G. Davies (Materials Research Society, Pittsburgh, PA, 1988), p. 179.
- ⁸⁵A. Ourmazd, W. Schröter, and A. Bourret, *J. Appl. Phys.* **56**, 1670 (1984).
- ⁸⁶S. K. Estreicher, *Phys. Rev. B* **41**, 9886 (1990).
- ⁸⁷B. Pajot, *Solid-State Electron.* **12**, 923 (1969).
- ⁸⁸H. J. Hrostowski and R. H. Kaiser, *Phys. Rev.* **107**, 966 (1957).
- ⁸⁹R. C. Newman, *Infrared Studies of Crystal Defects* (Taylor and Francis, London, 1973).
- ⁹⁰F. Shimura, Y. Ohnishi, and H. Tsuya, *Appl. Phys. Lett.* **38**, 867 (1981).
- ⁹¹P. E. Freeland, *J. Electrochem. Soc.* **127**, 754 (1980).
- ⁹²B. Pajot, *Analisis* **5**, 293 (1977).
- ⁹³A. Baghdadi, W. M. Bullis, M. C. Croarkin, Y.-Z. Li, R. I. Scace, R. W. Series, P. Stallhofer, and M. Watanabe, *J. Electrochem. Soc.* **136**, 2015 (1989).
- ⁹⁴F. Schomann and K. Graff, *J. Electrochem. Soc.* **136**, 2025 (1989).
- ⁹⁵T. Tsuya, M. Kanamori, M. Takeda, and K. Yasuda, in *VLSI Science and Technology 1985*, edited by W. B. Bullis and S. Broydo (The Electrochemical Society, Pennington, NJ, 1985), p. 517.
- ⁹⁶A. S. Oates and W. Lin, *J. Cryst. Growth* **89**, 117 (1988).
- ⁹⁷A. Borghesi, M. Geddo, G. Guizzetti, and P. Geranzani, *J. Appl. Phys.* **68**, 1655 (1990).
- ⁹⁸T. Iizuki, S. Takasu, M. Tajima, T. Arai, M. Nozaki, N. Inoue, and M. Watanabe, in *Defects in Silicon*, edited by W. M. Bullis and L. C. Kimerling (The Electrochemical Society, Pennington, NJ, 1983), p. 265.
- ⁹⁹H. Shirai, *J. Electrochem. Soc.* **138**, 1784 (1991).
- ¹⁰⁰P. Wagner, *Appl. Phys. A* **53**, 20 (1991).
- ¹⁰¹J. A. Baker, *Solid-State Electron.* **13**, 1431 (1970).
- ¹⁰²H. J. Rath, P. Stallhofer, D. Huber, and B. F. Schmitt, *J. Electrochem. Soc.* **131**, 1920 (1984).
- ¹⁰³G. Stinger, S. Gara, S. Pahlke, H. Schwenk, E. Guerrero, and M. Grasserbauer, *Fresenius Z. Anal. Chem.* **333**, 576 (1989).
- ¹⁰⁴R. W. Shaw, R. Bredeweg, and P. Rossetto, *J. Electrochem. Soc.* **138**, 582 (1991).
- ¹⁰⁵S. Pahlke and W. Hauer, in *Technical Proceedings of SEMICON/ EUROPA '90* (SEMI, Zürich, 1990), p. 64.
- ¹⁰⁶P. Williams, R. K. Lewis, C. A. Evans, Jr., and P. R. Hanley, *Anal. Chem.* **49**, 1399 (1977).
- ¹⁰⁷K. Wittmaack, *Nucl. Instrum. Methods* **218**, 327 (1983).
- ¹⁰⁸R. J. Bleiler, R. S. Hockett, P. Chu, and E. Strathman, in *Oxygen, Carbon, Hydrogen, and Nitrogen in Crystalline Silicon*, edited by J. C. Mikkelsen, Jr., S. J. Pearton, J. W. Corbett, and S. J. Pennycook (Materials Research Society, Princeton, NJ, 1986), p. 73.
- ¹⁰⁹V. R. Deline, W. Katz, C. A. Evans, Jr., and P. Williams, *Appl. Phys. Lett.* **33**, 578 (1978).
- ¹¹⁰M. Goldstein, P. K. Chu, and R. J. Bleiler, *J. Vac. Sci. Technol. B* **11**, 92 (1993).
- ¹¹¹S. M. Hu, *Appl. Phys. Lett.* **36**, 561 (1980).
- ¹¹²S. M. Hu, *J. Appl. Phys.* **52**, 3974 (1981).
- ¹¹³N. Inoue, J. Osaka, and K. Wada, *J. Electrochem. Soc.* **129**, 2780 (1982).
- ¹¹⁴S. M. Hu, *Materials Research Society Symp.* **59**, 249 (1986).
- ¹¹⁵N. Inoue, K. Watanabe, K. Wada, and J. Osaka, *J. Cryst. Growth* **84**, 21 (1987).
- ¹¹⁶J. Vanhellemont and C. Claeys, *J. Appl. Phys.* **62**, 3960 (1987).
- ¹¹⁷J. Vanhellemont and C. Claeys, *J. Appl. Phys.* **71**, 1073 (1992).
- ¹¹⁸J. Burke, in *The Kinetics of Phase Transformations in Metals* (Pergamon, London, 1965), Chaps. 6 and 7.
- ¹¹⁹K. V. Ravi, *J. Electrochem. Soc.* **121**, 1090 (1974).
- ¹²⁰A. J. R. de Kock and W. M. Van de Wijert, *Appl. Phys. Lett.* **38**, 888 (1981).
- ¹²¹A. J. R. de Kock, in *Proceedings of the ECS Satellite Symposium on Aggregation Phenomena of Point Defects in Silicon*, Munich, 1982, p. 1.
- ¹²²G. S. Oehrlein, J. L. Lindstrom, and J. W. Corbett, *Appl. Phys. Lett.* **40**, 241 (1982).
- ¹²³K. Wada, H. Nakanishi, H. Takaoka, and N. Inoue, *J. Cryst. Growth* **57**, 535 (1982).
- ¹²⁴R. A. Craven, *Materials Research Society Symp.* **36**, 159 (1985).
- ¹²⁵T. Y. Tan and C. Y. Kung, *J. Appl. Phys.* **59**, 917 (1986).

- ¹²⁶ N. Inoue, K. Wada, and J. Osaka, in *Defects and Properties of Semiconductors: Defect Engineering*, edited by J. Chikawa, K. Sumino, and K. Wada (KIT Scientific, Tokyo, 1987), p. 197.
- ¹²⁷ W. Zulehner, in *Proceedings of the STEP Europe Conference 1988*, p. 68.
- ¹²⁸ H. Furuya, I. Suzuki, Y. Shimanuki, and K. Murai, *J. Electrochem. Soc.* **135**, 677 (1988).
- ¹²⁹ N. Inoue, K. Wada, and J. Osaka, in *Semiconductor Silicon, 1981*, edited by H. R. Huff, R. J. Kriegler, and Y. Takeishi (The Electrochemical Society, Princeton, NJ, 1981), p. 282.
- ¹³⁰ H. Bender and J. Vanhellemont, in *Handbook on Semiconductors*, 2nd ed., edited by S. Mahajan (North-Holland, Amsterdam, 1994), Vol. 3, p. 1637.
- ¹³¹ N. I. Puzanov and A. M. Eidenzan, *Semicond. Sci. Technol.* **7**, 406 (1992).
- ¹³² K. Wada and N. Inoue, in *Semiconductor Silicon 1986*, edited by H. R. Huff, T. Abe, and B. Kolbesen (The Electrochemical Society, Pennington, NJ, 1986), p. 778.
- ¹³³ S. Kishino, Y. Matsushita, and M. Kanamori, *Appl. Phys. Lett.* **35**, 213 (1979).
- ¹³⁴ P. Fraundorf, G. K. Fraundorf, and F. Shimura, *J. Appl. Phys.* **58**, 4049 (1985).
- ¹³⁵ F. Shimura, *J. Appl. Phys.* **59**, 3251 (1986).
- ¹³⁶ Q. Sun, K. H. Yao, J. Lagowski, and H. C. Gatos, *J. Appl. Phys.* **67**, 4313 (1990).
- ¹³⁷ E. W. Hart, *Acta Metallurg.* **6**, 553 (1958).
- ¹³⁸ A. Borghesi, B. Pivac, and A. Sassella, *J. Cryst. Growth* **126**, 63 (1993).
- ¹³⁹ J. Osaka, N. Inoue, and K. Kohra, *Appl. Phys. Lett.* **34**, 288 (1980).
- ¹⁴⁰ F. S. Ham, *J. Phys. Chem. Solids* **6**, 335 (1958).
- ¹⁴¹ W. Patrick, E. Hearn, W. Westdorp, and A. Bohg, *J. Appl. Phys.* **50**, 7156 (1979).
- ¹⁴² K. Wada, N. Inoue, and K. Kohra, *J. Cryst. Growth* **49**, 749 (1980).
- ¹⁴³ R. C. Newman, M. J. Binns, W. P. Brown, F. M. Livingston, S. Messoras, R. J. Stewart, and J. G. Wilkes, *Physica B* **116**, 264 (1982).
- ¹⁴⁴ M. J. Binns, W. P. Brown, J. G. Wilkes, R. C. Newman, F. M. Livingston, S. Messoras, and R. J. Stewart, *Appl. Phys. Lett.* **42**, 525 (1983).
- ¹⁴⁵ J. C. Wilkes, *J. Cryst. Growth* **65**, 214 (1983).
- ¹⁴⁶ R. C. Newman, M. Claybourn, S. H. Kinder, S. Messoras, A. S. Oates, and R. J. Stewart, in *Semiconductor Silicon 1986*, edited by H. R. Huff, T. Abe, and B. Kolbesen (The Electrochemical Society, Pennington, NJ, 1986), p. 766.
- ¹⁴⁷ S. M. Hu, *Appl. Phys. Lett.* **48**, 115 (1986).
- ¹⁴⁸ Y. Matsushita, *J. Cryst. Growth* **54**, 588 (1981).
- ¹⁴⁹ F. A. Ponce and S. Hahn, *Materials Research Society Symp. Proc.* **31**, 153 (1984).
- ¹⁵⁰ W. A. Tiller, S. Hahn, and F. A. Ponce, *J. Appl. Phys.* **59**, 3255 (1986).
- ¹⁵¹ H. Bender, *Phys. Status Solidi A* **86**, 245 (1984).
- ¹⁵² C. S. Fuller and R. A. Logan, *J. Appl. Phys.* **28**, 1427 (1957).
- ¹⁵³ P. Capper, A. W. Jones, E. J. Wallhouse, and J. G. Wilkes, *J. Appl. Phys.* **48**, 1646 (1977).
- ¹⁵⁴ A. R. Bean and R. C. Newman, *J. Phys. Chem. Solids* **33**, 255 (1972).
- ¹⁵⁵ P. Gaworzewski and K. Schmalz, *Phys. Status Solidi A* **77**, 571 (1983).
- ¹⁵⁶ B. Goldsmith, L. Jastrzebski, and R. Soyden, in *Defects in Silicon*, edited by W. M. Bullis and L. C. Kimerling (The Electrochemical Society, Pennington, NJ, 1983), p. 142.
- ¹⁵⁷ H. D. Chiou and L. W. Shive, in *VLSI Science and Technology 1985*, edited by W. M. Bullis and S. Broydo (The Electrochemical Society, Pennington, NJ, 1985), p. 429.
- ¹⁵⁸ L. Jastrzebski, R. Soyden, J. McGinn, R. Kleppinger, M. Blumenfeld, G. Gillespie, N. Armour, B. Goldsmith, W. Henry, and S. Vecrumba, *J. Electrochem. Soc.* **134**, 1018 (1987).
- ¹⁵⁹ Y. Shimanuki, H. Furuya, I. Suzuki, and K. Murai, *Jpn. J. Appl. Phys.* **24**, 1594 (1980).
- ¹⁶⁰ G. Fraundorf, P. Fraundorf, R. A. Craven, R. A. Frederick, J. Moody, and R. W. Shaw, *J. Electrochem. Soc.* **132**, 1701 (1985).
- ¹⁶¹ F. Shimura and H. Tsuya, *J. Electrochem. Soc.* **129**, 1062 (1982).
- ¹⁶² Y. Matsushita, *J. Cryst. Growth* **56**, 516 (1982).
- ¹⁶³ C. J. Varker, J. D. Whitfield, and L. Fejes, in *Silicon Processing*, ASTM STP 804 (ASTM, Philadelphia, PA, 1983), p. 369.
- ¹⁶⁴ H. R. Huff, H. F. Schaake, J. T. Robinson, S. C. Baber, and D. Wong, *J. Electrochem. Soc.* **130**, 1551 (1983).
- ¹⁶⁵ A. Virzi and M. Porri, *Mater. Sci. Eng. B* **17**, 196 (1993).
- ¹⁶⁶ H. D. Chiou, *Solid State Technol. March*, **77** (1987).
- ¹⁶⁷ F. Shimura, *Appl. Phys. Lett.* **39**, 987 (1981).
- ¹⁶⁸ L. Jastrzebski, P. Zanzucchi, D. Thebault, and J. Lagowski, *J. Electrochem. Soc.* **129**, 1638 (1982).
- ¹⁶⁹ I. Fusegawa and H. Yamagishi, in *Proceedings of the 37th Symposium on Semiconductors and Integrated Circuits Technology* (The Electrochemical Society Japan, Tokyo, 1989), p. 31.
- ¹⁷⁰ K. Yang, J. Carle, and R. Kleinhenz, *J. Appl. Phys.* **62**, 4890 (1987).
- ¹⁷¹ P. Fraundorf, G. K. Fraundorf, and R. A. Craven, in *VLSI Science and Technology 1985*, edited by W. M. Bullis and S. Broydo (The Electrochemical Society, Pennington, NJ, 1985), p. 436.
- ¹⁷² H. F. Schaake, S. C. Baber, and R. F. Pinizzoto, in *Semiconductor Silicon 1981*, edited by H. R. Huff, R. J. Kriegler, and Y. Takeishi (The Electrochemical Society, Pennington, NJ, 1981), p. 273.
- ¹⁷³ I. Fusegawa, E. Iino, T. Hirohata, and H. Yamagishi, in *Defect Engineering in Semiconductor Growth, Processing and Device Technology*, edited by S. Ashok, J. Chevallier, K. Sumino, and E. Weber (Materials Research Society, Pittsburgh, PA, 1992), p. 683.
- ¹⁷⁴ H. D. Chiou, *J. Electrochem. Soc.* **139**, 1680 (1992).
- ¹⁷⁵ A. Bourret, in *Oxygen, Carbon, Hydrogen, and Nitrogen in Crystalline Silicon*, edited by J. C. Mikkelsen, Jr., S. J. Pearton, J. W. Corbett, and S. J. Pennycook (Materials Research Society, Princeton, NJ, 1986), p. 223.
- ¹⁷⁶ P. Wagner, C. Holm, E. Sirtl, R. Oeder, and W. Zulehner, *Adv. Solid State Phys.* **24**, 191 (1984).
- ¹⁷⁷ A. Bourret, in *Proceedings of the 13th International Conference on Defects in Semiconductors*, edited by L. C. Kimerling and J. M. Parsey, Jr. (The Metallurgical Soc. of AIME, Warrendale, PA, 1985), p. 129.
- ¹⁷⁸ L. C. Kimerling, in *Oxygen, Carbon, Hydrogen, and Nitrogen in Silicon*, edited by J. C. Mikkelsen, Jr., S. J. Pearton, J. W. Corbett, and S. J. Pennycook (Materials Research Society, Pittsburgh, PA, 1986), p. 83.
- ¹⁷⁹ R. C. Newman, in *Defects in Electronic Materials*, edited by M. Stavola, S. J. Pearton, and G. Davies (Materials Research Society, Pittsburgh, PA, 1988), p. 25.
- ¹⁸⁰ C. S. Fuller, J. W. Dietzenberger, N. B. Hannay, and E. Buehler, *Phys. Rev.* **96**, 833 (1954).
- ¹⁸¹ W. Kaiser, H. L. Frisch, and H. Reiss, *Phys. Rev.* **112**, 1546 (1958).
- ¹⁸² A. Kanamori and M. Kanamori, *J. Appl. Phys.* **50**, 8095 (1979).
- ¹⁸³ Y. Kamiura, F. Hashimoto, and K. Endo, *J. Appl. Phys.* **61**, 2478 (1987).
- ¹⁸⁴ J. L. Lindström, H. Weman, and G. S. Oehrlein, *Phys. Status Solidi A* **99**, 581 (1987).
- ¹⁸⁵ P. Wagner and J. Hage, *Appl. Phys. A* **49**, 123 (1989).
- ¹⁸⁶ M. Stavola and K. M. Lee, in *Oxygen, Carbon, Hydrogen, and Nitrogen in Crystalline Silicon*, edited by J. C. Mikkelsen, Jr., S. J. Pearton, J. W. Corbett, and S. J. Pennycook (Materials Research Society, Pittsburgh, PA, 1986), p. 95.
- ¹⁸⁷ M. Tajima, U. Gösele, J. Weber, and R. Sauer, *Appl. Phys. Lett.* **43**, 270 (1983).
- ¹⁸⁸ D. Wruck and P. Gaworzewski, *Phys. Status Solidi A* **56**, 557 (1979).
- ¹⁸⁹ S. Muller, M. Sprenger, E. G. Sieverts, and C. A. J. Ammerlaan, *Solid State Commun.* **25**, 987 (1978).
- ¹⁹⁰ J. Michel, J. R. Niklas, and J. M. Spaeth, in *Oxygen, Carbon, Hydrogen, and Nitrogen in Crystalline Silicon*, edited by J. C. Mikkelsen, Jr., S. J. Pearton, J. W. Corbett, and S. J. Pennycook (Materials Research Society, Pittsburgh, PA, 1986), p. 111.
- ¹⁹¹ H. H. P. T. Bekman, T. Gregorkiewicz, and C. A. J. Ammerlaan, *Mater. Sci. Forum* **38-41**, 601 (1989).
- ¹⁹² D. A. van Wezep, T. Gregorkiewicz, H. H. P. T. Bekman, and C. A. J. Ammerlaan, *Mater. Sci. Forum* **10-12**, 1009 (1986).
- ¹⁹³ L. C. Kimerling and J. L. Benton, *Appl. Phys. Lett.* **39**, 410 (1981).
- ¹⁹⁴ B. Pajot, H. Compain, J. Lerouille, and B. Clerjaud, *Physica* **117-118**, 110 (1983).
- ¹⁹⁵ W. Götz, G. Pensl, and W. Zulehner, *Phys. Rev. B* **46**, 4312 (1992).
- ¹⁹⁶ C. A. Londos, M. J. Binns, A. R. Brown, S. A. McQuaid, and R. C. Newman, *Appl. Phys. Lett.* **62**, 1525 (1993).
- ¹⁹⁷ V. Cazcarra and P. Zunino, *J. Appl. Phys.* **51**, 4206 (1980).
- ¹⁹⁸ P. Wagner, in *Oxygen, Carbon, Hydrogen, and Nitrogen in Crystalline Silicon*, edited by J. C. Mikkelsen, Jr., S. J. Pearton, J. W. Corbett, and S. J. Pennycook (Materials Research Society, Pittsburgh, PA, 1986), p. 125.
- ¹⁹⁹ M. Claybourn and R. C. Newman, *Appl. Phys. Lett.* **52**, 2139 (1988).
- ²⁰⁰ J. W. Cleland, *J. Electrochem. Soc.* **129**, 2127 (1982).
- ²⁰¹ W. Wijaranakula, *J. Appl. Phys.* **69**, 2737 (1991).
- ²⁰² A. Ourmazd and W. Schröter, *Appl. Phys. Lett.* **45**, 781 (1984).
- ²⁰³ M. Suezawa and K. Sumino, *Phys. Status Solidi A* **83**, 235 (1984).
- ²⁰⁴ J. T. Borenstein, D. Peak, and J. W. Corbett, *J. Mater. Res.* **1**, 527 (1986).
- ²⁰⁵ D. Helmreich and E. Sirtl, in *Semiconductor Silicon 1977*, edited by H.

- R. Huff and E. Sirtl (The Electrochemical Society, Princeton, NJ, 1977), p. 157.
- ²⁰⁶G. G. DeLeo, C. S. Milsted, and J. C. Kralik, Phys. Rev. B 31, 3588 (1985).
- ²⁰⁷D. Mathiot, Appl. Phys. Lett. 51, 904 (1987).
- ²⁰⁸H. M. Liaw and C. J. Varker, in *Semiconductor Silicon 1977*, edited by H. R. Huff and E. Sirtl (The Electrochemical Society, Princeton, NJ, 1977), p. 116.
- ²⁰⁹K. Schmalz and P. Gaworzewski, Phys. Status Solidi A 64, 151 (1981).
- ²¹⁰J. Lerouille, Phys. Status Solidi A 67, 177 (1981).
- ²¹¹S. Hahn, H. J. Stein, S. C. Shatas, and F. A. Ponce, in *Defect Control in Semiconductors*, edited by K. Sumino (North-Holland, Amsterdam, 1990), p. 227.
- ²¹²G. Pensl, M. Schulz, K. Hölzlein, W. Bergholz, and J. L. Hutchison, Appl. Phys. A 48, 49 (1989).
- ²¹³P. M. Grinshtein, G. V. Lazareva, E. V. Orlova, Z. A. Sal'nik, and V. I. Fistul, Sov. Phys. Semicond. 12, 68 (1978).
- ²¹⁴J. J. Qian, Z. G. Wang, S. K. Wan, and L. Y. Lin, J. Appl. Phys. 68, 954 (1990).
- ²¹⁵W. Wijaranakula and J. H. Matlock, J. Electrochem. Soc. 137, 1964 (1990).
- ²¹⁶J. A. Griffin, H. Navarro, J. Weber, L. Genzel, J. T. Borenstein, J. W. Corbett, and L. C. Snyder, J. Phys. C 19, L579 (1986).
- ²¹⁷J. A. Griffin, J. Hartung, and J. Weber, Mater. Sci. Forum 38-41, 619 (1989).
- ²¹⁸Y. Kamiura, F. Hashimoto, and M. Yoneta, J. Appl. Phys. 65, 600 (1989).
- ²¹⁹Y. Kamiura, M. Suezawa, K. Sumino, and F. Hashimoto, Jpn. J. Appl. Phys. 29, L1937 (1990).
- ²²⁰Y. Kamiura, F. Hashimoto, and M. Yoneta, J. Appl. Phys. 66, 3926 (1989).
- ²²¹K. Tempelhoff, F. Spiegelberg, and R. Gleichmann, in *Semiconductor Silicon 1977*, edited by H. R. Huff and E. Sirtl (The Electrochemical Society, Princeton, NJ, 1977), p. 585.
- ²²²K. Tempelhoff, F. Spiegelberg, R. Gleichmann, and D. Wruck, Phys. Status Solidi A 56, 213 (1979).
- ²²³K. Tempelhoff, B. Hahn, and R. Gleichmann, in *Semiconductor Silicon 1981*, edited by H. R. Huff, R. J. Kriegler, and Y. Takeishi (The Electrochemical Society, Pennington, NJ, 1981), p. 244.
- ²²⁴M. Reiche and O. Breitenstein, Phys. Status Solidi A 101, K97 (1987).
- ²²⁵F. A. Ponce, T. Yamashita, and S. Hahn, in *Defects in Silicon*, edited by W. M. Bullis and L. C. Kimerling (The Electrochemical Society, Pennington, NJ, 1983), p. 105.
- ²²⁶C. Prunier, E. Ligeon, A. Bourret, A. C. Chami, and J. C. Oberlin, Nucl. Instrum. Methods B 17, 227 (1986).
- ²²⁷A. Bourret, Inst. Phys. Conf. Ser. 87, 39 (1987).
- ²²⁸J. A. Lambert and P. S. Dobson, Philos. Mag. A 44, 1043 (1981).
- ²²⁹I. G. Salisbury and M. H. Loreto, Philos. Mag. A 39, 317 (1979).
- ²³⁰N. Yamamoto, P. M. Petroff, and J. R. Patel, J. Appl. Phys. 54, 3475 (1983).
- ²³¹A. Bourret, J. Phys. (Paris) Colloq. 44, 227 (1983).
- ²³²T. Y. Tan, Philos. Mag. A 44, 101 (1981).
- ²³³H. Bender and J. Vanhellemont, Phys. Status Solidi A 107, 455 (1988).
- ²³⁴P. Gaworzewski, E. Hild, F. G. Kirscht, and L. Vecsernyés, Phys. Status Solidi A 85, 133 (1984).
- ²³⁵M. Reiche, J. Reichel, and W. Nitzsche, Phys. Status Solidi A 107, 851 (1988).
- ²³⁶R. W. Carpenter, Y. L. Chen, M. J. Kim, and J. C. Barry, Inst. Phys. Conf. Ser. 100, 543 (1989).
- ²³⁷T. Y. Tan and U. Gösele, Appl. Phys. Lett. 39, 86 (1981).
- ²³⁸M. Servidori, S. Cannavo, G. Ferla, A. La Ferla, S. U. Campisano, and E. Rimini, Nucl. Instrum. Methods B 19/20, 317 (1987).
- ²³⁹V. G. Eremenko and V. I. Nikitenko, Phys. Status Solidi A 14, 317 (1972).
- ²⁴⁰P. Pirouz, R. Chaim, and J. Samuels, in *Proceedings of the 5th International Conference on Structure and Properties of Dislocations in Semiconductors* (Bulletin of the Academy of Sciences of the USSR, Moscow, 1986).
- ²⁴¹G. B. Bronner and J. D. Plummer, J. Appl. Phys. 61, 5286 (1987).
- ²⁴²H. J. Mayer, H. Mehrer, and K. Maier, Inst. Phys. Conf. Ser. 31, 186 (1977).
- ²⁴³A. Parisini and A. Bourret, Philos. Mag. A 67, 605 (1993).
- ²⁴⁴W. Bergholz, M. J. Binns, G. R. Booker, J. C. Hutchison, S. H. Kinder, S. Messoloras, R. C. Newman, R. J. Stewart, and J. G. Wilkes, Philos. Mag. B 59, 499 (1989).
- ²⁴⁵F. A. Ponce and S. Hahn, Mater. Sci. Eng. B 4, 11 (1989).
- ²⁴⁶R. W. Carpenter, I. Chan, H. L. Tsai, C. Varker, and L. J. Demer, in *Defects in Semiconductors II*, edited by S. Mahajan and J. W. Corbett (North-Holland, Amsterdam, 1983), p. 195.
- ²⁴⁷W. M. Skiff, H. L. Tsai, and R. W. Carpenter, in *Oxygen, Carbon, Hydrogen, and Nitrogen in Crystalline Silicon*, edited by J. C. Mikkelsen, Jr., S. J. Pearton, J. W. Corbett, and S. J. Pennycook (Materials Research Society, Princeton, NJ, 1986), p. 241.
- ²⁴⁸A. Borghesi, A. Piaggi, A. Sassella, A. Stella, and B. Pivac, Phys. Rev. B 46, 4123 (1992).
- ²⁴⁹B. Pivac, A. Borghesi, M. Geddo, A. Sassella, and A. Stella, Appl. Surf. Sci. 63, 245 (1993).
- ²⁵⁰S. Gupta, S. Messoloras, J. R. Schneider, R. J. Stewart, and W. Zulehner, Semicond. Sci. Technol. 5, 783 (1990).
- ²⁵¹S. Messoloras, J. R. Schneider, R. J. Stewart, and W. Zulehner, Semicond. Sci. Technol. 4, 340 (1989).
- ²⁵²T. Takeda, S. Komura, A. Ohsawa, and K. Honda, Jpn. J. Appl. Phys. 26, 106 (1987).
- ²⁵³J. J. Wortman and R. A. Evans, J. Appl. Phys. 36, 153 (1965).
- ²⁵⁴W. A. Brantley, J. Appl. Phys. 44, 534 (1973).
- ²⁵⁵H. Liang, Y. Pan, S. Zhao, G. Qin, and K. Chin, J. Appl. Phys. 71, 2863 (1992).
- ²⁵⁶W. Wijaranakula, J. Appl. Phys. 72, 4026 (1992).
- ²⁵⁷Y. Matsushita, S. Kishino, and M. Kanamori, Jpn. J. Appl. Phys. 19, L101 (1980).
- ²⁵⁸T. Y. Tan and W. K. Tice, Philos. Mag. 34, 615 (1976).
- ²⁵⁹H. Bender and J. Vanhellemont, in *Defect Engineering in Semiconductor Growth, Processing and Device Technology*, edited by S. Ashok, J. Chevallier, K. Sumino, and E. Weber (Materials Research Society, Pittsburgh, PA, 1992), p. 15.
- ²⁶⁰F. Shimura, H. Tsuya, and T. Kawamura, Appl. Phys. Lett. 37, 483 (1980).
- ²⁶¹W. A. Tiller, J. Electrochem. Soc. 127, 619 (1980).
- ²⁶²J. Vanhellemont and C. Claeys, in *Defects in Silicon II*, edited by W. M. Bullis, U. Gösele, and F. Shimura (The Electrochemical Society, Pennington, NJ, 1991), p. 263.
- ²⁶³W. J. Taylor, T. Y. Tan, and U. Gösele, in *Defects in Silicon II*, edited by W. M. Bullis, U. Gösele, and F. Shimura (The Electrochemical Society, Pennington, NJ, 1991), p. 255.
- ²⁶⁴K. H. Yang, R. Anderson, and H. F. Kappert, Appl. Phys. Lett. 33, 225 (1978).
- ²⁶⁵F. A. Ponce, T. Yamashita, and S. Hahn, Appl. Phys. Lett. 43, 1051 (1983).
- ²⁶⁶D. M. Maher, A. Staudinger, and J. R. Patel, J. Appl. Phys. 47, 3813 (1976).
- ²⁶⁷S. Mahajan, G. A. Rozgonyi, and D. Brasen, Appl. Phys. Lett. 30, 73 (1977).
- ²⁶⁸K. Wada, N. Inoue, and J. Osaka, in *Defects in Semiconductors II*, edited by S. Mahajan and J. W. Corbett (North-Holland, Amsterdam, 1983), p. 125.
- ²⁶⁹J. R. Patel and A. Authier, J. Appl. Phys. 46, 118 (1975).
- ²⁷⁰M. Hasebe, Y. Takeoka, S. Shiroyama, and S. Naito, in *Defect Control in Semiconductors*, edited by K. Sumino (North-Holland, Amsterdam, 1990), p. 157.
- ²⁷¹M. S. Bawa, W. J. Bell, H. M. Grimes, and T. J. Shaffner, J. Cryst. Growth 94, 803 (1989).
- ²⁷²H. S. Cho, H. W. Lee, Y. K. Kim, D. Buck, J. Rigotti, J. Yeh, S. Hahn, and W. A. Tiller, in *Defects in Silicon II*, edited by W. M. Bullis, U. Gösele, and F. Shimura (The Electrochemical Society, Pennington, NJ, 1991), p. 189.
- ²⁷³J. R. Patel, in *Semiconductor Silicon 1977*, edited by H. R. Huff and E. Sirtl (The Electrochemical Society, Princeton, NJ, 1977), p. 521.
- ²⁷⁴J. Vanhellemont, S. Amerlinckx, and C. Claeys, J. Appl. Phys. 61, 2170 (1987).
- ²⁷⁵G. A. Hawkins and J. P. Lavine, J. Appl. Phys. 65, 3644 (1989).
- ²⁷⁶H. Walitzki, H. J. Rath, J. Reffle, S. Pahlke, and M. Blatte, in *Semiconductor Silicon 1986*, edited by H. R. Huff, T. Abe, and B. Kolbesen (The Electrochemical Society, Pennington, NJ, 1986), p. 86.
- ²⁷⁷F. Shimura, W. Dyson, J. W. Moody, and R. S. Hockett, in *VLSI Science and Technology 1985*, edited by W. M. Bullis and S. Broydo (The Electrochemical Society, Pennington, NJ, 1985), p. 507.
- ²⁷⁸C. W. Pearce, T. Kook, and R. J. Jaccodine, in *Impurity Diffusion and Gettering in Silicon*, edited by R. B. Fair, C. W. Pearce, and J. Washburn (Materials Research Society, Pittsburgh, PA, 1983), p. 231.

- ²⁷⁹ S. K. Bains, D. P. Griffiths, J. G. Wilkes, R. W. Series, and K. G. Barraclough, *J. Electrochem. Soc.* **137**, 647 (1990).
- ²⁸⁰ K. Wada, *Phys. Rev. B* **30**, 5884 (1984).
- ²⁸¹ K. G. Barraclough, *J. Cryst. Growth* **99**, 654 (1990).
- ²⁸² S. Hahn, F. A. Ponce, W. A. Tiller, V. Stojanoff, D. A. P. Bulla, and W. E. Castro, Jr., *J. Appl. Phys.* **64**, 4454 (1988).
- ²⁸³ S. Hahn, F. A. Ponce, P. Masher, S. Dannefaer, D. Kerr, W. Puff, V. Stojanoff, W. W. Furtado, D. A. P. Bulla, P. B. S. Santos, S. Ishigami, and W. A. Tiller, in *Defects in Silicon II*, edited by W. M. Bullis, U. Gösele, and F. Shimura (The Electrochemical Society, Pennington, NJ, 1991), p. 297.
- ²⁸⁴ S. Matsumoto, I. Ishihara, H. Kaneko, H. Harada, and T. Abe, *Appl. Phys. Lett.* **46**, 957 (1985).
- ²⁸⁵ T. Fukuda and A. Ohsawa, *Appl. Phys. Lett.* **58**, 2634 (1991).
- ²⁸⁶ T. Nozaki and Y. Itoh, *J. Appl. Phys.* **59**, 2562 (1986).
- ²⁸⁷ S. Gupta, S. Messoloras, J. R. Schneider, R. J. Stewart, and W. Zulehner, *Semicond. Sci. Technol.* **7**, 443 (1992).
- ²⁸⁸ F. Secco d'Aragona and P. L. Fejes, *Appl. Phys. Lett.* **48**, 665 (1986).
- ²⁸⁹ K. G. Barraclough and J. G. Wilkes, in *Semiconductor Silicon 1986*, edited by H. R. Huff, T. Abe, and B. Kolbesen (The Electrochemical Society, Pennington, NJ, 1986), p. 889.
- ²⁹⁰ B. O. Kolbesen and A. Mühlbauer, *Solid-State Electron.* **25**, 759 (1982).
- ²⁹¹ F. Shimura, J. P. Baiardo, and P. Fraundorf, *Appl. Phys. Lett.* **46**, 941 (1985).
- ²⁹² M. Ogino, *Appl. Phys. Lett.* **41**, 847 (1982).
- ²⁹³ W. E. Bailey, R. A. Bowling, and K. E. Bean, *J. Electrochem. Soc.* **132**, 1721 (1985).
- ²⁹⁴ M. Kanamori and H. Tsuya, *Jpn. J. Appl. Phys.* **24**, 557 (1985).
- ²⁹⁵ C. Y. Kung, in *VLSI Science and Technology 1985*, edited by W. B. Bullis and S. Broydo (The Electrochemical Society, Pennington, NJ, 1985), p. 446.
- ²⁹⁶ M. Schrems, P. Pongratz, M. Budil, H. W. Pötzl, J. Hage, E. Guerrero, and D. Huber, in *Semiconductor Silicon 1990*, edited by H. R. Huff, K. G. Barraclough, and J. Chikawa (The Electrochemical Society, Pennington, NJ, 1990), p. 144.
- ²⁹⁷ S. Hahn, M. Arst, K. N. Ritz, S. Shatas, H. J. Stein, Z. U. Rek, and W. A. Tiller, in *Defects in Electronic Materials*, edited by M. Stavola, S. J. Pearton, and G. Davies (Materials Research Society, Pittsburgh, PA, 1988), p. 201.
- ²⁹⁸ H. Bender, C. Claeys, J. Van Landuyt, G. Declercq, S. Amerlinckx, and R. Van Overstraten, in *Proceedings of the 13th International Conference on Defects in Semiconductors*, edited by L. C. Kimerling and J. M. Parsey (The Metallurgical Soc. of AIME, Warrendale, PA, 1984), p. 587.
- ²⁹⁹ F. Shimura, R. S. Hockett, D. A. Reed, and D. H. Wayne, *Appl. Phys. Lett.* **47**, 794 (1985).
- ³⁰⁰ S. Gupta, S. Messoloras, J. R. Schneider, R. J. Stewart, and W. Zulehner, *Semicond. Sci. Technol.* **7**, 6 (1992).
- ³⁰¹ W. J. Taylor, U. M. Gösele, and T. Y. Tan, *Jpn. J. Appl. Phys.* **32**, 4857 (1993).
- ³⁰² T. Abe, H. Harada, N. Ozawa, and K. Adomi, in *Oxygen, Carbon, Hydrogen, and Nitrogen in Crystalline Silicon*, edited by J. C. Mikkelsen, Jr., S. J. Pearton, J. W. Corbett, and S. J. Pennycook (Materials Research Society, Pittsburgh, PA, 1986), p. 537.
- ³⁰³ F. Shimura and R. S. Hockett, *Appl. Phys. Lett.* **48**, 224 (1986).
- ³⁰⁴ A. Hara, T. Fukuda, T. Miyabo, and L. Hirai, *Appl. Phys. Lett.* **54**, 626 (1989).
- ³⁰⁵ Q. Sun, K. H. Yao, H. C. Gatos, and J. Lagowski, *J. Appl. Phys.* **71**, 3760 (1992).
- ³⁰⁶ R. C. Newman, in *Defects in Silicon II*, edited by W. M. Bullis, U. Gösele, and F. Shimura (The Electrochemical Society, Pennington, NJ, 1991), p. 271.
- ³⁰⁷ E. E. Haller, *Semicond. Sci. Technol.* **6**, 73 (1991).
- ³⁰⁸ C. D. Lamp and D. J. James II, *Appl. Phys. Lett.* **62**, 2081 (1993).
- ³⁰⁹ A. Hara, M. Aoki, T. Fukuda, and A. Ohsawa, *J. Appl. Phys.* **74**, 913 (1993).
- ³¹⁰ J. S. Pearton, W. Corbett, and M. Stavola, *Hydrogen in Crystalline Semiconductors* (Springer, Berlin, 1992).
- ³¹¹ S. Muto, S. Tukada, M. Hirata, and T. Tanabe, *J. Appl. Phys.* **70**, 3505 (1991).
- ³¹² W. T. Stacy, M. C. Arst, K. N. Ritz, J. G. de Groot, and M. H. Norcott, in *Defects in Silicon*, edited by W. M. Bullis and L. C. Kimerling (The Electrochemical Society, Pennington, NJ, 1983), p. 423.
- ³¹³ M. C. Arst and J. G. de Groot, *J. Electron. Mater.* **13**, 763 (1984).
- ³¹⁴ H. Shirai, A. Yamaguchi, and F. Shimura, *Appl. Phys. Lett.* **54**, 1748 (1989).
- ³¹⁵ H. Harada, T. Abe, and J. Chikawa, in *Semiconductor Silicon 1986*, edited by H. R. Huff, T. Abe, and B. Kolbesen (The Electrochemical Society, Pennington, NJ, 1986), p. 76.
- ³¹⁶ A. Ikari, H. Haga, O. Yoda, A. Uedono, and Y. Ujihira, in *Defect Engineering in Semiconductor Growth, Processing and Device Technology*, edited by S. Ashok, J. Chevallier, K. Sumino, and E. Weber (Materials Research Society, Pittsburgh, PA, 1992), p. 69.
- ³¹⁷ T. Hallberg and J. L. Lindström, *J. Appl. Phys.* **72**, 5130 (1992).
- ³¹⁸ 1990 Annual Book of ASTM Standards, Vol. 10.05, F 416; F 47.
- ³¹⁹ D. C. Miller and G. A. Rozgonyi, in *Handbook of Semiconductors*, edited by S. P. Keller (North-Holland, Amsterdam, 1982), Vol. 3, p. 217.
- ³²⁰ *Quick Reference Manual for Silicon Integrated Circuit Technology*, edited by W. E. Beadle, J. C. C. Tsai, and R. D. Plummer (Wiley, New York, 1985).
- ³²¹ B. O. Kolbesen and H. P. Strunk, in *VLSI Electronics*, edited by N. G. Einspruch and H. Huff (Academic, Orlando, FL, 1985), p. 143.
- ³²² E. Sirtl and A. Adler, *Z. Metallk.* **52**, 529 (1961).
- ³²³ F. Secco d'Aragona, *J. Electrochem. Soc.* **119**, 948 (1972).
- ³²⁴ M. Wright Jenkins, *J. Electrochem. Soc.* **124**, 757 (1977).
- ³²⁵ D. G. Schimmel, *J. Electrochem. Soc.* **126**, 479 (1979).
- ³²⁶ K. H. Yang, in *Semiconductor Processing*, edited by D. C. Gupta (ASTM, Philadelphia, PA, 1984), p. 309.
- ³²⁷ G. Nomarski and A. R. Weill, *Bull. Soc. Franc. Miner. Cryst.* **77**, 840 (1954).
- ³²⁸ W. Zulehner, in *Landolt-Börnstein—Numerical Data and Functional Relationships in Science and Technology*, edited by O. Madelung (Springer, Berlin, 1989), Vol. 22, Subvol. b, p. 391.
- ³²⁹ A. Bouret, *Materials Research Society Symp. Proc.* **59**, 223 (1986).
- ³³⁰ W. K. Tice and T. C. Huang, *Appl. Phys. Lett.* **24**, 157 (1974).
- ³³¹ H. Bender and J. Vanhellemont, *Materials Research Society Symp. Proc.* **262**, 15 (1992).
- ³³² H. Bender and J. Vanhellemont, in *Encyclopedia of Advanced Materials*, edited by D. Bloor, R. J. Brook, M. C. Flemings, and S. Mahajan (Pergamon, Oxford, 1994), p. 1906.
- ³³³ R. Swaroop, N. Kim, W. Lin, M. Bullis, L. Shive, A. Rice, E. Castel, and M. Christ, *Solid State Technol. March*, 85 (1987).
- ³³⁴ Annual Book of ASTM Standards, F 1239-89.
- ³³⁵ W. J. Patrick, in *Silicon Device Processing*, National Bureau of Standards Special Publication No. 337 (U.S. GPO, Washington DC, 1970).
- ³³⁶ S. M. Hu and W. J. Patrick, *J. Appl. Phys.* **46**, 1869 (1975).
- ³³⁷ G. A. Rozgonyi and C. W. Pearce, *Appl. Phys. Lett.* **31**, 343 (1977).
- ³³⁸ P. Gaworzewski, E. Hild, and K. Schmalz, *Phys. Status Solidi A* **90**, K151 (1985).
- ³³⁹ S. M. Hu, *J. Appl. Phys.* **51**, 5945 (1980).
- ³⁴⁰ L. Genzel and T. P. Martin, *Phys. Status Solidi B* **51**, 91 (1972).
- ³⁴¹ L. Genzel and T. P. Martin, *Surf. Sci.* **34**, 33 (1973).
- ³⁴² G. Hoffmann, A. Nagy, and L. Puskás, *J. Phys. D* **8**, 1044 (1975).
- ³⁴³ C. Y. Kung, *J. Appl. Phys.* **65**, 4654 (1989).
- ³⁴⁴ X.-T. Meng, *Phys. Status Solidi A* **129**, K131 (1992).
- ³⁴⁵ A. Borghesi, M. Geddo, B. Pivac, A. Sassella, and A. Stella, *Appl. Phys. Lett.* **58**, 2099 (1991).
- ³⁴⁶ A. Borghesi, M. Geddo, and B. Pivac, *J. Appl. Phys.* **60**, 7251 (1991).
- ³⁴⁷ Q. Sun, J. Lagowski, and H. C. Gatos, *Mater. Res. Symp. Proc.* **104**, 205 (1988).
- ³⁴⁸ B. Pivac, A. Borghesi, M. Geddo, A. Sassella, and A. Stella, *Mater. Sci. Forum* **83-87**, 1069 (1992).
- ³⁴⁹ A. Borghesi, M. Geddo, B. Pivac, A. Stella, and P. Lupano, *Appl. Phys. Lett.* **58**, 2657 (1991).
- ³⁵⁰ M. Geddo, B. Pivac, A. Borghesi, A. Stella, and M. Pedrotti, *Appl. Phys. Lett.* **57**, 1511 (1990).
- ³⁵¹ B. Pivac, A. Borghesi, M. Geddo, and A. Stella, *Phys. Scr. T* **39**, 265 (1991).
- ³⁵² A. Sassella and A. Borghesi, *SPIE* **1575**, 562 (1992).
- ³⁵³ A. Borghesi, B. Pivac, and A. Sassella, *Appl. Phys. Lett.* **60**, 871 (1992).
- ³⁵⁴ A. Borghesi, M. Geddo, B. Pivac, A. Sassella, and A. Stella, in *The Physics of Semiconductors*, edited by P. Jiang and H.-Z. Zheng (World Scientific, Singapore, 1992), Vol. 1, p. 1649.
- ³⁵⁵ Y. Shimanuki, H. Furuya, and I. Suzuki, *J. Electrochem. Soc.* **136**, 2058 (1989).
- ³⁵⁶ A. Sassella, Ph.D. thesis, Università degli Studi di Pavia, 1993.
- ³⁵⁷ D. W. Berreman, *Phys. Rev. B* **130**, 2193 (1963).
- ³⁵⁸ H. Ono and T. Ikarashi, *Appl. Phys. Lett.* **63**, 3303 (1993).

- ³⁵⁹ S. Messoloras, J. R. Schneider, R. J. Stewart, and W. Zulehner, *Nature* **336**, 364 (1988).
- ³⁶⁰ S. Messoloras, B. C. Pike, R. J. Stewart, and C. G. Windsor, *Metal. Sci.* **18**, 311 (1984).
- ³⁶¹ S. Gupta, S. Messoloras, J. R. Schneider, R. J. Stewart, and W. Zulehner, *J. Appl. Cryst.* **24**, 576 (1991).
- ³⁶² C. F. Bohren and D. R. Huffman, *Absorption and Scattering of Light by Small Particles* (Wiley, New York, 1983).
- ³⁶³ V. Vaud, K. Vedom, and R. Stein, *J. Appl. Phys.* **37**, 2551 (1966).
- ³⁶⁴ K. Moriya and T. Ogawa, *Philos. Mag.* **A 44**, 1085 (1981).
- ³⁶⁵ K. Moriya and T. Ogawa, *Jpn. J. Appl. Phys.* **22**, L207 (1983).
- ³⁶⁶ K. Moriya, *Jpn. J. Appl. Phys.* **55**, 6 (1986).
- ³⁶⁷ T. Ogawa and N. Nango, *Rev. Sci. Instrum.* **57**, 1135 (1986).
- ³⁶⁸ M. Castagné, J. P. Fillard, and J. Bonnafé, *Solid State Commun.* **54**, 653 (1985).
- ³⁶⁹ P. Gall, J. P. Fillard, J. Bonnafé, M. Castagné, J. Weyher, and A. George, in *Proceedings of the DRIP II Symposium*, edited by E. Weber, *Mater. Sci. Monographs No. 44* (Elsevier, Amsterdam, 1987), p. 215.
- ³⁷⁰ P. Gall, J. P. Fillard, M. Castagné, J. L. Weyher, and J. Bonnafé, *J. Appl. Phys.* **64**, 5161 (1988).
- ³⁷¹ J. P. Fillard, P. Gall, M. Castagné, and J. Bonnafé, *Solid State Phenom.* **687**, 403 (1989).
- ³⁷² J. P. Fillard, P. Gall, J. Bonnafé, M. Castagné, and T. Ogawa, *Semicond. Sci. Technol.* **7**, 283 (1992).
- ³⁷³ J. P. Fillard, P. C. Montgomery, P. Gall, M. Castagné, and J. Bonnafé, *J. Cryst. Growth* **103**, 109 (1990).
- ³⁷⁴ T. Rakatomavo, Ph.D. thesis, Université de Montpellier, 1991.
- ³⁷⁵ P. Gall, J. P. Joly, V. Robert, J. P. Fillard, M. Castagné, and J. Bonnafé, *Electron. Lett.* **25**, 429 (1989).
- ³⁷⁶ T. Wilson and C. Sheppard, *Theory and Practice of Scanning Optical Microscopy*, (Academic, London, 1984).
- ³⁷⁷ P. Kidd, G. R. Booker, and D. J. Sirtland, *Appl. Phys. Lett.* **51**, 1331 (1987).
- ³⁷⁸ Z. Laczik, G. R. Booker, R. Falster, and W. Bergholz, *Appl. Phys. Lett.* **55**, 2625 (1989).
- ³⁷⁹ Z. Laczik, G. R. Booker, R. Falster, and N. Shaw, in *Proceedings of the Conference on Microscopy of Semiconducting Materials* (Oxford University Press, Oxford, 1989), p. 807.
- ³⁸⁰ G. R. Booker, Z. Laczik, and P. Kidd, *Semicond. Sci. Technol.* **A 7**, 110 (1992).
- ³⁸¹ Z. Laczik, P. Török, G. R. Booker, and R. Falster, in *Proceedings of the Conference on Microscopy of Semiconducting Materials* (Oxford University Press, Oxford, 1989), p. 785.
- ³⁸² Z. Laczik, G. R. Booker, R. Falster, and P. Török, *Mater. Sci. Forum* **83-87**, 1496 (1992).
- ³⁸³ R. Falster, Z. Laczik, G. R. Booker, A. R. Bhatti, and P. Török, in *Defect Engineering in Semiconductor Growth*, edited by S. Ashok, J. Chevallier, K. Sumino, and E. Weber (Materials Research Society, Pittsburgh, PA, 1992), p. 945.
- ³⁸⁴ B. K. Tanner, *X-ray Diffraction Topography* (Pergamon, Oxford, 1976).
- ³⁸⁵ G. A. Rozgonyi and D. C. Miller, *Thin Solid Films* **31**, 185 (1976).
- ³⁸⁶ A. R. Lang, *Acta Metall.* **5**, 358 (1957).
- ³⁸⁷ A. R. Lang, *J. Appl. Phys.* **29**, 597 (1958).
- ³⁸⁸ A. R. Lang, *J. Appl. Phys.* **30**, 1748 (1959).
- ³⁸⁹ W. Hartmann, in *X-ray Optics*, edited by H. J. Queisser, *Topics in Applied Physics* (Springer, Berlin, 1977), Vol. **22**, p. 191.
- ³⁹⁰ J. R. Patel and B. W. Batterman, *J. Appl. Phys.* **34**, 2716 (1963).
- ³⁹¹ J. R. Patel, *J. Appl. Phys.* **44**, 3903 (1973).
- ³⁹² T. Abe, in *VLSI Electronics*, edited by N. G. Einspruch and H. Huff (Academic, London, 1983), p. 3.
- ³⁹³ P. E. Freeland, K. A. Jackson, C. N. Lowe, and J. R. Patel, *Appl. Phys. Lett.* **30**, 31 (1977).
- ³⁹⁴ W. F. Berg, *Naturwissenschaften* **19**, 391 (1931).
- ³⁹⁵ C. S. Barrett, *Trans. Metall. Soc. AIME* **161**, 15 (1945).
- ³⁹⁶ R. W. James, *The Optical Properties of the Diffraction of X rays* (Cornell University Press, Ithaca, New York, 1965).
- ³⁹⁷ M. A. G. Halliwell, J. B. Childs, and S. O'Hara, in *Proceedings of the 1972 Symposium on GaAs* (Inst. of Phys., London, 1973), p. 98.
- ³⁹⁸ B. K. Tanner and D. K. Bowen, *Characterization of Growth Defects by X-ray Methods* (Plenum, New York, 1979).
- ³⁹⁹ A. J. Holland, G. S. Green, B. K. Tanner, and M. Zhenhong, *Materials Research Society Symp.* **209**, 475 (1991).
- ⁴⁰⁰ E. P. Bochkarev, S. N. Gorin, G. N. Petrov, and T. M. Tkacheva, *Mater. Sci. Forum* **83-87**, 1075 (1992).
- ⁴⁰¹ C.-O. Lee and P. J. Tobin, *J. Electrochem. Soc.* **133**, 2147 (1986).
- ⁴⁰² J. R. Patel, K. A. Jackson, and H. Reiss, *J. Appl. Phys.* **48**, 5279 (1978).
- ⁴⁰³ P. Wang, L. Chang, L. J. Demer, and C. J. Varker, *J. Electrochem. Soc.* **131**, 1948 (1984).
- ⁴⁰⁴ J. A. Rossi, W. Dyson, L. G. Hellwig, and T. M. Hauley, *J. Appl. Phys.* **58**, 1798 (1985).
- ⁴⁰⁵ D. Huber and J. Reffle, *Solid State Technol.* **August**, 137 (1983).
- ⁴⁰⁶ S. M. Hu, *J. Appl. Phys.* **70**, R53 (1991).
- ⁴⁰⁷ J. R. Patel and A. R. Chaudhury, *J. Appl. Phys.* **34**, 2788 (1963).
- ⁴⁰⁸ B. Leroy and C. Plougonven, *J. Electrochem. Soc.* **127**, 961 (1980).
- ⁴⁰⁹ K. Yasutake, M. Umeno, and H. Kawabe, *Appl. Phys. Lett.* **37**, 789 (1980).
- ⁴¹⁰ S. Takasu, H. Otsuka, N. Yoshihiro, and T. Oxu, *Jpn. J. Appl. Phys.* **20**, 25 (1981).
- ⁴¹¹ N. Yoshihiro, H. Otsuka, T. Oxu, and S. Takasu, *J. Electrochem. Soc.* **126**, 693 (1979).
- ⁴¹² L. E. Miller, in *Properties of Elemental and Compound Semiconductors*, edited by H. C. Gatos (Wiley, New York, 1960), p. 303.
- ⁴¹³ P. C. Parekh, *Solid-State Electron.* **14**, 273 (1971).
- ⁴¹⁴ F. Barson, M. S. Hess, and M. M. Roy, *J. Electrochem. Soc.* **116**, 304 (1969).
- ⁴¹⁵ J. E. Lawrence, in *Semiconductor Silicon 1973*, edited by H. R. Huff and R. R. Burgess (The Electrochemical Society, Pennington, NJ, 1973), p. 17.
- ⁴¹⁶ D. K. Schroder, in *Gettering and Defect Engineering in the Semiconductor Technology*, edited by M. Kittler (Sci-Tech, Vaduz, 1989), p. 383.
- ⁴¹⁷ D. K. Schroder, J. D. Whitefield, and C. J. Varker, *IEEE Trans. Electron Devices* **ED-31**, 463 (1984).
- ⁴¹⁸ D. K. Schroder, J. M. Hwang, J. S. Kang, A. M. Goodman, and B. L. Sopori, in *VLSI Science and Technology 1985*, edited by W. M. Bullis and S. Broydo (The Electrochemical Society, Pennington, NJ, 1985), p. 419.
- ⁴¹⁹ K. H. Yang, H. F. Kappet, and G. H. Schwuttke, *Phys. Status Solidi A* **50**, 221 (1984).
- ⁴²⁰ C. J. Varker, J. D. Whitfield, and P. Fejes, in *Defects in Semiconductors II*, edited by S. Mahajan and J. W. Corbett (North-Holland, New York, 1983), p. 187.
- ⁴²¹ M. Miyagi, K. Wada, J. Osaka, and N. Inoue, *Appl. Phys. Lett.* **40**, 719 (1982).
- ⁴²² S. N. Chakravarti, P. L. Gabarino, and K. Murty, *Appl. Phys. Lett.* **40**, 581 (1982).
- ⁴²³ J. M. Hwang and D. K. Schroder, *J. Appl. Phys.* **59**, 2476 (1986).
- ⁴²⁴ H. S. Kim, E. K. Kim, and S.-K. Min, *J. Appl. Phys.* **69**, 6979 (1991).
- ⁴²⁵ S. Kawado, T. Maruyama, T. Suzuki, N. Isawa, and K. Hoshi, *J. Electrochem. Soc.* **133**, 171 (1986).
- ⁴²⁶ T. Higuchi, E. Gaylord, G. A. Rozgonyi, and F. Shimura, *Appl. Phys. Lett.* **53**, 1850 (1988).
- ⁴²⁷ K. Hoshi, N. Isawa, T. Suzuki, and Y. Ohkubo, *J. Electrochem. Soc.* **132**, 693 (1985).
- ⁴²⁸ S. K. Pang and A. Rohatgi, *J. Electrochem. Soc.* **138**, 523 (1991).
- ⁴²⁹ C. J. Varker and K. V. Ravi, *J. Appl. Phys.* **45**, 272 (1974).
- ⁴³⁰ A. Y. Liang and C. J. Varker, in *Lifetime Factors in Silicon* (ASTM, Philadelphia, PA, 1980), p. 73.
- ⁴³¹ H. J. Queisser and A. Goetzberger, *Philos. Mag.* **8**, 1063 (1963).
- ⁴³² E. Simoen, J. Vanhellemont, A. Kaniava, and C. Claeys, *The Electrochemical Society Extended Abstracts* **93-2** 1993, p. 420.
- ⁴³³ J. Vanhellemont, E. Simoen, C. Claeys, A. Kaniava, E. Ganbas, A. Blondeel, and P. Clauws, in *Seventh International Symposium on Silicon Materials Science and Technology*, The Electrochemical Society Spring Meeting, San Francisco, CA, 1994.
- ⁴³⁴ W. J. Patrick, S. M. Hu, and W. A. Westdorp, *J. Appl. Phys.* **50**, 1399 (1979).
- ⁴³⁵ K. D. Beyer, S. Chakravarti, P. L. Garbarino, and K. Yang, *J. Electrochem. Soc.* **134**, 1753 (1987).
- ⁴³⁶ K. W. Tice and T. Y. Tan, *Appl. Phys. Lett.* **28**, 564 (1976).
- ⁴³⁷ T. Y. Tan, E. E. Gardner, and W. K. Tice, *Appl. Phys. Lett.* **30**, 175 (1977).
- ⁴³⁸ K. Nagasawa, Y. Matsushita, and S. Kishino, *Appl. Phys. Lett.* **37**, 622 (1980).
- ⁴³⁹ J. M. Andrews, C. A. Clark, S. Muller, and G. A. Rozgonyi, in *First International Symposium on VLSI Science and Technology Proceedings*, edited by C. J. Dell'Oca and W. M. Bullis (The Electrochemical Society, Pennington, NJ, 1982), p. 43.
- ⁴⁴⁰ K. Kugimiga, S. Akiyama, and S. Nakamura, in *Semiconductor Silicon*

- 1981, edited by H. R. Huff, R. J. Kriegler, and Y. Takeishi (The Electrochemical Society, Pennington, NJ, 1981), p. 294.
- ⁴⁴¹J. Andrews, in *Defects in Silicon*, edited by W. Murray Bullis and L. C. Kimerling (The Electrochemical Society, Pennington, NJ, 1993), p. 133.
- ⁴⁴²F. F. Villa and L. Paciaroni, in *Symposium on High Voltage and Smart Power ICs*, edited by M. Ayman Shibib (The Electrochemical Society, Pennington, NJ, 1989), p. 228.
- ⁴⁴³C. Weigel, J. Reifle, and D. Huber, in Seminar Data for Wacker's Tutorial Program on Silicon Materials Technology, 1986, p. B 20.
- ⁴⁴⁴M. A. Palmieri, Tesi di Laurea, Politecnico di Milano, 1989.
- ⁴⁴⁵M. Ataka and T. Ogawa, J. Mater. Res. **8**, 2889 (1993).